Webster, David Mark (2018) *The fragment effect: an innovative new approach to apatite (U-Th)/He thermochronology*. PhD thesis.

The Fragment Effect: an Innovative New Approach to Apatite (U-Th)/He Thermochronology

David Mark Webster

MESci

Submitted in fulfilment of the requirements for the degree of Doctor of Philosophy

Supervisors: Prof. Roderick Brown, Dr. Cristina Persano, Prof. Finlay Stuart

Sgorr Dhonuill – Ballachulish Igneous Complex, Scotland

School of Geographical and Earth Sciences
College of Science and Engineering
University of Glasgow, UK
October 2017

ABSTRACT

The uniquely low temperature sensitivity of the apatite (U-Th)/He system makes it an invaluable tool for studying shallow crustal processes which are not accessible through other techniques. Major advancements in both the theoretical and practical aspects of the technique have taken place over the past decade or so, however the routine application of the process is often held back by the perceived problem of single grain age ‘over dispersion’, particularly when applied to old, slowly cooled geological settings. There persists a misconception that age dispersion is indicative of a problem with the apatite (U-Th)/He system.

A significant component of single grain age dispersion is inherent to the natural system, and therefore beneficial to reconstructing robust thermal histories. Variations in crystal grain size, accumulated amounts of radiation damage and changes to the helium concentration gradient within a grain due to fragmentation all contribute positively to age dispersion. Other, imposed factors such as crystal zoning and ^{4}He implantation (which are undesirable) can also contribute to dispersion, however in the vast majority of cases their effects are negligible and only contribute noise to the inherent natural dispersion signal.

The Ballachulish Igneous complex (BIC) in western Scotland has been used as a case study to demonstrate the range of age dispersion which should be expected when analysing large numbers of single grain aliquots per sample. Where 20+ grains are analysed, total dispersion will often be well in excess of 100% for old, slowly cooled samples, indeed dispersion in excess of 200% is possible. Such dispersion will often be as a consequence of outlying or apparently anomalous ages, however such ages should not be discounted unless there is sound analytical justification to do so. Apparent anomalous ages will often be ‘swallowed up’ by the data if more, or even different sized/shaped grains are analysed. Due to the competing effects of the three main causes of inherent natural dispersion, it should not be expected that large, well dispersed data sets will show any significant correlation between single grain age and either grain size or eU concentration. However a lack of correlation does not indicate poor quality data.

Brown, Beucher and co-workers (Brown *et al.*, 2013; Beucher *et al.*, 2013) proposed a new modelling approach to account for the common occurrence of broken crystals in apatite separates, demonstrating that the additional inherent natural age dispersion arising from analysing fragments can be exploited when reconstructing thermal histories. A new inversion technique – HelFRAG was developed, based on a finite length cylinder diffusion

model. The model is computationally demanding, therefore sampling based inversion methods requiring many forward model simulations become less practical. Consequently, an approximation of the finite cylinder diffusion model has been incorporated into the modelling software QTQt (Gallagher, 2012). Here, the approximation – QFrag has been demonstrated capable of returning comparable results to the full HelFRAG inversion technique when given the same synthetic data set, enabling the more routine application of the fragment model.

Both QFrag and HelFRAG modelling techniques have been used to model the new BIC AHe dataset. The purpose is twofold: to demonstrate the importance of the fragment model with a real dataset, and to provide a new thermochronological interpretation for the BIC. When using this dataset, modelling samples individually shows only subtle differences (if any) between modelling broken grains correctly as fragments, verses modelling them incorrectly as whole grains. A far greater difference in the model output is seen when only modelling 3-6 grains compared to 20+, irrespective of whether fragments are treated correctly or not. When multiple samples are modelled together in a vertical profile, the fragment effect becomes much more important. A very different thermal history interpretation arises when any broken grains are modelled incorrectly as whole grains compared to when modelled as fragments.

The new thermal history interpretation for the BIC involves a four stage cooling history from the time of intrusion (c. 424Ma). Very rapid cooling and uplift occurred immediately after intrusion over the first c. 20Myrs of the history (*Phase 1*). This brought the complex from c. 10km depths to within 2-3km of the surface. There followed much slower continued uplift between c. 404Ma and c. 300Ma, resulting in up to 1km of denudation (*Phase 2*). Over the next c. 150Myrs only a small volume of uplift occurred, however the geothermal gradient increased towards the end of this time period, suggesting crustal thinning (*Phase 3*). A final, rapid period of cooling and uplift occurred at c. 140Ma, bringing the top of the profile very near to the surface (*Phase 4*). No significant denudation has occurred since the end of this rapid uplift phase (10's to 100's of meters at most). The first two phases of cooling are interpreted as the final stages of the Caledonian orogeny, with erosion driven isostatic uplift causing continued denudation after the cessation of collisional tectonics. The end of phase three and the subsequent rapid uplift (*Phase 4*) are interpreted as the beginnings of crustal thinning and continental rifting which ultimately led to the opening of the North Atlantic Ocean.

TABLE OF CONTENTS:

LIST OF TABLES:

LIST OF FIGURES:

ACKNOWLEDGEMENTS:

I would like to thank: The lab technicians at the University of Glasgow - Robert MacDonald and John Gilleece for their guidance and assistance during sample preparation and mineral separation. The lab technician at SUERC, Dr. Luigia DiNicola for her guidance and instruction during the analytical procedure for ^{4}He extraction and ICPMS. Additionally I would like to thank my fellow Ph.D. students (at the time) Dr. Mark Wildman and Dr. Kasia Luszczak for their assistance and instruction in various aspects of the practical process, including (but not limited to) apatite picking and screening and mineral separation.

Thanks go to Prof. Kerry Gallagher (University of Rennes) for his constructive comments and feedback on Chapter 4, who at times acted as an unofficial 4th supervisor. Prof. Gallagher is also deserving of thanks for his patient and informative instruction in the use of QTQt, without which much of this project would not have been possible.

Thanks go to my fellow current Ph.D. student Awara Amin, who carried out all of the new fission track sample preparation and analyses included in this thesis. Awara also provided collaboration with joint modelling of the AFT and AHe datasets, a collaboration which is ongoing.

Thanks go to previous L4 student at the University of Glasgow Matt Forrester, who carried out the sampling of samples labelled $SD13 - 0x$, as well as the mineral separation process on those samples. This provided me with ready-made apatite separates to get to work on from the outset of the project, increasing productivity from the start. Thanks also go to Liza Turkova for her field work assistance (and driving) for the collection of samples labelled $BH13 - 0x$. This would not have been possible without the use of her car.

Finally a big thank you goes to my supervisor team – Prof. Rod Brown, Dr Cristina Persano and Prof. Fin Stuart for their guidance, direction and general overseeing of the project.

This research was supported by a NERC doctoral scholarship.

DECLARATION

I declare that, except where explicit reference is made to the contribution of others, this document is the result of my own work and has not been submitted for any other degree at the University of Glasgow or any other institution.

David M. Webster

Date:

LIST OF ABBREVIATIONS:

ADAM: Alpha-Damage Anealing Model

AFT: Apatite Fission Track dating

AHe: Apatite Helium dating

Ar: Argon

BF: Ballachulish Fault

BIC: Ballachulish Igneous Complex

CL: Cathodoluminescence

Cl: Chlorine

Cu: Copper

CYLON: CY(linder) L_0 N – fragment list generating program

EDM: External Detector Method (fission track dating)

eU: effective Uranium [U]+0.235*[Th]

F: Flourine

***F_T*:** alpha ejection Correction Factor

FT: Fission Track analysis/dating

GA: Genetic Algorithm

GBP: Grain Boundary Phase

GGF: Great Glen Fault

GVC: Glencoe Volcanic Complex

HBF: Highland Boundary Fault

He: Helium

HeFTy: Helium and Fission Track inverse modelling computer program

HelFRAG: Helium Fragment model inversion program

HF: Hydrofluoric acid

ICPMS: Inductively Coupled Plasma Mass Spectrometry

K: Potassium

LA-ICPMS: Laser Ablation - Inductively Coupled Plasma Mass Spectrometry

Ma: Mega Anum (million years)

MF: Moine Thrust Fault

Mo: Molybdenium

MTL: Mean Track Length (of fission tracks)

PAZ: Partial Annealing Zone

Pb: Lead

PPL: Plain Polarized Light

PRZ: Partial Retention Zone

Pt: Platinuim

RDAAM: Radiation Damage and Accumulation and Annealing Model

QFrag: QTQT Fragment model

SEM: Scanning Electron Microscope

Sm: Samarium

SUERC: Scottish Universities Environmental Research Centre

SUF: Southern Upland Fault

(S/V): Surface area to volume ratio

T_c: effective Closure Temperature

Th: Thorium

TIP: British Tertiary Igneous Province

TLD: Track length Distribution (of fission tracks)

U: Uranium

(U-Th)/He: (Uranium – Thorium) Helium dating

XPL: Cross Polarised Light

α: alpha particle (^{4}He)

0T: Zero crystal Terminations

1T: One intact crystal Termination

2T: Two intact crystal Terminations (i.e. a whole crystal)

CHAPTER 1

1. INTRODUCTION

(On fieldwork near Bamako – Mali)

1.1 Background

The apatite (U-Th)/He thermochronology technique (AHe) is unique in the thermochronology world as it is currently the only technique applicable to studying the temperature range characteristic of the upper c. 3-4km portion of the crust. This enables the study of geological processes not currently accessible through other thermochronological techniques (e.g. Farley, 2002; Ehlers and Farley, 2003). Like all radiometric dating techniques, it utilises the radioactive decay of a parent (or parents) isotope to a measurable daughter product. In this instance, ^{238}U, ^{235}U and ^{232}Th (+^{147}Sm) undergo α decay, producing ^{4}He (i.e. an α particle) (Rutherford, 1905; Strutt, 1905). The concentrations of ^{4}He and the parent isotopes can be measured to calculate an age, but as radiogenic ^{4}He diffuses out of a crystal over time at a rate dependant on the temperature of the host rock, the calculated age refers not to an absolute crystal age but rather a cooling age (Zietler *et al.*, 1987).

The cooling age relates to the systems effective Closure Temperature (T_c) – the temperature of the dated mineral at the time corresponding to its apparent age (Dodson, 1973). This refers to the temperature below which all radiogenic daughter products are retained within the crystal over geological timescales. For ^{4}He in apatite this temperature is c. 35°C, but varies depending on the grain size and cooling rate (Farley, 2000; Reiners and Farley, 2001). There exists a temperature window where the rate of production of radiogenic daughter products exceeds the rate of loss of the daughter through thermally active diffusion, but diffusive loss is still occurring. This results in the retention of a given percentage of the daughters produced, specific to the time spent in this temperature window. Along with the effective Closure Temperature (T_c), this window defines a Partial Retention Zone (PRZ) (Baldwin and Lister, 1998) which is c. 35-85°C for ^{4}He in ‘typical’ sized apatite grains of c. 30-90µm radius (Wolf *et al.*, 1998; Reiners and Farley, 2001). In the literature, the upper limit of the PRZ is often referred to as the systems ‘closure temperature’, but strictly speaking the lower limit more closely represents the Closure Temperature (T_c) as defined by Dodson (1973).

The uniquely low temperature range sensitivity of the apatite (U-Th)/He thermochronometer has proved invaluable for many branches of the geoscience community. Applications for the technique include:

- Studying the timing, rate and sense of major fault movements (e.g. McInnes *et al.*, 1999; Stockli *et al.*, 2000; Carter *et al.*, 2004; Clark *et al.*, 2010). This can support metalliferous ore exploration.
- Studying the thermal history of sedimentary basins for the purpose of hydrocarbon exploration (e.g. Crowhurst *et al.*, 2002; Green *et al.*, 2004).
- Dating river incisions to reconstruct palaeotopography (e.g. House *et al.*, 1998; Schildgen *et al.*, 2007; Flowers *et al.*, 2008; Flowers and Farley, 2012).
- Studying erosion patterns within a river catchment (e.g. Stock *et al.*, 2006; Tranel *et al.*, 2011).
- Studying regional scale uplift and denudation histories (e.g. Persano *et al.*, 2002; Blythe *et al.*, 2007; Wildman *et al.*, 2016).

In conjunction with other low temperature thermochronometers (e.g. Apatite Fission Track (AFT) and Zircon He/FT), Apatite Helium (AHe) dating can be used to build up a picture of the past history of the entire land surface and the tectonic processes which have led to its present day topography.

1.2 Rationale

Over the last decade or so major advancements have taken place in both the theoretical and practical aspects of the (U-Th)/He technique (e.g. Reiners and Farley, 2001; Farley, 2002; Shuster and Farley, 2005; Flowers *et al.*, 2009; Gautheron and Tassan-Got, 2010). However these advancements are often undermined by the perceived problem of age 'over dispersion' commonly observed for single grains within a sample. Age 'over dispersion' (dispersion greater than can be accounted for through analytical uncertainty alone (Vermeesch, 2010)) is especially evident in samples from slowly cooled terranes such as cratons, and its cause and consequences are still open to debate (e.g. Reiners and Farley, 2001; Fitzgerald *et al.*, 2006; Flowers *et al.*, 2007; Vermeesch *et al.*, 2007; Farley *et al.*, 2010). This has limited the routine application of the methodology in the past.

It has been argued that the observed dispersion within a sample can be ascribed to either natural variations in crystal grain size (e.g. Reiners and Farley, 2001) or variations in parent isotope abundances leading to differing levels of radiation damage affected ^{4}He diffusivity (e.g. Shuster *et al.*, 2006; Flowers *et al.*, 2007). When either grain size or U and Th concentrations correlate with age within a sample, then any 'over dispersion' may be able to be satisfactorily explained (this has traditionally been the view, but the system is now known to be more complex). However in many instances the single grain ages from a given sample are severely dispersed, and often uncorrelated with either grain size or U and Th content (e.g. Fitzgerald *et al.*, 2006; Kohn *et al.*, 2009; Flowers and Kelley, 2011). This suggests that there must be at least another common cause of dispersion other than absolute grain size or differences in ^{4}He diffusivity caused by radiation damage accumulation.

It is now standard practice to analyse single grains (e.g. Farley *et al.*, 2010) as opposed to the multi-grain aliquots used in the past (e.g. Persano *et al.*, 2007). The individual prismatic apatite crystals tend to become broken parallel to the weak cleavage plain orientated 90° to the C-axis during rock crushing and mineral separation (see figure **1.1**). This is indicated by the regular occurrence of only one or sometimes no crystal terminations in apatite mineral separates (e.g. Farley, 2002; Farley *et al.*, 2010). Brown *et al.* (2013) and Beucher *et al.* (2013) have shown that much of the age 'over dispersion' not accounted for by natural grain size and U and Th variation can be explained by treating these broken grains explicitly as fragments of larger whole grains of an unknown original length. This is then utilised in a new finite length cylinder diffusion model which is used to generate robust thermal histories with the new inverse computer modelling program HelFRAG. They show that, far from being problematic, 'over dispersion' is in fact desirable for reconstructing robust thermal histories.

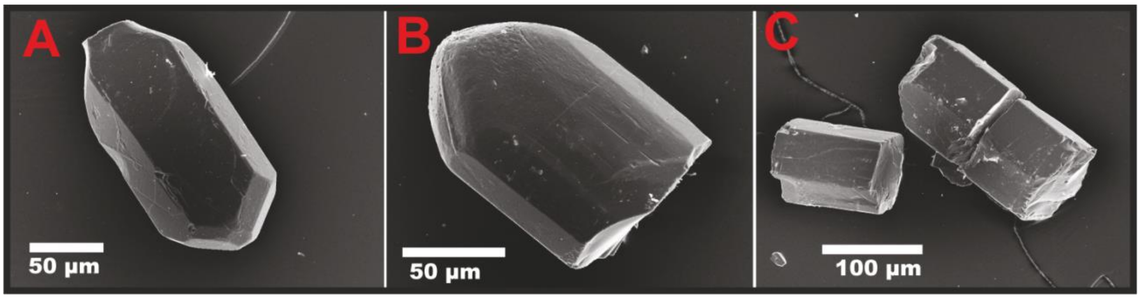

Figure 1.1: Typical euhedral apatite crystals.
SEM images of three apatite crystals picked from a medium grained gabbro from the Bushveld Complex, South Africa (BK1). **A**: characteristic euhedral whole (2T) grain. **B**: broken 1T (1 crystal termination) grain with clean fracture perpendicular to the crystallographic C-axis. **C**: two broken 0T grains (no crystal terminations) with fractures perpendicular to the C-axis. Such clean fractures are believed to have formed during the vigorous mineral separation process. After Brown *et al.* (2013).

1.3 Aims

The main aim of this thesis is to provide an empirical test of the new HelFRAG computer model, using the Ballachulish Igneous Complex (BIC) in western Scotland as a case study. An approximation of the finite cylinder diffusion model has been incorporated into the QTQt modelling software of Gallagher (2012) – QFrag. This will also be tested. QFrag provides a much swifter and less computationally demanding approximation to the approach used in HelFRAG, enabling the new modelling technique to be more easily applied. The thesis also aims to demonstrate the range and complex nature of single grain age dispersion typically found in samples from old and slowly cooled crustal terranes, using Highland Scotland as an example. Ultimately this work will also provide a new and updated comprehensive thermochronological study of the Ballachulish Igneous Complex (BIC). The new thermal history interpretation will further be discussed in relation to the thermal/tectonic evolution of the western Scottish Atlantic margin.

1.4 Case study area

The Ballachulish Igneous Complex is located at the junction of Lochs Linnhe and Leven in western Scotland. Its peaks form part of the Grampian belt of the Scottish Highlands, the mountainous terrain north of the Highland Boundary Fault (HBF) and south east of the Great Glen Fault (GGF). It is bounded on its north west by the Great Glen (and GGF) which connects the sea loch of Loch Linnhe in the south west through to the Moray Firth in the north east (figure **1.2**). It is a roughly cylindrical granitic intrusive complex with an exposure of c. 7.5 x 4.5km^2 which extends to a depth of about 4km (Rabbel and Meissner, 1991). It has a relief of 1001m, from sea level to the summit of Sgorr Dhonuill.

The BIC has been chosen as an appropriate case study because it has a well constrained geological history, having been extensively studied in the past (e.g. Anderson, 1937; Weiss and Troll 1989; Pattison and Harte, 2001). In addition, the work of Persano *et al.* (2007) provides a thermochronological framework on which to compare and contrast the results from this new study, allowing a first order assumption to be made on the ‘known’ thermal history. The work of Persano *et al.* (2007) also demonstrates that the BIC is a reliable source of good quality euhedral apatite grains with a range of sizes and eU concentrations, a component which is vital in this study. Although not strictly cratonic, the geology of the Scottish Highlands is old and complex, and is exactly the kind of region that can provide problematic ‘over dispersed’ AHe ages, making it a particularly suitable case to this study.

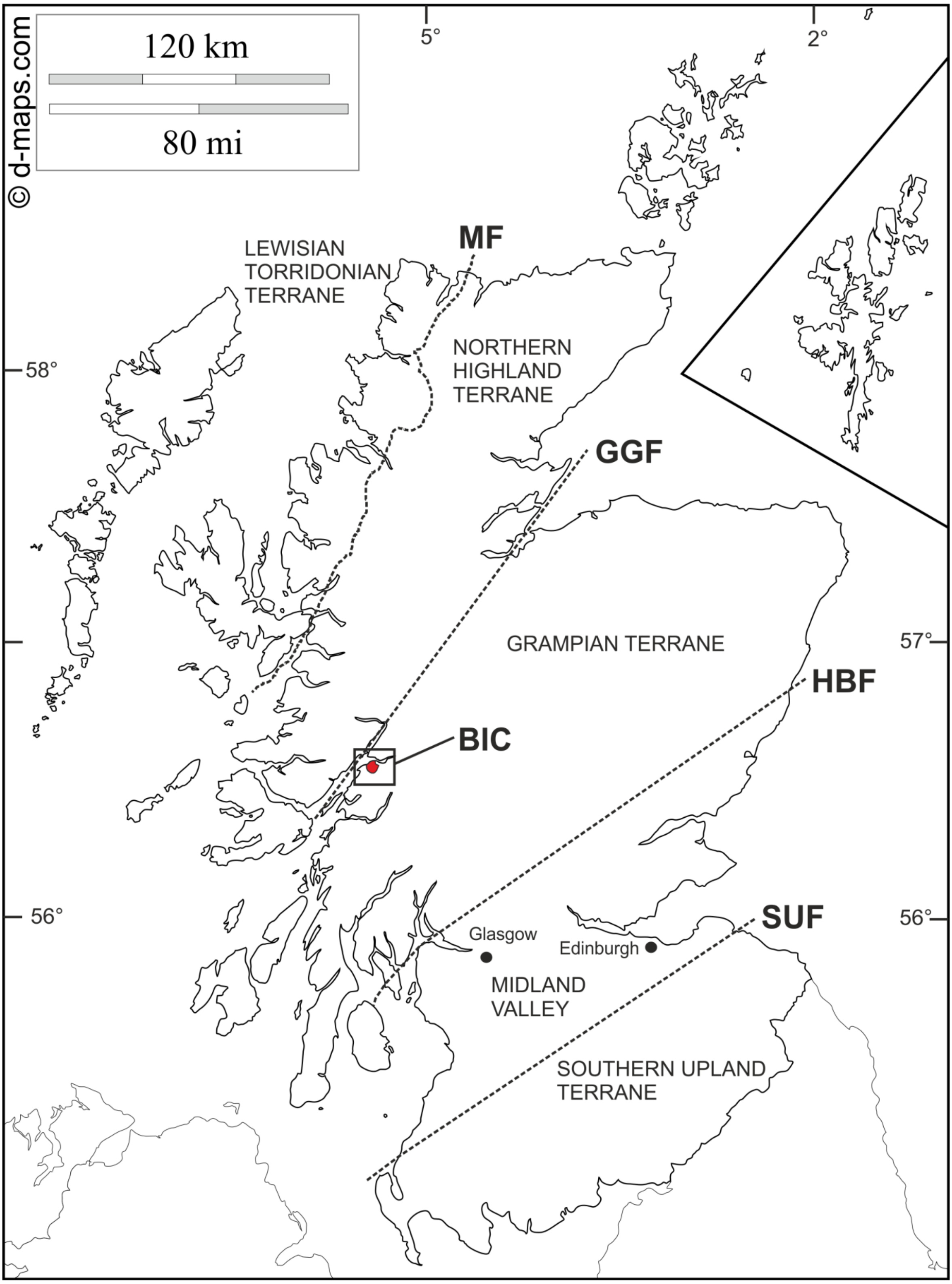

Figure 1.2: Location map**.**
Outline map of Scotland showing the case study location of the Ballachulish Igneous Complex (BIC - red circle). Also shown are the major faults that bound the distinct geological terranes of Scotland: Lewisian and Torridonian Terrane, Northern Highland Terrane, Grampian Terrane, Midland Valley Terrane and the Southern Upland Terrane. MF = Moine Thrust Fault, GGF = Great Glen Fault, HBF = Highland Boundary Fault and SUF = Southern Upland Fault.

1.5 Thesis outline

Below is a summary of the major contents of each chapter in this document:

1.5.1 *Chapter 2:*

Chapter 2 provides a comprehensive review of the history of the apatite (U-Th)/He technique, with a focus on the discussions and developments surrounding single grain age ‘over dispersion’. This supports the rationale behind the project, with a detailed explanation of the new fragment model of Brown *et al.* (2013) and Beucher *et al.* (2013).

1.5.2 *Chapter 3:*

Chapter 3 provides a summary of the key developments in the apatite fission track (AFT) technique and how this can complement AHe analyses. The future of fission track dating is also discussed, with recent developments in automation and double dating techniques highlighted.

1.5.3 *Chapter 4:*

In chapter 4, the approximation of the finite cylinder diffusion model which has been incorporated into the QTQt modelling software (QFrag) is tested. This provides a demonstration of the effectiveness of the approximation at replicating the results of HelFRAG, ultimately justifying the extensive use of QFrag in **Chapter 6**.

1.5.4 *Chapter 5:*

Chapter 5 presents the raw AHe data from the Ballachulish Igneous Complex (BIC) and provides an in depth analysis of the nature and extent of single grain age dispersion. This includes a detailed discussion on the causes of the dispersion and its implications for thermal history modelling.

1.5.5 *Chapter 6:*

In chapter 6, the raw data are modelled extensively using QTQt, with additional modelling using the HelFRAG modelling software. This provides both an analysis of the fragment effect and an updated thermal history interpretation for the BIC. A discussion is provided on best practices for modelling single grain AHe data, and on the geological interpretations of the newly generated thermal history.

1.5.6 *Chapter 7:*

Chapter 7 provides a brief summary of the content discussed in each chapter, plus an outline of potential future work related to this thesis. Finally the chapter summarises the main conclusions developed throughout the thesis.

CHAPTER 2

2. MAJOR DEVELOPMENTS IN AHe THERMOCHRONOLOGY

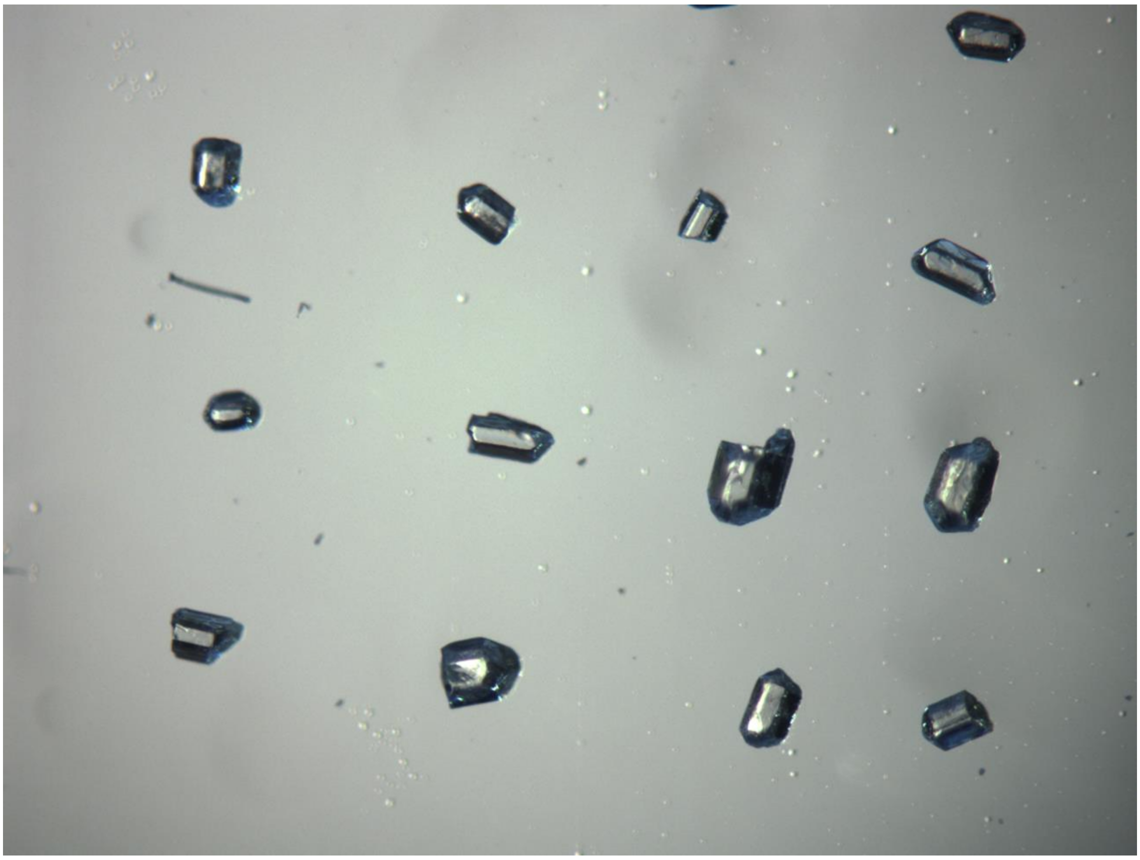

(Selection of apatites from sample *SD07-6* as viewed under the standard picking microscopes)

2.1 Early work on the (U-Th)/He system

The radioactive decay of uranium and thorium to helium was one of the first radioactive decay series to be studied (e.g Rutherford, 1905; Strutt, 1905). Strutt discovered that almost no helium was present in minerals except where thorium was also present. This led him to theorise that within minerals the helium must be produced by the radioactive decay of thorium. He also speculated that helium is the primary product of α-decay, something which we now know to be the case (an α-particle is an ^{4}He isotope). He recognised that this could be used as a tool for the dating of minerals (and therefore by extrapolation rocks), essentially giving birth to geochronology.

Following the initial studies into the method, the technique was seldom used, and when it was it often returned unreasonably young ages (e.g. Hurley, 1954; Leventhal, 1975; Ferreira *et al.*, 1975). The U-Th-He dates were consistently much younger than those from other dating techniques (such as K-Ar) and did not fall within the “known” geological age as constrained through different techniques such as biostratigraphy and dendrochronology. This led the authors to state that He is lost from the system over time, and to speculate as to the potential causes of this He loss. For example Levanthal (1975) theorised that He can ‘leak’ out of a grain surface along crystal defects and radiation damage tracks.

Zietler *et al.* (1987) first noticed the potential of U-Th-He dating as a thermochronometer, particularly when applied to apatite. Through their experience with Apatite Fission Track (AFT) dating, they suspected that Apatite Helium (AHe) dating could prove a useful low temperature thermochronometer. They suggested that many of the too-young AHe ages reported in the literature were too young because helium had been lost by thermal diffusion, providing actual evidence of its usefulness for reconstructing thermal histories, and not of recalcitrance on the U-Th-He system.

Zeitler *et al.*’s (1987) paper did not initially stimulate a major response, and it was not until the late 1990’s that (U-Th)/He thermochronology really took off as a low temperature thermochronometer, greatly aiding in our understanding of shallow crustal processes. To facilitate this, a detailed analysis of the nature of α-ejection and ^{4}He diffusion within apatite was required.

Wolf *et al.* (1996) carried out long duration incremental out-gassing experiments on a series of apatites including Durango flourapatites to study the rate of helium loss as a function of temperature. From this, they proposed that helium loss occurs via volume diffusion from a sub grain domain <60µm across which is nearly identical in size in all their samples, irrespective of the actual grain size and composition. They also discovered that below 290°C the diffusivity of helium out of the crystal obeys a highly linear Arrhenius relationship, and this suggests an activation energy of 36 kcal mol^{-1}. Above 290°C the diffusivity and activation energy changes, but this was considered largely irrelevant to thermochronology as above that temperature essentially all helium is lost over geological time.

Farley *et al.* (1996) investigated the kinetics of α-decay within the common U-Th bearing accessory minerals (apatite, zircon and titanite). This was to ascertain the effective stopping distance of α-particles within the host rocks. They calculated that α-particles in apatite have mean stopping distances of 19.68µm, 22.83µm and 22.46µm respectively for the ^{238}U, ^{235}U and ^{232}Th decay series. The relatively long stopping distances have implications for the routine methodology, as for a given apatite crystal a certain percentage of radiogenic helium will be directly ejected from the crystal and lost from the system (figure **2.3**), which is independent to diffusive loss. To account for α-ejection, Farley *et al.* (1996) introduced a "correction factor" (F_T) which is now routinely used in AHe dating.

Further to the work of Wolf *et al.* (1996), Farley (2000) found the diffusion domain of helium in apatite to be the physical grain itself, as opposed to a sub grain domain; making the actual grain size an important parameter to be measured (this was down to improvements in the precision of the analytical procedure). Therefore the closure temperature must vary with grain size as the whole grain is the diffusion domain. This contrasted with the findings of Wolf *et al.* (1996). The slightly lower activation energy of 33kcal mol^{-1} reported in his paper lead to a slightly lower closure temperature (68°C ± 5°C - grain of 90µm radius and cooling rate of 10°C Myr^{-1}) for the thermochronological system than the closure temperature previously reported (75°C ± 7°C).

As it was accepted that the physical grain represents the helium diffusion domain, it was important to be able to model the production and diffusion of helium for realistic crystal geometries (Meesters and Dunai, 2002a; 2002b). It is standard practice to use spherical grain geometries when modelling helium diffusion, but this is not a true representation of an apatite crystal. The authors provided an efficient solution for the production-diffusion equation for a finite cylinder geometry, which more accurately represents an apatite crystal (as well as other geometries for other minerals). They demonstrated however that using a spherical geometry for the calculation with the same surface-to-volume ratio as the original whole crystal is an adequate approximation, and this holds true even when moderate U-Th zonation is taken into account.

Gautheron and Tassan-Got (2010) developed a Monte Carlo simulation for ^{4}He diffusion which can be applied to any realistic crystal shape (i.e. a hexagonal prism with two pyramidal terminations such as a euhedral apatite crystal). Although this made the modelling of specific grain shapes possible, they also support the assumption that modelling grains as spheres with the same surface area to volume ratio as the true crystal can adequately simulate diffusive loss, but only when diffusion within a crystal is isotropic (as is believed to be the case for apatite). For anisotropic diffusion (such as ^{4}He in zircon) they introduced a new concept – the 'active radius', which deals with the extra complexities of anisotropic diffusion enabling the spherical assumption to still be utilised.

2.2 Age dispersion

A recurring problem (or perceived problem) with AHe thermochronological studies is age dispersion of single grain ages determined for the same sample (e.g. Reiners and Farley, 2001; Fitzgerald *et al.*, 2006; Green and Duddy, 2006). This is defined as the range (maximum age – minimum age) divided by the mean (Brown *et al.*, 2013). Dispersion is used in reference to the data as opposed to standard deviation because the distribution of single grain ages is often strongly skewed, therefore the standard deviation isn't a particularly useful statistical measure of variation. Particularly in old/slowly cooled samples, single grain age dispersion can often exceed 100% (e.g. Kohn *et al.*, 2009; Flowers and Kelly, 2011; Fillion *et al.*, 2013; Gautheron *et al.*, 2013a) and this has cast doubt as to the validity of the AHe system (e.g. Green and Duddy, 2006). Causes of dispersion can be subdivided into two types – inherent natural dispersion ('good') and imposed extraneous dispersion ('bad') (Brown *et al.*, 2013).

2.2.1 *Inherent natural dispersion*

This is dispersion caused by inherent components of the (U-Th)/He system, which can be considered 'good' dispersion. They include: grain size variation (e.g. Farley, 2000; Reiners and Farley, 2001), variable eU (effective uranium) (e.g. Shuster *et al.*, 2006; Flowers *et al.*, 2007; Flowers, 2009; Kohn *et al.*, 2009), crystal fragmentation (Brown *et al.*, 2013; Beucher *et al.*, 2013) and variable crystal composition (Gautheron *et al.*, 2013b; Djimbi *et al.*, 2015). These are causes which are always present, and actually prove useful to the thermochronologist.

‘Good’ dispersion is useful because it is impossible to derive a unique thermal history from a single age measurement, even if that age represents a mean (or another representative average) based on multiple single grain analyses. Many different temperature-time (T-t) paths can result in any given single age. Having a range of single grain ages, which all must have undergone the same thermal history, enables a common and unique thermal history to be modelled for the sample (or even better, for a range of samples in a profile).

2.2.1.1 Grain Size: The physical grain has been demonstrated to represent the helium diffusion domain in apatite (Farley, 2000). This means that the true proportions of the grain are an important parameter when reconstructing thermal histories. Specifically the surface area to volume ratio is critical. Small apatite crystals have larger surface area/volume (S/V) ratios than larger crystals, meaning a greater proportion of the radiogenic ^{4}He will be close to the grain boundary and therefore have less far to travel to diffuse out of the crystal than in larger crystals. This means a greater proportion of the ^{4}He will be lost over a given time for a given thermal history than for a bigger crystal, resulting in a younger AHe age (e.g. Reiners and Farley, 2001). Where there is a range of grain sizes in a sample, the grain size effect can result in a positive correlation between grain size and age when size is represented by the equivalent spherical radius of a grain with the same (S/V) ratio (R*). This can be seen for a number of samples in this thesis, examples of which are shown in figure **2.1**.

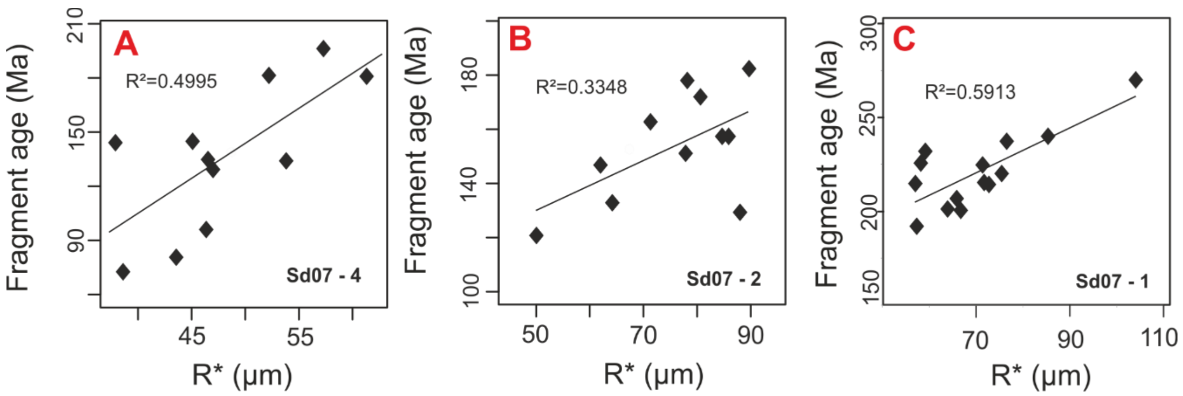

Figure 2.1: Examples of the age – grain size positive correlation.
Three examples of samples from the Ballachulish Igneous Complex (Scotland) presented in this thesis which show a positive correlation between grain size (in terms of the equivalent spherical radius, R*) and age. **A**: *SD07 – 4*, **B**: *SD07 – 2* and **C**: *SD07 – 1*. However the correlation is less evident in the majority of samples presented in this thesis, see **Chapter 5** (and figures therein) for the full sample set and a breakdown of the raw data.

2.2.1.2 eU Concentration: Effective uranium (eU) concentration is calculated as:

$$\mathrm{eU} = [\mathrm{U}] + 0.235[\mathrm{Th}]$$

It is a measure of the relative importance to α-decay of the different parent nuclides: ^{238}U, ^{235}U and ^{232}Th. Average eU concentration can prove to be quite variable between different grains within a sample. The current models for the effect of radiation damage and accumulation imply that these differences in eU may produce very large differences in age for some thermal histories (e.g. Flowers *et al.*, 2007; Flowers, 2009; Gautheron *et al.*, 2009). These models predict that grains with a higher eU yield older ages than those with lower eU for the same thermal history due to the effect of radiation damage (from α-particle recoil and spontaneous fission) on the crystal lattice. Fission and α recoil tracks create 'traps' within the crystal structure which impede ^{4}He diffusion, so a grain with a higher eU will have more 'traps' and therefore retain more ^{4}He than a lower eU grain for the same thermal history, giving an older age (figure **2.2**) (Shuster *et al.*, 2006). It is possible that as eU increases above a certain threshold the damage tracks can become interlinked, creating a pathway for ^{4}He loss as opposed to 'traps'. This would lead to progressively younger ages as eU increases, as is the case in the zircon helium (ZHe) system (Guenthner *et al.*, 2013). The effect of radiation damage accumulation is an area of ongoing research for the AHe system (e.g. Gerin *et al.*, 2017), so currently a positive relationship is assumed in the radiation damage models incorporated into thermochronological software.

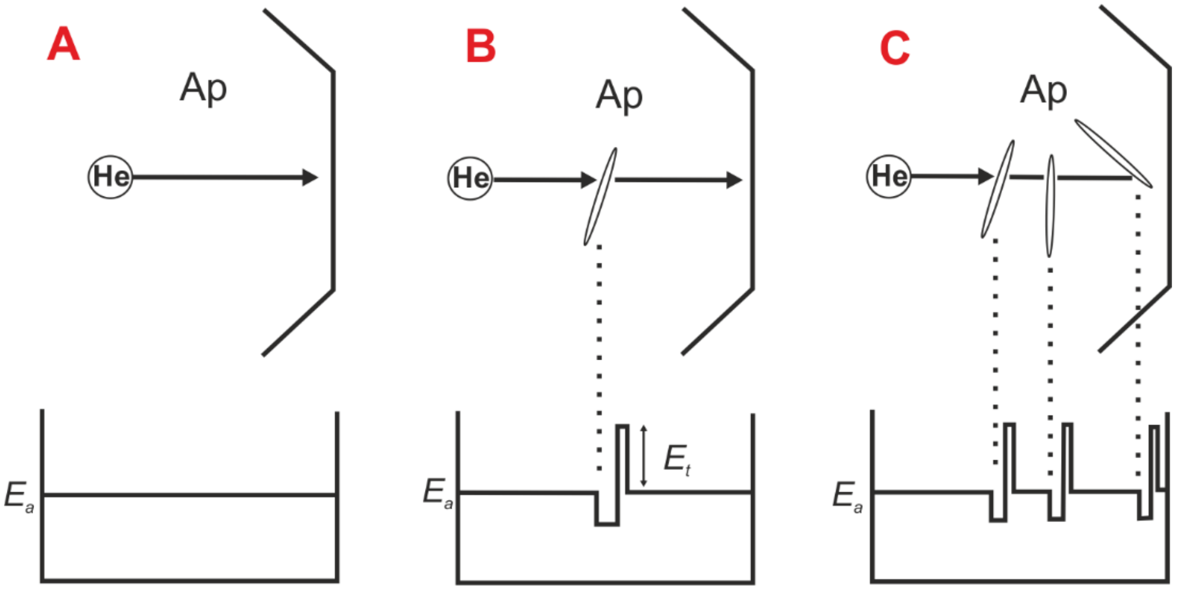

Figure 2.2: Cartoon representation of the 'trapping' model for accumulated radiation damage. Figure highlighting the fact that as more radiation damage accumulates, more energy is required for ^{4}He diffusion (after Shuster *et al.*, 2006). **A**: diffusion of a ^{4}He atom through an undamaged apatite crystal. **B**: diffusion of a ^{4}He atom across the same distance but encountering a radiation damage site (depicted here as a fission track, but also includes alpha recoil damage). **C**: diffusion of a ^{4}He atom across the same distance but encountering multiple damage sites (fission tracks). Upper panels are cartoon representations of a crystal cross section, lower panels are plots of the effective activation energy for diffusion of a ^{4}He atom across the crystal. Ap = apatite crystal. **He** = ^{4}He atom. E_a = activation energy for volume diffusion. E_t = energy required to move up out of a 'trap' back into the undamaged crystal.

2.2.1.3 Fragmentation: This has been largely overlooked as a cause of inherent natural dispersion, but Brown *et al.* (2013) and Beucher *et al.* (2013) have demonstrated its importance and this will be developed further in this thesis. Whole grains are often absent or rare after mineral separation (see figure **1.1**), and this is largely down to the vigorous mineral separation process (Farley *et al.*, 1996; 2010; Farley, 2002). This can prove problematic as treating a fragment as a whole grain is misleading. Depending on which section of the original whole grain the fragment represents, it can either result in an age too old for the original whole crystal, or too young (Brown *et al.*, 2013). For a full description of the fragment effect, see section **2.3** of this chapter.

2.2.1.4 Compositional variation: Apatite crystals vary compositionally between three main end members: flourapatite, chlorapatite and hydroxylapatite depending on the relative abundances of F^-, Cl^- and OH^- ions. Compositional variation, particularly between the F^- and Cl^- rich end members is known to have an effect on fission track annealing rates, and therefore AFT ages (Gleadow and Duddy, 1981; Green *et al.*, 1986; Laslett *et al.*, 1987). It is considered likely to also have an effect on the AHe system as it will affect radiation damage dependent ^{4}He diffusivity (Gautheron *et al.*, 2013b). Composition not only affects radiation damage annealing, but also the ^{4}He retentivity of undamaged apatite. Increased Cl^- content can increase ^{4}He retentivity, leading to older AHe ages (Djimbi *et al.*, 2015). ^{4}He diffusion has a higher activation energy (E_a) across chlorine atoms (166.7kJ mol^{-1}) than fluorine (95.5 - 106.1kJ mol^{-1}) in the crystal lattice, resulting in a closure temperature up to 12°C higher for apatites with $Cl_{0.25}$ chlorine content (Djimbi *et al.*, 2015). Compositional effects on diffusion is an area of new and ongoing research, so composition can currently be considered ‘bad’ dispersion as its effects are not fully quantified. It is however a characteristic inherent to the natural system and therefore relevant to the inherent natural dispersion once better understood.

2.2.2 *Imposed extraneous dispersion*

This is dispersion which is external to the ideal system, that is to say something which it is hoped to avoid when carrying out the standard methodology. It can therefore be considered ‘bad’ dispersion. These causes can ‘muddy the water’ for the natural dispersion signal, complicating the matter of reconstructing thermal histories. Within the bounds of the pre-existing methodology, every effort is made to mitigate the imposed causes of dispersion, or account for them in the computational/mathematical models.

2.2.2.1 U-Th Zonation: When carrying out AHe dating, a homogeneous distribution of the parent elements is usually assumed (and is ideally required). But parent homogeneity isn't always the case (e.g. Ault and Flowers, 2012). A crystal may in fact be zoned in U and Th, with either rim-rich or core-rich end member's possible (figure **2.3**). If a crystal is rim-rich, then a greater proportion of the daughter ^{4}He will end up near the outer edge of the crystal, meaning it will take less time (and energy) for it to diffuse out of the crystal. This will result in less helium retained within the crystal, causing a younger age. The effects of radiation damage on diffusion will also be heterogeneous, further dispersing the age. In addition to the effects on diffusion a far greater proportion of the ^{4}He will be lost from the crystal through α-ejection (see section *2.2.2.2*), giving a younger age. The reverse of the above is true when a crystal is core-rich, which can give an unexpectedly old age (Meesters and Dunai, 2002b; Gautheron *et al.*, 2012).

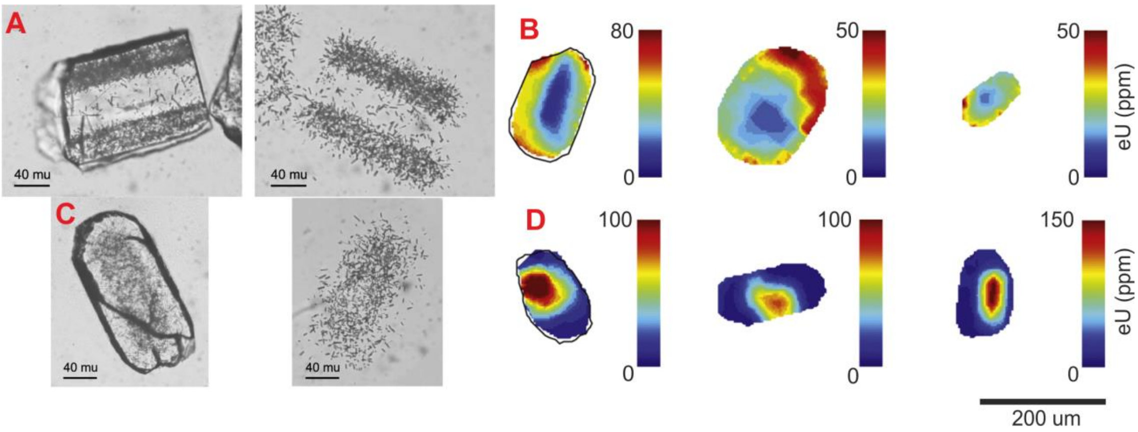

Figure 2.3: Example zoning profiles across apatite crystals.
A: a typical rim-rich crystal as seen through the crystals fission track density of spontaneous (left) and induced (right) tracks. **B**: example rim-rich apatite crystals as seen through eU mapping by ICPMS. **C**: a typical core-rich crystal as seen through the crystals fission track density of spontaneous (left) and induced (right) tracks. **D**: example core-rich apatite crystals as seen through eU mapping. After Meesters and Dunai (2002b) (**A** and **C**, photos courtesy of Bart Hendricks) and Ault and Flowers (2012) (**B** and **D**).

Both Gautheron *et al.* (2012) and Ault and Flowers (2012) carried out a detailed analyses of the effects of apatite zonation on age dispersion. Ault and Flowers first analysed a typical sample of apatites to see if zonation is present, and to what extent. This involved examination with an electron microprobe, Cathodoluminescence (CL) and eU mapping using ICPMS.

The electron microprobe appeared to show no appreciable zonation, but the CL did show a complex and varied array of zonation (however CL does not necessarily correlate with U and/or Th zonation). The CL investigation was used to select a subset of crystals for eU mapping (figure **2.3** **B** and **D**). The eU mapping found that all crystals exhibit some degree of U and Th zonation. In a few instances this can be quite extreme (they report cases with a factor of up to 8.1), but typically crystals are zoned to a factor of 1.2-2.4. They found that (as expected) zonation will cause age dispersion; eU rich rims will result in younger AHe ages and eU rich cores will result in older ages. The magnitude of this in the vast majority of cases though is fairly negligible. Even in cases of extreme end member zonation, the resulting dispersion rarely exceeded 15%. Therefore they concluded that in the vast majority of cases the assumption of eU homogeneity is adequate for AHe thermochronological studies (however it is important for ^{4}He/^{3}He studies (Fox *et al.*, 2017)).

Gautheron *et al.* (2012) carried out simulations on synthetic grains as opposed to a real data set. They found that above a zonation factor of about 2, the dispersion caused by eU heterogeneity can become significant, and in extreme cases can exceed 50%. This differs from the findings of Ault and Flowers (2012), but is largely because they are considering much greater zonation factors in their calculations than those Ault and Flowers (2012) found to be realistic in their data set. When you consider a zonation factor of less than 2.4 then Gautheron *et al.*'s (2012) calculations are largely in agreement with those of Ault and Flowers (2012), further enforcing the interpretation that eU zonation has a negligible effect on age dispersion in most circumstances. Additionally Gautheron *et al.* (2012) show that their computational model can actually account for zonation where information on the zonation of a crystal is known, making its effect on age dispersion quantifiable and therefore manageable even for zonation factors >2.

As it is analytically impractical to carry out zonation investigations and AHe analyses on the same crystals (due to the destructive nature of the techniques), parent homogeneity is always assumed for calculating AHe ages. Hypothetically, where zonation information is available on a crystal then this can be incorporated into the calculations for thermal history modelling (Meesters and Dunai, 2002b; Gautheron *et al.*, 2012; Fox *et al.*, 2017) but this is rarely the case. Samples can be screened for potentially problematic zonation by analysing the corresponding fission track mounts. Strong zonation in the track density (e.g. figure **2.3 A** and **C**) will correspond with a heterogeneous U and Th distribution within the crystal. Where this is found to be a common occurrence within a sample then the sample can be rejected for AHe dating, or flagged in case of anomalous AHe ages.

2.2.2.2 α-Particle ejection: During radioactive α-decay, the ^{4}He is ejected from the parent nuclide at a specific energy (c.5-6 MeV for ^{238}U, ^{235}U, ^{232}Th (Farley *et al.*, 1996)) and this results in it travelling a specific distance depending on the density and (to a lesser extent) chemistry of the host material. For example, the mean stopping distance for an α-particle ejected from decaying ^{238}U in apatite is 19.68µm (Farley *et al.*, 1996). This means that there is a statistical chance that any given parent nuclide undergoing α-decay within c. 20µm of the crystal boundary could eject its α-particle out of the apatite crystal (figure **2.4**). If left unaccounted for, the ^{4}He loss through α-ejection will give an erroneously young age.

A correction factor (F_{T}) is used to account for α-ejection (Farley *et al.*, 1996). This is calculated as:

$$F_{\mathrm{T}} = 1 - \frac{3S}{4R} + \frac{S^3}{16R^3}$$

Where S = α stopping distance and R = radius of a spherical crystal (conversions are made from the realistic crystal geometry to a sphere with the same (S/V) ratio). The correction is then applied to the calculated age as follows:

$$\text{Corrected Age} = \frac{\text{Measured Age}}{F_{\mathrm{T}}}$$

The F_{T} correction doesn't take into account the subsequent effects of α-ejection on ^{4}He diffusivity and retention, as ejection depletes the rim, altering the crystals diffusion profile. For young and/or rapidly cooled samples this is irrelevant as minimal diffusive loss of ^{4}He has occurred, but for samples that have undergone protracted residence time in the PRZ this has been shown to lead to potentially large overcorrections (Meesters and Dunai, 2002b; Gautheron *et al.*, 2012). However for most realistic samples Gautheron *et al.* (2012) state that the overcorrection falls within the typical range of AHe analytical error (±10%) so is still applicable.

It is routine to publish both the raw and F_{T} corrected age, but some argue that an F_{T} 'puts back' ^{4}He that will have since diffused out the crystal, so doing so is misleading (and leads to further over corrections). In AHe thermochronology the 'true' age of an individual crystal can be considered unimportant. It is the composite of a suite of crystal ages that is used to construct a thermal history, so trying to 'correct' an age value to find a 'true' age for each individual crystal ads an unnecessary layer of complexity. Ultimately this single age doesn't represent any specific single event (such as the age of formation in geochronology), so the F_{T} corrected age is no more or less 'correct' than the raw age. The desire for this correction stems from the roots of thermochronology in the geochronology field of research, but is not necessary or recommended for thermochronological applications. It is the raw age that is used as the input for most thermal history inverse modelling programs (e.g. QTQt).

2.2.2.3 Implantation: Another consequence of the long stopping distance of α-particles is that ^{4}He can become implanted in an apatite crystal from a neighbouring source (Spiegel *et al*., 2009; Gautheron *et al*., 2012; Murray *et al*., 2014). Any adjoining crystal containing radioactive isotopes which undergo α-decay may implant ^{4}He into the apatite crystal. This is particularly a problem if a rock contains a high concentration of other U and Th bearing accessory minerals such as zircon and monazite (figure **2.4**). Implanted ^{4}He is 'parentless', as the source of ^{4}He is outwith the analysed crystal, causing an older than expected AHe age.

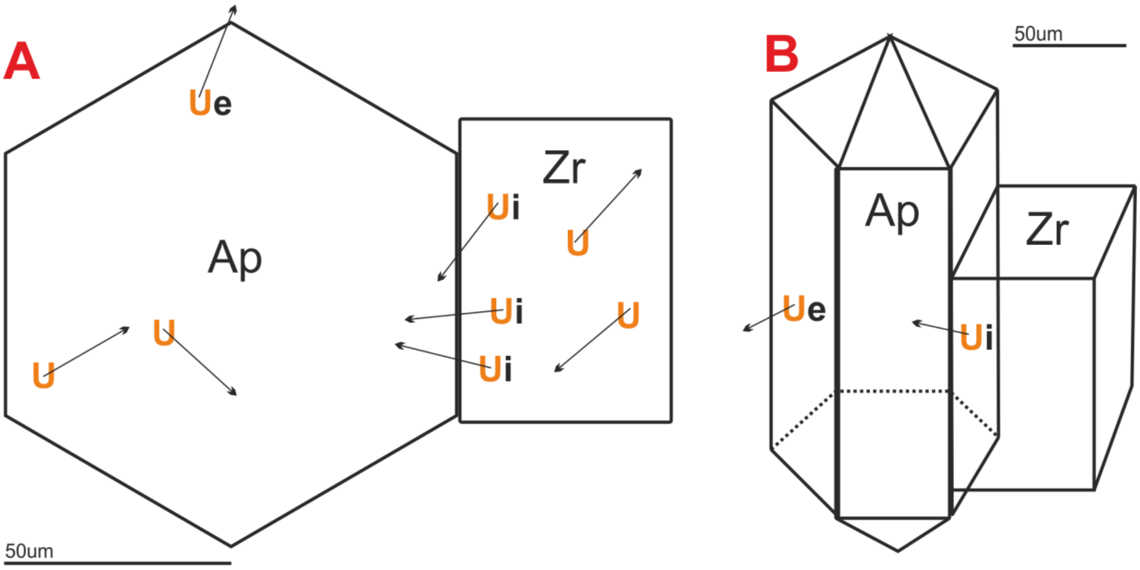

Figure 2.4: Example of the effects of the long α-particle stopping distances (c. 20μm) on radiogenic ^{4}He. U indicates an alpha-emitting parent isotope such as ^{238}U. Ue indicates an alpha particle which is ejected from the apatite grain; Ui indicates an alpha particle that is implanted into the apatite grain from a 'bad neighbour', in this instance zircon. **A**: a cross section through a typical euhedral apatite crystal. **B**: a 3D representation of alpha-particle ejection and implantation. Arrows are approximately to scale (20μm). After Gautheron *et al*. (2012).

Spiegel *et al*. (2009) first examined the implantation effect by removing the outer 20μm of apatite crystals from a set of young volcanic samples which had returned AHe ages older than their corresponding AFT ages. Occurrences of AFT-AHe age crossover are common in 'over dispersed' slowly cooled rocks (e.g. Soderlund *et al*., 2005; Green and Duddy, 2006; Green *et al*., 2006; Fitzgerald *et al*., 2006), but are less common in young/rapidly cooled rocks. They showed that for their data set the AFT-AHe age crossover could not be caused by eU zonation (see section *2.2.2.1*) or micro-inclusions (see section *2.2.2.4*) as had been suggested by other authors for different data sets. Optical screening showed their grains to be inclusion free, SEM, ICPMS and electron microprobe characterization showed their grains to be un-zoned. The action of abrasion appeared to correct the problem of 'too old' AHe dates in their samples; giving evidence that implantation was the cause of the 'too old' ages in their case. This is because removing the outer 20μm of the crystal removes the zone where it is possible to have gained implanted ^{4}He.

Gautheron *et al.*, (2012) modelled potential implantation scenarios computationally to quantify its effects. Implantation is only an issue when there is a strong contrast in eU between the apatite and its neighbour (higher eU in the neighbour). They found that for a typical zircon (eU = 200-500ppm) adjacent to an apatite with eU of 20ppm (e.g. figure **2.4**), the resulting AHe age can be increased by in excess of 20% due to implantation. The problem becomes even more pronounced if the apatite is surrounded by multiple 'bad neighbours'. Their calculations suggest an increase in AHe age of 200-300% is possible if the apatite is adjacent to only three or four zircons with much higher eU concentration than the apatite.

Implantation has the potential to cause a substantial negative impact on age dispersion. It is however incredibly unlikely to cause a regular and routine problem. This is due to the very low statistical chance of any given apatite crystal being surrounded by 'bad neighbours', and the even smaller statistical chance that the same apatite crystal will then be selected for AHe analysis (Gautheron *et al.*, 2012). It can however be seen as a plausible explanation towards individual crystals with an AHe age in excess of the crystallisation age of the host rock, which are hard to explain through other means. It is possible to screen samples against potential implantation by analysing the rock in thin section to see if there are abundant U and Th-bearing accessory minerals associated with the apatite, but this can still miss potential 'freak' occurrences.

Abrasion of the outer 20μm of the crystal has been used as a means of eliminating the problem of implantation, and also removes the need for an α-ejection correction factor (F_T) (e.g. Min *et al.*, 2006; Blackburn *et al.*, 2007; Danisik *et al.*, 2008; Spiegel *et al.*, 2009). However Gautheron *et al.*, (2012) caution its effectiveness. They state that a significant proportion of the implanted ^{4}He will diffuse further into the crystal, down the concentration gradient caused by implantation. Removal of the outer 20μm will not account for this additional helium. In addition, the removal of the rim reduces the thermal information from the lowest temperature ranges, and introduces further complications and biases to the procedure. For example it will necessitate the selection of even larger grains, losing the potential thermal history information from smaller sized grains.

2.2.2.4 Micro/fluid Inclusions: Many apatite crystals can be found to contain micro-inclusions of either fluids or other mineral phases (e.g. Figure **2.5**) (e.g. Fitzgerald *et al.*, 2006; Vermeesch *et al.*, 2007). Depending on the mineralogy of these inclusions this can either affect the distribution of ^{4}He within the apatite crystal (leading to the problems already discussed with zonation), or it may create 'parentless helium' within the crystal, leading to an erroneously old AHe age. This is only a problem when involving other U and Th rich accessory minerals/fluids such as zircon and monazite (Vermeesch *et al.*, 2007). Zircon and monazite are not dissolved during standard apatite dissolution procedures for ICPMS as they require the use of the more dangerous hydrofluoric (HF) acid, therefore the parent isotopes responsible for producing excess ^{4}He go unmeasured.

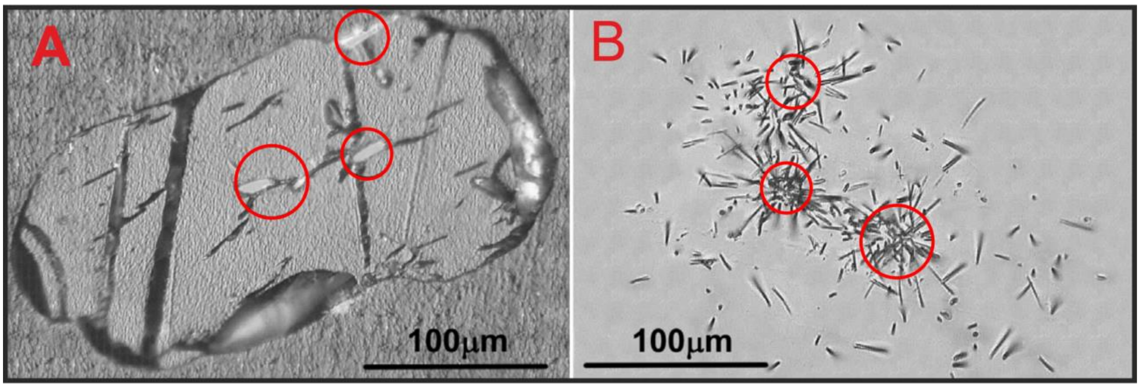

Figure 2.5: Example apatite with three high U-Th concentration mineral inclusions (circled in red). **A**: apatite grain fission track mount with low spontaneous track density. **B**: the corresponding mica detector sheet with low induced track density, but 'stars' of much higher track density in the regions of the highlighted inclusions. These inclusions appear to have much higher eU than the host apatite, and therefore could be considered problematic sources of 'parentless' ^{4}He. However the authors consider their impact to be negligible due to the small size relative to the 3D volume of the host crystal. After Vermeesch *et al.* (2007).

Inclusions within apatite are often given as a cause for excessive age dispersion (e.g. Lippolt *et al.*, 1994; Fitzgerald *et al.*, 2006). This has led to the routine screening of crystals during the mineral picking process using petrographic microscopes. A petrographic microscope enables inclusions to be observed which would otherwise be missed under the standard picking microscopes due to using higher magnifications and both plain polarised (PPL) and cross polarised (XPL) light. Although all labs agree that this screening step is necessary, there is little quantitative evidence that mineral/fluid inclusions actually have a significant impact on age dispersion. Zietler *et al.* (2017) have found that micro-fluid inclusions may act as traps for ^{4}He which affects diffusivity. This may be contributing to dispersion, but is due to increased ^{4}He retention and not parentless helium.

Vermeesch *et al.*, (2007) point out that for micro-inclusions of zircon (as an example) with realistic eU concentration and dimensions in a typical apatite grain, the amount of parentless helium is negligible. This is based on some simple order-of-magnitude calculations which highlight the fact that an inclusion 10% of the length, width and height of an apatite crystal needs an eU concentration 1000 times higher than the apatite to produce the same amount of helium. Therefore inclusions in the order of a few microns (i.e. the inclusions assumed to be overlooked during screening) are unlikely to cause appreciable amounts of parentless helium. Zircons typically have 100 times more U and Th than apatite, so it would require a very large 'typical' zircon to have a significant effect on the AHe age. An inclusion of this size would easily be observed during screening and subsequently avoided.

An additional factor to consider is that U and Th rich inclusions can change the diffusive parameters of the crystal, in much the same way as eU zonation. An α-emitting inclusion will create concentrated radiation damage around its perimeter, which can act to alter the effective closure temperature (T_c) of the crystal. Radiation damage is routinely assumed to be uniform due to homogeneous U and Th distributions, but heterogeneous radiation damage can have a minor but not insignificant effect on age dispersion (Gautheron *et al.*, 2012). Vermeesch *et al.*, (2007) calculate the effect of α-emitting inclusions on closure temperature as a result of radiation damage to be <5°C for most realistic situations.

2.2.2.5 Anhedral grains/other flaws: It is generally assumed that good euhedral apatite crystals are required to carry out reliable AHe analyses (figure **2.6 A**). Where crystals have pre-existing fractures (fractures not caused by the mineral separation process) then these fractures can act as diffusion pathways, facilitating the loss of ^{4}He. Other defects such as pitting/staining of the crystal surface and large chips/deformities are also considered potentially problematic. It is common practice to avoid picking such grains where possible.

Dark orange/red staining (described as 'grain boundary phases' – GBP) has been found to be potentially high in U and Th, in some cases up to 1000ppm (Murray *et al.*, 2014), and can therefore lead to significant ^{4}He implantation. The significance of this hinges on the grain size, grain (S/V) ratio and thickness of the GBP, as well as the timing of formation of the GBP relative to cooling of the host rock. Under certain scenarios, the authors found that ages can become positively dispersed in the order of hundreds of percent as a result of a GBP high in U and Th. This can be particularly problematic as the GBP may not be preserved through to the time of grain picking, so the effects may be impossible to avoid through the screening process.

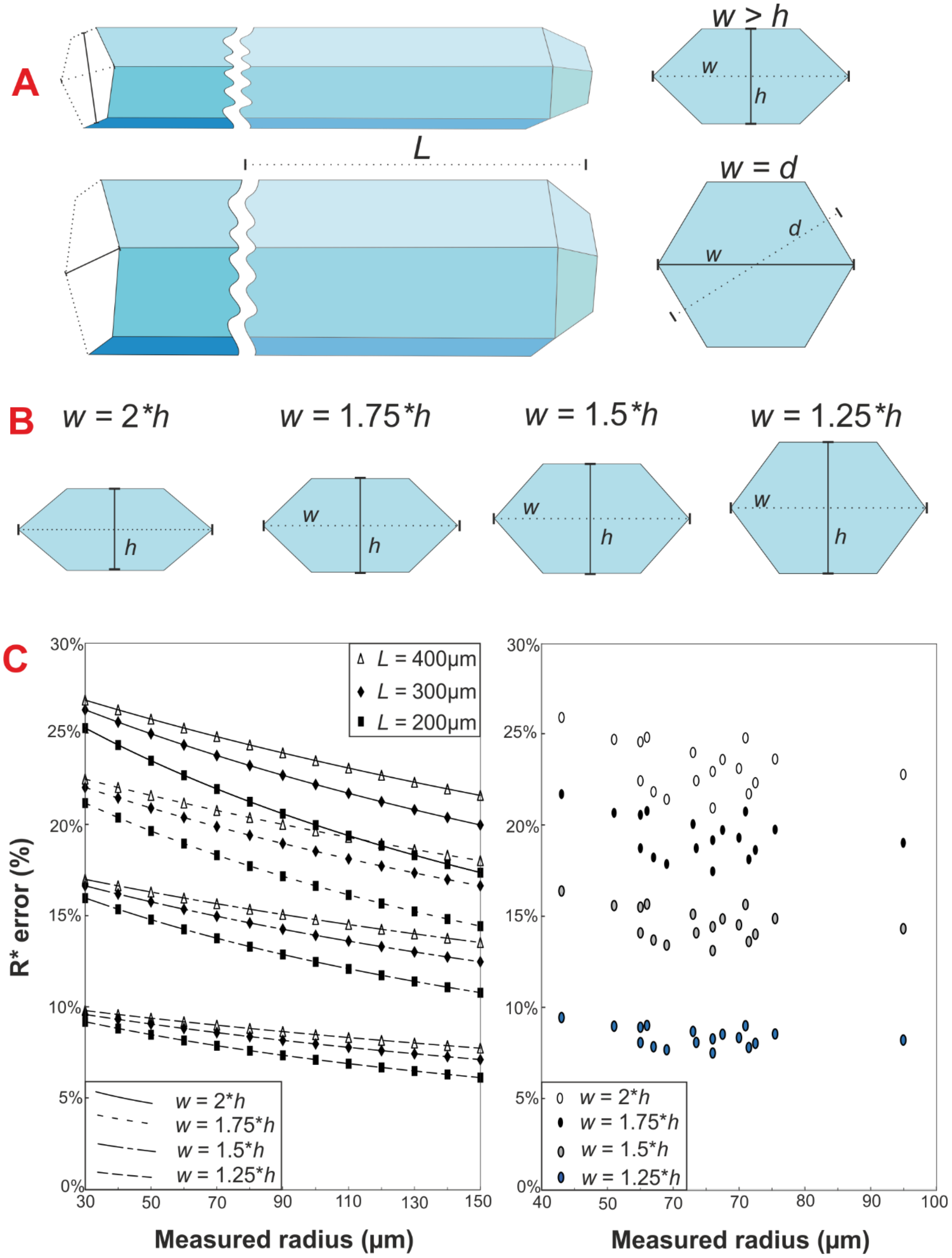

Figure 2.6: Cartoon representation of euhedral apatite grains, demonstrating the R* calculation error. Apatite crystals are usually assumed to be perfect hexagons in cross section (*w* = *d*). In many instances they are flattened where *w* > *h*. This results in an error in the R* conversion. **A**: a typical 'flattened' grain as is often found in mineral separates, in comparison to a grain with a perfect hexagonal cross section. If only one thickness dimension is measured then this will be the width, leading to an overestimate in the R* conversion. *L* = the length of the whole grain, regardless of if the grain has 0T, 1T or 2T's. **B**: the grain aspect ratios used to plot C. **C**: plots of the percentage over estimate in R* grain volume for given measured lengths and widths. Left panel shows the error for theoretical grain dimensions with radii of 30-150µm and lengths of 200µm, 300µm and 400µm. Right panel shows the actual error calculated for grains from sample *SD07 – 1* (this thesis) for the hypothetical aspect ratios shown in B.

Imperfections in crystal shape increase the error associated with the R* conversion. This can lead to an inaccurate (S/V) ratio and inaccurate crystal volume which is then used in the thermal history models. Although not contributing to age dispersion, this error will decrease the reliability of the resultant thermal history model outputs. To reduce the error, certain labs measure two dimensions for the thickness of a grain – width and height, instead of a single diameter. This accounts for the fact that some apatite crystals have a flattened cross section profile, as opposed to the perfect hexagonal cross section found in ideal grains (see figure **2.6 A**). This approach is physically challenging and labour intensive to carry out, so is only practical when analysing a small number of grains. It also carries a high risk of damaging or losing the selected grain, so is not routine in every lab. Analysing a larger number of grains per sample and accepting the higher measuring error can be deemed preferential for robust thermal history modelling.

The error associated with flattened crystals will always result in an over estimate in the crystal volume. A crystal will naturally rest with its widest dimension parallel to the glass slide surface (e.g. as shown in figure **2.6 B**), therefore the measured width will always be greater than the unmeasured height (if un-equant). The greater the aspect ratio, the bigger the over estimation will be. For an aspect ratio of 2:1 ($w = 2*h$) the over estimation can be in excess of 25% for the thinnest grains (figure **2.6 C**). The impact is also greater on longer grains, so long and thin grains will have a much larger over estimate than short and fat grains. An aspect ratio of 2:1 can be considered quite extreme, it is unlikely that many grains of this dimension will be selected for analysis because the shape will make them hard to distinguish from other mineral phases such as zircon. But even an aspect ratio of 8:7 ($w = 1.25*h$) results in an over estimate of the crystal volume by c. 7-10% for realistic grain dimensions. A grain with such a ratio will be almost indistinguishable from a grain with a perfect hexagonal cross section by the naked eye, therefore even if only grains which are considered to be truly hexagonal are selected for analysis, there is still likely to be a small but not insignificant over estimation in the crystal volume on many of the chosen grains. As an estimate based on the samples analysed in this thesis, the vast majority of grains will fall somewhere in the region of a 5-15% volume over estimation (figure **2.6**).

For some samples, particularly those of non-igneous origin, euhedral grains may be rare or even absent. Apatites tend to become deformed during metamorphism, resulting in clean but irregular shapes. This can make determining a length and width difficult. Detrital apatites tend to become rounded and pitted during the sedimentary process, again making it difficult to determine an accurate length and width. It can also make it difficult to spot large inclusions, and even result in zircons being picked by mistake. It is therefore preferential to sample igneous rocks, particularly plutonic rocks such as granites. This isn't always possible however, so when analysing imperfect grains, the greater level of uncertainty needs to be taken into account (e.g. figure **2.6**).

2.2.2.6 Radiation damage: eU variation has already been highlighted as a component of inherent natural dispersion (see section *2.2.1.2* and figure **2.2**). This is due to the effects of radiation damage on ^{4}He diffusivity. Currently, two different radiation damage models have been developed and incorporated into modelling software that aim to quantify the effect of radiation damage accumulation and annealing on ^{4}He diffusivity; Radiation Damage and Accumulation and Annealing Model (RDAAM) (Flowers *et al.*, 2009) and the radiation damage model of Gautheron *et al.* (2009). There are key differences in the formulation and parameterisation of each model, and ultimately neither may be correct, therefore they can impose additional uncertainties on the modelling of AHe data. Radiation damage is intrinsic to the system but it is poorly understood, which makes it worthy of note as a 'bad' factor contributing to dispersion.

Currently both radiation damage models utilise a positive relationship between damage accumulation and ^{4}He retention (as seen in figure **2.7 A** and **B**), but the model of Gautheron *et al.* (2009) follows a linear relationship, whereas RDAAM (Flowers *et al.*, 2009) follows a cubed relationship. Therefore there can be quite a substantial difference in thermal history output when using one radiation damage model compared to the other if high eU grains are analysed. Recent studies (e.g. Gerin *et al.*, 2017) suggest that as radiation damage increases to the point where tracks/defects become interconnected, ^{4}He retention begins to decrease, as is the case with ZHe (Guenthner *et al.*, 2013). This is because the interconnected defects act as pathways as opposed to traps, facilitating ^{4}He diffusion. It is therefore likely that both current models are inaccurate and poor at dealing with high eU grains.

Both models assume that the annealing kinetics of α-recoil defects are the same as for those of fission tracks. Their published data largely suggests that this was a valid working assumption, but the subsequent experimental work of Willet *et al.* (2017) has shown that there are important differences between the annealing kinetics of fission tracks and α-recoil defects. α-recoil damage annealing rate scales proportionally with damage content, whereas fission track annealing rate is constant in each track, and only dependent on temperature. Therefore in low eU grains α-recoil damage anneals slower than fission tracks, but above a certain threshold (dependent on the thermal history) the relationship is reversed.

Willet and co-workers have introduced an alpha-damage annealing model (ADAM) which is independent to the fission track annealing kinetics and has an empirical fit to their diffusion kinetics data (Willet *et al.*, 2017). As ADAM is sensitive to damage content, the resultant predicted ages can differ by hundreds of Ma from those which are generated using either RDAAM or the model of Gautheron *et al.* (2009) for thermal histories which experience protracted residence time in the PRZ or significant reburial. The thermal histories shown in figure **2.7 C** can result in as much as 65% difference in the calculated ages between ADAM and RDAAM when a sample is held at 60°C for as little as 75Ma. The difference would be much greater for even longer residence times in the PRZ. Maximum differences between the calculated ages of the two models are found for eU values in the range of c. 20-50ppm, which can be considered ‘typical’ eU concentration in apatite. The differences are less pronounced for very low or high eU grains, but grains such as these are less common.

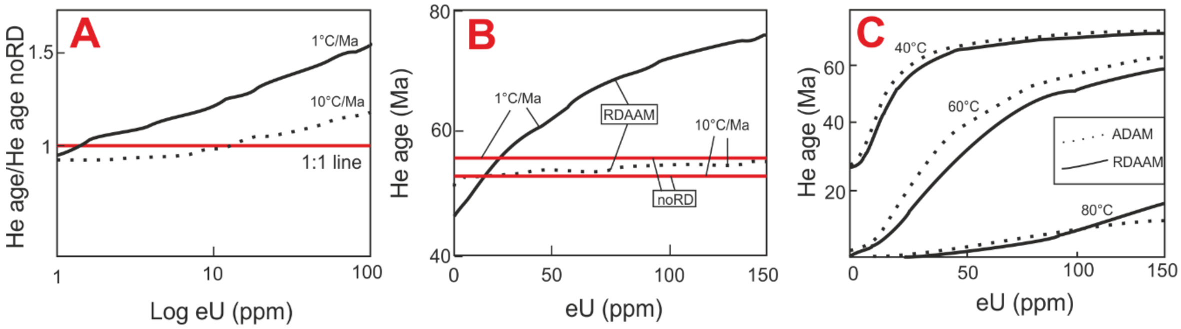

Figure 2.7: Comparisons of RDAAM, ADAM and the model of Gautheron *et al*. (2009).
The predicted ^{4}He age as a function of eU for the three radiation damage models verses no radiation damage model. **A**: (after Gautheron *et al*., 2009) difference in predicted ^{4}He age as a function of eU for 1°C/Ma (solid line) and 10°C/Ma (dashed line) monotonic cooling rates when modelled using the radiation damage model of Gautheron *et al*. (2009) compared to the standard Durango diffusion kinetics. Solid red line indicates 1:1 equiline. **B**: (after Flowers *et al*., 2009) predicted ^{4}He age as a function of eU for 1°C/Ma (solid line) and 10°C/Ma (dashed line) monotonic cooling rates when modelled using RDAAM (Flowers *et al*., 2009). Solid red line indicates predicted ages when using no radiation damage model. **C**: (after Willet *et al*., 2017) predicted ^{4}He age as a function of eU for an isothermal holding of 40°C, 60°C and 80°C for 75Ma. Comparison between ages predicted by RDAAM (solid line) and ADAM (dashed line).

There may also be other as of yet unknown components of the radiation damage and annealing system which are contributing to the eU affected age dispersion, as evidenced by the various outliers in each published dataset (Flowers *et al.*, 2009; Gautheron *et al.*, 2009). As eU variation is often the dominant factor on inherent natural dispersion, addressing the uncertainties surrounding the radiation damage models is arguably the most important challenge facing the AHe thermochronology community.

2.3 Fragment model

Much of the age dispersion which doesn't correlate with either grain size or eU can be explained by the presence of incomplete grains (fragments) in the analysis (Brown *et al.*, 2013; Beucher *et al.*, 2013). Apatite crystals readily fracture along their weak basal cleavage plane perpendicular to the crystallographic C-axis (figure **1.1**) during the mineral separation process (Farley, 2002) and so treating grain fragments as whole grains is misleading. The fractured surface doesn't represent a grain boundary where diffusive loss has taken place (assuming the fracture occurred during mineral separation), so a fractured grain will exhibit a different diffusive profile to that of an intact apatite crystal (figure **2.8**). This is not a problem for young/rapidly cooled samples, which have experienced minimal diffusive loss, but for any sample that has experienced a protracted residence time in the PRZ the resulting differential in age between a whole crystal and its corresponding fragments can be quite large (Brown *et al.*, 2013).

The fractured surface also requires alterations to be made to the F_T (if this is being applied), because the surface doesn't represent a crystal face at which ^{4}He loss will have occurred through α-ejection (Farley *et al.*, 1996; Gautheron *et al.*, 2012). The routine practice to account for this is to simply multiply the length of the fragment by 1.5 (Farley, 2002). More sophisticated calculations exist for changing the F_T for a range of geometries and U-Th distributions (e.g. Gautheron *et al.*, 2012) but these are still unsatisfactory for accounting for broken grains. However, as discussed in section *2.2.2.2*, applying any kind of F_T correction to the raw age is unnecessary and ill-advised for thermochronological applications (note – this does not mean that α-ejection can be ignored, rather that it is dealt with during the thermal history modelling stage of the process).

2.3.1 *Fragment – whole crystal age difference*

Figure **2.8** demonstrates the ^{4}He concentration gradient across a typical apatite crystal. As ^{4}He diffuses out of a crystal via the grain boundary, the rim of a crystal will inevitably become depleted in ^{4}He relative to the core. Taking the left 'fragment' from figure **2.8** as an example, the grain will have proportionally less ^{4}He for a given eU concentration than its original whole grain, as a greater percentage of the fragment consists of the depleted rim. Conversely, the right hand 'fragment' will have proportionally more ^{4}He than the whole grain because a smaller percentage of the crystal is made up of the depleted rim.

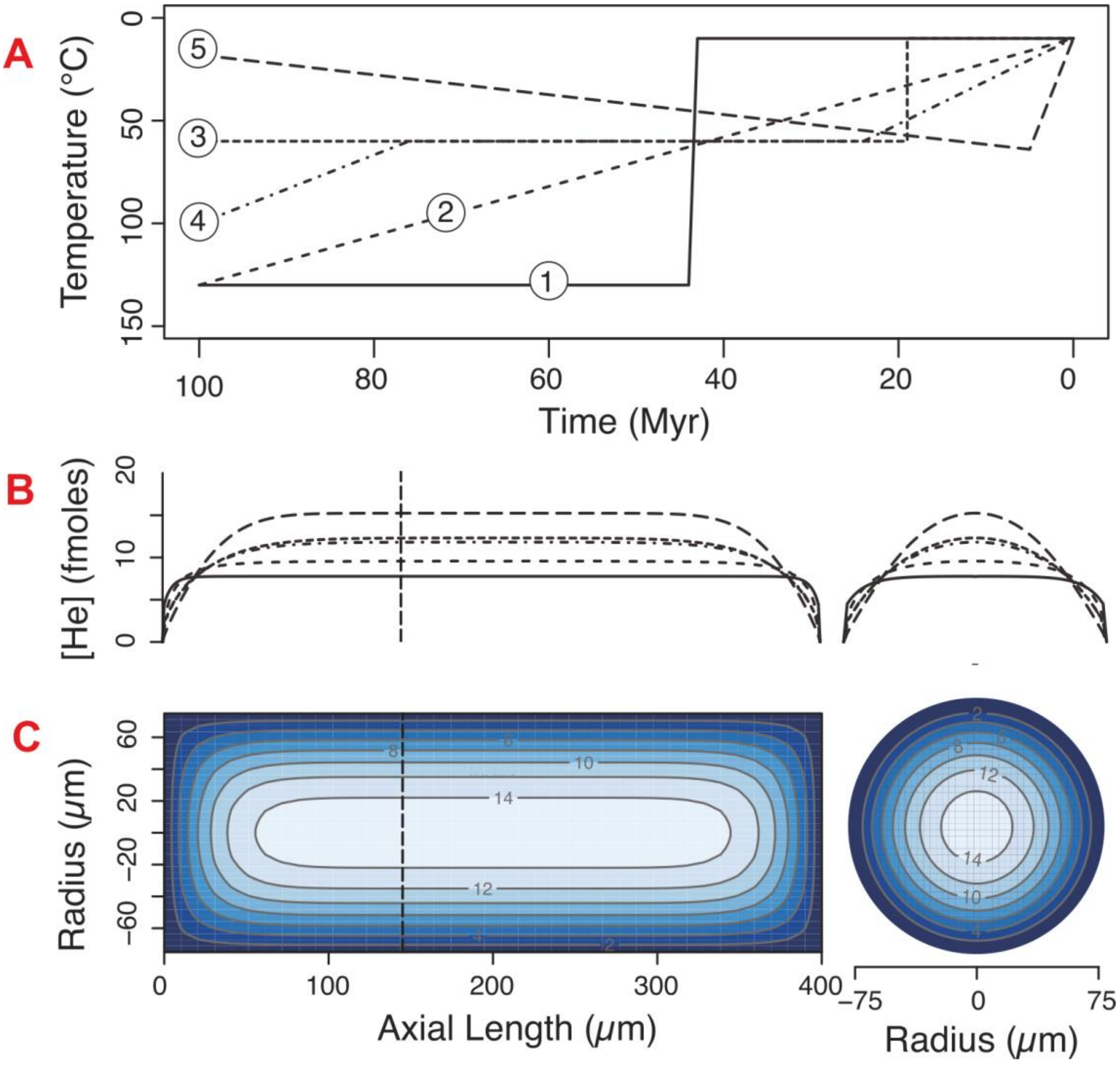

Figure 2.8: ^{4}He concentration gradient in apatite that has undergone different theoretical thermal histories. **A**: the 5 theoretical thermal histories of Wolf *et al.* (1998). **B**: axial (left) and radial (right) ^{4}He diffusion profiles (in femto moles/m^3) for the 5 WOLF thermal histories shown in A. Histories involving protracted residence time in the PRZ (i.e. WOLF-5) show the greatest differential between ^{4}He concentration in the core compared to the rim. **C**: contoured panels showing the spatial distribution of ^{4}He in an apatite crystal of length = 400 μm, radius = 75 μm, U = 20 ppm and Th = 20 ppm that has undergone the WOLF-5 thermal history (steady reheating/burial followed by rapid exhumation). Vertical dashed line in B and C represents a hypothetical fracture in the crystal, demonstrating the effect on the spatial distribution of ^{4}He in a 1T crystal verses a 2T (whole) crystal. After Brown *et al.* (2013).

The rim depletion becomes increasingly more pronounced the longer a sample has spent in the PRZ. Figure **2.8 B** shows how the concentration gradient varies for different theoretical thermal histories (the five histories of Wolf *et al.* (1998)). The largest gradient is found when samples have undergone a gradual reheating (i.e. burial) into the PRZ (WOLF-5) and the smallest gradient is found in samples that have undergone rapid cooling through the PRZ to the surface (WOLF-1). This demonstrates that treating fragments incorrectly as whole grains will have an increasingly important impact on reconstructing thermal histories the longer a sample spends in the PRZ.

Figure **2.9** shows how the age for a fragment differs from the corresponding whole crystal age depending on its relative length and the section of the whole crystal it represents. Where L_0 = the original whole grain length, a 1T fragment > $L_0/2$ in length (Type II, Beucher *et al.* (2013)) will have an age older than the 2T age of the crystal. A 1T fragment < $L_0/2$ in length (Type I, Beucher *et al.* (2013)) will have an age progressively younger than the 2T crystal age the shorter the fragment becomes. For very short 1T sections the age can be significantly younger than the original whole crystal. 1T fragments exactly half of the length of the 2T grain will have the same age as the 2T grain, but chances of this occurring in a mineral separate are very small.

For 0T fragments the picture is more complex. Fragments of different lengths but from the middle section of the whole grain can have the same age, but this will always be older than the 2T crystal age. Fragments of the same length, but where one is from very near the crystal termination and the other is from the central section will have different ages, but neither will represent the 2T age. The fragment from near the crystal termination will always be too young, and again this can be much younger for fragments from right at the very end of the original crystal.

If only 1T fragments are analysed, then for most thermal histories the resultant mean age will be younger than the hypothetical 2T mean age for the sample (figure **2.9 C**). If only 0T grains are analysed, the resultant mean age will be older than the hypothetical 2T mean age. If a combination of 0T, 1T (and even 2T) grains are analysed, then the mean age will still likely be older than the hypothetical 2T mean age, but younger than if only 0T fragments were analysed. This is because it is most likely that any 0T grains will be from a central section of a crystal, as opposed to right at the termination (which would likely give a 1T grain), so a greater number of crystals will have an older age than their original 2T crystal. 1T crystals are equally likely to be the short segment (Type I), which are younger, or the long segment (Type II), which are older, as every broken 2T grain will create one of each.

Calculating a mean age for a mixed sample is therefore unhelpful, as the age only represents the ‘average age for the average grain analysed’, and does not correspond to any meaningful geological event. It only serves to provide qualitative inter-sample comparisons (Brown *et al.*, 2013). The calculation of mean AHe ages is a hangover from the techniques early development as a geochronometer. There is no singular ‘AHe age’ for a given sample, rather a range of single grain ages which can be used to reconstruct a representative thermal history. This is a message that it is important to get across, as the desire to find reproducible mean

AHe ages has led to the misconception of age ‘over dispersion’ in the first place, and this is halting progress on the development of the AHe technique.

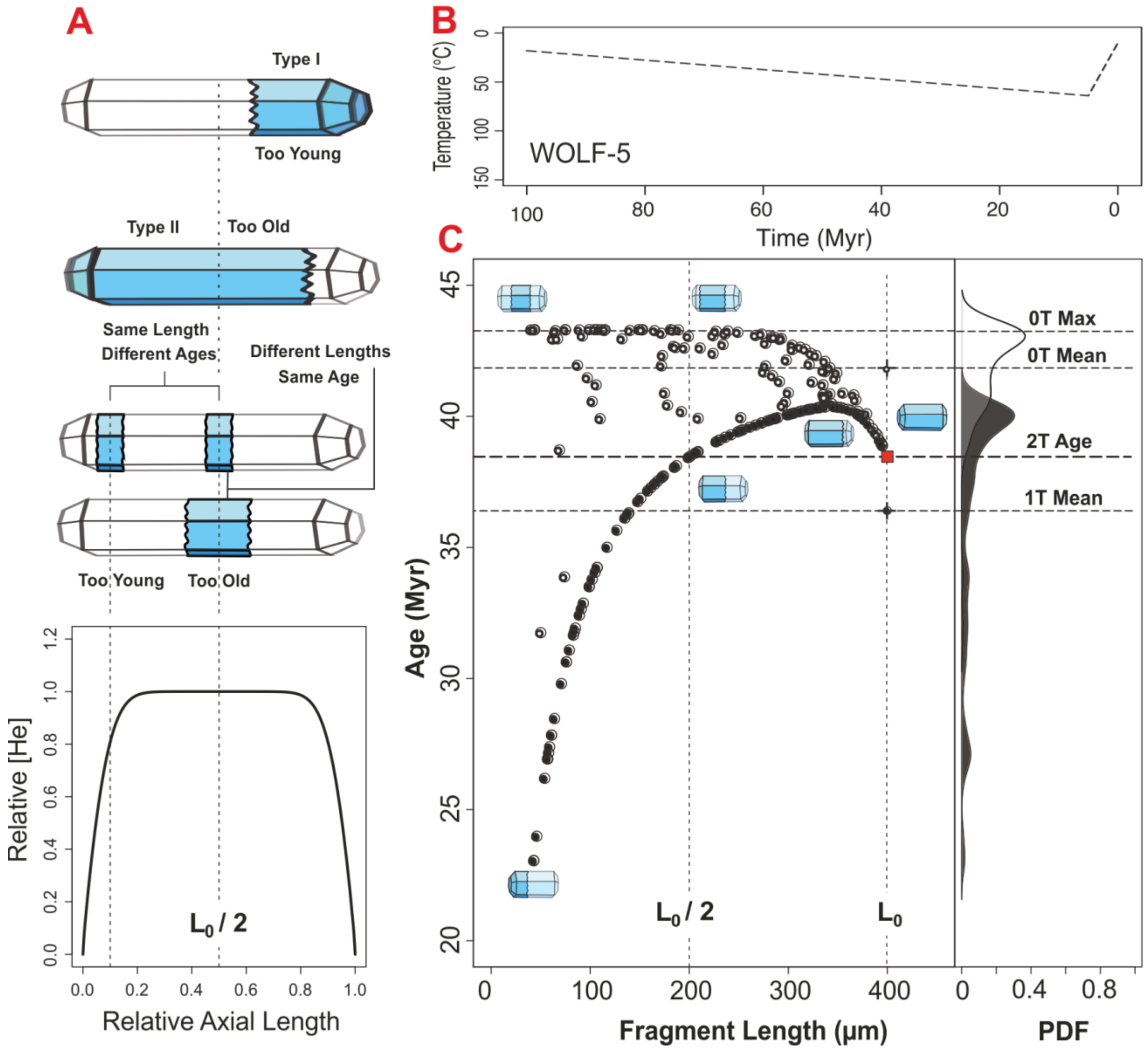

Figure 2.9: Example of the effects of different segments of a crystal on fragment age.
A: cartoon representation of different types of 1T and 0T fragments cut from the same original 2T crystal. Type I = a 1T fragment < L_0/2 in length. This will always give an age younger than the original whole crystal age. Type II = a fragment > L_0/2 in length. This will always give an age older than the original whole crystal. 0T fragments can have the same length, but different ages, and be of different lengths yet have the same age. **B**: WOLF-5 thermal history used in the modelling of C. **C**: Age Dispersion Fragment Distribution (ADFD) plot for random fragments generated from an initial whole crystal of L_0 = 400µm, R = 75µm, U concentration = 20ppm and Th concentration = 20ppm. The initial whole grains were forward modelled using the WOLF-5 thermal history. Open circles indicate 0T fragments, solid black circles indicate 1T fragments and the red square is the initial 2T crystal the fragments are generated from. This scenario can very easily generate > 100% age dispersion in a random selection of grains for a thermal history such as WOLF-5. After Brown *et al.* (2013).

2.3.2 *Effects on single grain age dispersion*

Brown *et al.*, (2013) show through forward modelling the five WOLF histories that when only the fragment effect is considered (i.e. all crystals have the same initial grain size of R = 75µm and L_0 = 400µm, and eU concentration of U and Th = 20ppm), single grain age dispersion increases from c.7% for rapid monotonic cooling (c. 10°C/Ma) to over 50% for complex histories with protracted residence time in the PRZ. When grain size is also treated as a variable (initial grain sizes ranging from R = 50-150µm and L_0 = 150-400µm), the single grain age dispersion increases to over 60% for complex thermal histories. When variable eU is added to the simulation (eU ranging from 5-100ppm) the resultant age dispersion can exceed 100% for slowly cooled or complex thermal histories. This can be considered a feasible explanation for much of the 'over dispersed' AHe ages reported in the literature from old crustal terranes (e.g. Soderlund *et al.*, 2005; Green and Duddy, 2006; Fitzgerald *et al.*, 2006; Kohn *et al.*, 2009; Fillion *et al.*, 2013).

The fragment effect also acts to decouple the expected correlation between either grain size or eU with grain age. In some instances a strong correlation can be found (e.g. Reiners and Farley, 2001 (grain size); Flowers *et al.*, 2007 (eU)) but in most instances the three main causes of inherent natural dispersion compete with each other, decoupling the expected correlation. This does not mean that there is no correlation, but the competing factors act against each other, dispersing the data spread on the standard age vs grain size and age vs eU plots. Figure **2.10** gives a cartoon representation of how the data are dispersed by the three competing factors on age vs R* (**A**) and age vs eU (**B**) plots respectively. Each component 'pulls' the data off of the expected positive correlation trend, producing a more typical 'shotgun' scatter of ages (as shown by unpublished data from west Africa in **C**).

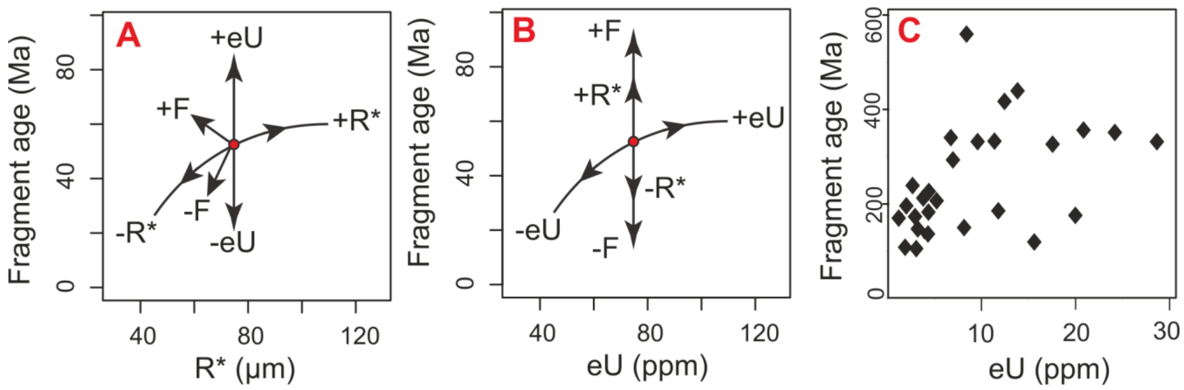

Figure 2.10: Cartoon illustrations of the decoupling effect of the three main competing factors of inherent natural dispersion on age-size and age-eU correlations.
On each plot R* represents the grain size effect, F represents the fragment effect and eU represents the radiation damage effect on decoupling the expected correlation. The red circle represents an initial whole grain of the given size and composition which has an age of 50Ma. **A**: fragment age vs R* schematic. **B**: fragment age vs eU schematic. **C**: real data plot of fragment age vs eU highlighting the typical 'shotgun' scatter of ages as a result of the competing factors on dispersion. Personal data from a transect in Benin – west Africa (unpublished). **A** and **B** after Brown *et al.* (2013).

2.3.3 *HelFRAG*

Far from being a problem, large age dispersion is actually desirable for reconstructing robust thermal histories, provided it is predictable (i.e. inherent natural dispersion). All crystals from a sample must have experienced an identical thermal history, so a large spread of ages enables a well constrained, unique thermal history to be computed. Beucher *et al*., (2013) demonstrate this through the development of their new inverse modelling technique – HelFRAG. This utilises a finite cylinder diffusion approach which treats fragments explicitly as fragments of initially larger whole grains of unknown original lengths. The original length parameter can be solved, but this is deemed unnecessary provided a sufficiently large initial length is ascribed to the crystal. Solving for the initial length would add additional model run time to the already computationally demanding process. The authors find that a suitable value for L_0 is given by the maximum fragment length plus two times the maximum crystal radius. This approach demonstrably works well for 1T crystals, but currently there is no comparable solution for dealing with 0T crystals.

To test the new model the authors generated a synthetic suite of crystal fragments for each of the five theoretical WOLF thermal histories (Wolf *et al*., 1998). They then tested the ability of the new model to return each of the five thermal histories for each ‘sample’. This experiment was carried out three times, firstly the fragments were all randomly ‘cut’ from the same initial whole grain, so that fragment length was the only free variable. Secondly they varied the initial whole crystal grain size as well as fragment length, but kept eU the same. Finally eU was also made a variable so that all three known factors of inherent natural dispersion were working simultaneously. They found that the dispersion created from fragmentation alone is sufficient to resolve each of the five thermal histories reasonably well. The accuracy of the models is improved further as first grain size, and then eU are varied to increase dispersion (figure **2.11)**.

The HelFRAG inversion technique has the setback of being computationally demanding. A single simulation can take days to weeks, or even months to complete (i.e. the modelling of sample *SD07 – 3* in this thesis took over four days to complete using parallel processing with 48 cores, a single processor would have taken c. 6 months!), which limits its routine application. An approximation of the finite cylinder diffusion model utilised in HelFRAG has been incorporated into the QTQt modelling software – Qfrag (Gallagher, 2012). This has the benefit of being much swifter to run, with a user friendly interface. A robust test of the QFrag approximation is presented in this thesis, **Chapter 4**.

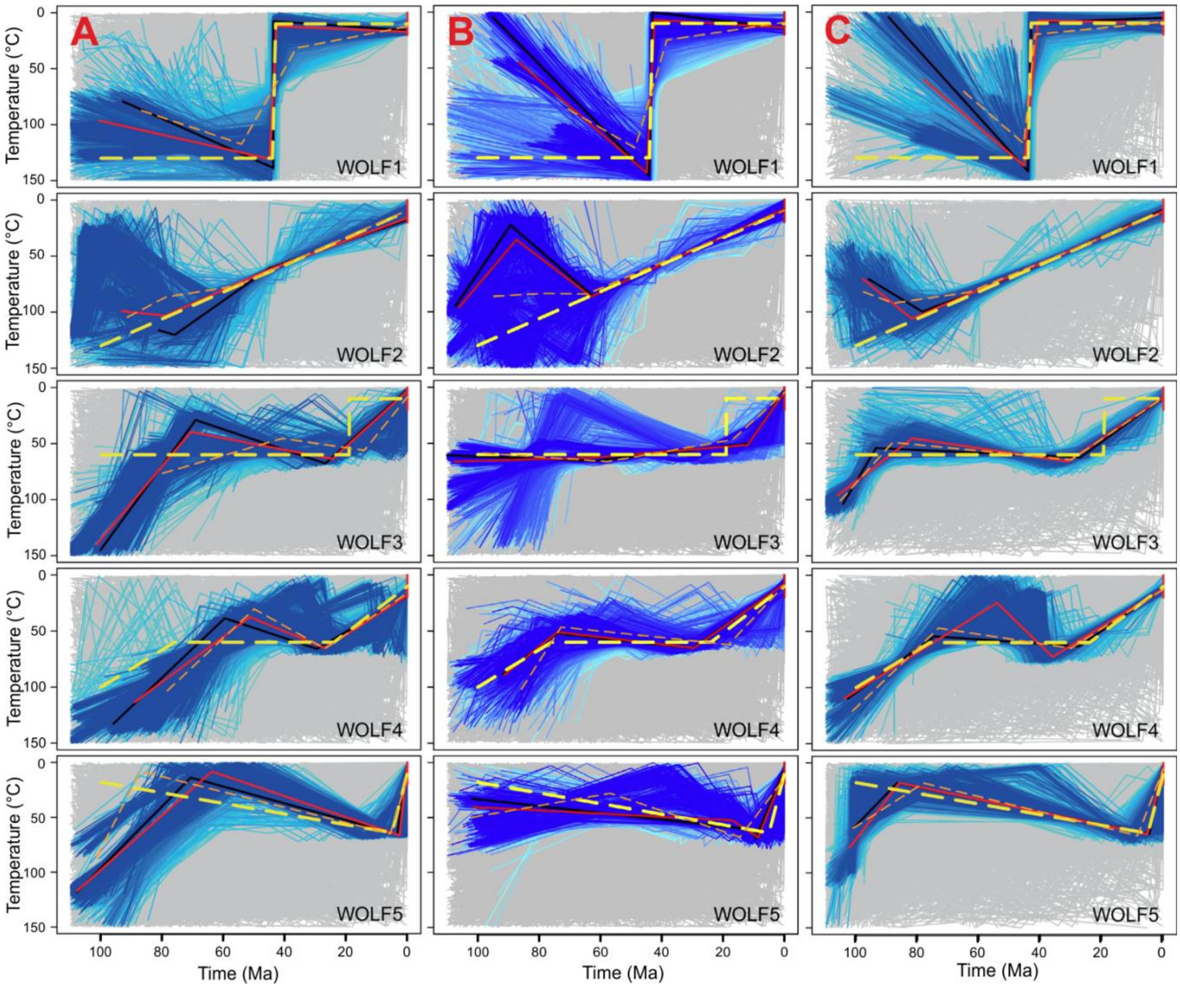

Figure 2.11: HelFrag inversion models of the five WOLF thermal histories.
Dashed yellow line = true thermal history (used to generate the fragment lists), solid red lines indicate the best fit thermal history, solid black lines indicate the average acceptable thermal history, dashed orange lines indicate the Bayesian expected model, blue shading indicates the acceptable fit field (darker = better) and gray shading indicates the rejected field of solutions. Panel **A**: model results for 25 random length fragments 'cut' from the same initial whole grain of L_0 = 400µm, R = 75µm and U and Th concentrations = 20ppm respectively. Panel **B**: model results for 25 random length fragments cut from variably sized initial whole grains (L_0 = 200-600µm, R = 50-100µm) with the same eU (U and Th = 20ppm). Panel **C**: model results of 25 random fragments cut from grains of variable size and eU (sizes as for B, eU range of 8-150ppm). Even with only fragmentation contributing to inherent natural dispersion the HelFrag model returns each thermal history reasonably well. The accuracy is increased as first grain size and then eU are also varied. After Beucher *et al*. (2013).

2.4 Concluding remarks

Apatite (U-Th)/He thermochronology has become established as one of the most useful low temperature thermochronometers over the last couple of decades. The technique is constantly being improved and refined, leading to much more robust thermal history reconstructions. It still has its problems and limitations, and age dispersion is an ever present topic of debate at thermochronology conferences around the world. However many of the debates surrounding the imposed causes of dispersion have largely been resolved (e.g. implantation (Vermeesch *et al.*, 2007)). In particular the two main areas of ongoing developments are: improvements in our understanding of radiation damage and annealing and its impact on diffusion kinetics (e.g. Gerin *et al.*, 2017), and developments in our understanding of the effects of compositional variation on diffusion kinetics (e.g. Djimbi *et al.*, 2015). In addition to these the work of this thesis will shed light on a previously largely overlooked contributor to age dispersion – fragmentation, which will complement other developments in the technique.

CHAPTER 3

3. MAJOR DEVELOPMENTS IN AFT THERMOCHRONOLOGY

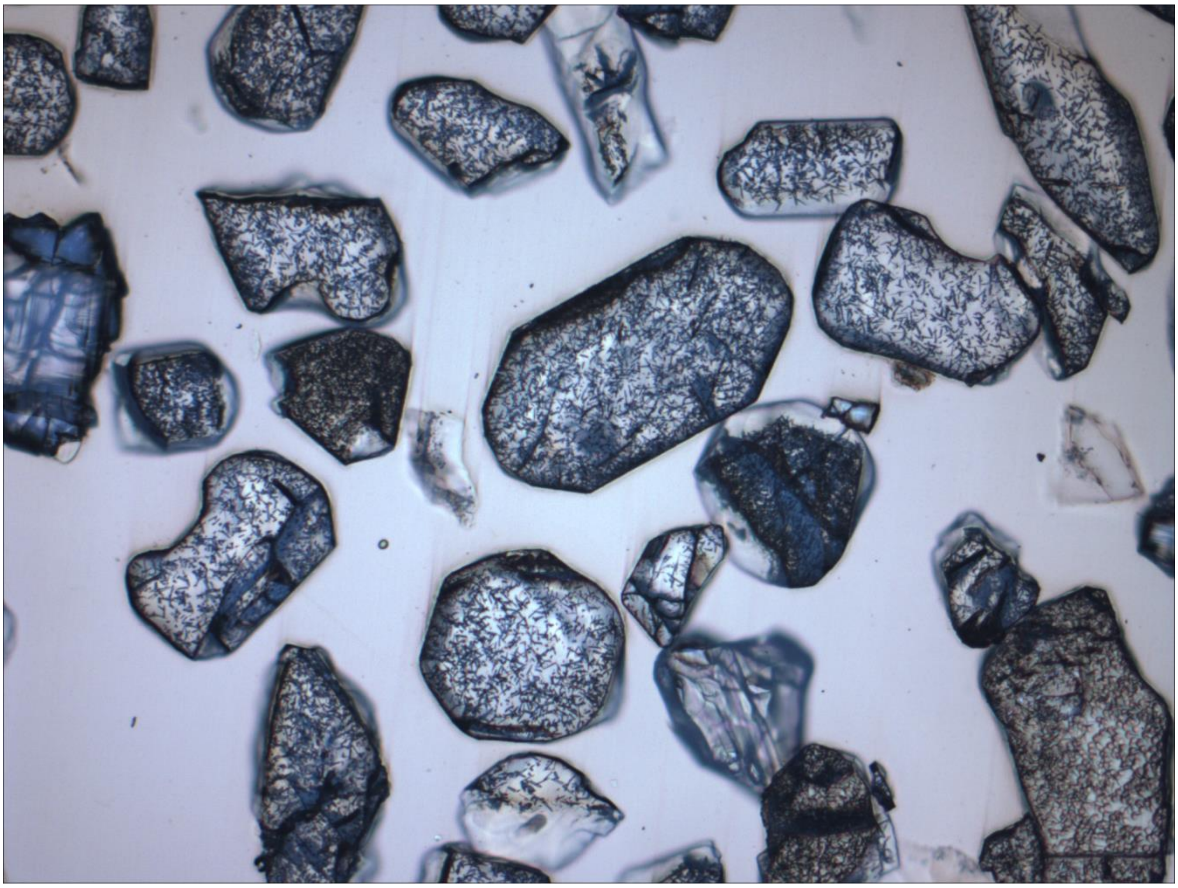

(Fission track mount of sample *BH15 – 05*)

3.1 History of Apatite Fission Track dating

Low temperature thermochronological studies often combine AHe with AFT (e.g. Fitzgerald *et al.*, 2006; Persano *et al.*, 2007). This is because both techniques are easily carried out simultaneously due to the same mineral separation process, and both systems have overlapping temperature sensitivities, complementing each other. This enables more detailed and robust thermal histories to be generated, covering a greater range of crustal depths (and therefore time).

Fission track analyses utilise the decay of ^{238}U through spontaneous nuclear fission, as opposed to the α-decay path used by the AHe method. This generates two positively charged daughter products (of roughly equal atomic mass) plus one or more neutrons. The daughter products cause recoil damage to the crystal lattice of the host mineral as they repel from each other, generating an observable linear defect/track (figure **3.1**). The ratio of parent (^{238}U) to daughter (tracks) is used to calculate an age, but as tracks thermally anneal over time, measuring the length of the tracks also provides thermal history information. This makes AFT an invaluable thermochronometer.

3.1.1 *Fission track dating*

The α-decay of U was one of the earliest radioactive decay series to be studied (e.g Rutherford, 1905; Strutt, 1905), but the spontaneous fission of ^{238}U wasn't observed until the work of Flerov and Petrzhak (1940). They discovered that fission reactions had occurred in a uranium glass, creating defects. The uranium hadn't been exposed to neutron irradiation, a method of inducing nuclear fission. They experimented in a bunker deep underground, which eliminated the potential interference of cosmic rays on nuclear fission.

Fission tracks were first proposed as a potential tool for dating rocks with the discovery of countable accumulations of charged particle tracks in micas by Price and Walker (1963). The authors noticed that crystals of mica contain a natural background of charged particle tracks which can be revealed when the crystal surface is chemically etched. 'Fossil tracks' were first observed through the use of an electron microscope (Silk and Barnes, 1959; Price and Walker, 1962a, b) but Price and Walker (1963) subsequently developed a technique for viewing the tracks using a general optical microscope, making the dating method much more accessible. This involved the immersion of the sample in HF (hydrofluoric acid) for a specific period of time and at a specific temperature (depending on the crystal phase analysed) which enlarged the tracks to a point observable under relatively low magnification.

They demonstrated that the most likely source of the natural fission tracks was the spontaneous fission of ^{238}U (and showed other potential sources to be unlikely), and that this could be used as a way to date the age of samples when both tracks (daughter) and uranium (parent) can be measured.

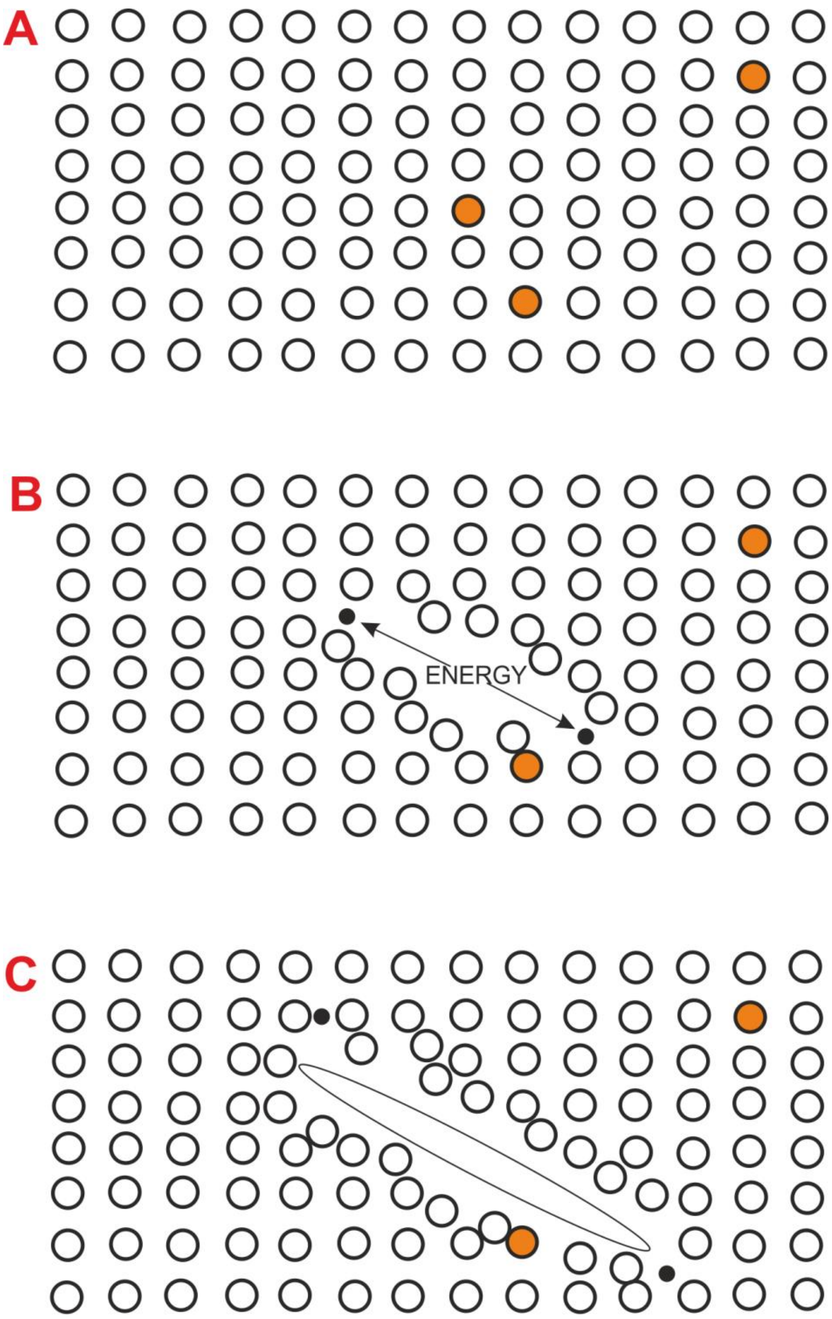

Figure 3.1: Cartoon diagram of fission track formation.
A: trace amounts of unstable ^{238}U are randomly distributed through the crystal lattice (orange filled circles). **B**: a ^{238}U atom undergoes spontaneous fission, generating two large charged particles (black dots) which repel from each other due to coulomb repulsion, while also releasing energy. These particles also interact with the surrounding crystal lattice, causing further repulsion. **C**: The particles eventually come to a rest after a specific distance, which relates to the density and chemistry of the host crystal, leaving a damage trail or fission track. The track is optically observable when chemically etched. After Gallagher *et al*. (1998).

Due to the very low concentration of uranium occurring naturally in micas, standard methods of measuring its concentration (such as fluorimetry) were not very effective. Instead, samples were exposed to a flux of neutrons (irradiated) to induce the fission of ^{235}U, and the corresponding fission tracks were measured from an adjoining mica detector sheet which was etched after irradiation (the external detector method, see figure **3.2** and Appendix 2). The ratio of ^{238}U/^{235}U in nature is effectively a constant [137.818 ± 0.045 (2σ)], so the number of induced tracks from ^{235}U can be used as a proxy for the concentration of ^{238}U in a sample (Condon *et al.*, 2010; Hiess *et al.*, 2012). The ratio of induced tracks to spontaneous tracks can then be used to calculate the age for the sample. This methodology has seen little change through to the present.

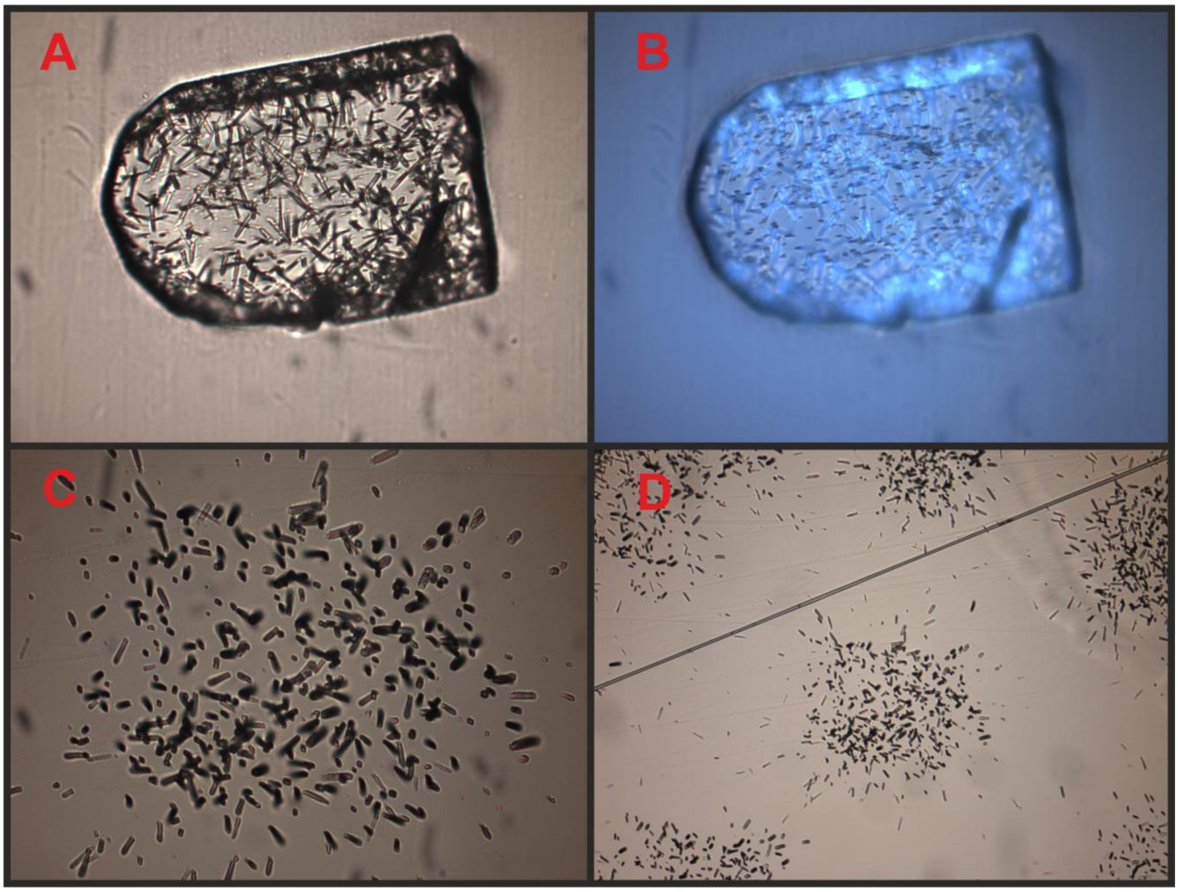

Figure 3.2: Spontaneous and induced fission tracks.
Example fission track slides from sample *BH15 – 05* (this thesis) showing: **A**: spontaneous tracks viewed under transmitted light. **B**: the same grain and tracks viewed under reflected light, showing the sub-horizontally aligned etch pits (black dashes). **C**: induced tracks of the same grain on a mica detector sheet, viewed under transmitted light. **D**: the same grain print viewed under a lower magnification (centre of image). Each cluster of tracks indicates the print of a different corresponding grain.

Price and Walker (1963) recognised the potential problem of track annealing over time and its relationship to temperature, viewing it as a limitation of the system, not a useable feature. While work on this was ongoing, various studies had reported fission track ages on (particularly Pre-Cambrian) rocks to be significantly younger than ages determined by radioisotopes (e.g. Fleischer *et al.*, 1964; Maurette *et al.*, 1964). This problem limited the potential use of fission track analysis as a geochronometer, particularly with samples older than a few tens of millions of years. However Fleischer *et al.* (1965) extensively demonstrated the effect of temperature on annealing (and discounted pressure and ionization as negligible) for a number of mineral phases (but not apatite), which hinted at the future usefulness of fission tracks for thermochronology (though they themselves were yet to recognise this as a useful artefact of thermochronology).

Initially workers attempted to correct for the age under-estimation when dealing with the thermal annealing of tracks (e.g. Mehta and Rama, 1969; Storzer and Wagner, 1969) instead of recognising its usefulness. However Storzer and Wagner (1969) also measured the width of spontaneous etch pits and tentatively suggested at this as a means of deriving thermal histories instead of just an absolute age. The technique was employed further by Storzer (1970) and Wagner and Storzer (1972) who noticed distinct populations of track/etch pit sizes, implying that some tracks had been thermally altered prior to a cooling event whereas others had formed after the event and retained their original size. The different ages of the two populations enabled the timing of the cooling event to be inferred. Other workers began to measure spontaneous track lengths as an alternative and used the distribution of these to derive thermal histories (e.g. Green, 1981; Laslett *et al.*, 1982; Laslett, 1984; Gleadow *et al.*, 1986a,b). Despite this, fission track dating was still largely seen as a geochronological tool at the time (e.g. Ross *et al.*, 1977; 1978; Hurford and Green, 1982).

3.1.2 *Fission tracks in apatite*

Fairly early on it was noticed that apatite in particular was very susceptible to temperature induced track annealing (e.g. Wagner, 1968; Naeser and Faul, 1969; Wagner and Reimer, 1972). It was noted that over timescales of 10^6-10^8 Myrs., fission tracks would be completely erased when exposed to temperatures of only 80-170°C. This described a 'closure temperature' (Dodson, 1973) of the system, a nominal temperature below which a radiogenic daughter product is effectively retained. At the time this was unique, as all other radiogenic systems had a closure temperature of at least a few hundred degrees Celsius. The economic importance of this feature of the AFT system was highlighted by Gleadow *et al.* (1983), as this temperature range closely corresponds to that at which liquid hydrocarbons are generated. The authors used the distribution of confined track lengths (spontaneous tracks) to give unique thermal history information for temperatures from 20-125°C.

Gleadow and Fitzgerald (1987) first coined the term Partial Annealing Zone (PAZ) to describe the temperature window where a proportion of spontaneous tracks are retained over geological timescales. This followed the initial idea of a partial stability zone suggested by Gleadow and Duddy (1981) after comparing AFT ages from down profile of a series of deep boreholes. The PAZ is the FT equivalent of the PRZ (Baldwin and Lister, 1998) which is more widely applicable to all thermochronometers. AFT has a PAZ of c.70-130°C (Gleadow and Fitzgerald, 1987).

3.1.3 *Fission track annealing*

To fully utilise AFT as a thermochronometer, a quantitative understanding of the annealing rate of fission tracks was required. Green *et al.* (1986) provided a qualitative assessment of the thermal annealing of tracks, crucially describing its anisotropy (first reported by Green and Durrani (1977)) and variation with apatite composition (first suggested by Gleadow and Duddy (1981)). The authors then proceeded to provide a quantitative assessment of annealing based on extensive laboratory experiments using a Durango apatite (now a common standard), constructing an empirical mathematical description of the annealing process (Laslett *et al.*, 1987).

3.1.3.1 Anisotropy: Green and Durrani (1977) first reported the anisotropy of track annealing in apatite (it had long been recognised in micas), finding that when the track density of an annealed sample reduced to 0.25 of its un-annealed value, predominantly only tracks parallel to the crystallographic C-axis of apatite remained. They noted that this coincides with the minimum density direction and therefore implies that the anisotropic effect is due to diffusion being greater in the crystal planes parallel to the c-axis. They found this surprising, as apatite has a weak cleavage plain perpendicular to its C-axis. However the authors considered the significance of annealing anisotropy to be fairly small at the time as it didn’t appear to alter the observed track density, which was the thermal parameter used.

Green *et al.* (1986) carried out extensive annealing experiments on a single Durango apatite crystal heated for a range of times (20mins. – 500 days) over a range of temperatures (95° - 400°C). They measured confined track lengths as opposed to track density, and this made annealing anisotropy much more significant. They found that the degree of anisotropy in track length increased as the amount of annealing increased. As the mean track length approached zero, only tracks parallel to the C-axis remained. The annealing of tracks occurred by two processes, the progressive shortening of the tracks from each end, and the breakup of tracks into discontinuous portions. For low degrees of annealing (<0.65) type 1 dominates, with tracks perpendicular to the C-axis shortening more rapidly. For high degrees of annealing (>0.65) type 2 dominates. Following on from these findings, Laslett *et al.* (1987) quantified the anisotropy of the annealing process, whereby different crystal orientations possess different activation energies for the diffusion of atoms (due in part to a heterogeneous distribution of chemical species within the crystal lattice).

To account for annealing anisotropy, when measuring confined track lengths the angle to the crystallographic C-axis is also recorded. It is then possible to carry out a C-axis projection correction, which calculates the length that a confined track would be if orientated with the C-axis (Donelick *et al.*, 1999). Using a C-axis projection also compensates for observer bias (users are more likely to measure longer tracks), increasing the reproducibility of track length data (Ketcham *et al.*, 2007). The C-axis projection correction can either be carried out prior to inputting the data into thermal history reconstructions, or be carried out as part of the computer model (e.g. QTQt).

3.1.3.2 Compositional effects: Gleadow and Duddy (1981) first speculated that different apatite's have different thermal annealing rates, and this is likely caused by differences in their composition. They found that the temperature required to produce a given degree of annealing varied by around 20°C in their study, and this was comparable to the variation seen between different laboratory annealing experiments. The temperature range is greater than the expected experimental uncertainty, and a compositional difference between their apatite's was suggested as an explanation. This theory wasn't expanded upon further.

Green *et al.* (1986) showed that the ratio of Cl (chlorine) to F (fluorine) in apatite was the likely compositional control on annealing rate. Apatite has two end members (plus a third not considered here), chlorapatite (Cl rich) and flourapatite (F rich). Any suite of samples will tend to span the compositional range. They found that in their sample suite, Cl rich crystals showed minimal annealing, whereas F rich crystals showed almost total annealing for the same temperature exposure. This gave a span of ages for the same sample ranging from zero to near the age of formation (which can be referred to as dispersion). Laslett *et al.* (1987) attributed the variation in annealing to the different chemical species Cl^- and F^- having differing activation energies for atomic diffusion, therefore apatite's with different Cl:F ratios will have different bulk diffusion rates.

The composition of an apatite will affect its calculated AFT age, and therefore Cl/F content acts like 'Inherent natural dispersion' in AHe dating. This is 'good' dispersion and helps in the generation of robust thermal histories, but in order for this to work the composition of the apatite needs to be measured during analysis. Green *et al.* (1986) used an electron microprobe to determine the composition on their samples, but this is a costly and time consuming procedure, and therefore impractical for routine application. Instead, the compositional effect on bulk etch rates (D_{par}) is employed as a proxy for ascertaining composition (Donelick, 1993; 1995) (although strictly speaking D_{par} isn't a proxy for composition, but rather an entity in its own right, but is often incorrectly referred to as such (See Donelick *et al.*, 2005)). D_{par} is a measure of the mean etch figure maximum length in a crystal (an etch figure is the intersection of an etch pit on the polished surface), which occurs parallel to the C-axis on a correctly aligned crystal. By measuring a sufficient number of etch figures per crystal, a D_{par} value can be calculated and used in the thermal modelling.

3.1.3.3 Annealing model limitations: For any laboratory observations to be applicable to nature, a scaling up is required from the short timescales of lab experimentation (hours to weeks), to the millions of years which equate to geological timescales. Therefore any potential errors, or differences between competing theoretical models become magnified when extrapolated over geological timescales. This is evident in the observable differences between the parallel and fanning model's Arrhenius plots for annealing rate (Laslett *et al.*, 1987). Both models fit the lab experimental data equally well, but this may not be the case when applied to a geological scenario. The scaling effect also requires lab based observations to be made over much higher temperature ranges to account for the short time scales. This necessitates the assumption that kinetic parameters behave in a proportional manner when scaled up to higher temperatures, which may not always be the case. For example, Wolf *et al.* (1996) found that ^{4}He diffusion behaviour deviates from a linear Arrhenius relationship above c. 290°C while investigating the AHe diffusion kinetics. Similar thresholds may exist for AFT kinetic parameters.

Ketcham *et al.* (2000) point out that there is a potential unquantified source of uncertainty in all annealing models. Annealing models are derived from an empirical fit to a finite number of experiments, and the experimental cases may or may not be representative of all apatite's. In fact, a significant proportion of annealing experiments were carried out on Durango apatite, or other extreme end members which were deliberately chosen in part due to their unique characteristics. They are therefore rather unrepresentative of the apatite's more commonly used for AFT dating (Ketcham *et al.*, 2000; Ketcham, 2005). The same can also be said of the AHe system, with many of the empirical relationships used to define kinetic parameters being based on the unique properties of Durango flourapatite.

3.1.4 Zeta (ζ) calibration

In the early days of fission track dating, discrepancies existed inter-lab in the method of calculating ages. Different workers used different values for functions of the age equation which are defined as physical constants. Despite this, the different labs returned comparable ages for known standards which validated their work. This meant that systematic discrepancies must exist in the methods of calculation and calibration employed by the different labs (Hurford and Green, 1982; 1983). To address this, Hurford and Green (1982; 1983) introduced the Zeta (ζ) calibration, which circumvented the problem of variable 'constants' and created parity between different labs.

Fission track ages are calculated by the following equation (after Price and Walker, 1963; Naeser, 1967):

$$T = \frac{1}{\lambda_D} ln \left[1 + \frac{\lambda_D \phi \sigma I \rho_s}{\lambda_f \rho_i}\right]$$

The term λ_f = spontaneous fission decay constant of ^{238}U, but the value applied to that constant varied considerably lab to lab (e.g. Thiel and Herr, 1976; Bigazzi, 1981). This, along with the thermal neutron fluence (Φ), was selected to give a calibration ratio (Φ/λ_f) which was used to find the age of an independently known sample (standard). Different labs reported ‘correct’ ages with either differing values of λ_f or with differing procedures for measuring and calculating Φ. This meant that comparison of fission track data from different labs was impossible.

Hurford and Green (1982) replaced the decay constant (λ_f) and neutron fluence (Φ) (along with σ and I) with a zeta factor (ζ) in the age equation. This enabled the comparison of future fission track data between labs, creating a much more robust technique. The new age equation is as follows:

$$T_{UKN} = \frac{1}{\lambda_D} ln \left[1 + \xi \lambda_D \frac{\rho_s}{\rho_i}\right]$$

The zeta factor is calculated as:

$$\xi = \frac{[e^{\lambda_D T_{STD}} - 1]}{\lambda_D\,[\rho_S/\rho_i]STD}$$

Where λ_D = total decay constant of ^{238}U, T_{UKN} = age of the unknown sample, T_{STD} = age of standard; and ρ_S/ρ_i = spontaneous/induced fission track density ratio in the standard. In practice this requires the irradiation of one or more known standards in every irradiation tube, and the calculation of track densities for the standards, along with uranium bearing glass dosimeters at each end of the irradiation tube. This removes the need to know the decay constant (λ_f), greatly improving the reproducibility of fission track data.

Initially this method was developed exclusively with zircons, but the authors later extended it to include both apatite and sphene (titanite) (Green, 1985). This required the introduction of new standards for both apatite and sphene, in line with the existing standards for zircon. A suitable age standard requires the following: (a) the sample should come from a geologically well-documented horizon, where the sample is both accessible and abundant. (b) The sample should be homogeneous in age, and consist of a single generation of crystals (i.e. not derived from older rocks). (c) The independent radiometric ages should be unambiguous and compatible with known stratigraphy. (d) The fission-track age must relate to the independent age and neither to the age of an inherited component, nor to a subsequent overprinting event (Hurford and Green, 1983).

Fission track calibrations were formally standardised with the report by the Fission Track Working Group (Hurford, 1990) during the 6th Fission Track Dating Workshop at Besancon, France 1988. This set out the methodology by which all future FT studies should be carried out, and listed the standards to be used for each mineral to enable inter-lab comparisons to be made.

3.2 Interpreting thermal histories

The fact that all fission tracks anneal at a rate dependent on the thermal history they have experienced enables fairly robust qualitative thermal history interpretations to be derived purely from their track length distributions (TLD) and mean track length (MTL) (Gleadow *et al.*, 1986a). All tracks form with an initial etchable track length of 16 ± 1µm (Green *et al.*, 1986; Donelick *et al.*, 1990). While the host rock is hotter than c. 130°C any tracks created anneal almost instantaneously. When the rock cools below c. 70°C any new tracks remain un-annealed, while existing tracks are 'locked in' at their partially annealed length. Therefore the MTL is indicative of the rate of cooling through the PAZ, with rapidly cooled samples having a longer MTL than those that cooled more slowly through the PAZ (figure **3.3**). The TLD is also important, as rapidly cooled samples have a narrow and symmetrical distribution, whereas more slowly cooled samples show a wider and negatively skewed TLD (figure **3.3**). The more complex the thermal history, the more complex the TLD. A bimodal distribution is particularly useful as indicative of a two stage cooling history (Gleadow *et al.*, 1986a).

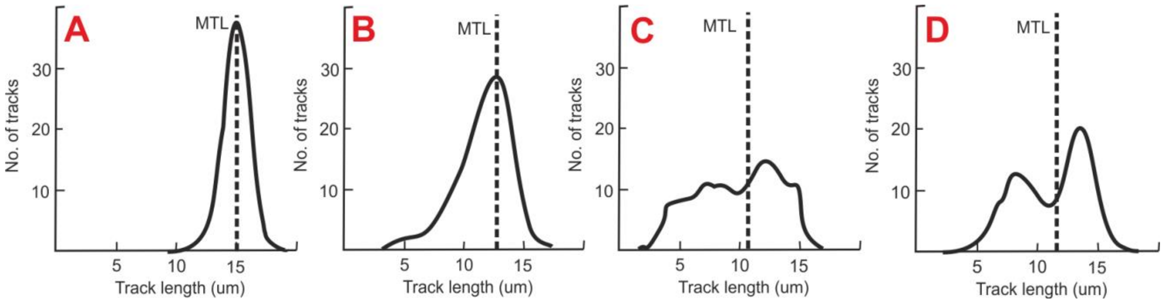

Figure 3.3: Track length distribution (TLD) plots for example thermal histories.
A: young, rapidly cooled samples have a symmetrical TLD, with a MTL c. 15µm and STD of c. 1µm. **B**: slowly cooled cratonic samples have a negatively skewed TLD and a shorter MTL of c. 13µm. **C**: complex thermal histories have a broad and non-symmetrical TLD and a short MTL. **D**: the most distinctive 'mixed' TLD is a bi-modal distribution, indicating two stages of cooling. After Gleadow *et al.* (1986a) and Galbraith and Laslett (1993).

3.2.1 *Inverse Modelling*

With the advent of computational inverse modelling techniques, it became possible to provide a quantitative thermal history interpretation of FT data. Corrigan (1991) developed a stochastic inversion technique to model synthetic data for a range of theoretical thermal histories. This demonstrated the possibility of quantifying thermal history information from AFT data, although the author was fairly disparaging about the poor resolution of the generated inversions (± 10°C at best). The lack of resolution was considered largely down to the uncertainties in the annealing models available at the time, as opposed to the inversion technique itself.

Gallagher (1995) developed on the principles established by Corrigan (1991), adding a multi-dimensional line search technique to the Genetic Algorithm (GA) procedure of Corrigan (1991). The new technique enabled statistically defined confidence regions to be applied to the best fit model, quantifying the uncertainty. The models were still limited by uncertainties in annealing models available at the time (see section 3.1.3), but as with the model of Corrigan (1991), updates in the annealing models could subsequently be incorporated into the existing program.

Ketcham *et al.* (2000) introduced a new program – AFTSolve, which incorporated a new FT annealing model that took into account the effects of compositional variation and anisotropy on track annealing. This greatly improved the reliability of the annealing model used to generate thermal histories, however the authors acknowledge that there are still limitations to their annealing model (as described in section 3.1.3). The program provided the first user friendly graphical interface for inverse thermal history modelling, and was a precursor to the now widely used HeFTy (Ketcham, 2005). Other programs, such as QTQt (Gallagher, 2012) exist in a similar format, and can be used to model data from a range of different thermochronometers (such as AHe and ZHe).

3.3 Recent FT developments

The future of FT dating is to move towards a fully automated system. Currently the FT counting technique is very labour intensive, with a slow sample turn-around time. It requires many operator hours to complete a sufficient number of counts for a robust analysis, and also requires the handling and transportation of radioactive materials. At the forefront of the movement towards automation is the Melbourne work group (University of Melbourne/Autoscan).

3.3.1 *FT Automation*

The first steps towards automation were made in the 80's (e.g. Gold *et al.*, 1984; Smith and Leigh-Jones, 1985). This involved the development of an automated microscope scanning stage which made movement between the mount and its corresponding external detector sheet quick and simple, greatly saving on the time spent searching for the matching crystal and 'print' (Smith and Leigh-Jones, 1985). It also made finding low track density prints much easier and removed the possibility of counting the wrong 'print' on the detector.

Over the next few decades little progress was made towards the goal of a fully automated system, though it remained a key area of research (e.g. Wadatsumi and Masumoto, 1990; Belloni *et al.*, 2000; Petford *et al.*, 2003). Particular problems to overcome involved distinguishing tracks from other non-track defects (e.g. scratches and inclusions), resolving multiple track overlap and identifying small tracks amongst similarly sized defects. Although the above authors made progress in specific aspects of this, none managed to resolve all the issues stated. Gleadow *et al.* (2009) developed a new image-analysis technique – coincidence mapping, which provided the first practical solution which addressed all of the established problems, paving the way for the development of a fully automated system. The authors demonstrated that the automated system has comparable, if not better error rates for recognising and counting tracks than achieved by a human operator alone.

Version 1 of the automated system still required a human operator to measure confined track lengths, so the system couldn't yet be considered 'fully' automated. It did however provide a major step forward, saving a significant amount of researcher time from track counting. Recent improvements in the software have now enabled the measurement of 3D semi-track lengths (Version 3 of the software), and an automated confined track measurement tool is under development, having shown promising results (see Autoscan company website (website 1)). The system is compatible with both the traditional external detector method (EDM) and LA-ICPMS techniques (see section 3.3.2).

3.3.2 *LA-ICPMS Fission Track dating*

Currently the routine method of establishing the concentration of the parent isotope (^{238}U) is the external detector method (EDM). The fission of ^{235}U is induced through proton irradiation in a nuclear reactor and the subsequent tracks are counted on an external mica detector sheet (see figure **3.2**). A new alternative method is the in-situ measurement of ^{238}U through LA-ICPMS (Hasebe *et al.*, 2004). This approach leads to significant savings on sample turn-around time, as it removes the need to send samples off for proton irradiation (which typically takes several weeks/months). It also negates the need for transportation and handling of radioactive materials, improving the safety of the AFT procedure. As only spontaneous tracks require counting, the analysis time itself is also greatly reduced. An additional benefit is that the technique circumvents the need for a zeta (ζ) calibration.

The LA-ICPMS approach has been adopted in a number of studies (e.g. Abdullin *et al.*, 2015; Fernandes *et al.*, 2015; Cogne *et al.*, 2016; Lui *et al.*, 2017). Seiler *et al.* (2013) provided a direct comparison of the LA-ICPMS technique with the EDM, and showed that the results are broadly concordant with each other, and scatter symmetrically around the 1:1 correlation line. The two techniques do however diverge in their correlation for the very high and very low ^{238}U grains. The authors found that for very low U grains (less than a few ppm) the ages obtained through LA-ICPMS are consistently older than those obtained through the

EDM, and for very high ^{238}U grains LA-ICPMS yields consistently younger ages. For the very low ^{238}U grains, the EDM is considered more robust, as the LA-ICPMS appears to underestimate the amount of ^{238}U in the sample, whereas for very high ^{238}U concentration grains, the LA-ICPMS technique is considered more robust due to the difficulties involved in counting induced tracks with a very high track density.

The LA-ICPMS technique also opens up the possibility for double, or even triple dating samples (e.g. Carrapa *et al.*, 2009; Chew and Donelick, 2012; Lui *et al.*, 2014). Double dating enables a crystallisation age and a cooling age to be simultaneously calculated through the combination of a low and high temperature thermochronometer. In the case of AFT this is usually U-Pb dating, which has a temperature sensitivity of c. 450-550°C (e.g. Carrapa *et al.*, 2009). Triple dating introduces an additional thermo/geochronometer, further increasing the thermal history information gleaned from a single crystal. This can also include AHe (e.g. Carrapa *et al.*, 2009).

3.4 Concluding remarks

The FT system is generally considered to be well constrained and is now widely used. Despite this, advancements in other techniques such as AHe continue to pose new questions on aspects of the FT technique, and areas such as annealing kinetics are therefore undergoing constant refinement. The future of FT is to move towards a fully automated process, reducing analyser imposed biases and greatly saving on labour hours. Increasingly a greater number of labs are switching from the EDM to LA-ICPMS techniques for establishing ^{238}U content, and this has opened up the door for the multi-dating of samples. Whichever method is used to carry out AFT, it is a reliable and invaluable tool in a low temperature thermochronometer's toolbox, complementing any AHe investigation.

CHAPTER 4

4. QFrag – THE QTQt APPROXIMATION OF THE FINITE CYLINDER DIFFUSION MODEL

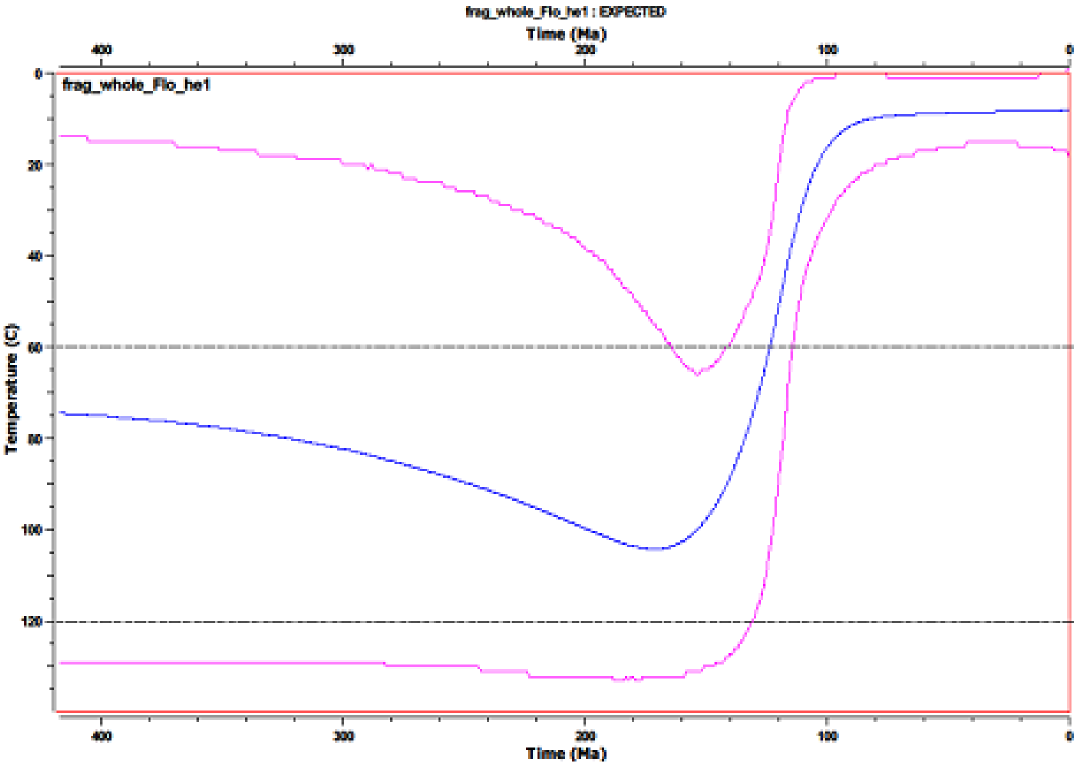

(QTQt output thermal history from *GM14-13*, Guinea)

4.1 Introduction

The fragment model of Brown *et al.*, (2013) and Beucher *et al.*, (2013) involves a new finite cylinder diffusion model (HelFRAG) which is used to reconstruct thermal histories. This takes account of the fact that often mineral separates include broken crystal fragments which have a different diffusive profile to a whole grain and therefore need to be modelled differently. An approximation of this model has been incorporated into the user-friendly modelling software QTQt (Gallagher, 2012) – QFrag. Both HelFRAG and QFrag are currently designed for use with 1T crystal fragments, which can be in combination with whole crystals. This chapter provides the first comprehensive test of the QFrag approximation, demonstrating its ability to replicate the results of the more complex HelFRAG computer code. This precedes the extensive use of QFrag for modelling a real data set in **Chapter 6** of this thesis.

4.1.1 *Rationale*

From the early 1990’s, computer based inverse modelling techniques have been applied to fission track data to reproduce thermal histories (e.g. Corrigan, 1991; Gallagher, 1995; Ketcham *et al.*, 2000). The forward modelling computer program DECOMP (Bikker *et al.*, 2002; Meesters and Dunai, 2002a,b) enabled (U-Th)/He data sets to be combined with fission track generated inverse models using programs such as AFTSolve (Ketcham *et al.*, 2000) in a qualitative way (e.g. Persano *et al.*, 2007), but this was limited to simple monotonic cooling histories. Advances in the understanding of ^{4}He diffusion kinetics (e.g. Farley, 2000; Rainers and Farley, 2001; Meesters and Dunai, 2002a, b) and the effects of radiation damage on ^{4}He diffusion (Flowers *et al.*, 2009; Gautheron *et al.*, 2009) have allowed more sophisticated predictive models for (U-Th)/He to be incorporated into inverse modelling software such as HeFTy (Ketcham, 2005) and QTQt (Gallagher, 2012). It is now routine to produce thermal history inversions based on the joint modelling of fission track and (U-Th)/He datasets, incorporating data from multiple mineral phases if desired.

A perceived problem with the (U-Th)/He system is the often observed (and misunderstood) ‘over dispersion’ (dispersion beyond the formal analytical uncertainty (Vermeesch, 2010)) of single grain ages from a given sample (e.g. Fitzgerald *et al.*, 2006). The potential causes of this have been discussed in C**hapter 2**; in particular broken grains are a significant and previously overlooked contributor to this dispersion (Brown *et al.*, 2013). Intact (2T) crystals are often rare or absent in a sample mineral separate due to the vigorous separation process (e.g. Farley *et al.*, 1996; Farley, 2002), more common are 1T (1 termination intact) or 0T (no terminations intact) fragments. However, modelling such fragments as whole crystals can lead to perfectly sensible but ultimately incorrect thermal histories (Beucher *et al.*, 2013).

It has been shown that 'inherent natural dispersion', far from being problematic, is in fact desirable for generating robust thermal histories, provided broken grains are dealt with appropriately. HelFRAG (Brown *et al.*, 2013; Beucher *et al.*, 2013) can reliably deal with the complexities arising from broken grains retaining one intact crystal termination (1T) when reconstructing thermal histories. However, it is computationally demanding. An approximation of the finite cylinder model utilised in HelFRAG - QFrag has been incorporated into the modelling software QTQt (Gallagher, 2012). The approximation is less computationally demanding, and allows a more routine application of the fragment technique.

4.1.2 *Approximation of the finite cylinder model*

QTQt is a program for generating thermal history reconstructions inferred from low temperature thermochronological data (such as AHe and AFT). As such, it is an inversion technique (but can also generate forward models) – the user inputs their data and the program explores potential Temperature-time paths consistent with such data. To do this, the program implements a Bayesian transdimensional Markov chain Monte Carlo (MCMC) inversion sampling scheme (Gallagher, 2012). Unlike other inversion programs (such as HelFRAG) the data determines the complexity of the thermal history, the number of temperature time points is not pre-defined. The Bayesian approach does however favour simpler solutions (fewer T-t points). Normally QTQt carries out the production-diffusion equations for He in apatite on a spherical or infinite cylinder geometry, but an approximation of the HelFRAG model has been developed to accommodate broken (1T) grains.

The QFrag approximation describes each crystal in terms of a cylindrical central part of length L_c and radius R with two hemispherical terminations of radius R at each end (see figure **4.1**), giving a full grain length of $L_c + 2R$. Two 1-D solutions for the generalised diffusion-production equation are used, as below:

$$\frac{\partial C}{\partial t} = \frac{1}{r^p}\frac{\partial}{\partial r}\left(r^p D \frac{\partial C}{\partial r}\right) + H$$

Where *C* is concentration (of ^{4}He), *D* is diffusivity, *r* is a spatial co-ordinate, and *H* is the rate of production of ^{4}He (by radioactive decay). The parameter *p* selects the geometry of the diffusion domain, with $p = 0$ representing an infinite length slab, $p = 1$ representing an infinite length cylinder, and $p = 2$ representing a sphere. QFrag uses the infinite cylinder solution ($p = 1$) for the cylindrical region between R and $L_c + R$, and the spherical solution ($p = 2$) for the two hemispherical terminations. The boundary conditions are $C = 0$ at the boundaries of the crystal, and $\partial C/\partial r = 0$ in the centre of the cylinder and sphere (Gallagher *et al.*, in press and pers. comm.).

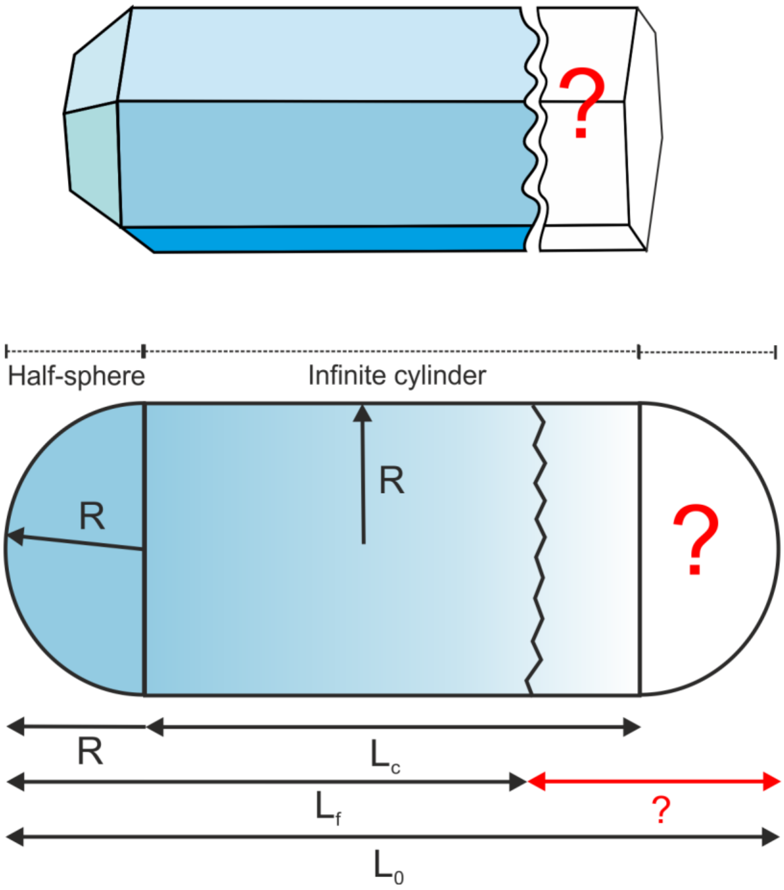

Figure 4.1: Schematic representation of the QFrag model.
The whole grain (L_0) is approximated by a cylindrical section (L_c) and two hemispheres equal to the cylindrical radius (R). L_0 = the initial whole grain length, L_f = the 1T fragment length (L_0 – an unknown missing length). If $L_f < R$ then the 1T fragment is represented by a hemispherical cap of width $L_f < R$. If $L_f > R$ but $< L_c + R$ then the left hand termination plus an infinite cylinder is used. If $L_f > L_c + R$ then the 1T fragment is represented by a full hemispherical termination on the left ($R = R_c$), the full cylindrical segment (L_c) and a hemispherical segment of width $L_f - (L_c - R)$ on the right. After Gallagher *et al.*, in press.

To calculate the age of a fragment of length L_f, the ^{4}He concentration is integrated over the spherical and cylindrical portions of the fragment. The left hand termination defines $x = 0$ for the fragment and if $L_f < R$, then only the appropriate proportion of the left hand spherical termination is used (a hemispherical cap of width L_f,). If $L_f > R$ but $< L_c + R$ then the left hand termination plus an infinite cylinder is used. If $L_f > L_c + R$, then the appropriate portion of the right hand hemispherical termination is also used (a spherical segment of length L_f - (L_c – R)) in addition to the left hand hemisphere and the central infinite cylinder (Gallagher *et al.*, in press and pers. comm.).

QFrag uses a default initial grain length (L_0) of three times the 1T fragment length (L_f) or three times the radius (R) if the fragment length is less than the radius. So when $L_f > R$ then $L_0 = 3L_f$, the length of the cylindrical portion being $L_c = 3L_f - 2R$. When $L_f < R$ then $L_0 = 3R$ and $L_c = R$. It is possible to treat the initial whole crystal length (L_0) as a parameter to be solved (Beucher *et al.*, 2013), but this is not calculated routinely in QFrag. As shown by Beucher *et al.* (2013) and Brown *et al.* (2013), under most conditions it is possible to model age data from fragments successfully without knowing the initial length.

4.1.3 *Application of QFrag to inverse thermal history modelling*

To test the QFrag approximation, three sets of synthetic AHe age data made up of 24 grains have been generated by the program CYLON using the five WOLF thermal histories (figure **4.2** (Wolf *et al.*, 1998)). The geometries of the grains are identical to those used in the models from Brown *et al.* (2013) and Beucher *et al.* (2013) (for full fragment lists, see Appendix 5). Three separate experiments were devised to assess the ability of QFrag to return the correct thermal history (see table **4-1**):

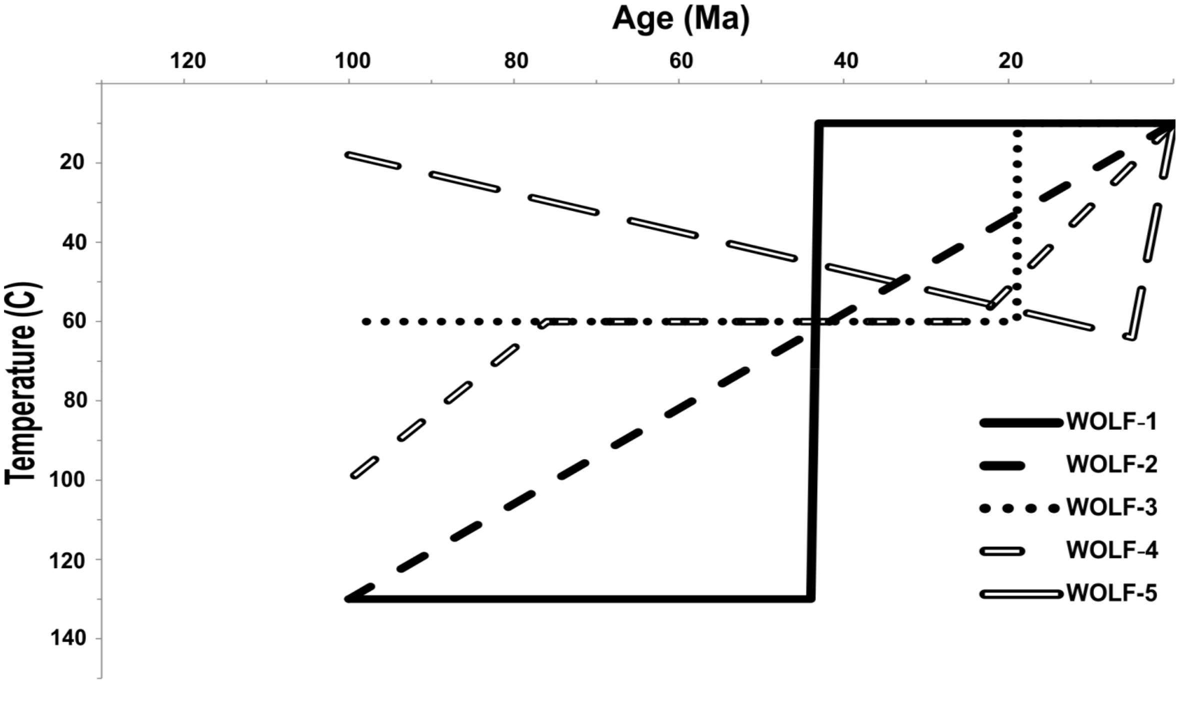

Figure 4.2: The five theoretical WOLF thermal histories (Wolf *et al.*, 1998).
WOLF-1: represents a single rapid cooling event through the PRZ at 44-43Ma starting at 130°C. **WOLF-2**: represents monotonic cooling from 130°C to surface temperatures over 100Myrs. **WOLF-3**: represents a

protracted residence time in the PRZ (held at 60°C) followed by very rapid cooling to the surface at 19Ma. **WOLF-4**: represents cooling from 100°C to 60°C at 100Ma-76Ma, followed by a protracted residence time in the PRZ. Cooling from 60°C to surface temperatures then occurs over 24Ma-0Ma. **WOLF-5**: represents reheating from the surface into the PRZ over 100Ma-5Ma (reaching 64°C), followed by rapid cooling to the surface.

4.1.3.1 Experiment 1 (figures ***4.3-4.4****):* 24 identical grains were generated from each WOLF history with an initial length (L_0) of 400μm, a radius (R) of 75μm and nominal uranium ($^{235}U+^{238}U$) and thorium (^{232}Th) values of 19.7ppm and 19.9ppm respectively. These were then randomly 'broken' along the basal cleavage plane to give 24 1T (1 intact termination) fragments from each WOLF history of lengths (L_f) ranging from 40-385μm (**table 4-1**). Each 'sample' was then modelled in QTQt for 1,000,000 model iterations with the only T-t constraint being an initial box at 120°C ± 10°C and 120Ma ± 10Ma. The purpose of the constraint was to force the general thermal history to start at high temperatures before the time we expect the data to be able to resolve the actual thermal history. This helps to better reconstruct thermal histories with rapid cooling from high temperatures. For example, data from WOLF-1 can be well explained by a thermal history starting around 45Ma with a constant temperature of around 20°C to the present. This would suggest rapid cooling just prior to 45Ma from an unknown (and unimportant) initial temperature. Adding the older, high temperature constraint lets the data decide directly when they cool into the PRZ.

The modelling was done twice per 'sample', firstly with the fragment model switched off (i.e. all grains incorrectly modelled as whole grains) and secondly with the fragment model switched on (all grains modelled correctly as fragments). The 'no radiation damage model' option was selected for this experiment because all grains have an identical eU concentration, so will follow the same diffusion kinetics, making a radiation damage model redundant.

4.1.3.2 Experiment 2 (figure ***4.5-4.6****):* 24 random grains were generated from each WOLF history with variable grain size (L_0 range: 219-593μm, R range: 57-100μm) and nominal uranium ($^{235}U+^{238}U$) and thorium (^{232}Th) values of 19.7ppm and 19.9ppm respectively. These were then randomly 'broken' along the basal cleavage plane to give 24 1T fragments from each WOLF history of lengths (L_f) ranging from 61-444μm (table **4-1**). Each 'sample' was then modelled as for Experiment 1, both incorrectly as whole grains and correctly as fragments. The 'no radiation damage model' option was still applied because eU concentration (and therefore diffusion kinetics) remained identical between each grain.

4.1.3.3 Experiment 3 (figure ***4.7-4.12****):* 24 random grains were generated from each WOLF history with variable grain size (L_0 range: 219-593µm, R range: 57-100µm) and variable uranium and thorium content (U range: 6.25-116.35ppm, Th range: 6.39-118.98ppm). These were then randomly 'broken' along the basal cleavage plane to give 24 1T fragments from each WOLF history of lengths (L_f) ranging from 61-444µm (table **4-1**). Each 'sample' was then modelled as for Experiment 1 and 2, both incorrectly as whole grains and correctly as fragments, but this time the radiation damage model of Flowers *et al.* (2009) (RDAAM) was enabled to account for the variation in eU (and therefore radiation damage accumulation) across the grains. Comparable results have been obtained with shorter test runs using the radiation damage model of Gautheron *et al.* (2009) (not presented here). RDAAM was chosen ahead of the radiation damage model of Gautheron *et al.* (2009) so as to replicate the experiments of Beucher *et al.* (2013) who used RDAAM in their paper. This enables like for like comparisons between the QFrag and HelFRAG inverse models.

A sub-set of modelling has been carried out using WOLF histories 2, 3 and 5, with the grain and fragment dimensions of Experiment 3, but smaller ranges of eU (5ppm, 25ppm and 50ppm respectively). These have also been modelled both incorrectly as whole grains and correctly as fragments, using the radiation damage model RDAAM (Flowers *et al.*, 2009). Having a large range in eU can result in radiation damage becoming dominant over the other causes of inherent natural dispersion, making it difficult to interpret the fragment effect. Using smaller ranges of eU enables the QFrag approximation to be tested with a radiation damage model switched on (in this instance RDAAM) without the radiation damage induced inherent natural dispersion dominating over the fragment effect.

Table 4-1: Experiment matrix
Matrix of variables as per each experiment. L_f = the 1T fragment length, L_0 = the initial whole grain length, R = grain radius and eU = effective Uranium.

Experiment No.	L_f	L_0	R	eU
Experiment 1	Range (40-385µm)	Fixed (400µm)	Fixed (75µm)	Fixed (24.38ppm)
Experiment 2	Range (40-385µm)	Range (219-593µm)	Range (57-100µm)	Fixed (24.38ppm)
Experiment 3	Range (40-385µm)	Range (219-593µm)	Range (57-100µm)	Range (7.75-144.31ppm)
Experiment 3a				Range (3-8ppm)
Experiment 3b				Range (3-28ppm)
Experiment 3c				Range (3-53ppm)

Experiment 1 limits the inherent natural dispersion solely to the fragment effect, with grain size and eU being controlled. Experiment 2 introduces a second variable – grain size - contributing to natural dispersion, whilst maintaining the same eU value. This may be realistic for some real life samples which have a very small range in eU values. Experiment 3 replicates the levels of dispersion that are likely to be seen within real datasets (such as the data presented in **Chapter 5**), whereby all three causes of inherent natural dispersion are at play, maximising dispersion (see table **4-1**). The purpose of the three experiments is to demonstrate how increasing the natural dispersion improves the ability of the models to return the true histories. For a full discussion of this, see Brown *et al.* (2013) and Beucher *et al.* (2013).

4.2 Results and discussion

Figures **4.3-4.12** show the model outputs for each experiment (left panel). The black dashed line indicates the true thermal histories of WOLF 1-5 (Wolf *et al.*, 1998) as shown in figure **4.2**, which were forward modelled to generate the synthetic grains. The pink solid lines represent 95% credibility intervals and the solid blue line the expected thermal history. The red box is the model prior and the black box the specified T-t constraint. The colour fill represents the marginal probability distributions, with the brighter colours (yellows and pinks) indicating higher probability, and the blues indicating lower probability (for full descriptions see Gallagher (2012) and the QTQt user manual). Also shown are the observed age verses predicted age plots for each model (right panel), with a nominal value of 5% for the input analytical error.

4.2.1 *Experiment 1 - fragments of random lengths with the same original grain size (L_0 and R) and eU concentration*

4.2.1.1 Fragments modelled as whole grains: Figure **4.3** shows the results of modelling the data incorrectly as (2T) whole grains. For each model a perfectly sensible thermal history is generated with a very strong data fit (see observed vs. predicted plots). But with the exception of WOLF-1, each generated thermal history is incorrect (even WOLF-1 over predicts the timing of the onset of cooling by several million years). It comes as little surprise that the model can return a sensible result for WOLF-1 as this, rapidly cooled thermal history is the simplest thermal history that a sample can undergo, owing to the very rapid ascent through the PRZ. Indeed the model wants to follow this same simple thermal history in four of the five examples (WOLF 1-4). This is likely due to the lack of thermal history information retained in the data (as each initial crystal is effectively the same), leading the model to a simple thermal history solution.

In the Observed vs. predicted age plot for WOLF-5, the data point and horizontal error bars sit slightly above each vertical error bar, which at first appears illogical. This is because the data point (small green triangle) represents the intersection of the true ‘observed’ age with the predicted model age from the expected thermal history (and the horizontal error bars are the input errors of the true ‘observed’ age). The vertical error bars represent the predicted ages from all the accepted thermal histories within the 95% credibility intervals. The expected thermal history is not a T-t path generated by the model, but rather a weighted average of all the accepted thermal history T-t paths. It is therefore not sampled as part of the MCMC resampling to generate the model predictions (Gallagher, pers. com.). This means that it is possible for the predicted age from the expected thermal history to differ from the predicted ages from the accepted thermal histories, giving the mismatch seen on the observed vs. predicted plots. In the case of this experiment, the expected thermal history generates predicted ages which are older than the predicted ages from the accepted models, meaning that the data fit is less good than first appearances suggest.

4.2.1.2 Fragments modelled as fragments: Figure **4.4** shows the results of modelling the data correctly as (1T) fragments. Again each model generates a perfectly sensible looking thermal history with a very good data fit (except WOLF-5), but with the exception of WOLF-1 (which shows a slight improvement in the timing of the onset of rapid cooling) it is still an incorrect thermal history. This is in contrast to the same experiment modelled using HelFRAG, which returned more accurate results (Beucher *et al.*, 2013, see **Chapter 2**, figure **2.11**). The fragment effect alone carries sufficient thermal history information to reproduce the desired thermal histories when modelled using the full HelFRAG computer model, but when using the QFrag approximation there is still insufficient thermal history information within the data to accurately model these thermal histories. The comparison here is slightly biased, because the fragment list was generated using CYLON which is part of the HelFRAG program. Therefore the data is ‘perfect’ when using the HelFRAG model kinetics, but not strictly ‘perfect’ when using the QFrag model kinetics. Experiment 1 is unrealistic to a real dataset however, as there will always be some variation in either grain size and/or eU concentration within a natural sample.

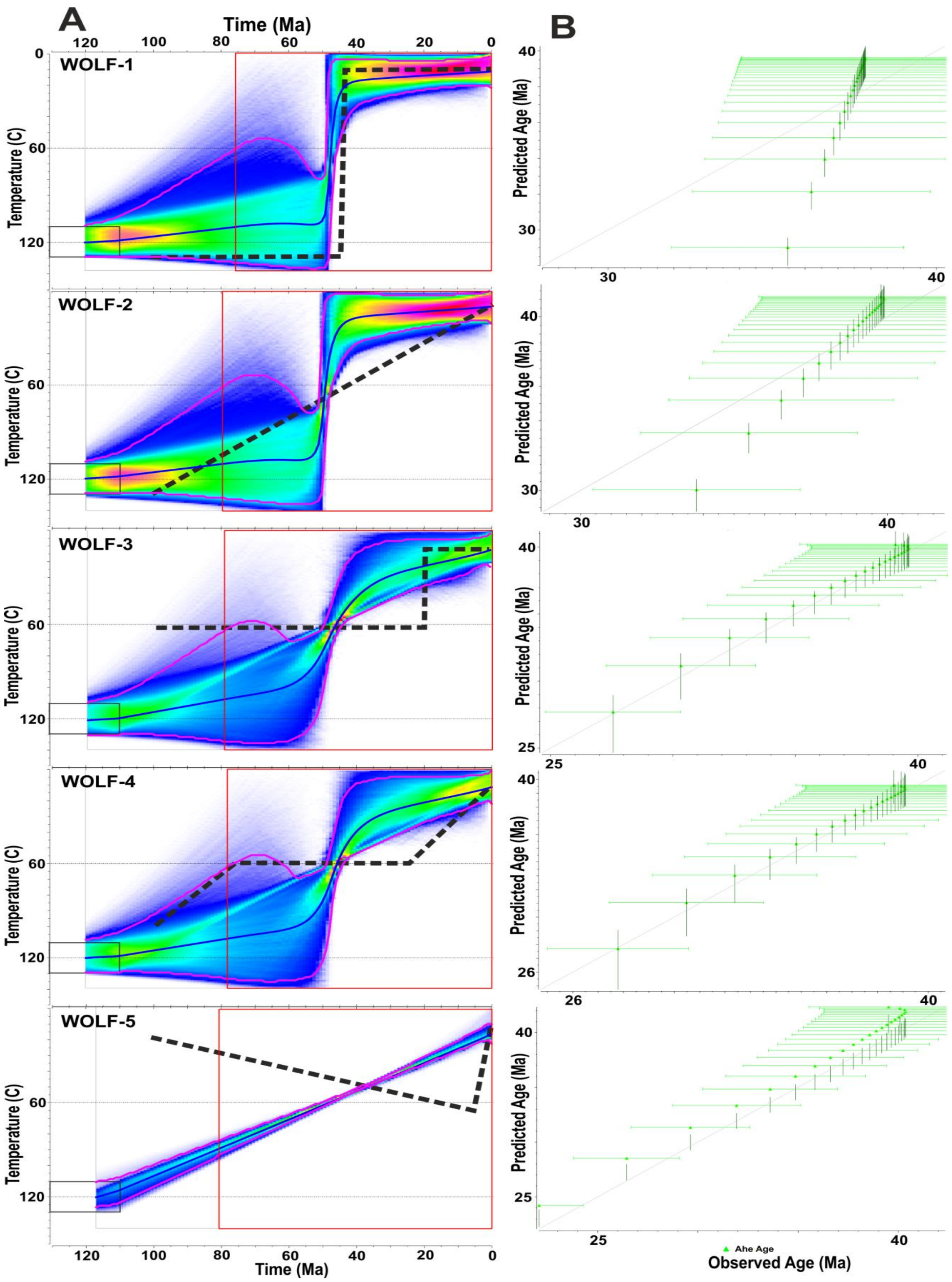

Figure 4.3: Experiment 1 - fragments modelled incorrectly as whole grains.
Inverse models (1,000,000 iterations) of synthetic sample grains generated from forward models of the 5 WOLF thermal histories (Wolf *et al*., 1998). Each sample comprises 24 1T (1 crystal termination) fragments of random lengths (range: 40-385µm), generated from the same initial whole crystal of length L=400µm, radius R=75µm, uranium (U_{235}+U_{238})=19.7ppm and thorium (Th_{232})=19.9ppm. Here the grains are incorrectly modelled as (2T) whole crystals. **A**: the generated thermal histories for WOLF-(1-5). Black dashed line = true thermal history (see figure **4.2**), pink solid lines = 95% credibility intervals, blue solid line = expected model, colour represents the marginal probability distribution of the thermal history (blues represent lower probability, greens through to red represent higher probability), black box = T-t constraint set at 120°C ± 10°C and 120Ma ± 10Ma, red box = model prior (see QTQt user manual). **B:** observed age vs. predicted age plots for the generated thermal history.

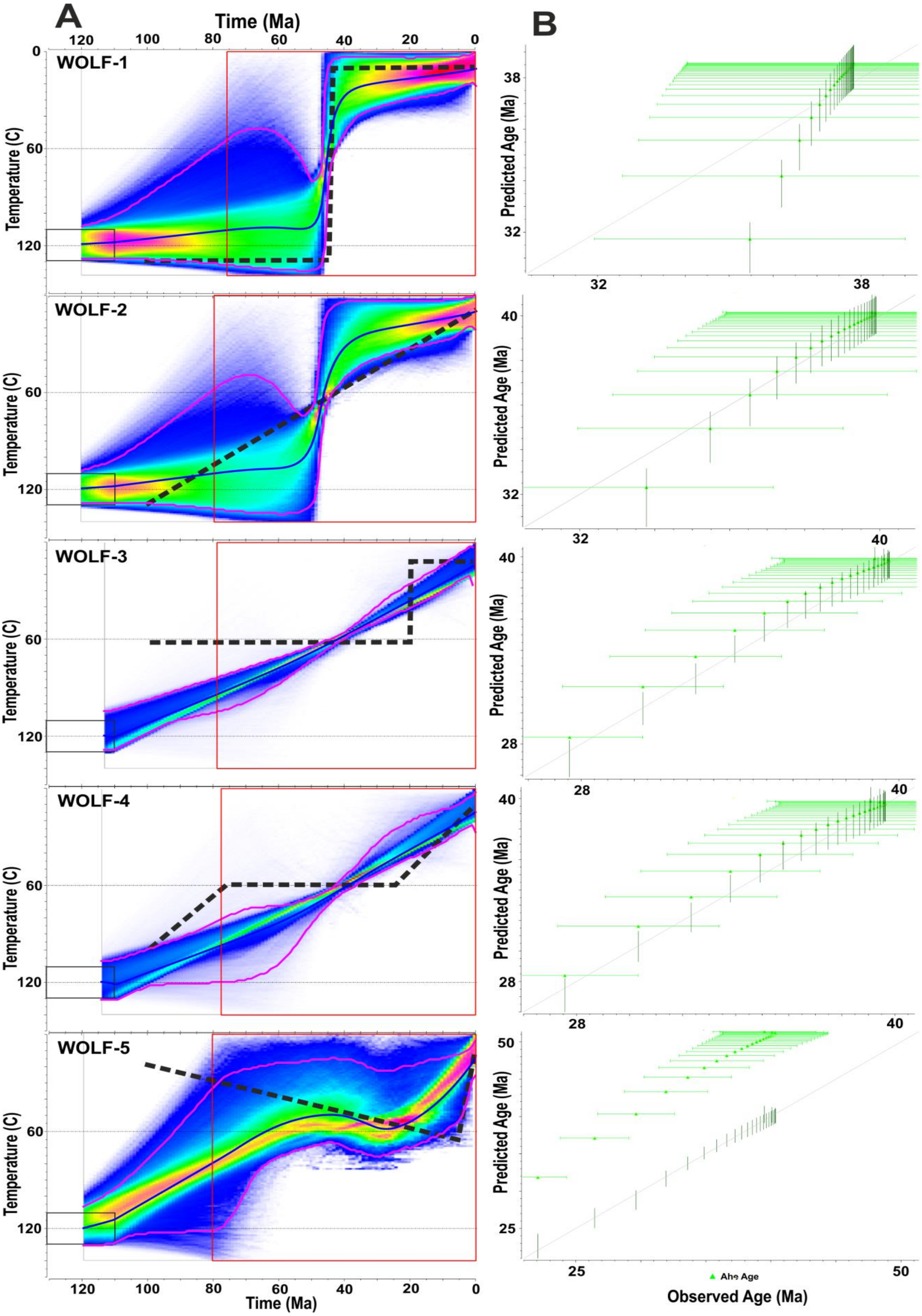

Figure 4.4: Experiment 1 - fragments modelled correctly as fragments.

Inverse models (1,000,000 iterations) using the same synthetic grains as for figure **4.3**. Here the grains are modelled correctly as (1T) crystal Fragments. **A**: the generated thermal histories for WOLF-(1-5). Black dashed line = true thermal history (see figure **4.2**), pink solid lines = 95% credibility intervals, blue solid line = expected model, colour represents the probability density of the thermal history (blues represent lower probability, greens through to red represent higher probability), black box = Temp-time constraint set at 120°C ± 10°C and 120Ma ± 10Ma, red box = model prior (see QTQt user manual). **B:** observed age vs. predicted age plots for the generated thermal history.

Again in the plot for WOLF-5, the expected model predictions sit above the accepted model 95% credibility interval predictions, in this case significantly above. This means that the expected model is actually a poor fit for the data, despite the accepted models giving a strong 1:1 observed vs. predicted linear trend. The offset is systematically above the 1:1 line because a significant number of accepted models experience histories with cooling and reheating, causing some ages to be reset, but the expected model averages these out, resulting in less reheating and no resetting of the ages. This results in the age predictions for the expected model being systematically older than the predictions from the accepted models.

It is worth noting that the models for WOLF-3 and WOLF-5 have been hampered by the initial T-t constraint placed at 120°C ± 10°C and 120Ma ± 10Ma, which for these models is inaccurate. The constraint was included in every model to maintain consistency and remove operator bias throughout the experiments. This T-t constraint was not used in the HelFRAG experiments, which may partially explain the more accurate results found using HelFRAG, however the models with the best model fit still want to start hot before cooling to the correct temperature even without the T-t constraint being utilised in HelFRAG (see Beucher *et al.*, 2013).

4.2.2 *Experiment 2 - fragments of random lengths, variable original grain size (L_0 and R) and identical eU concentration*

4.2.2.1 Fragments modelled as whole grains: Figure **4.5** shows the results of modelling the data incorrectly as (2T) whole grains. Again each model generates a perfectly sensible looking thermal history with an acceptable data fit (except WOLF-5), but with the exception of WOLF-1 the history is incorrect. There is still insufficient thermal history information retained within the natural dispersion generated by grain size variation alone.

The observed verses predicted age plots show a less accurate data fit than the corresponding plots in experiment 1 (more scatter around the 1:1 line), but this is purely down to the fact that there is an added variable in the original data (initial grain size) so there is greater natural age dispersion. The data fits for WOLF 1-4 would still be considered good when dealing with real data. Some of the predicted ages in WOLF-3 and 4 sit slightly above the vertical error bars for reasons already discussed. Again for WOLF-5 the expected model predictions are significantly older than the accepted model predictions, giving a poor data fit. From looking at the probability density (colour shading) of the accepted models it is clear that the expected model is trying to 'marry' two different sets of accepted models so it is unsurprising that the data fit is poor.

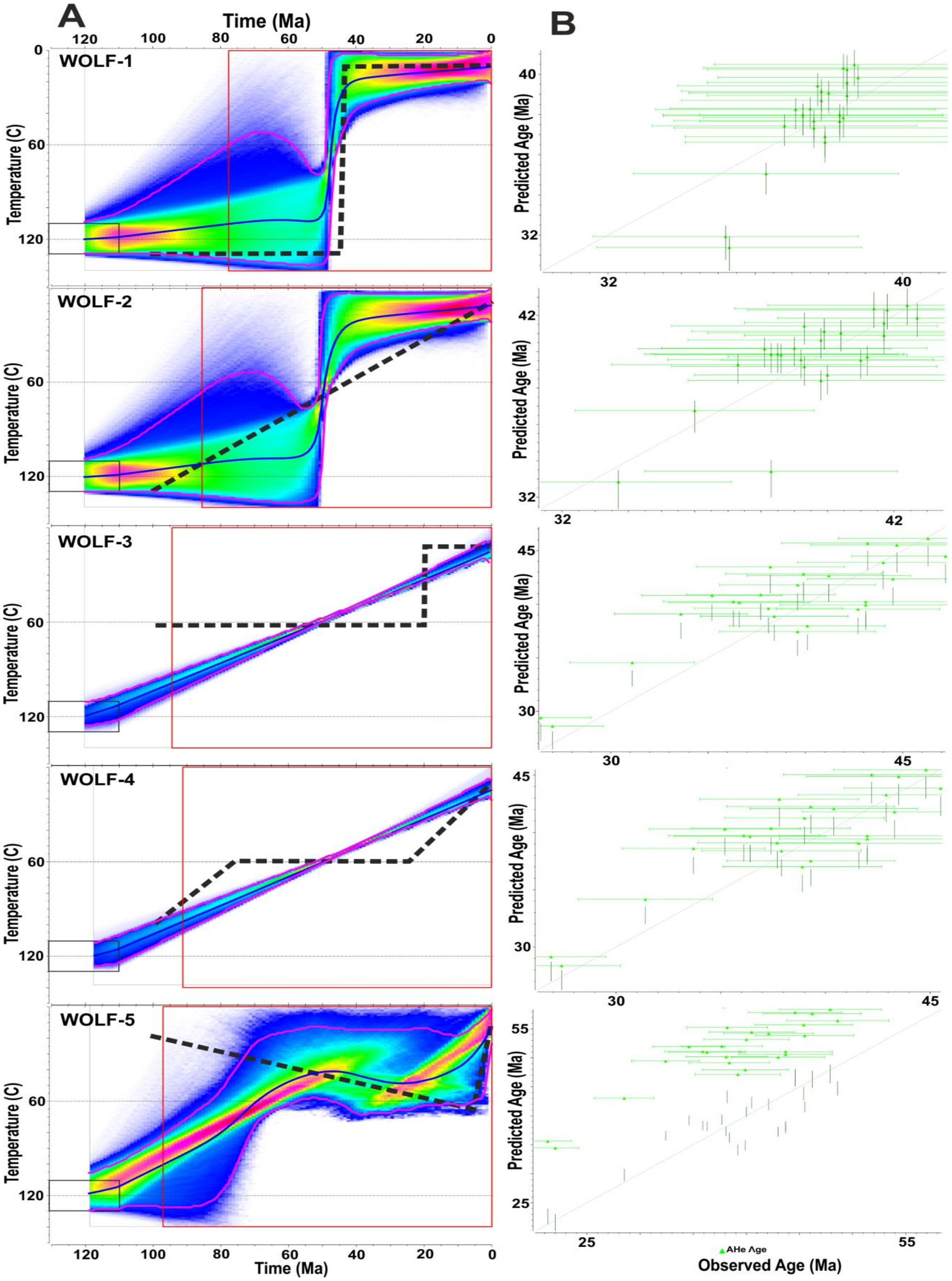

Figure 4.5: Experiment 2 - fragments modelled incorrectly as whole grains.

Inverse models (1,000,000 iterations) of synthetic sample grains generated from forward models of the 5 WOLF thermal histories (Wolf *et al*., 1998). Each sample comprises 24 1T fragments of random lengths (range: 40-385µm), generated from variably sized original whole crystals (L_0 range: 219-593µm, R_0 range: 57-100µm) with a nominal uranium (U_{235}+U_{238}) and thorium (Th_{232}) concentration of 19.7ppm and 19.9ppm respectively. Here the grains are incorrectly modelled as (2T) whole crystals. **A**: the generated thermal histories for WOLF-(1-5). Black dashed line = true thermal history (see figure **4.2**), pink solid lines = 95% credibility intervals, blue solid line = expected model, colour represents the marginal probability distribution of the thermal history (blues represent lower probability, greens through to red represent higher probability), black box = T-t constraint set at 120°C ± 10°C and 120Ma ± 10Ma, red box = model prior (see QTQt user manual). **B:** observed age vs. predicted age plots for the generated thermal history.

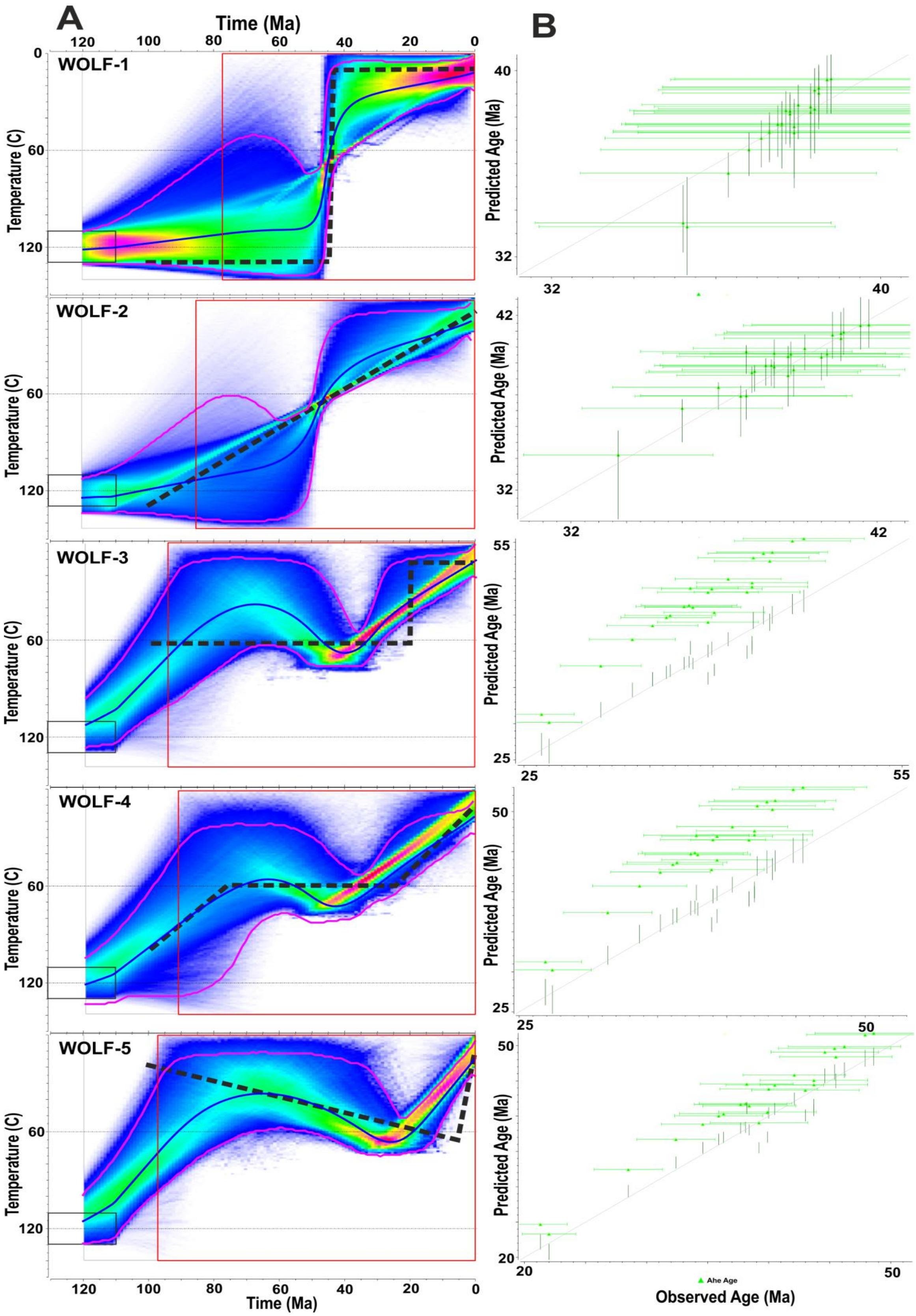

Figure 4.6: Experiment 2 - fragments modelled correctly as fragments.
Inverse models (1,000,000 iterations) using the same synthetic grains as in figure **4.5**. Here the grains are modelled correctly as (1T) crystal Fragments. **A**: the generated thermal histories for WOLF-(1-5). Black dashed line = true thermal history (see figure **4.2**), pink solid lines = 95% credibility intervals, blue solid line = expected model, colour represents the marginal probability distribution of the thermal history (blues represent lower probability, greens through to red represent higher probability), black box = T-t constraint set at 120°C ± 10°C and 120Ma ± 10Ma, red box = model prior (see QTQt user manual). **B:** observed age vs. predicted age plots for the generated thermal history.

4.2.2.2 Fragments modelled as fragments: Figure **4.6** shows the results of modelling the data correctly as (1T) fragments. Here there is a marked improvement in the reproducibility of all five thermal histories:

WOLF-1 is successfully reproduced, with a very slight improvement in the accuracy of the timing of rapid cooling found when modelling fragments as fragments (this slight improvement was also the case in experiment 1). The results are actually better than the results for the HelFRAG equivalent, which favours solutions which start cool and reheat before rapidly cooling again at the correct time. This may be due to the lack of an initial T-t constraint in the HelFRAG models as the data provides no constraint on the history prior to the rapid cooling through the PRZ.

WOLF-2 still appears to show a rapid cooling history comparable to WOLF-1, but the marginal probability distributions of this model show that monotonic cooling matching the true thermal history is strongly favoured within the acceptable range of thermal histories. Although rapid cooling is possible with this data (and implied by the expected model), monotonic cooling is the more probable model outcome in this case. Here the model is better constrained in the early part of the history than the HelFRAG equivalent, and less so in the later part of the history (which is very accurate using HelFRAG). The improved reproducibility on the early part of the history is likely provided by the initial T-t constraint as opposed to the ability of the data itself to constrain this part of the history. Overall the HelFRAG model is more able to constrain this thermal history than the QFrag approximation.

WOLF-3 shows a reasonable approximation to the true thermal history, and this could potentially be improved by removing the initial T-t constraint box which forces the model to start much hotter than it needs to. The model accurately predicts the temperature of c. 60°C that the 'sample' was held at in the PRZ, but it initially ‘overshoots’ this temperature when cooling from the initial T-t constraint. This results in the model favouring a reheating episode prior to cooling, but this can be prevented in QTQt by forcing the model to discount possible T-t paths that undergo reheating (see QTQt user manual and **Chapter 6**). This would be a perfectly valid assumption to make as reheating requires burial of the sample, which typically leaves evidence in the geological record for real samples. Preventing reheating has not been implemented here however so as to maintain the same boundary conditions for each model set to avoid user bias, but would be a valid assumption for a real sample.

The model still struggles to predict the very rapid rate and timing of cooling from the PRZ to the surface, and this was also the case when modelling WOLF-3 with HelFRAG (Beucher *et al.*, 2013). Even without the incorrect initial T-t constraint, a number of the favoured HelFRAG solutions still wanted to start hot and then cool, overshooting the PRZ before reheating to the correct temperature.

WOLF-4 shows a very strong relation to the true history, although it also favours a slight reheating episode. Again this could be prevented in the model and it would be a valid assumption to do so. The overshoot followed by reheating was also the case (although less pronounced) with the HelFRAG equivalent (Beucher *et al.*, 2013).

WOLF-5 has an overall similarity with the true history, but the timing of the late stage cooling to the surface is over predicted. The model accurately predicts the temperature of c. 60°C that the sample needs to be reheated to, but wants to cool slightly earlier in its history. If this were a real sample, there would likely be evidence of reheating in the surrounding geology, so allowing the model to undergo reheating would be sensible. The HelFRAG equivalent is very similar, even without the inaccurate initial T-t constraint, but it does more accurately predict the timing of the late stage cooling than the QFrag version.

The observed vs. predicted plots for WOLF 1, 2 and 5 show very good data fit, and show less scatter than in figure **4.5**. This supports the fact that treating fragments as fragments generates more accurate thermal histories than treating them as whole grains. The plots for WOLF 3 and 4 (and to a lesser extent 5) show the same discord between the expected and accepted model fits as has been seen in some of the models from the previous figures. This is again systematic, with the expected model ages always older than the accepted.

Experiment 2 is a realistic representation of some natural samples, which may have a very limited range of eU values (all within analytical error of each other). It highlights the importance of modelling fragments correctly as fragments when other causes of natural dispersion are minimal, as figures **4.5** and **4.6** show how different the modelled thermal history can be when modelling fragments as fragments verses whole grains. This experiment demonstrates that the QFrag approximation of the finite cylinder model works when grain size variations are controlling dispersion, and that the results are comparable to those using the HelFRAG model (in some instances slightly better, in others slightly worse, but overall comparable).

4.2.3 *Experiment 3 - fragments of random lengths, variable original grain size and variable eU concentration*

This experiment is the most realistic representation of real datasets, which will have a range of grain sizes and eU concentrations. All three known causes of inherent natural dispersion: fragmentation, grain size variation and eU concentration will contribute to the range of single grain ages within a sample, and this may lead to well in excess of 100% single grain age dispersion (Brown *et al.*, 2013).

Figure **4.7** shows the data modelled incorrectly as 2T grains, and figure **4.8** shows the data modelled correctly as 1T grains. In this case there is negligible difference between modelling the data as fragments or whole grains, and neither way is more accurate than the other. This is because the effects of radiation damage and annealing dominate the other causes of natural dispersion. Radiation damage is still a component of the AHe system which is yet to be fully understood, indeed we currently use two very different diffusion kinetics models (Flowers *et al.* (2009) and Gautheron *et al.* (2009)) within modelling software, and each may ultimately be inaccurate (e.g. see **Chapter 2**, section *2.2.2.6* for discussion of damage interconnection). As the data used here is synthetic data, and was therefore generated using the diffusion kinetics of the existing models, the data behaves as expected when modelled using the radiation damage model/s, but this may not be the case with real datasets.

WOLF-1: As in Experiments 1 and 2, the only difference between the thermal histories when modelled as fragments or as whole grains is a marginal shift in the timing of the onset of rapid cooling towards the true thermal history when modelled correctly as fragments. WOLF -1 is a very simple thermal history to reconstruct. Similarly to Experiment 2, the results are actually more accurate than in the equivalent HelFRAG experiment (see figure **4.9**), which favours models which start near the surface and reheat before cooling rapidly again, for the same reasons as in Experiment 2.

WOLF-2: Both models appear to initiate cooling too early, but this is purely an artefact of the initial T-t constraint, which forces the model to start 20Ma before the true thermal history began. This means that the gradient of the monotonic cooling is slightly lower than the true history, but the model accurately reproduces a simple monotonic cooling history. This type of thermal history can also be considered relatively simple, and as such, it is sometimes the history which is settled upon when there is insufficient thermal history information within the data as an alternative to the rapid cooling style of WOLF-1. This can be seen in a number of the previous figures such as for WOLF-3 and 4 in figures **4.4** and **4.5**. Again the early part of this history is actually better constrained than in the HelFRAG equivalent (see figure **4.12**), but this is due to the initial T-t constraint used in QTQt.

WOLF-3: As with Experiment 2, figure **4.6**, both models successfully reproduce the holding of the 'sample' at c. 60°C in the PRZ (in fact, the marginal probability distribution suggests that in this experiment, the data works better when not modelled as fragments), but struggle to reproduce the late stage rapid cooling, preferring a slower rate of cooling. Both models ‘overshoot’ the 60°C mark when cooling from the initial constraint, and this leads to a degree of reheating being required for the expected model. As with Experiment 2, figure **4.6** this reheating could be prevented by the modelling software, likely improving the reproducibility of the thermal history. Removing the initial T-t constraint may also achieve this. The HelFRAG equivalent similarly fails to predict the timing and rate of the late stage cooling (see figure **4.12**). This type of thermal history is clearly problematic to accurately reconstruct using either software.

WOLF-4: Both models accurately reproduce the two-stage cooling with a residence time in the PRZ at c. 60°C. The accuracy may be improved further by not allowing reheating in the models. As it stands both models still overshoot with the first stage of cooling before needing to reheat slightly to the correct temperature. This was also the case with the HelFRAG equivalent (see figure **4.9**).

WOLF-5: Both models accurately reproduce the reheating history, despite the initial T-t constraint. There is greater certainty around the rate of this reheating when modelled as fragments, as shown by the marginal probability distribution. When modelled as fragments there is also a slight improvement in the timing of the rapid cooling event at the latter stages of the history. Both models provide a very close replication of the HelFRAG solution (see figure **4.12**).

The data fit on the observed vs. predicted plots is marginally stronger when modelling fragments as fragments (figure **4.8**) verses modelling fragments as whole grains (figure **4.7**). In both instances there are a number of predicted ages which don’t intersect the vertical credibility intervals, particularly for WOLF-3 and 4, but where this is the case the offset is smaller when modelling fragments as fragments. This provides evidence that modelling fragments correctly as fragments produces models with a better data fit than when modelling fragments as whole grains.

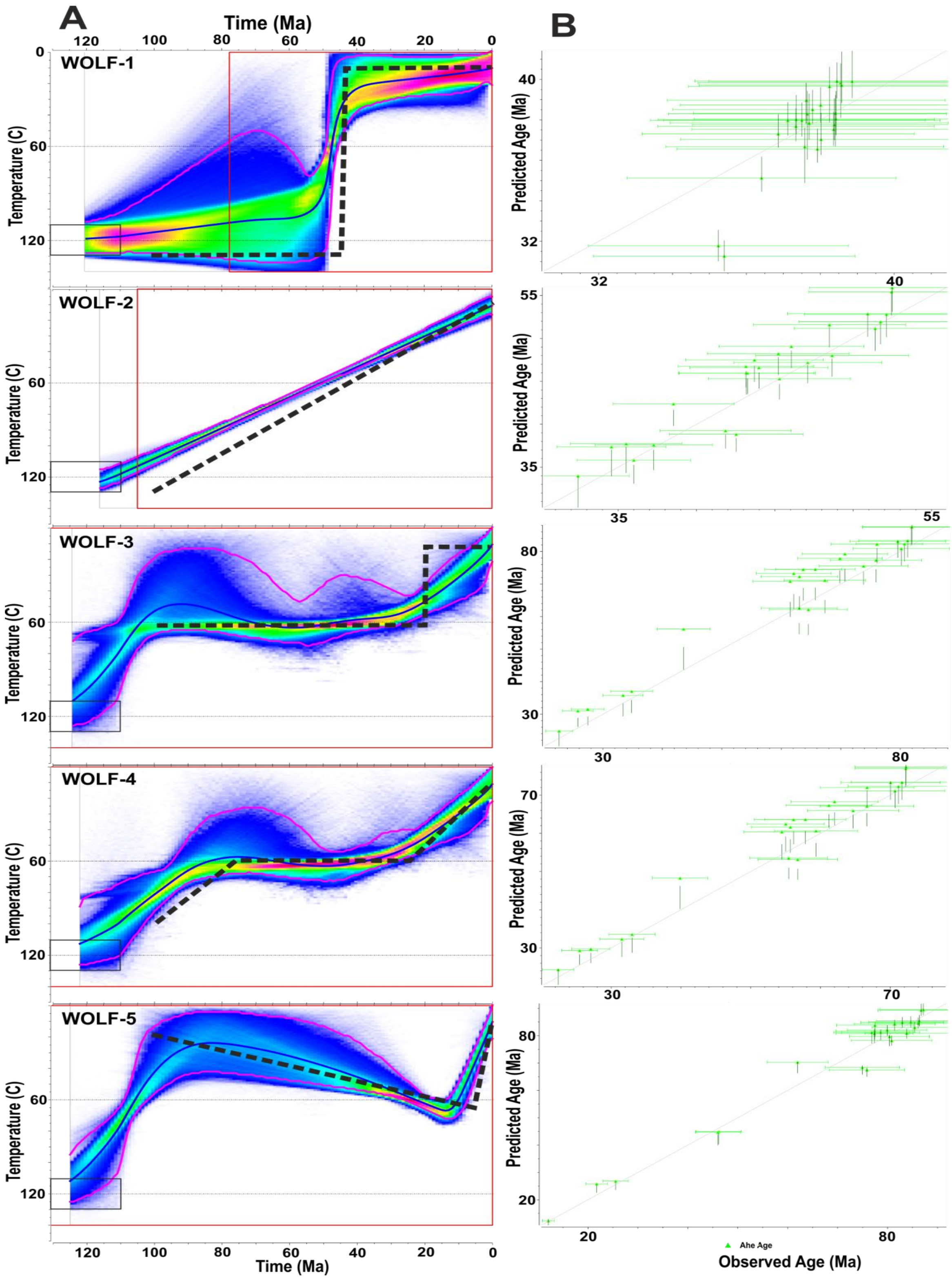

Figure 4.7: Experiment 3 - fragments modelled incorrectly as whole grains.

Inverse models (1,000,000 iterations) of synthetic sample grains generated from forward models of the 5 WOLF thermal histories (Wolf *et al*., 1998). Each sample comprises 24 1T fragments of random lengths (range: 40-385µm), generated from variably sized original whole crystals (L_0 range: 219-593µm, R_0 range: 57-100µm) with a realistic range of eU values (U range: 6.25-116.35ppm, Th range: 6.39-118.98ppm). Here the grains are incorrectly modelled as (2T) whole crystals. **A**: the generated thermal histories for WOLF-(1-5). Black dashed line = true thermal history (see figure **4.2**), pink solid lines = 95% credibility intervals, blue solid line = expected model, colour represents the marginal probability distribution of the thermal history (blues represent lower probability, greens through to red represent higher probability), black box = T-t constraint set at 120°C ± 10°C and 120Ma ± 10Ma, red box = model prior (see QTQt user manual). **B:** observed age vs. predicted age plots for the generated thermal history.

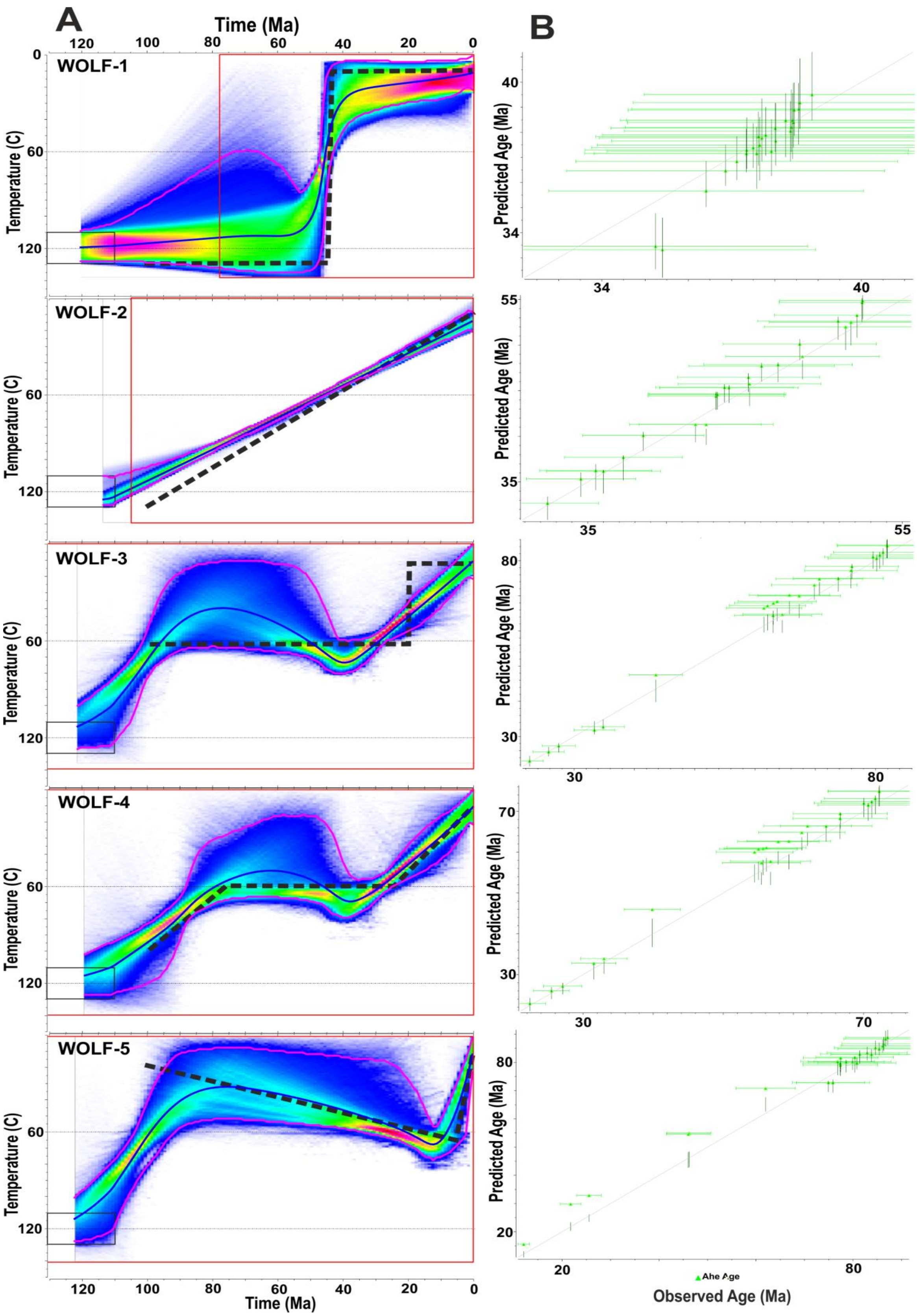

Figure 4.8: Experiment 3 - fragments modelled correctly as fragments.
Inverse models (1,000,000 iterations) using the same synthetic grains as in figure **4.7**. Here the grains are modelled correctly as (1T) crystal fragments. **A**: the generated thermal histories for WOLF-(1-5). Black dashed line = true thermal history (see figure **4.2**), pink solid lines = 95% credibility intervals, blue solid line = expected model, colour represents the marginal probability distribution of the thermal history (blues represent lower probability, greens through to red represent higher probability), black box = T-t constraint set at 120°C ± 10°C and 120Ma ± 10Ma, red box = model prior (see QTQt user manual). **B:** observed age vs. predicted age plots for the generated thermal history.

Experiment 3 shows that when the level of inherent natural dispersion is sufficiently high as a result of the combined grain size and eU variation, then it becomes unnecessary to model fragments explicitly as fragments using QTQt (this may also have been the case using HelFRAG, but experiments modelling fragment data incorrectly as whole grains were not published in Beucher *et al.* (2013)). There are subtle differences between the two sets of models (figure **4.7** and **4.8**), but factors such as adjusting/removing T-t constraints and preventing/enabling reheating in the models are likely to have a greater effect on the output than modelling fragments as fragments verses whole grains. For real datasets however, it is impossible to quantify exactly what 'sufficient grain size and eU variation' means in practice, so it may not be safe to assume that it is ok to model data exclusively as whole grains just because there is a range of eU values within the sample.

4.2.3.1 Experiment 3a – reduced eU range of 5ppm: To explore the fragment effect when utilising a radiation damage model, without radiation damage induced inherent natural dispersion dominating over the effect, a sub-set of experiments have been carried out with smaller ranges of damage content (lower values and smaller ranges of eU, all other grain properties remain identical to Experiment 3). This sub-set has been carried out on only three thermal histories: WOLF-2, 4 and 5. This is because WOLF-1 has been easily resolved regardless of the fragment effect in Experiments 1, 2 and 3, whereas WOLF-3 is still not fully resolved even by Experiment 3. To reduce model run time the models have been carried out for 100,000 iterations (10,000 burn in period) as opposed to the 1,000,000 iterations of the main experiment.

Experiment 3a uses grains with eU values between 3-8ppm (see table **4-1**). This is both an unrealistically low value and small range for most natural samples, and is most akin to the scenario of Experiment 2. The results can be seen in figures **4.9 - 4.11**. WOLF-2 clearly shows a difference in the model output when fragments are treated as whole grains (panel **A**) verses fragments (panel **B**) (figure **4.9**). Although within the confines of the 95% credibility intervals, a single rapid cooling event is possible when modelling fragments correctly as fragments, the marginal probability distribution strongly favours steady monotonic cooling comparable to the true thermal history (although the gradient is shallower due to the initial T-t constraint, as already discussed in section *4.2.2.2*). In contrast, when modelled incorrectly as whole grains, the thermal history favours a rapid cooling solution comparable to WOLF-1.

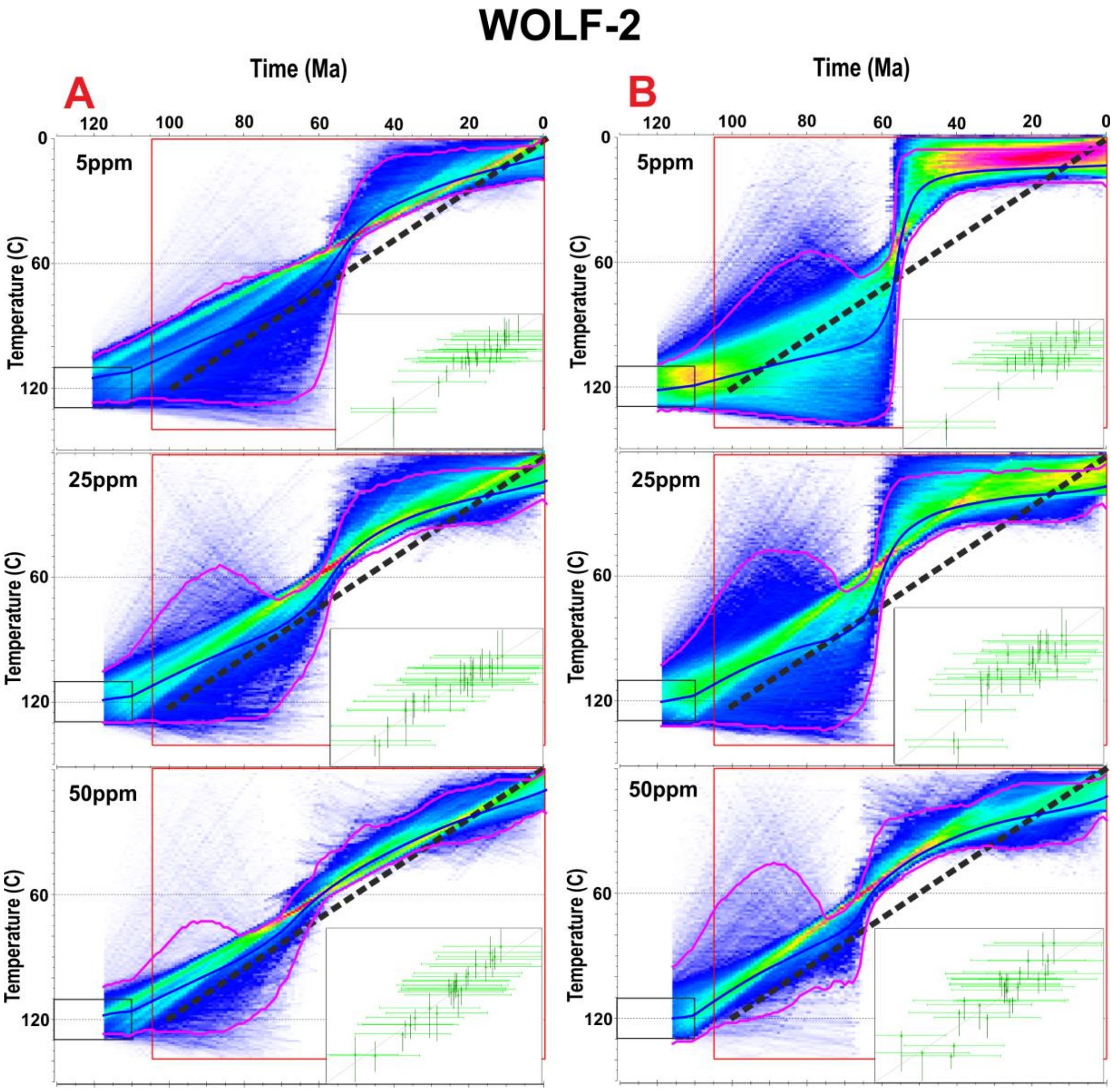

Figure 4.9: Experiment 3a, b and c – Wolf-2.
Inverse models (100,000 iterations after 10,000 iteration burn-in period) using the same synthetic grains as for figures **4.7** and **4.8** but with smaller ranges in eU – 5ppm, 25ppm and 50ppm respectively. **A**: fragments modelled correctly as fragments. **B**: fragments modelled incorrectly as whole grains. Black dashed line = true thermal history (see figure **4.2**), pink solid lines = 95% credibility intervals, blue solid line = expected model, colour represents the marginal probability distribution of the thermal history (blues represent lower probability, greens through to red represent higher probability), black box = T-t constraint set at 120°C ± 10°C and 120Ma ± 10Ma, red box = model prior (see QTQt user manual). Inset: observed age vs. predicted age plots for the generated thermal history.

WOLF-4 also demonstrates a noticeable difference between the model outputs when modelling fragments as fragments verses whole grains (figure **4.10**). When modelled as fragments, the thermal history can accommodate a 3 stage cooling history comparable to the true thermal history, with a residence time in the PRZ (all be it the highest probability distribution is around a two stage cooling history with a change in cooling rate at 80Ma and 60°C), whereas when modelled incorrectly as whole grains the thermal history depicts a shallowing off curve inconsistent with the true history.

WOLF-5 also shows minor differences when modelled with the fragment effect on or off (figure **4.11**), however both model outputs are inaccurate and poorly resolve the true thermal history, with neither reproducing the reheating of the true thermal history. This could be as a result of insufficient model iterations to find the true history, as when the fragment model was used in Experiment 2, the thermal history was adequately resolved. It is therefore illogical that the results of this experiment would be less accurate than the results of Experiment 2, which has less inherent natural dispersion.

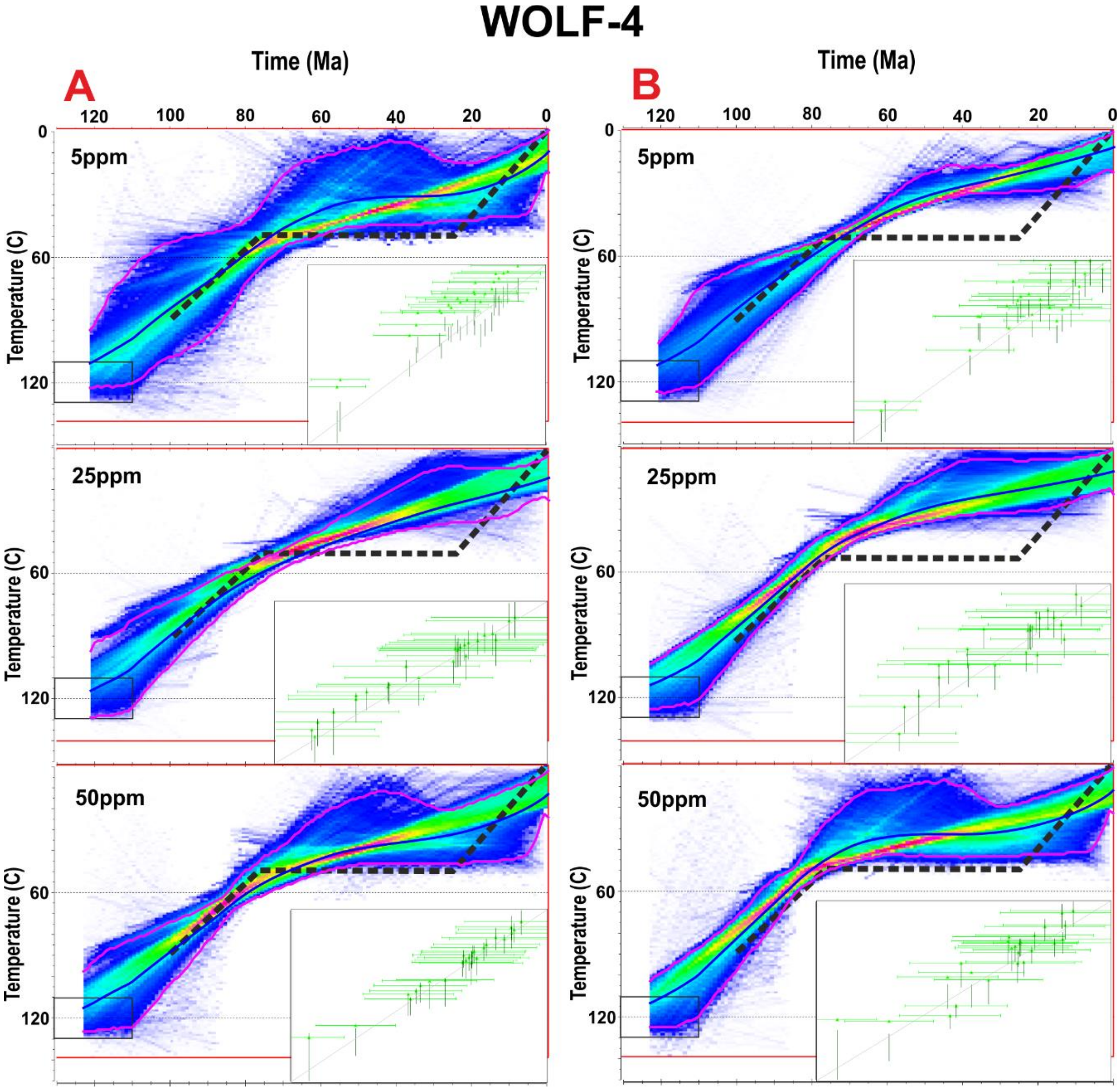

Figure 4.10: Experiment 3a, b and c – Wolf-4.
Inverse models (100,000 iterations after 10,000 iteration burn-in period) using the same synthetic grains as for figures **4.7** and **4.8** but with smaller ranges in eU – 5ppm, 25ppm and 50ppm respectively. **A**: fragments modelled correctly as fragments. **B**: fragments modelled incorrectly as whole grains. Black dashed line = true thermal history (see figure **4.2**), pink solid lines = 95% credibility intervals, blue solid line = expected model, colour represents the marginal probability distribution of the thermal history (blues represent lower probability, greens through to red represent higher probability), black box = T-t constraint set at 120°C ± 10°C and 120Ma ± 10Ma, red box = model prior (see QTQt user manual). Inset: observed age vs. predicted age plots for the generated thermal history.

4.2.3.2 Experiment 3b - reduced eU range of 25ppm: Experiment 3b uses grains with eU values between 3-28ppm (figures **4.9 - 4.11**). This is a small but realistic range of eU for many natural samples, particularly when only a small number of grains are analysed per sample, but is still low in terms of total eU value. WOLF-2 again shows differences between modelling fragments as fragments or whole grains, but these are less drematic than for Experiment 3a. The larger range of eU enables the model to better resolve the thermal history even when fragments are treated incorrectly as whole grains. Both models show the potential for a rapid cooling path comparable to WOLF-1, but with marginal probability distributions favouring steady monotonic cooling paths. However the true monotonic cooling path is better constrained when the fragment model is used (panel **A**), with the greens of the marginal probability depicting more of a curve in the later part of the history when modelled incorrectly as whole grains (panel **B**).

WOLF-4 is inexplicably less accurate to the true three stage thermal history when modelled using the fragment model, compared to Experiment 3a. It is also less accurate than the equivalent model in Experiment 2 (figure **4.6**). The only partial explanation for this is that there were insufficient model iterations to find the correct thermal history, but that should also have applied to Experiment 3a. Without the use of the fragment model the output is comparable to the output of Experiment 3a. WOLF-5 is again poorly resolved, and here there is very little difference between having the fragment model on or off.

4.2.3.3 Experiment 3c - reduced eU range of 50ppm: This is the most realistic of the three sub-set experiments, as can be seen from the data tables in this thesis (table **5-2**). Experiment 3c uses grains with eU values between 3-53ppm, and most of the samples recorded in table **5-2** have a majority of grains with eU values of ~15-60ppm.

WOLF-2 shows subtle differences between the model outputs when the fragment model is used or not, with modelling fragments as fragments producing a better constrained and more accurate thermal history reconstruction. Indeed the model output is very close to the results of Experiment 3. Without the use of the fragment model the resultant thermal history is less accurate, but still converging on the true monotonic cooling thermal history.

WOLF-4 shows very little difference between the model outputs when the fragment model is on or off. Both versions are comparable to the true thermal history, all be it with the marginal probability distribution favouring a two stage instead of a three stage cooling history. The true three stage history with a residence time in the PRZ is compatible within the bounds of the 95% credibility intervals.

WOLF-5 again fails to resolve the true thermal history, however a component of the accepted T-t paths are favouring reheating pathways comparable to the true history. It may be that a greater number of iterations could result in a greater proportion of model pathways favouring the reheating thermal history. There is not much difference between the outputs when modelling fragments correctly as fragments or not, however in this instance there is actually a stronger component of the T-t paths following reheating pathways when fragments are modelled incorrectly as whole grains. This was also the case in some instances in Experiment 3 (see figure **4.8** and **4.9**). The model output is still less accurate than the results for WOLF-5 when using the fragment model in Experiment 2, which is again illogical, and must be as a result of running fewer model iterations here than in the main experiments.

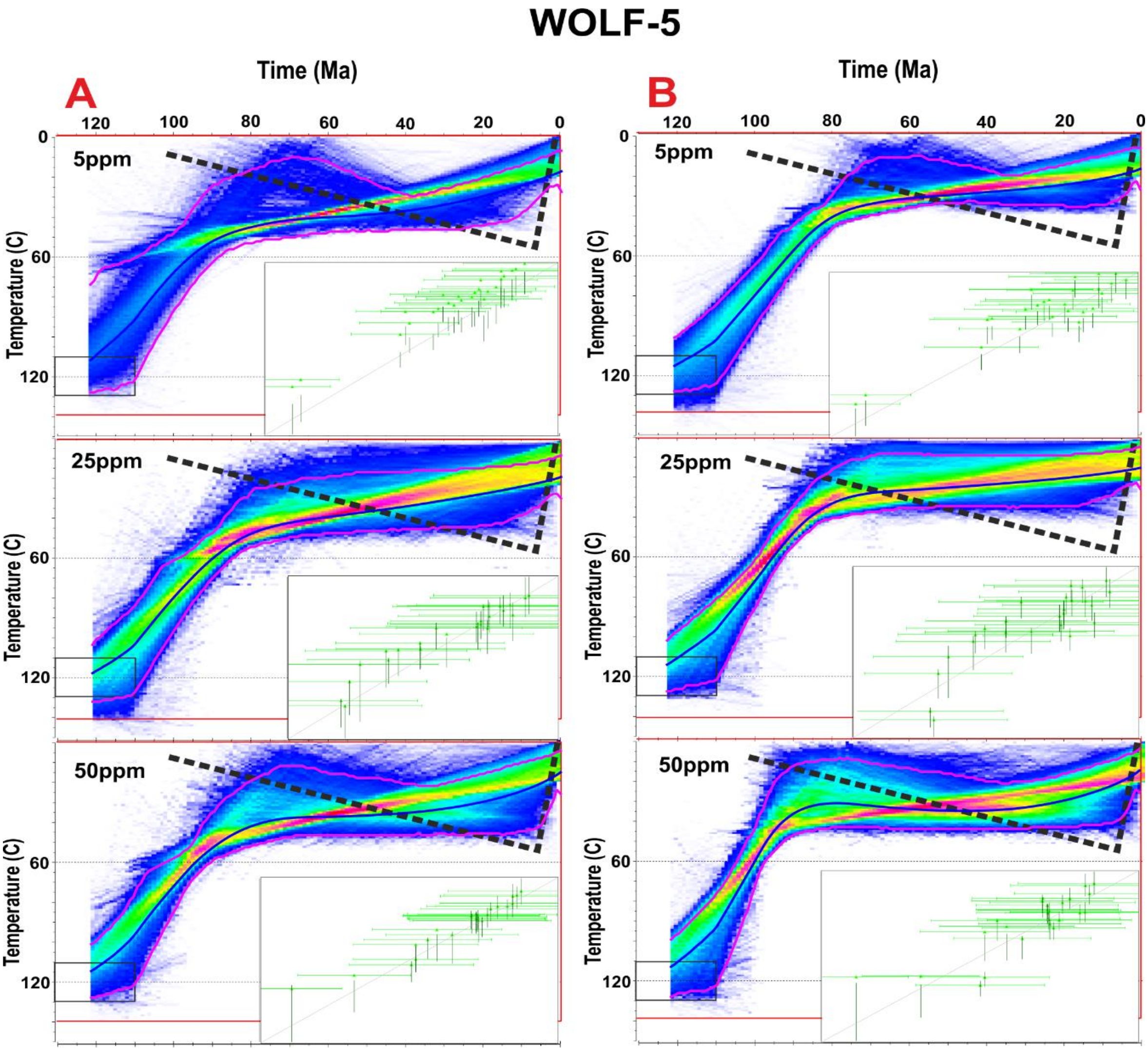

Figure 4.11: Experiment 3a, b and c – Wolf-5.
Inverse models (100,000 iterations after 10,000 iteration burn-in period) using the same synthetic grains as for figures **4.7** and **4.8** but with smaller ranges in eU – 5ppm, 25ppm and 50ppm respectively. **A**: fragments

modelled correctly as fragments. **B**: fragments modelled incorrectly as whole grains. Black dashed line = true thermal history (see figure **4.2**), pink solid lines = 95% credibility intervals, blue solid line = expected model, colour represents the marginal probability distribution of the thermal history (blues represent lower probability, greens through to red represent higher probability), black box = T-t constraint set at 120°C ± 10°C and 120Ma ± 10Ma, red box = model prior (see QTQt user manual). Inset: observed age vs. predicted age plots for the generated thermal history.

Although subtle, the sub set of experiments does provide evidence that the eU effect is dominating over the fragment effect in Experiment 3 due the high range of eU values used in Experiment 3 (range > 100ppm). It can be seen, particularly when applied to the WOLF-2 thermal history, that there is a noticeable difference between modelling fragments correctly as fragments compared to incorrectly as whole grains when the eU range is low. Modelling fragments correctly returns a more accurate thermal history. As the eU range increases, the accuracy of the thermal history generated without the fragment model increases, ultimately resulting in the correct thermal history being returned regardless of if fragments are modelled correctly as fragment or incorrectly as whole grains.

It is impossible to say categorically at what range of eU values the fragment effect becomes redundant in a natural sample. The magnitude of the radiation damage effect will differ for every thermal history (as can be seen in Experiments 3a, b and c). Simpler and more rapidly cooled thermal histories (such as WOLF-1 and 2) will generate less radiation damage induced dispersion (due to less radiation damage accumulation) than more complex or slowly cooled thermal histories (such as WOLF-4 and 5) and therefore the fragment effect will likely be more important. For more complex thermal histories, the radiation damage effect will become more dominant with smaller ranges in eU. In addition (as previously discussed) the data used here is synthetic, and generated using the current radiation damage models. It therefore behaves as would be expected in terms of diffusion kinetics, whereas in reality our current radiation damage models are likely incomplete/inadequate to fully describe how natural samples will behave. It is therefore best practice to model using the fragment model as a matter of routine, as we can’t quantify at what eU range the fragment effect becomes redundant.

4.2.3.4 Comparison with HelFRAG: Experiments 2 and 3 demonstrate that the QFrag approximation can adequately replicate the results of the more complex HelFRAG program. This is shown in figure **4.12** which plots the results of QFrag directly against the published results of HelFRAG (Beucher *et al.*, 2013) as per Experiment 3 (figure **4.8**). Each of the five WOLF thermal histories is replicated between QFrag and HelFRAG, allowing for the fact that an initial T-t constraint was used in the QFrag models but not HelFRAG. Indeed the results for WOLF-1 and 2 are arguably even better using QFrag instead of HelFRAG, though

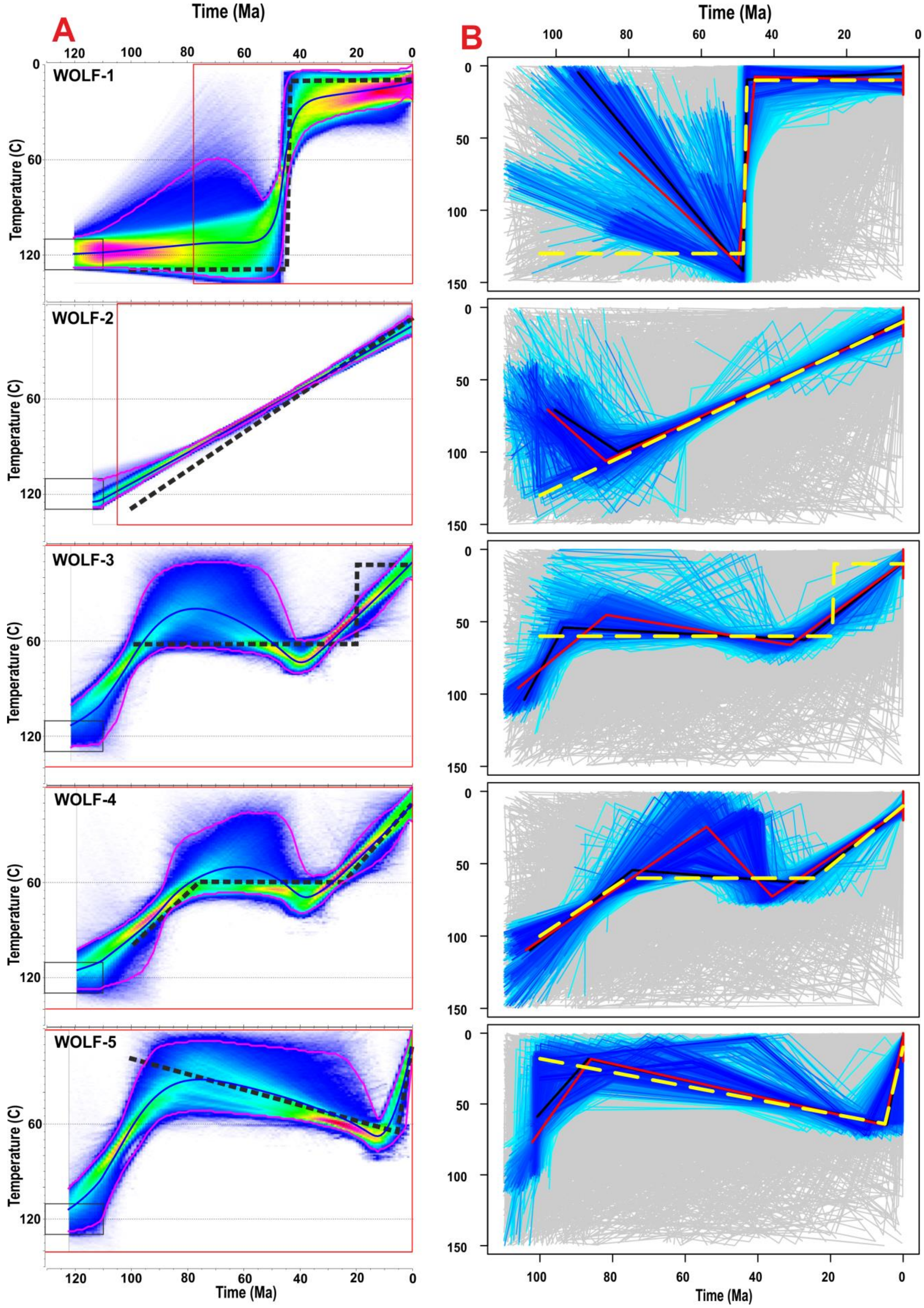

Figure 4.12: Experiment 3 - comparison of QFrag and HelFRAG model outputs.

Fragments modelled as fragments as per experiment 3 (left panel), as a direct comparison of model#7 fig. 9 of Beucher *et al*. (2013) (right panel). Yellow dashed line = true thermal history, solid red lines = the best fit thermal history, solid black lines = the average acceptable thermal history. Blue lines indicate the accepted field of solutions (darker = better) and grey lines indicate the rejected field of solutions based on the NA algorithm. Note different vertical scales used on left and right panels, and no T-t constraints used on right panel.

-this could largely be down to the initial T-t constraint used in QTQt which gives the model a realistic start point. The ‘humpback’ effect seen for WOLF-3, 4 and 5 in the QTQt outputs is also seen in the HelFRAG models, so this is not a limitation of the QFrag model. If the pink 95% credibility intervals from the QTQt models were to be overlain onto the HelFRAG models, they would provide a very close match with the blue accepted fit fields, especially for WOLF 3, 4 and 5. This shows that although there are differences in the best fit models (due to differences in the statistics for how this is calculated between the programs), the overall model output is strongly comparable between each software program.

Brown *et al.* (2013) and Beucher *et al.* (2013) demonstrated the importance of analysing a minimum of 15-20 individual apatite grains per sample, ideally 20-30. This is contrary to the common practice in most labs of only analysing c. 2-6 grains (e.g. Spotila *et al.*, 1998; House *et al.*, 1999; Farley *et al.*, 2002; Danisik *et al.*, 2008). In Experiment 3 the 24 grains analysed provide sufficient inherent natural dispersion to return accurate thermal histories without taking fragmentation into account, however this might not be the case had a much smaller sample size been used. A smaller sample size may limit the range of natural dispersion provided by grain size and eU variation, meaning the fragment effect becomes much more important.

4.3 Conclusions

The new HelFRAG modelling technique provides a step forward in the inverse modelling of AHe data for thermochronology reconstructions, allowing the previously overlooked factor of broken grains to be adequately accounted for. It is however computationally demanding, which limits its usefulness for routine application. The approximation of the finite cylinder diffusion model which has been incorporated into the QTQt modelling software (QFrag (Gallagher, 2012)) provides an adequate solution to the problem, enabling its routine application. In particular, when modelling AHe data using QTQt:

- The fragment effect alone provides insufficient natural age dispersion to find the correct thermal history using QFrag. However this scenario is unrealistic for real samples which will always have some variation in grain size and/or eU concentration.

- Increasing the natural age dispersion by picking grains with a wide range of grain sizes improves the ability of the models to return the correct thermal history when fragments are treated explicitly as fragments, but not when modelled incorrectly as whole grains.

- With sufficient natural age dispersion (i.e. a large variation in grain size and eU concentration within the sample), it may be unnecessary to model fragments as fragments in QTQt, provided a sufficiently large number of grains (c. 20-30) are analysed. However this is likely to only be the case with a synthetic dataset, as the radiation damage effect is also synthetic, i.e. the same radiation damage model was used to generate the fragment list and eU related dispersion as was used to model the thermal history. Therefore the eU related dispersion was 'perfect'. In nature this is unlikely to be the case due to the uncertainties surrounding our current radiation damage models (see **Chapter 2**) so it may be unwise to assume it is safe to model fragments as whole crystals.

- A large eU range can 'swamp' the fragment effect, however it is impossible to quantify exactly what range of eU is required to make using the fragment model redundant. This is because the eU range required for radiation damage induced dispersion to become dominant will differ depending on the original thermal history, therefore it should become best practice to always model fragments as fragments.

- If natural age dispersion (or sample size) is insufficient, modelling fragments incorrectly as whole crystals can return perfectly sensible looking thermal histories, with adequate data fit, which are ultimately incorrect. This has potentially led to many inaccurate, or even incorrect interpretations of AHe data over the years.

CHAPTER 5

5. BALLACHULISH IGNEOUS COMPLEX: AN ANALYSIS OF SINGLE GRAIN AGE DISPERSION

(Ballachulish Igneous Complex seen from across Loch Linnhe)

5.1 Introduction

The aim of this thesis is to provide an empirical test of the fragment model of Brown *et al.* (2013) and Beucher *et al.* (2013). The Ballachulish Igneous Complex was chosen as a case study for reasons outlined in **Chapter 1**. A number of samples from two vertical transects were collected to be analysed for single grain AHe dating (with supporting AFT dating also carried out by A. Amin, see Appendix 6). The inverse modelling of the AHe data is presented in **Chapter 6**; this chapter provides a detailed analysis of the single grain age dispersion observed within each sample, and its underlying causes.

5.1.1 *Geological overview*

The Ballachulish Igneous Complex (BIC) is located in western Scotland, in the Grampian terrane of the central highlands (see figures **1.2** and **5.2**). It is one of an array of calk-alkaline affinity igneous bodies which intruded the metamorphic rocks of what are now the Scottish highlands during the Caledonian Orogeny. The metamorphic country rocks of the Grampian terrane comprise the lower-middle section of the Dalradian Supergroup (Bailey and Maufe, 1916). The protoliths were sandstones, siltstones, mudstones and limestones deposited during the late Proterozoic and possibly early Cambrian. They underwent extensive deformation and regional metamorphism during the Cambrian and Ordovician periods (early Caledonian orogeny), plus contact metamorphism during the emplacement of the Caledonian granitoids (Bailey and Maufe, 1916; Harte and Voll, 1991; Pattison and Voll, 1991).

5.1.1.1 Caledonian orogeny: The 'Caledonian period' loosely describes the time involving the events which lead to the assembly of the major tectonic segments of Scotland (and the rest of the British Isles) (Pattison and Harte, 2001). This involved major strike-slip displacement (e.g. along the GGF) and thrusting (e.g the MF) as well as the closure of the Iapetus Ocean, bringing together the northern and southern sections of Britain and Ireland. These were on the separate continental blocks of Laurentia (Scotland and the north of Ireland) and Avalonia (England, Wales and the south of Ireland), separated by the Iapetus Ocean (figure **5.1**). These events dominantly occurred during the Silurian and Devonian periods (c. 440-360Ma).

In a wider context the 'Caledonian period' can be used to describe all the collisional events between the continental blocks of Laurentia, Baltica and Avalonia (plus additional island arcs) which lead to the complete closure of the Iapetus Ocean (figure **5.1**). Laurentia collided first with Baltica in the late Ordovician; Balonia (Baltica + Laurentia) then collided with Laurentia during the early Silurian (Cocks and Fortey, 1982; Cocks *et al.*, 1997). This formed the Caledonian mountains, a continuous mountain chain which stretched from present day Scandinavia, through northern Britain and into North America (the present day Appalachians). The entire orogenic sequence encompasses a time period covering some 200Ma, from the early Cambrian (c.540Ma) through to the late Devonian (c.360Ma) (McKerrow *et al.*, 2000).

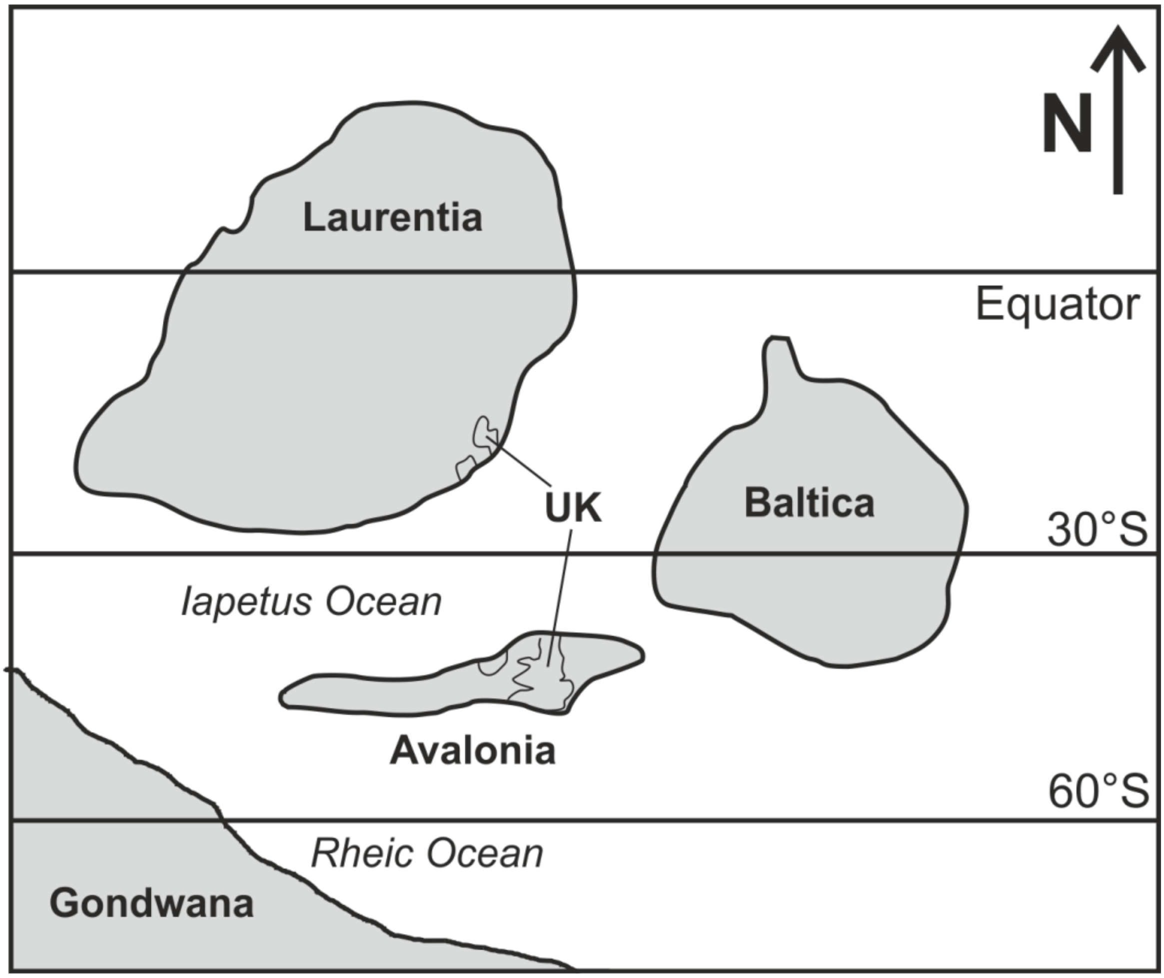

Figure 5.1: Palaeogeograhpic reconstruction of the Iapetus Ocean during the Caradoc (Upper Ordovician - c.455 Ma).

The position of the southern and northern parts of the UK are indicated on Avalonia and Laurentia respectively. One or more island arcs also existed within the Iapetus Ocean (omitted for simplicity) and contributed to the collisions of the 'Caledonian orogeny'. Remnants of these can also be found in the geology of the UK. After Cocks *et al*. (1997) and McKerrow *et al*. (2000).

5.1.1.2 Caledonian granites: The igneous rocks of the Caledonian Orogeny are subdivided into two groups: 'early' and 'late'. This is in relation to their emplacement prior to or subsequent to the bulk of the regional deformation and metamorphism of the orogeny in Scotland (Read, 1961). The 'early' granites are S-type and coincide with the peak of regional metamorphism at c. 470Ma (Stephens, 1988; Dewey and Mange, 1999; Atherton and Ghani, 2002). The BIC belongs to the ‘newer’ or ‘late’ I-type granites which formed c. 435-390Ma with magmatism peaking between c. 410-400Ma (Atherton and Ghani, 2002). It is part of the Argyll suite of predominantly calc-alkaline affinity igneous intrusions which lie NW of the mid-Grampian line and formed between c. 430-400Ma, the other major suite being the Cairngorm suite to the east (Stephens and Halliday, 1984; Stephens, 1988). U-Pb zircon dating places the intrusion of the BIC at 424 ± 4 Ma (Fraser *et al.*, 2000), which makes it one of the older ‘late’ intrusive complexes.

The igneous activity that formed the Caledonian granites is a result of the subduction of the Iapetus Oceanic crust along a north westwards dipping subduction zone to the south of present day Scotland (Iapetus Suture), and the subsequent continent – continent collision of Balonia and Laurentia. The ‘late’ granites predominantly formed after the closure of the Ocean (c.430Ma in the UK region) and are therefore not typical arc magmas despite their calc-alkaline affinity. The older ‘late’ granites such as the BIC may still be associated with the subducted slab, but one theory suggests a ‘slab breakoff’ mechanism of magmatism (Atherton and Ghani, 2002). Post-collision, ‘slab breakoff’ is the natural consequence of the attempted subduction of Balonia below Laurentia (Davies and von Blanckenburg, 1995). This would allow asthenospheric upwelling into the ‘gap’, which could have led to decompression melting of enriched mantle in the ‘gap’ and the thermal erosion of the lower crust (Atherton and Ghani, 2002).

5.1.2 *The Ballachulish Igneous Complex*

The current exposure of the BIC was originally emplaced at a crustal depth of c. 10km (Fraser *et al.*, 2000). It was likely associated with overlying volcanic sequences, but none of these are preserved (Pattison and Harte, 2001). The region was undergoing rapid uplift during the time of emplacement (c. 0.5km/Ma) associated with the ongoing Caledonian orogeny. This is supported by the presence of volcanic sequences in the younger nearby igneous complexes of Glencoe (403 ± 4Ma (Fraser *et al.*, 2000)) and Ben Nevis (Pattison and Harte, 2001). This implies that the current exposure of the BIC must have been uplifted to near surface depths by c. 403Ma.

A major NE-SW trending strike-slip fault – the Ballachulish Fault (BF) splits the intrusion through its centre (figure **5.2**). This has a post intrusion sinstral displacement of 600-800m (Pattison, 1985) and extends for a distance of at least 80km. Due to its proximity and alignment with the GGF, it is considered to be a splay of this major fault zone (Johnson and

Frost, 1977). The occurrence of contact metamorphism in some of the fault rocks of the BF suggests that the fault was active before as well as after the emplacement of the BIC (Pattison and Harte, 2001). The fault may therefore have played a role in the location of the BIC, acting as a conduit for the ascending magma.

The igneous complex has a zoned appearance (figure **5.2**). It consists of an outer ring of monzodiorite/quartz diorite which has a flow and deformation foliation, surrounding a core of variably porphyritic pink-grey ‘granite’ with a small leucogranite centre (Weiss and Troll, 1989; Pattison and Harte, 2001). The outer ring was emplaced first at a temperature of c. 1100°C (Weiss and Troll, 1989). This was intruded by the inner ‘granite’ which had an estimated emplacement temperature of c. 850°C (Weiss and Troll, 1989). The contact between the core and outer ring is variable, forming a sharp contact in places and a hybrid mixing zone in others. This implies that the outer ring was still at least partially molten when the inner body intruded (Weiss and Troll, 1989). The leucogranite is a late stage formation and is associated with sericitic alteration and weak Cu-Mo mineralisation (Pattison and Harte, 2001).

5.1.2.1 Outer ‘diorite’ ring: The outer ring consists of monzodiorite and quartz diorite which grade into each other. The monzodiorite occupies the more southern and eastern parts of the intrusion and forms a greenish-grey, predominantly medium-coarse grained orthopyroxine bearing, hornblende + biotite ± augite rock. The rock shows both flow and deformation structures, the latter related to the intrusion of the inner ‘granitic’ core while the outer ring was still in a ductile state (Weiss and Troll, 1989). The quartz diorite occupies the more marginal, northern, north western and southern parts of the intrusion. It forms a grey, hornblende + biotite ± augite rock of variable grainsize (Weiss and Troll, 1989) (see figure **5.2**).

5.1.2.2 ‘Granitic’ core: The inner portion of the intrusion consists of a variably porphyritic, pink, biotite ± hornblende granite and granodiorite with alkali feldspar megacrysts. In the centre of the intrusion a fine grained, aphyric leucogranite stock is found (figure **5.2**). This exhibits strong hydrothermal alteration and is associated with Cu-Mo mineralisation (Weiss and Troll, 1989). Broad hybrid mixing zones between the main granite and quartz diorite occur in parts of the intrusion (see figure **5.2**).

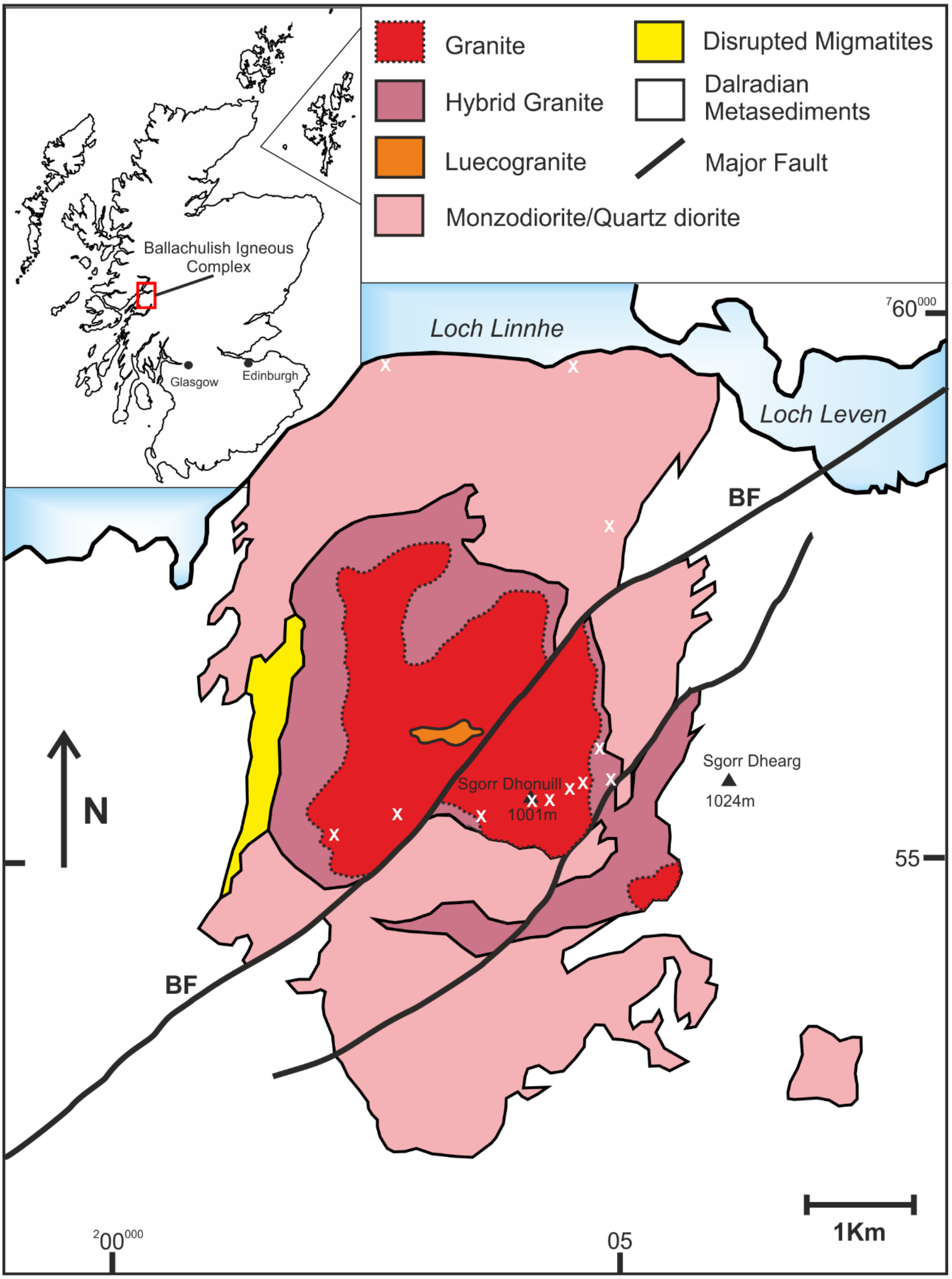

Figure 5.2: Simplified geological map of the BIC – Scotland.

Shown are the major petrological units of the intrusion: the outer 'doirite' ring of undifferentiated monzodiorite and quartz diorite, and the 'granitic' core of granite and granodiorite with a hybrid granite mixing zone between the core and outer ring. Also shown are the leucogranite stock in the centre of the core and a disrupted migmatite zone on the western rim of the intrusion. White crosses indicate the location of all samples which have been analysed for AHe, see **Figure 5.3** for sample numbers. BF = Ballachulish Fault. After Pattison and Harte (2001) and Piazolo *et al*. (2005).

5.1.3 *Sample locations*

A total of 24 samples were collected from two vertical profiles across the BIC at c. 100m (vertical) intervals (figures **5.3** and **5.4**). The first (described here onwards as the 2013 transect) reaches from the summit of Sgorr Dhonuil (1001m) down the south west side of the complex, and the second (described here onwards as the 2007 transect) reaches from the summit down to the sea on the north of the complex (figure **5.3**). Six samples (labelled *SD07 – x*) were acquired from the work of Persano *et al.* (2007), a further six (labelled *SD13 – 0x*) were acquired from the undergraduate project of Matt Forrester at the University of Glasgow (unpublished). The remaining samples were collected specifically for this project (see table **5-1**). All major units of the igneous complex were sampled (see figure **5.2**). Additionally samples were collected from the adjacent metaquartzite (Sgorr Dhearg summit - 1024m, *BH15 - 01*) and appinite suite (*BH15 – 10*) associated with the complex.

Table 5-1: Sample locations, elevation, lithology and sampler for each transect.

Transect	Sample no.	OS Grid ref. (NN)	Altitude (m)	Lithology	Sampler
2007 (North)					
	SD07 - 1	203985,755525	1001	Granite	Persano *et al.* 2007
	SD07 - 2	204299,755545	907	Granite	Persano *et al.* 2007
	SD07 - 3	204386,755714	804	Granite	Persano *et al.* 2007
	SD07 - 4	204501,755772	700	Granite	Persano *et al.* 2007
	SD07 - 5	204671,755773	605	Granite	Persano *et al.* 2007
	SD07 - 6	204638,756050	512	Granite	Persano *et al.* 2007
	BH15 - 02	20298,75666	505	Granodiorite	D. Webster
	BH15 - 03	20320,75671	390	Granite	D. Webster
	BH15 - 04	20375,75675	290	Granodiorite	D. Webster
	BH15 - 05	20425,75760	220	Monzodiorite	D. Webster
	BH15 - 06	20469,75812	105	Granodiorite	D. Webster
	BH13 - 01	20540,75960	0	Doirite	D. Webster
	SD13 - 06	20403,75947	0	Quartz diorite	M. Forrester
2013 (South)					
	BH15 - 01	20569,75578	1024	Metaquartzite	D. Webster
	SD13 - 01	204062,755536	1001	Granite	M. Forrester
	SD13 - 02	203382,755210	867	Granite	M. Forrester
	SD13 - 03	202711,755482	755	Granite	M. Forrester
	SD13 - 04	202111,755443	628	Granite	M. Forrester
	SD13 - 05	201832,755367	508	Granite	M. Forrester
	BH15 - 07	20165,75525	410	Hybrid granite	D. Webster
	BH15 - 08	20145,75575	315	Granodiorite	D. Webster
	BH15 - 09	20150,75430	175	Quartz diorite	D. Webster
	BH15 - 10	20045,75515	75	Appinite	D. Webster
	BH13 - 02	20230,75932	0	Quartz diorite	D. Webster

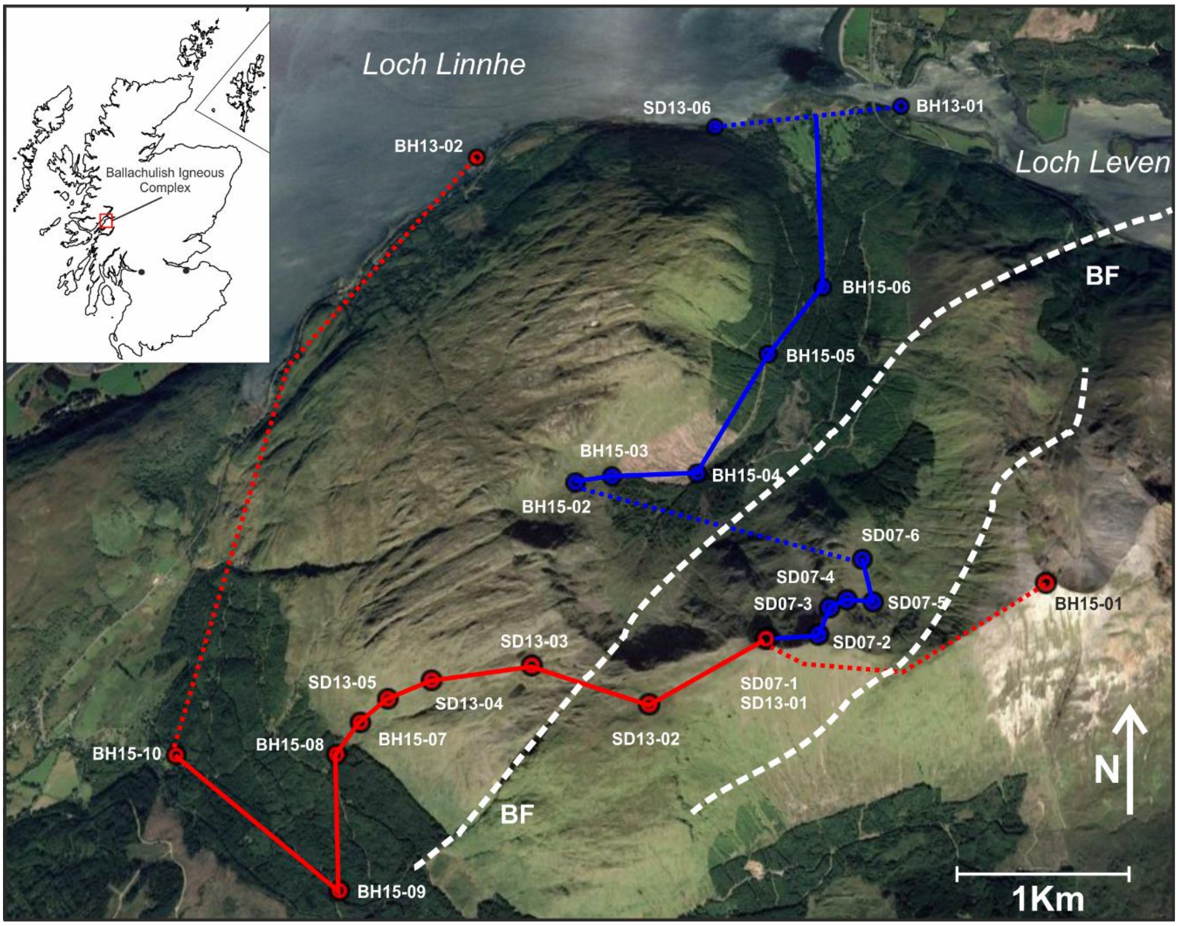

Figure 5.3: Map of sample locations.

Showing the two ‘vertical’ profiles from the summit of Sgorr Dhonuill – 1001m (plus an additional sample from the summit of Sgorr Dhearg – 1024m) to sea level. The location of sampling sites was dictated by the limited availability of safely accessible outcrops at roughly 100m vertical spacing’s. Blue = 2007 transect (inc. Persano *et al*., 2007 samples), red = 2013 transect (inc. Forrester (unpublished) samples). White dashed line indicates the Ballachulish fault (BF) and subsidiary fault, as seen on **Figure 5.4**.

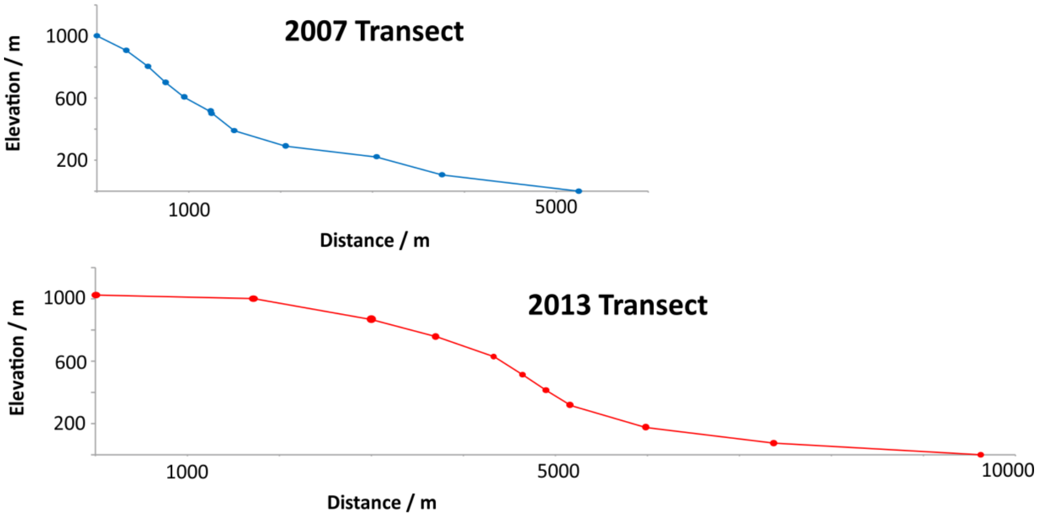

Figure 5.4: Vertical profiles of the two transects with exaggerated vertical scales.

Colours correspond with figure **5.3** colourings. Blue and red circles indicate the sample locations. The dashed line between samples *SD07-6* and *BH15-02* on the 2007 transect (figure 5.3) has been omitted to bring the upper and lower segment together (as both samples have approximately the same altitude).

5.1.4 *Methodology*

5.1.4.1 Mineral separation: Samples *SD07 – [1-6]* and *SD13 – [01-06]* were acquired as mineral separates. The remaining samples (labelled *BH13/15 – x*) were crushed and separated at the University of Glasgow to produce apatite separates. For a full outline of the lab techniques used see Appendix 1. Samples *BH15 – 01* and *BH15 – 10* were found to contain no useable apatite, but all remaining samples generated variable amounts of good quality apatite.

5.1.4.2 Picking and Screening: For each sample the aim was to analyse at least 20 individual grains (with up to 50 for two or three selected samples), which meant initially picking in the order of 100-200+ crystals per sample. This was done using a Zeiss Stemi 2000-c binocular microscope with magnifications of x20-100. Every effort was made to pick as wide a range of grain sizes and shapes (i.e. short and fat, long and thin) as possible to maximise the inherent natural dispersion, with 0T, 1T and 2T crystals all chosen. Where possible only the best quality grains in terms of shape and clarity were picked for reasons outlined in **Chapter 2**, section **2.2,** whilst also trying to avoid any inherent biases this may introduce. For example, a selection of the largest grains was still picked, despite very large grains being inherently more likely to become chipped and fractured during the mineral separation process.

After the picking process each crystal was then further screened by one or two independent analysts for micro/fluid inclusions using a Leitz Wetzlar 780306 petrographic microscope with up to x500 magnification in both plain Polarised (PPL) and cross polarised (XPL) light. XPL can reveal inclusions which are otherwise missed due to differences in the refractive index of fluids/other minerals to the host crystal. This is on top of an initial screening during the picking process to avoid inclusions visible under the lower powered picking microscope. Vermeesch *et al.* (2007) highlighted the fact that micro-inclusions have very little effect on age dispersion in most realistic situations (see **Chapter 2**, section *2.2.2.4*), however for the purpose of this investigation, each crystal was still screened meticulously for inclusions to minimise the potential noise generated from the imposed extraneous factors on dispersion, enabling the focus to be placed on the inherent natural dispersion.

Typically c. 90% of crystals would fail screening, leading to the large number of grains being initially picked. Unfortunately screening for inclusions does impart an inherent bias, as larger crystals are far more likely to have inclusions for purely volumetric reasons. Despite this, some very large crystals were still able to be analysed (though these were all 0T or 1T fragments). The selected crystals were then numbered and packed into platinum (Pt) foil tubes ready for analysis.

5.1.4.3 (U-Th)/He analysis: The geochemical analyses were carried out in the noble gas laboratories at the Scottish Universities Environmental Research Centre (SUERC). ^{4}He extraction was carried out via laser heating and analysed using a quadropole mass spectrometer. U, Th and Sm concentrations were subsequently calculated using isotopic dissolution ICPMS. For a full description of the analytical methodology, see Appendix 1.

5.1.4.4 AFT analysis: Each sample that was successfully analysed for (U-Th)/He was also analysed for AFT (analysis carried out by A. Amin). Mounts were made from the apatite mineral separates, which were then polished, etched and irradiated before being analysed using the EDM (see Appendix 2). This was carried out on an Axioplan 2 *imaging* microscope with a GTCO CalComp Drawing Board VI FT Stage Systems at the University of Glasgow. For a full description of the AFT sample preparation and analytical technique, see Appendix 2. In addition, AFT data was made available for sample *SD07 – 3* (and *SD9* which wasn't analysed for AHe) from the work of Persano *et al.* (2007).

5.2 Data

Single grain AHe ages were obtained from 20+ crystals for a total of 7 of the 24 samples, with 10+ grains analysed for a further 5 (<20 crystals were analysed from each of the sea level samples, but these data sets have been combined to reach the desired number of crystals, which is a logical step). The samples cover the full elevation range from both transects. Purely due to time constraints, the majority of these samples are from the upper 500m of the profiles, as these were the samples acquired from previous works and therefore required less sample preparation. The data for the analysed samples is presented in table **5-2,** along with the AHe data of Persano *et al.* (2007). The age standards for each analytical run are presented in table **5-3**.

Table 5-2: (U-Th)/He data table.

a: eU = effective uranium concentration and is calculated as [U]+0.235*[Th]. **b**: R* = the equivalent spherical radius for a sphere of equal (S/V) ratio as the true crystal and is calculated as (3*(R*L))/(2*(R+L)). **c**: number of crystal terminations where 2T = a whole crystal, 1T and 0T = crystal fragments. A. error = the true calculated analytical error and Std. error = standardised error of a nominal 10% to take into account the additional uncertainty provided by the range in age of analysed standards (Durango apatite) as seen in table **5.3**. ****SDx***: data from Persano *et al*. (2007). Apparent anomalous ages/outliers are highlighted orange and discussed in the main text of section 5.2.2. For the full raw data and calculation spreadsheets, see electronic annex.

Sample no.	Crystal no.	Alt. (m)	^{4}He (ncc/g)	^{238}U (ppm)	^{235}U (ppm)	^{232}Th (ppm)	^{147}Sm (ppm)	eU^{a} (ppm)	Length (µm)	Radius (µm)	R* ^{b} (µm)	T^{c}	Age (Ma)	A. error	Std. error
SD07 – 1															
	3	1001	6.51E+05	14.9	0.11	58.2	31.0	28.7	159	57	63	2	183.2	2.30	18.3
	7	1001	9.46E+05	17.3	0.13	76.7	105.0	35.5	152	59	64	1	212.0	2.49	21.2
	12	1001	9.86E+05	21.6	0.16	76.0	15.2	39.5	284	63	77	2	202.7	2.10	20.3
	13	1001	3.20E+05	7.6	0.05	24.8	25.0	13.5	156	66	70	1	191.1	3.07	19.1
	14	1001	8.90E+05	18.2	0.13	72.5	40.4	35.4	173	55	63	2	202.8	2.39	20.3
	15	1001	4.40E+05	10.0	0.07	36.2	25.5	18.6	200	63.5	72	1	190.5	2.40	19.0
	21	1001	1.07E+06	20.7	0.15	85.5	45.8	40.9	232	66	77	2	211.1	2.23	21.1
	24	1001	1.01E+06	19.4	0.14	83.4	46.2	39.2	276	67.5	81	2	207.2	2.15	20.7
	28	1001	8.49E+05	17.0	0.12	71.4	41.4	33.9	195	71.5	78	1	202.1	2.15	20.2
	31	1001	4.99E+05	21.7	0.16	68.4	63.2	38.0	292	55	69	1	106.2	1.12	10.6
	32	1001	1.12E+06	23.6	0.17	95.1	47.0	46.1	320	56	71	1	195.5	2.04	19.6
	39	1001	1.37E+06	26.2	0.19	104.3	50.2	50.9	281	51	65	2	217.8	9.76	21.8
	42	1001	4.94E+05	10.0	0.07	33.4	24.5	17.9	255	70	82	1	222.1	19.97	22.2
	49	1001	3.70E+05	4.2	0.03	32.6	37.4	11.9	311	95	110	1	250.0	25.35	25.0
	50	1001	5.03E+05	9.5	0.07	35.9	44.5	18.0	223	75.5	91	2	224.4	10.03	22.4
	(No. of xtls)		*(Cm³)*	*(ng)*		*(ng)*									
***SD1**	*1 (1)*	*1001*	*78.9E-9*	*1.9*		*5.2*					*77*		*207.0*		*20.7*
	2 (5)	*1001*	*38.0E-9*	*1.5*		*2.1*					*71*		*207.0*		*20.7*
	3 (5)	*1001*	*30.0E-9*	*1.0*		*1.9*					*82*		*214.0*		*21.4*
SD07 – 2a															
	1	907	9.70E+05	23.9	0.17	68.4	43.1	40.2	219	58	69	2	195.1	2.50	19.5
	2	907	2.18E+05	6.3	0.05	22.2	23.1	11.5	164	92	88	1	151.6	2.18	15.2
	3	907	7.67E+05	19.0	0.14	70.8	26.1	35.7	238	46	58	2	174.0	2.45	17.4
	4	907	2.48E+05	5.2	0.04	18.5	19.9	9.6	180	75.5	80	1	207.4	3.59	20.7
	5	907	1.26E+06	18.2	0.13	72.6	29.4	35.4	187	75	80	1	285.6	3.77	28.6
	6	907	6.56E+05	16.0	0.12	56.6	33.0	29.4	135	82	77	1	180.2	2.40	18.0
	7	907	5.63E+05	13.3	0.10	46.8		24.4	309	70.5	86	1	188.2	2.42	18.8
	8	907	1.01E+06	21.3	0.15	94.3	45.3	43.6	221	76	85	0	187.5	2.45	18.8
	9	907	6.38E+05	12.4	0.09	46.8		23.5	189	88.5	90	1	221.3	2.89	22.1

Sample no.	Crystal no.	Alt. (m)	^{4}He (ncc/g)	^{238}U (ppm)	^{235}U (ppm)	^{232}Th (ppm)	^{147}Sm (ppm)	eU^{a} (ppm)	Length (µm)	Radius (µm)	R* ^{b} (µm)	T^{c}	Age (Ma)	A. error	Std. error
	10	907	1.17E+06	36.0	0.26	132.2	103.0	67.1	191	34.5	44	1	140.5	2.07	14.1
	11	907	9.61E+05	20.0	0.14	68.7	34.2	36.0	155	76.5	77	1	215.6	2.79	21.6
	12	907	6.56E+05	49.5	0.36	1057.0	99.2	298.3	116	40	45	0	18.0	0.27	1.8
	13	907	8.89E+05	25.2	0.18	89.0	34.7	46.3	201	50.5	61	2	155.9	2.10	15.6
SD07 – 3															
	2	804	1.17E+06	39.9	0.29	44.6	21.4	50.6	255	80.5	92	1	188.3	1.88	18.8
	7	804	5.21E+05	13.1	0.09	44.2	30.9	23.5	207	76	83	1	178.4	1.92	17.8
	12	804	2.25E+05	7.3	0.05	21.1	14.4	12.3	237	63.5	75	2	147.7	2.10	14.8
	17	804	9.07E+05	25.5	0.19	89.6	38.1	46.8	137	30	37	1	157.4	3.43	15.7
	20	804	4.87E+05	12.7	0.09	50.0	31.8	24.6	249	35	46	1	160.0	2.81	16.0
	22	804	1.21E+06	37.4	0.27	114.7	54.1	64.6	120	42.5	47	1	151.6	1.97	15.2
	23	804	6.87E+05	22.0	0.16	105.3	55.0	46.9	157	59	64	0	118.6	1.32	11.9
	27	804	8.09E+05	14.8	0.11	52.3	31.0	27.2	255	45.5	58	1	239.2	3.05	23.9
	28	804	3.77E+05	13.5	0.10	49.2	31.9	25.2	246	32	42	1	121.4	2.44	12.1
	29	804	8.50E+05	28.7	0.21	102.7	46.6	53.1	146	38.5	46	0	130.0	1.82	13.0
	33	804	9.85E+05	24.3	0.18	93.9	47.3	46.6	180	50.5	59	2	171.1	1.94	17.1
	35	804	4.37E+05	16.5	0.12	61.6	34.5	31.1	99	43.5	45	1	114.1	2.43	11.4
	41	804	8.29E+05	20.1	0.15	68.1	44.9	36.3	196	50.5	60	1	184.6	2.20	18.5
	43	804	2.68E+05	10.1	0.07	32.0	25.4	17.7	131	45.5	51	1	122.6	3.18	12.3
	44	804	1.51E+06	26.7	0.19	96.0	39.4	49.4	136	41	47	2	247.2	3.49	24.7
	46	804	1.40E+06	38.0	0.28	28.8	14.7	45.1	138	62	64	1	251.6	3.29	25.2
	47	804	8.26E+05	23.6	0.17	89.1	42.5	44.7	178	31	40	1	149.7	2.62	15.0
	49	804	1.98E+06	43.0	0.31	147.9	60.5	77.2	144	36	43	1	207.6	2.65	20.8
	50	804	1.32E+06	29.8	0.22	109.2	55.3	55.7	198	45	55	2	191.2	**2.16**	19.1
	56	804	6.31E+05	15.6	0.11	59.9	34.4	29.8	124	51	54	1	171.0	2.60	17.1
	57	804	1.50E+06	32.3	0.23	115.0	49.5	59.6	198	49	59	2	203.4	2.20	20.3
	63	804	7.13E+05	18.6	0.13	81.9	44.8	38.0	69	56	46	0	151.9	2.48	15.2
SD07 – 3a	1	804	8.55E+05	21.2	0.15	67.3	46.8	37.2	143	44	50	1	185.4	3.34	18.5
	2	804	9.65E+05	27.0	0.20	109.5	62.5	52.9	172	29	37	1	147.4	2.83	14.7
	3	804	2.75E+05	10.0	0.07	25.5	18.5	15.2	102	61	57	1	146.8	3.59	14.7
	4	804	1.27E+06	28.2	0.20	110.0	38.4	54.2	176	51.5	60	2	189.2	2.55	18.9
	5	804	3.10E+05	9.1	0.07	17.0	16.7	13.2	153	59	64	1	189.6	4.39	19.0
	6	804	9.69E+05	35.1	0.25	119.8	55.5	63.5	97	31	35	1	123.7	2.85	12.4
	7	804	3.86E+05	12.7	0.09	35.2	21.3	21.1	169	60.5	67	1	148.2	2.26	14.8
	8	804	6.69E+05	29.4	0.21	76.8	28.5	47.6	178	45	54	2	114.5	2.05	11.4
	9	804	2.37E+05	10.1	0.07	34.1	26.7	18.2	193	41	51	2	105.5	2.44	10.6
	10	804	9.59E+05	33.2	0.24	99.6	33.3	56.9	192	35	44	2	137.1	2.09	13.7
	11	804	1.92E+05	41.3	0.30	39.5	15.5	50.9	92	42	43	1	31.1	1.69	3.1

Sample no.	Crystal no.	Alt. (m)	^{4}He (ncc/g)	^{238}U (ppm)	^{235}U (ppm)	^{232}Th (ppm)	^{147}Sm (ppm)	eU^{a} (ppm)	Length (µm)	Radius (µm)	R* ^{b} (µm)	T^{c}	Age (Ma)	A. error	Std. error
	13	804	2.56E+05	14.4	0.10	36.2	17.7	23.0	134	60	62	1	90.6	1.86	9.1
	(No. of xtls)		*(Cm^{3})*	*(ng)*		*(ng)*									
***SD3**	*1 (4)*	*804*	*25.8E-9*	*3.6*		*3.1*					*91*		*177.0*		*17.7*
	2 (2)	*804*	*49.5E-9*	*5.6*		*6.1*					*160*		*190.0*		*19.0*
	3 (7)	*804*	*65.2E-9*	*8.2*		*8.2*					*86*		*182.0*		*18.2*
SD07 – 4															
	2	700	8.66E+05	29.1	0.21	98.8	30.6	52.5	165	45	53	2	134.3	1.61	13.4
	12	700	6.39E+05	9.5	0.07	39.3	16.8	18.8	184	57.5	66	2	273.4	3.79	27.3
	16	700	5.85E+05	29.3	0.21	83.6	46.6	49.2	130	41.5	47	2	96.8	1.43	9.7
	17	700	5.49E+05	35.8	0.26	78.5	41.4	54.5	194	35.5	45	2	82.1	1.14	8.2
	19	700	9.35E+05	36.8	0.27	82.0	38.2	56.3	137	41	47	0	135.0	1.89	13.5
	20	700	9.86E+05	26.2	0.19	122.9	53.1	55.3	215	30.5	40	2	144.6	2.02	14.5
	24	700	1.27E+06	37.3	0.27	82.1	38.1	56.8	154	44.5	52	1	180.8	2.24	18.1
	26	700	1.01E+06	21.9	0.16	84.4	48.3	41.9	128	52.5	56	0	195.2	2.46	19.5
	30	700	5.85E+05	18.2	0.13	76.6	54.6	36.3	83	51.5	48	0	130.0	2.17	13.0
	33	700	4.77E+05	34.9	0.25	75.2	39.1	52.8	120	35.5	41	0	73.8	1.41	7.4
	37	700	4.99E+05	14.6	0.11	55.9	38.6	27.8	184	37	46	1	145.0	2.70	14.5
	40	700	1.07E+06	25.1	0.18	95.6	54.5	47.7	184	50	59	2	180.5	2.05	18.0
SD07 – 5															
	20	605	1.14E+06	25.0	0.18	93.9	53.4	47.2	119	46	50	1	194.9	2.68	19.5
	22	605	1.17E+06	29.8	0.22	96.4	53.5	52.7	222	43	54	1	180.1	2.04	18.0
	23	605	4.00E+05	15.3	0.11	58.3	43.0	29.1	97	56	53	1	111.1	1.78	11.1
	31	605	8.98E+05	24.9	0.18	97.9	46.2	47.9	141	37.5	44	1	152.0	2.33	15.2
	34	605	1.14E+06	25.9	0.19	95.5	44.9	48.6	158	34	42	1	189.4	3.04	18.9
	36	605	1.61E+06	23.7	0.17	85.4	41.9	43.9	86	54	50	1	294.8	4.22	29.5
	38	605	5.39E+05	14.3	0.10	42.1	29.1	24.3	143	44.5	51	1	179.0	3.55	17.9
	44	605	1.35E+06	29.6	0.21	109.4	9.2	55.5	256	46	59	2	198.3	2.14	19.8
	60	605	4.77E+04	1.3	0.01	3.9	7.9	2.2	367	76	94	1	170.0	4.55	17.0
	63	605	4.57E+05	13.6	0.10	44.8	59.2	24.2	130	65	65	1	151.1	2.00	15.1
SD07 – 6															
	5	505	3.75E+05	14.3	0.10	36.6	162.0	23.0	186	70.5	77	1	126.2	1.44	12.6
	10	505	5.14E+05	18.6	0.14	50.0	28.4	30.5	381	96	115	2	136.6	1.34	13.7
	17	505	3.57E+05	12.2	0.09	42.8	7.5	22.3	295	107	118	1	130.3	1.32	13.0
	18	505	6.77E+05	22.9	0.17	48.3	165.7	34.4	195	54	63	1	154.7	1.85	15.5
	23	505	4.23E+05	15.2	0.11	30.0	10.9	22.4	280	102.5	113	2	153.5	1.52	15.3
	27	505	4.00E+05	12.4	0.09	35.4	34.1	20.8	299	71	86	2	154.8	1.64	15.5

Sample no.	Crystal no.	Alt. (m)	^{4}He (ncc/g)	^{238}U (ppm)	^{235}U (ppm)	^{232}Th (ppm)	^{147}Sm (ppm)	eU^{a} (ppm)	Length (µm)	Radius (µm)	R* ^{b} (µm)	T^{c}	Age (Ma)	A. error	Std. error
	39	505	4.71E+05	19.9	0.14	52.4	13.2	32.3	208	76	83	1	118.9	1.23	11.9
	44	505	1.74E+05	14.8	0.11	34.5	37.4	23.0	137	67	67	1	61.4	0.82	6.1
	46	505	5.57E+05	21.6	0.16	48.6	43.9	33.2	241	45.5	57	2	135.7	1.71	13.6
	53	505	4.53E+05	21.0	0.15	40.1	42.4	30.5	174	63.5	70	2	120.1	1.41	12.0
	54	505	5.61E+05	21.1	0.15	47.7	24.8	32.5	205	65.5	74	1	140.3	1.52	14.0
	59	505	4.45E+05	17.1	0.12	62.4	35.8	31.9	133	64.5	65	0	113.0	1.35	11.3
	61	505	4.05E+05	24.1	0.18	52.4	58.0	36.6	193	48	58	2	89.6	1.14	9.0
	63	505	4.74E+05	17.2	0.13	46.6	37.6	28.3	177	68	74	1	135.4	1.52	13.5
SD07 – 6a	1	505	2.81E+05	20.9	0.15	37.1	24.2	29.8	207	67.5	76	2	77.1	0.95	7.7
	2	505	3.07E+05	20.3	0.15	27.1	26.1	26.8	153	59	64	2	93.2	1.45	9.3
	3	505	2.04E+05	10.0	0.07	26.4	17.6	16.2	332	109	123	2	102.0	1.24	10.2
	4	505	4.40E+05	17.0	0.12	62.9	30.4	31.9	155	56.5	62	1	112.0	1.65	11.2
	5	505	7.00E+05	23.7	0.17	48.9	31.7	35.4	229	63	74	2	160.3	1.93	16.0
	6	505	3.57E+05	15.1	0.11	45.5	34.8	25.9	228	104.5	107	1	111.5	1.37	11.2
	(No. of xtls)		*(Cm³)*	*(ng)*		*(ng)*									
***SD6**	*1 (4)*	*505*	*21.8E-9*	*1.7*		*2.5*					*86*		*104.0*		*10.4*
	2 (6)	*505*	*36.5E-9*	*1.7*		*2.2*					*70*		*105.0*		*10.5*
***SD13**	*1 (6)*	*329*	*8.1E-9*	*1.2*		*1.2*					*65*		*62.0*		*6.2*
	2 (9)	*329*	*3.8E-9*	*0.6*		*0.9*					*45*		*51.0*		*5.1*
***SD14**	*1 (16)*	*290*	*14.1E-9*	*1.4*		*1.6*					*45*		*64.0*		*6.4*
	2 (13)	*290*	*17.2E-9*	*1.4*		*1.6*					*60*		*77.0*		*7.7*
	3 (3)	*290*	*16.2E-9*	*1.9*		*2.3*					*47*		*55.0*		*5.5*
	4 (2)	*290*	*13.3E-9*	*1.4*		*1.2*					*55*		*65.0*		*6.5*
***SD9**	*1 (3)*	*195*	*2.7E-9*	*0.4*		*0.5*					*60*		*63.0*		*6.3*
	2 (11)	*195*	*12.4E-9*	*1.4*		*1.9*					*59*		*68.0*		*6.8*
SD13 – 02															
	D6	867	1.07E+06	34.1	0.25	80.2	62.7	53.1	354	37	50	2	163.5	1.46	16.3
	D8	867	8.84E+05	22.2	0.16	37.1	44.7	30.9	230	60	71	2	229.3	1.48	22.9
	D24	867	9.06E+05	31.2	0.23	56.8	49.2	44.7	316	52	67	2	164.0	1.98	16.4
	D27	867	8.24E+05	33.7	0.24	53.6	39.1	46.5	178	40.5	49	2	144.1	3.26	14.4
	M43	867	9.07E+05	26.1	0.19	45.8	41.0	37.0	296	87.5	101	2	197.5	0.18	19.8
	D20	867	9.28E+05	14.2	0.10	23.0	45.0	19.7	293	87	101	2	371.3	1.43	37.1
	D21	867	6.05E+05	171.9	1.25	289.0	347.3	241.0	334	89	105	2	20.5	1.19	2.0
	D37	867	5.57E+05	13.7	0.10	22.8	26.6	19.2	173	71	76	**1**	235.4	1.58	23.5
	M9	867	3.86E+05	12.0	0.09	20.0	22.6	16.8	150	85.5	82	1	185.0	2.06	18.5

Sample no.	Crystal no.	Alt. (m)	^{4}He (ncc/g)	^{238}U (ppm)	^{235}U (ppm)	^{232}Th (ppm)	^{147}Sm (ppm)	eU[a] (ppm)	Length (µm)	Radius (µm)	R* [b] (µm)	T[c]	Age (Ma)	A. error	Std. error
	M31	867	4.10E+05	14.3	0.10	26.2	33.2	20.6	205	86.5	91	1	160.6	1.50	16.1
	M32	867	5.01E+05	13.9	0.10	31.3	35.0	21.3	236	91.5	99	1	188.8	1.62	18.9
	M38	867	6.17E+05	14.3	0.10	44.0	42.6	24.8	325	76	92	1	200.1	1.42	20.0
	M40	867	9.25E+05	23.2	0.17	53.0	51.4	35.8	356	61.5	79	1	208.0	1.71	20.8
	D7	867	1.14E+06	36.6	0.27	73.6	56.4	54.1	163	60	66	0	170.7	1.88	17.1
	D32	867	9.12E+05	22.9	0.17	99.1	61.5	46.3	127	42.5	48	0	160.6	1.89	16.1
	M1	867	3.95E+05	11.4	0.08	33.9	45.7	19.5	149	85	81	0	162.7	1.74	16.3
SD13 – 02a	1	867	7.57E+05	52.1	0.38	78.5	25.0	71.0	193	43.5	53	2	87.3	1.07	8.7
	3	867	8.10E+05	47.9	0.35	82.1	60.7	67.5	183	39.5	49	2	97.6	1.30	9.8
	4	867	1.46E+06	76.5	0.55	107.5	49.6	102.3	142	48.5	54	2	116.1	1.32	9.8
	5	867	6.80E+05	35.1	0.25	57.2	24.0	48.8	227	53.5	65	2	113.7	1.34	11.6
	6	867	7.55E+05	29.0	0.21	92.4	44.5	50.9	170	59	66	0	120.6	1.55	11.4
	8	867	4.78E+05	41.4	0.30	32.5	35.5	49.3	226	66	77	2	79.1	0.82	12.1
	9	867	1.01E+06	74.6	0.54	72.8	18.4	92.3	217	66	77	2	89.9	0.90	7.9
	10	867	6.88E+05	32.6	0.24	53.6	40.7	45.4	171	60	71	2	123.0	1.43	9.0
	11	867	1.60E+06	69.5	0.50	106.2	62.6	94.9	268	50	58	2	136.8	1.54	12.3
	12	867	3.34E+05	14.9	0.11	25.7	64.4	21.0	186	65.5	79	2	126.8	1.59	13.7
	13	867	2.16E+06	78.5	0.57	128.7	26.7	109.3	317	60	68	1	161.0	1.77	12.7
	14	867	2.10E+05	9.9	0.07	17.8	8.6	14.1	140	81	97	1	121.2	1.46	16.1
	15	867	4.68E+05	23.7	0.17	35.8	14.7	32.3	181	65	67	2	118.1	1.58	12.1
	16	867	2.53E+06	106.8	0.77	185.5	104.2	151.1	225	35.5	45	1	136.2	1.59	11.8
	17	867	3.27E+05	8.2	0.06	35.6	17.5	16.6	92	53	64	0	159.4	2.62	13.6
SD13 – 03															
	D7	755	3.84E+05	16.7	0.12	68.1	48.5	32.8	140	57	61	2	94.8	1.19	9.5
	D13	755	4.15E+05	13.6	0.10	56.0	21.3	26.9	185	48.5	58	2	125.7	0.93	12.6
	D14	755	3.38E+05	10.1	0.07	34.3	22.9	18.2	231	62.5	74	2	150.1	1.41	15.0
	D17	755	5.52E+05	16.2	0.12	55.7	20.2	29.4	187	48	57	2	152.8	1.21	15.3
	D19	755	7.83E+05	26.9	0.20	108.8	38.0	52.7	283	32.5	44	2	121.0	1.43	12.1
	D22	755	8.98E+05	26.2	0.19	63.5	44.3	41.3	172	50.5	59	2	175.8	1.59	17.6
	M11	755	1.02E+06	25.2	0.18	99.6	45.3	48.8	222	63.5	74	2	170.2	1.46	17.0
	D2	755	2.70E+05	9.6	0.07	36.0	20.5	18.1	156	50.5	57	1	121.2	1.10	12.1
	D15	755	1.02E+06	26.6	0.19	100.2	22.7	50.4	187	60	68	1	163.9	1.18	16.4
	D20	755	3.55E+05	9.4	0.07	33.4	20.2	17.3	197	72	79	1	165.7	1.59	16.6
	M26	755	5.38E+05	17.2	0.12	93.5	40.2	39.3	214	84.5	91	1	111.3	1.54	11.1
	M36	755	7.85E+05	24.3	0.18	14.5	7.3	27.9	293	74.5	89	1	228.2	1.62	22.8
	D10	755	4.12E+05	12.9	0.09	41.2	21.9	22.6	186	59	67	0	147.5	1.10	14.8
	D18	755	2.84E+05	11.2	0.08	36.7	29.2	19.9	160	43	51	0	116.3	1.91	11.6
	M37	755	5.79E+05	17.8	0.13	78.5	42.7	36.4	165	77.5	79	0	129.0	1.24	12.9

Sample no.	Crystal no.	Alt. (m)	^{4}He (ncc/g)	^{238}U (ppm)	^{235}U (ppm)	^{232}Th (ppm)	^{147}Sm (ppm)	eU[a] (ppm)	Length (µm)	Radius (µm)	R* [b] (µm)	T[c]	Age (Ma)	A. error	Std. error
SD13 – 03a	1	755	4.86E+05	15.7	0.11	42.7	16.1	25.8	248	72.5	84	2	153.2	1.91	15.3
	2	755	3.14E+05	8.3	0.06	31.4	15.4	15.7	196	71	78	1	161.8	2.36	16.2
	4	755	1.39E+06	75.8	0.55	173.6		117.2	137	28	35	2	97.2	1.52	9.7
	5	755	3.79E+05	19.1	0.14	42.1	7.4	29.1	146	55.5	60	1	106.5	1.64	10.6
	6	755	7.78E+05	27.4	0.20	76.8	52.7	45.7	144	40.5	47	2	138.0	2.29	13.8
	7	755	1.17E+06	9.9	0.07	103.7	35.1	34.3	127	41	46	1	275.6	5.10	27.6
SD13 – 04															
	D12	628	5.00E+05	4.9	0.04	40.4	34.7	14.4	283	85.5	98	2	281.6	2.84	28.2
	D19	628	5.50E+05	28.8	0.21	97.0	53.6	51.8	221	33.5	44	2	87.1	1.48	8.7
	D29	628	6.81E+05	29.5	0.21	80.6	43.4	48.7	134	46	51	2	114.8	0.79	11.5
	M32	628	3.58E+05	9.8	0.07	34.0	24.6	17.8	278	75.5	89	2	164.0	1.56	16.4
	M44	628	5.17E+05	11.8	0.09	39.8	32.3	21.3	276	80.5	93	2	198.2	1.02	19.8
	D28	628	6.77E+05	17.6	0.13	64.1	35.8	32.8	186	65.5	73	1	168.2	1.24	16.8
	D31	628	7.33E+05	23.5	0.17	92.0	52.6	45.3	203	70	78	1	132.3	1.37	13.2
	M17	628	2.98E+05	8.7	0.06	33.2	26.1	16.5	313	84	99	1	147.1	1.12	14.7
	M26	628	5.28E+05	14.1	0.10	39.0	29.8	23.3	312	75	91	1	184.4	1.62	18.4
	M41	628	8.57E+05	25.3	0.18	118.1	48.0	53.2	148	49	55	1	131.8	1.51	13.2
	D17	628	5.37E+05	13.9	0.10	59.1	32.6	27.9	185	47.5	57	0	157.5	1.26	15.8
SD13 – 04a	1	628	7.48E+05	21.9	0.16	72.7	42.3	39.1	189	45.5	55	2	154.7	1.81	15.5
	2	628	1.02E+06	32.6	0.24	123.3	50.6	61.8	130	57	59	1	133.9	1.80	13.4
	3	628	7.98E+05	20.6	0.15	79.4	29.1	39.5	143	55	60	2	164.0	2.35	16.4
	4	628	7.87E+05	27.6	0.20	87.6	42.6	48.4	204	39	49	2	132.1	1.94	13.2
	5	628	3.29E+05	10.0	0.07	38.7	22.4	19.1	195	49	59	2	139.1	2.47	13.9
	6	628	7.25E+05	24.6	0.18	75.7	71.2	42.5	121	51.5	54	0	137.6	2.08	13.8
	7	628	3.37E+05	11.7	0.09	45.4	25.4	22.5	187	47.5	57	1	121.4	2.10	12.1
	8	628	9.91E+05	29.4	0.21	120.3	38.8	57.9	212	45	56	2	139.3	1.89	13.9
	9	628	4.94E+05	13.9	0.10	52.8	25.0	26.4	260	68	81	0	151.6	2.00	15.2
	10	628	4.29E+05	14.3	0.10	64.3	34.9	29.5	165	52	59	1	117.9	1.82	11.8
	11	628	6.84E+05	20.2	0.15	79.3	28.0	39.0	190	47	57	2	142.5	2.07	14.2
	12	628	4.05E+05	16.1	0.12	52.1	28.6	28.4	197	75.5	82	1	115.7	1.49	11.6
	13	628	6.96E+05	19.9	0.14	80.8	31.8	39.1	175	55	63	1	144.6	2.00	14.5
	14	628	5.58E+05	22.9	0.17	97.3	37.2	45.9	97	47	47	0	98.8	1.67	9.9
	15	628	2.56E+05	12.4	0.09	38.0	114.2	21.4	190	71.5	78	0	94.1	1.27	9.4
	16	628	4.10E+05	10.3	0.07	37.7	34.3	19.3	358	95	113	1	170.9	2.17	17.1
	17	628	9.12E+05	20.0	0.14	101.0	34.1	43.8	134	57.5	60	1	168.6	2.40	16.9
	18	628	2.98E+05	11.0	0.08	36.8	20.4	19.7	135	51.5	56	1	122.5	2.51	12.2
	19	628	3.57E+05	15.3	0.11	40.2	28.7	24.9	188	52.5	62	2	116.5	1.79	11.7

Sample no.	Crystal no.	Alt. (m)	^{4}He (ncc/g)	^{238}U (ppm)	^{235}U (ppm)	^{232}Th (ppm)	^{147}Sm (ppm)	eU^{a} (ppm)	Length (µm)	Radius (µm)	R* ^{b} (µm)	T^{c}	Age (Ma)	A. error	Std. error
BH15 – 05															
	1	220	8.33E+05	65.4	0.47	57.0	26.5	79.3	204	46	56	2	86.0	0.97	8.6
	2	220	1.92E+05	24.1	0.18	42.4	27.7	34.3	103	47	48	1	45.9	1.00	4.6
	3	220	6.62E+05	56.2	0.41	76.7	29.9	74.6	175	38.5	47	2	72.8	0.96	7.3
	4	220	4.40E+05	42.3	0.31	73.3	30.8	59.9	186	58	66	1	60.2	0.70	6.0
	5	220	2.78E+05	20.0	0.15	31.5	14.3	27.6	282	89.5	102	2	82.6	0.90	8.3
	6	220	5.51E+05	49.6	0.36	53.7	17.3	62.6	165	77	79	1	72.3	0.75	7.2
	7	220	8.08E+05	103.2	0.75	52.8	37.4	116.3	146	33	40	2	57.0	0.91	5.7
	8	220	9.68E+05	51.1	0.37	71.9	24.9	68.4	187	64.5	72	1	115.6	1.25	11.6
	9	220	5.85E+05	32.7	0.24	66.4	25.7	48.5	138	58	61	0	98.3	1.26	9.8
	10	220	5.11E+05	41.8	0.30	62.3	20.0	56.7	214	40	51	2	73.8	0.98	7.4
	11	220	7.19E+05	50.4	0.37	71.8	34.7	67.6	220	69	79	1	86.9	0.93	8.7
	12	220	6.62E+05	48.4	0.35	44.8	32.9	59.2	156	61	66	1	91.4	1.04	9.1
	13	220	4.77E+05	33.0	0.24	64.9	24.9	48.5	144	53	58	1	80.4	1.06	8.0
	14	220	No photo	-	-	-	-	-	-	-	-	-	53.1	0.70	5.3
	16	220	3.39E+05	38.6	0.28	70.2	33.8	55.4	152	37.5	45	1	50.2	0.83	5.0
	17	220	3.44E+06	175.6	1.27	327.7	143.7	253.9	187	37.5	45	1	110.5	1.29	11.1
	18	220	5.26E+05	37.1	0.27	54.6	21.3	50.2	152	67.5	74	1	85.6	0.97	8.6
	19	220	3.46E+04	6.5	0.05	8.5	5.2	8.5	106	61.5	66	0	33.3	1.13	3.3
	20	220	1.17E+07	611.9	4.44	1083.9	416.6	871.1	227	28	33	1	110.1	1.25	11.0
	21	220	1.26E+05	8.2	0.06	9.9	4.6	10.6	157	86.5	94	2	97.9	1.37	9.8
SD13 - 06															
	4	0	1.69E+05	14.6	0.11	36.0	25.6	23.1	167	54.5	62	1	59.5	0.88	5.9
	6	0	1.92E+05	13.6	0.10	36.0	24.7	22.1	245	59	71	2	70.6	0.83	7.1
	9	0	1.71E+05	18.8	0.14	48.4	22.0	30.4	212	32.5	42	2	46.0	0.95	4.6
	18	0	4.21E+04	5.5	0.04	19.2	10.8	10.1	110	55	55	0	34.2	1.18	3.4
	25	0	1.20E+05	18.1	0.13	46.0	16.9	29.1	106	35.5	40	1	33.8	1.13	3.4
	31	0	2.37E+05	20.1	0.15	51.0	21.5	32.3	114	35.5	41	1	59.9	1.70	6.0
	52	0	3.12E+05	28.9	0.21	60.2	24.1	43.3	167	36.5	45	1	59.0	1.00	5.9
BH13 – 02															
	1	0	6.18E+05	45.5	0.33	51.0	10.7	57.8	141	66	67	0	87.8	0.96	8.8
	6	0	1.39E+05	14.4	0.10	43.5	15.6	24.7	132	86	78	1	45.9	0.51	4.6
	13	0	3.64E+05	19.0	0.14	59.1	19.7	33.0	165	59	65	2	90.0	1.06	9.0
	16	0	2.40E+05	20.3	0.15	52.5	17.3	32.8	143	46.5	53	1	59.9	0.94	6.0
	21	0	1.78E+05	11.4	0.08	37.9	21.7	20.4	216	98	101	0	71.3	0.74	7.1
	39	0	1.68E+05	19.5	0.14	54.6	12.4	32.5	178	38.5	47	1	42.6	0.73	4.3
	40	0	8.91E+04	178.0	1.29	71.1	12.2	196.0	77	42.5	41	1	3.8	0.06	0.4

Sample no.	Crystal no.	Alt. (m)	^{4}He (ncc/g)	^{238}U (ppm)	^{235}U (ppm)	^{232}Th (ppm)	^{147}Sm (ppm)	eU^{a} (ppm)	Length (μm)	Radius (μm)	R* ^{b} (μm)	T^{c}	Age (Ma)	A. error	Std. error
	42	0	1.86E+05	21.8	0.16	50.8	6.2	33.9	57	32	31	0	45.2	2.93	4.5
	50	0	2.03E+05	53.4	0.39	98.1	31.9	76.8	107	31.5	37	1	21.7	0.43	2.2
	75	0	2.40E+05	29.8	0.22	60.7	13.3	44.3	120	34.5	40	2	44.4	1.03	4.4
	87	0	2.58E+05	16.6	0.12	37.3	14.3	25.5	89	36.5	39	1	82.6	3.60	8.3
	91	0	1.51E+05	13.9	0.10	44.9	16.1	24.5	85	39.5	40	1	50.4	1.83	5.0
	93	0	2.65E+05	22.1	0.16	58.9	14.4	36.1	126	37	43	1	60.2	1.32	6.0
	94	0	2.03E+05	20.3	0.15	45.1	11.6	31.0	73	41.5	40	1	53.6	1.85	5.4
	95	0	2.73E+05	27.3	0.20	63.7	18.5	42.5	164	28.5	36	2	52.6	1.29	5.3

Table 5-3: Durango apatite age standards.

a – Durango apatite has a standardised age of 31.44 ± 0.18Ma (McDowell *et al*., 2005) determined from ^{40}Ar – ^{39}Ar dating of the stratigraphically adjacent ignimbrites. Ages within 10% of the standardised age (31 ± 3.1Ma) are considered reproducible, any ages outside this are considered anomalous and highlighted orange in the table. **b** – Durango apatite has a variable Th/U ratio, but the Durango used at SUERC typically has a ratio of c. 25 (Stuart, personal com.). Any major deviations from this are highlighted red in the table. * - The anomalous ages for these pans have not been used to calculate the mean and dispersion as they will dominate the mean age. Mean age is listed with ± 1 standard deviation (1σ).

Year	Pan	Crystal no.	Age^{a} (Ma)	A. error	Disp.	Th/U b	Error	^{4}He	Reheat	^{238}U (ng)	^{232}Th (ng)	Comments
2014	**21**											
		Dur14-21-01	35.12	0.39		23.62	0.40	2.24E-09		0.06	1.38	Only marginally outside of expected age range
		Dur14-21-02	29.05	0.33		28.46	0.51	1.68E-09		0.04	1.28	
		Dur14-21-03	20.38	0.21		7.42	0.12	1.5E-09		0.16	1.19	Low Th/U ratio but also young age
		Dur14-21-04	32.41	0.36		23.66	0.37	2.31E-09	4.31E-12	0.07	1.54	
		Dur14-21-05	27.98	0.30		14.35	0.23	1.26E-09		0.06	0.88	Low Th/U ratio
		Mean Age	**28.99**	**± 5.58**	**50.84%**							
2014	**31**											
		Dur14-31-D1	32.35	0.37		24.57	0.49	3.97E-08	6.19E-12	0.25	6.18	
		Dur14-31-D2	31.04	0.36		25.38	0.51	3.23E-08	6.41E-12	0.21	5.27	
		Dur14-31-D3	32.66	0.38		24.38	0.49	5.17E-08	9.5E-12	0.33	7.96	
		Dur14-31-D4	32.49	0.38		24.42	0.49	2.67E-08	8.4E-12	0.17	4.14	
		Dur14-31-D5	31.53	0.37		26.22	0.54	3.87E-08		0.24	6.25	
		Mean Age	**32.01**	**± 0.70**	**5.07%**							

Year	Pan	Crystal no.	Age[a] (Ma)	A. error	Disp.	Th/U[b]	Error	^{4}He	Reheat	^{238}U (ng)	^{232}Th (ng)	Comments
2014	**32**											
		Dur14-32-11	31.61	0.36		23.15	0.47	2.73E-08	2.79E-11	0.20	4.61	
		Dur14-32-12	32.00	0.37		24.20	0.49	2.52E-08	1.44E-11	0.17	4.22	
		Dur14-32-13	31.16	0.36		22.62	0.46	2.7E-08		0.20	4.60	
		Dur14-32-14	33.03	0.38		24.99	0.51	3.5E-08	1.64E-11	0.23	5.71	
		Dur14-32-15	34.21	0.40		24.89	0.50	3.68E-08	1.87E-11	0.23	5.81	
		Mean Age	**32.40**	**± 1.22**	**9.42%**							
2016	**2**											
		Dur16-2-1	30.89	1.14		23.54	0.98	1.27E-08	3.19E-11	0.16	3.85	
		Dur16-2-2	30.93	1.13		20.19	0.83	1.33E-08	3.28E-11	0.19	3.94	Slightly low Th/U ratio
		Dur16-2-3	38.19	1.36		13.10	0.54	1.4E-08		0.23	3.05	Low Th/U ratio possibly explains older age
		Dur16-2-4	31.05	1.14		22.34	0.93	1.32E-08		0.18	3.96	
		Dur16-2-5	16.86	0.61		15.14	0.63	4.12E-09	2.27E-11	0.14	2.10	Low Th/U ratio but also low ^{4}He overpowering age
		Mean Age	**29.59**	**± 7.77**	**72.1%**							
2016	**3**											
		Dur16-3-6	30.92	0.41		25.68	0.50	9.01E-09		0.15	3.96	
		Dur16-3-7	29.16	0.39		24.94	0.49	7.92E-09	1.27E-11	0.15	3.67	
		Dur16-3-8	26.19	0.35		24.13	0.48	5.4E-09	1.39E-11	0.11	2.77	Slightly young age
		Dur16-3-9	30.15	0.40		24.84	0.48	9.2E-09		0.17	4.13	
		Dur16-3-10	26.92	0.36		24.46	0.47	9.31E-09	1.28E-11	0.19	4.66	Slightly young age
		Mean Age	**28.67**	**± 2.04**	**16.48%**							
2016	**12**											
		Dur16-12-11	31.65	0.95		23.66	0.83	1.21E-08	1.08E-11	0.20	4.85	
		Dur16-12-12	31.93	0.96		24.03	0.85	1.01E-08	8.29E-12	0.17	4.01	
		Dur16-12-13	30.97	0.93		24.20	0.85	1.23E-08	8.73E-12	0.21	5.05	
		Dur16-12-14	29.83	0.90		23.42	0.82	1.15E-08		0.21	4.88	
		Dur16-12-15	5240.35	2607.40		5.11	6.81	7.97E-09	7.96E-12	0.00	0.01	No U and Th, missing crystal/ICPMS problem?
		Mean Age*	**31.10**	**± 0.94**	**6.75%**							
2016	**14**											
		Dur16-14-16						6.78E-09	4.31E-12			Lost sample
		Dur16-14-17	29.75	0.44		21.23	0.42	2.19E-08		0.17	3.70	
		Dur16-14-18	153.50	2.67		1.44	0.05	1.36E-08	1.99E-11	0.10	0.14	Very little U and Th, crystal not properly dissolved?
		Dur16-14-19	29.21	0.43		24.18	0.49	1.87E-08	2.52E-11	0.14	3.29	
		Dur16-14-20						1.29E-08	8.29E-12			Lost sample
		Mean Age*	**29.48**	**± 0.38**	**1.83%**							

Year	Pan	Crystal no.	Age[a] (Ma)	A. error	Disp.	Th/U [b]	Error	^{4}He	Reheat	^{238}U (ng)	^{232}Th (ng)	Comments
2016	**15**											
		Dur16-15-21	29.26	0.43		24.68	0.49	2.56E-08		0.18	4.52	
		Dur16-15-22	31.40	0.46		23.50	0.46	4.91E-08		0.34	8.03	
		Dur16-15-23	26.90	0.40		23.43	0.46	3.06E-08	2.02E-11	0.25	5.83	Slightly young age
		Dur16-15-24	29.61	0.44		25.47	0.50	2.95E-08	2.14E-11	0.20	5.17	
		Dur16-15-25	29.59	0.43		19.18	0.37	2.91E-08	2.11E-11	0.25	4.89	Low Th/U ratio
		Mean Age	**29.35**	**± 1.61**	**15.31%**							
	Total	**Mean Age***	**30.23**	**± 3.68**	**70.56%**							

5.2.1 *Omitted data*

A very small number of individual grains have been omitted from the data table for reasons outlined below. Despite this, strong outliers/anomalous ages are still included where there has been no analytical justification to omit them. This is contrary to what was often the standard practice of the past of only publishing 'reproducible' ages and trying to find a satisfactory 'mean' age. The outliers have been highlighted in table **5.2** and will also be discussed below (section 5.2.2).

A couple of crystals with ages significantly older than a billion years (>1000Ma) have been omitted from sample *SD07 – 1*. These were most likely zircons mistakenly picked instead of apatite. This is because zircon has a much higher eU concentration than apatite, but isn't dissolved during the standard apatite dissolution procedure for ICPMS. This leads to the crystals recording exceptionally high concentrations of ^{4}He with almost no U and Th, therefore giving unreasonably old ages (and having the same effect as parentless ^{4}He on the (U-Th)/He isochron plot, see figure **5.8**).

A couple of crystals have ages at, or older than the age of intrusion of the BIC (424 ± 4Ma) and so have also been omitted. These ages are impossible to be accurate as the crystals can't begin accumulating ^{4}He before they have formed. One (or more) of the imposed extraneous contributors to dispersion must be responsible for these 'too old' ages (see section 2.2.2). The most likely factor is that of ^{4}He implantation from one or more 'bad neighbours' as shown by Gautheron *et al.* (2012). The omitted crystals are from: *SD07 – 3a* (635.8 Ma) and *BH13 – 02* (423.1 Ma). Each crystal can be seen to have gained significant parentless ^{4}He in the (U-Th)/He isochron plots (figures **5.11 C** and **5.18 C**) (Vermeesch, 2008) supporting implantation as the likely cause. Any other omitted crystals have sound analytical justification for doing so, for example the crystal not being fully degassed (low ^{4}He) or not fully dissolved (low U and/or Th).

5.2.2 *Outliers/anomalies*

Any apparent outliers have been highlighted orange in table **5.2**, and can be seen in figure **5.5**. No statistical measure has been applied to distinguish an 'outlier' as the aim is not to omit apparent 'outliers' from the dataset. All data which has no analytical justification for exclusion will be used for thermal history modelling (**Chapter 6**). The discussed 'outliers' have been highlighted purely from the observations made of figure **5.5**, but this is also supported by the (U-Th)/He isochron plots in figures **5.8** - **5.18** (see section 5.3.2 for discussion of isochron plots).

The two or three sigma (σ) test is often used to eliminate outliers from 'over dispersed' AHe data to attain a reproducible mean age. This is where any ages which fall outwith either two (2σ) or three (3σ) standard deviations of the mean (depending on the desired level of reproducibility) are eliminated from the dataset. This is a valid method where the aim is to generate a robust mean age value, but as discussed in **Chapter 3**, in AHe dating the mean is not a particularly helpful statistical measure as it bears no specific significance to a geological event. In addition, dispersed data are often highly skewed (e.g. figure **5.15 D**), and don't follow a normal distribution (Brown *et al*., 2013) therefore there is little justification to expect data to fall within 2σ or 3σ of the arithmetic mean. However it is still worth highlighting and discussing the observed outliers which have been determined through qualitative means alone.

SD07 – 1 (31): Age – 106.2 ± 1.12Ma (analytical error). This crystal stands out as younger than the rest of the sample (figure **5.5**). It also stands out on the (U-Th)/He isochron plot as having less ^{4}He than it should (figure **5.8 C**) giving the erroneously young age (for a full explanation of the isochron plots and what they show, see section 5.3.2). It is a 1T crystal and one of the smallest from the sample, which may account for the young age, but it is not significantly smaller than most grains (figure **5.8 A**). It has typical eU concentrations so this does not appear to impact on the age. It is a good, clear euhedral crystal.

SD07 – 2a (5): Age – 285.6 ± 3.77Ma. This crystal stands out as older than the rest of the sample. It is a 1T crystal and one of the largest from the sample, which may account for the old age, but it is not significantly larger than the rest. It has a typical eU concentration so this does not account for the old age. It is euhedral with good clarity. It appears to have gained parentless ^{4}He, as seen by the (U-Th)/He isochron plot (figure **5.9 C**), leading to implantation being the likely cause of the erroneous age.

SD07 – 2a (12): Age – 18.0 ± 0.27Ma. This crystal stands out as much younger than the rest of the sample. It is a 0T crystal which makes its behaviour in terms of fragmentation induced age dispersion much more unpredictable. It is also fairly thin, which makes the impact of ^{4}He loss through α-ejection potentially significant, but its width is still greater than 60µm so it would not be rejected during screening for being too thin. Most notably it has an exceptionally high eU concentration for apatite (nearly 300ppm) which is c. 10x that of a typical apatite crystal. Under our current radiation damage models (Flowers *et al.*, 2009; Gautheron *et al.*, 2009) the age should increase with increased radiation damage. But given the exceptionally high eU value it is plausible that the radiation damage has become interconnected, providing pathways rather than traps for ^{4}He diffusion (see **Chapter 2**, section *2.2.1.2*). The (U-Th)/He isochron plot (figure **5.9 C**) shows that this crystal has far less ^{4}He than it should, providing evidence to support the work of Gerin *et al.* (2017) that very high eU leads to reduced ^{4}He retentivity.

SD07 – 3a (11): Age – 31.1 ± 1.69Ma. This crystal also stands out as young for the sample. It is a 1T crystal which is one of the smallest in the sample, but not exceptionally small. α-ejection might be an issue but it is still greater than 60μm in diameter. It is euhedral with good clarity. It has a typical eU concentration so this is not a factor on the young age. It does have a slightly higher % of analytical error than other crystals in the sample (c. 5% vs. c. 1-2%) which is down to one (or more) of the measurements being close to blank level, increasing the uncertainty, but there is no explanation as to why the measurement/s was low. The (U-Th)/He isochron plot (figure **5.11 C**) shows this crystal to have slightly less ^{4}He than it should, which could mean that ^{4}He has been lost through an undetected fracture.

SD07 – 4 (12): Age – 273.4 ± 3.79Ma. This crystal stands out as old for the sample (it is also older than the AFT age for sample SD07 – 3). It is a 2T crystal so fragmentation does not play a part in the age dispersion. It is a good, clear euhedral crystal. The crystal is not exceptionally big, but it is the largest (in terms of R*) in the sample. This sample shows a fairly strong positive correlation between R* and age (see figure **5.13 A**) so the large size can satisfactorily explain the older age. The crystal has the lowest eU concentration of the sample, so grain size is clearly the dominant factor on age dispersion in this sample. There was a question mark over if there was a tiny fluid inclusion in this crystal, which may have contributed to the older age, but the work of Vermeesch *et al.* (2007) suggests this is unlikely. However the crystal does sit above the (U-Th)/He isochron in the plot in figure **5.13**, suggesting that it has possibly inherited parentless ^{4}He, so an inclusion could contribute to the old age.

SD07 – 5 (36): Age – 294.8 ± 4.22Ma. This crystal stands out as old for the sample (it is also older than the AFT age for sample *SD07 – 3*). It is a 1T crystal (though it is unclear if it has 1 or 0 terminations) with a typical grain size and eU concentration. It does sit slightly above the (U-Th)/He isochron (figure **5.15 C**) suggesting that it has inherited some parentless ^{4}He, so implantation may be the cause of the old age.

SD13 – 02 (D20): Age – 371.3 ± 1.43Ma. This crystal stands out as much older than the rest of the sample (and all the other samples in the profile, including the AFT age). It is a 2T crystal so fragmentation does not play a part (although it does have a chipped termination so more like 1.5T, which may have a small effect). It is a very large crystal so it would be expected to be old, but there are a number of other very large crystals in this sample which don't have such old ages. It also has fairly low (but not unusually low) eU so that is not contributing to the old age. It has clearly gained parentless ^{4}He, as shown by the (U-Th)/He isochron plot where this crystal lies well above the isochron (figure **5.10** **C**) (Vermeesch, 2008). Implantation is therefore the most likely cause of the erroneously old age.

SD13 – 02 (D21): Age – 20.5 ± 1.19Ma. This crystal stands out as much younger than the rest of the sample. It is also a 2T crystal so fragmentation does not have an effect. It is euhedral with good clarity. It is a very large crystal so it would be expected to have an old age, but the stand out factor is the very high eU concentration (c. 240ppm) which again is c. 10x higher than a typical apatite crystal. As with crystal *SD07 – 2a (12)* this crystal supports the work of Gerin *et al.* (2017) that above a certain threshold ^{4}He retentively decrease as radiation damage increases. This is also supported by the (U-Th)/He isochron plot (figure **5.10** **C**).

SD13 – 03a (7): Age – 275.6 ± 5.1Ma. This crystal stands out as older than the rest of the sample (it is also older than the AFT age for sample SD07 – 3). It is a 1T crystal which is neither exceptionally large or with high/low eU. It is euhedral with good clarity. Fragmentation is likely to be the dominant effect on the old age, but it does sit slightly above the (U-Th)/He isochron (figure **5.12** **C**), implying that it may have inherited some Parentless ^{4}He.

SD13 – 04 (D12): Age – 281.6 ± 2.84Ma. This crystal stands out as older than the rest of the sample (it is also older than the AFT age for sample *SD07 – 3*). It is a 2T crystal so fragmentation does not play a part. It is euhedral with good clarity. It is one of the largest crystals but not the largest in the sample and it has a low eU. It has inherited some parentless ^{4}He, as shown by the (U-Th)/He isochron plot (figure **5.14** **C**), so implantation is the likely cause of the erroneously old age.

BH13 – 02 (40): Age – 3.8 ± 0.06Ma. This crystal appears to stand out as younger than the rest of the sample. It is a 1T crystal of fairly small size, but it is not the smallest in the sample and is thicker than 60µm in diameter. Significantly it has a very high eU concentration of nearly 200ppm. It is not quite as high as crystals *SD07 – 2a (12)* and *SD13 – 02 (D21)* but it also provides evidence that very high eU samples have a lower ^{4}He retentivity and do not conform to the recognised radiation damage models of Flowers *et al.* (2009) and Gautheron *et al.* (2009). This is also shown by the crystal falling significantly below the (U-Th)/He isochron (figure **5.18 C**), meaning it has less ^{4}He than it should.

Many of the highlighted outliers are unexceptional in their characteristics. It may be that if a higher number of grains had been analysed for each sample, then some of the additional grains would fill in the apparent age 'gap' meaning that these crystals are no longer outliers. Equally, if fewer grains had been analysed in some samples then this might create more 'outliers'. There is evidence from the (U-Th)/He isochron plots that a number of the 'too old' ages are as a result of parentless ^{4}He, and this may be either from implantation or α-emitting inclusions. This is not sufficient evidence however to avoid modelling these crystals as some crystals which do not stand out as outliers may have experienced the same causes on dispersion but have dispersed 'inwards' towards the median age.

There is grounds on which to avoid modelling crystals *SD07 – 2a (12), SD13 – 02 (D21)* and *BH13 – 02 (40),* as these samples appear not to fit in with the current radiation damage models of either Flowers *et al.* (2009) or Gautheron *et al.* (2009) which are incorporated into the available modelling software (e.g QTQt). These samples are in fitting with the recent work of Gerin *et al.* (2017) which is yet to be incorporated into modelling software.

5.2.3 *Age standards variation*

Durango flourapatite from Cerro de Mercado – Mexico has become the de facto age standard for (U-Th)/He dating techniques after its central use in many of the fundamental studies into the diffusion kinetics of ^{4}He in apatite (e.g. Zietler *et al.*, 1987; Wolf *et al.*, 1996; Farley, 2000). It has a standardised age of 31.44 ± 0.18Ma (McDowell *et al.*, 2005) which has been stratigraphically constrained by ^{40}Ar – ^{39}Ar dating of the over and underlying volcanic ignimbrite deposits. As it comes from a young volcanic source which cooled effectively instantaneously from formation to surface temperatures, its cooling age can be considered effectively identical to the crystallisation age, meaning that the ^{40}Ar – ^{39}Ar age provides clear constraints on the AHe age.

Despite the well constrained age, there can still be a spread of Durango AHe ages significantly beyond the analytical uncertainty (e.g. House *et al.*, 2000; Boyce and Hodges, 2005). This may be down to a systematic underestimation of the true analytical error, and the odd anomalous result is always inevitable. But Boyce and Hodges (2005) found that Durango apatites can exhibit remarkably strong zonation in the distribution of parent nuclei, and this can have a noticeable effect on age dispersion. As Durango standards are typically fragments crushed from much larger crystals, it is likely that different fragments will originate from different zones within the original crystal. Due to the effects of α-ejection (see **Chapter 2**, section *2.2.2.2*) this can mean that a fragment can inherit parentless ^{4}He from a zone of higher U and Th concentration prior to crushing, leading to an older than expected age. Durango apatite is also considered to be mostly inclusion free and therefore not screened in the same way as samples, but there is no guarantee that no inclusions are present. This means that the possibility of analysing a fragment with a significant inclusion cannot be ruled out, which may further disperse the ages.

The ages for the standards run for the duration of this project are shown in table **5.3** (five per pan). The overall mean age is 30.23 ± 3.68Ma (excluding the two very old ages in pans 12 and 14) which is slightly younger than the published age but within the accepted uncertainty. It can be seen that it is rare to achieve perfect reproduction of the true Durango age (within analytical uncertainty). Even sample sets without major anomalies typically show 5-10% age dispersion, which is much greater than the 1-2% expected through analytical uncertainty alone. This ads to the uncertainty of the unknowns analysed (the samples), leading to the use of a nominal 10% error throughout instead of the true analytical error (typically 1-2%) when thermal history modelling. This figure comes from the addition of the c. 5-10% age dispersion observed for 'good' Durango data sets on top of the true analytical error.

Another diagnostic used for considering Durango reproducibility is the Th/U ratio. Durango apatite can have considerable variation in its Th/U ratio (e.g. House *et al.*, 2000) but for each run/pan it can be expected that each measured Durango should have a comparable ratio. This is because each fragment should have originated from the same part of the same original crystal (but this may not always be the case, depending on the origin of the crushed Durango). The Durango currently used at SUERC has been shown to have a Th/U ratio of c. 25 (Stuart, pers. com., see Appendix 3) and the analyses during this project are broadly in agreement with this (table **5.3** and Appendix 3). It is useful to consider the ratio because any major deviation from the typical range (whatever that may be in a given pan) can be indicative of a problem in the analysis. Examples are highlighted red in table **5.3**.

Unusually low Th/U ratios can indicate that the crystal has been overheated during the ^{4}He extraction process, leading to the volatisation of parent isotopes (House *et al.*, 2000). Th is volatised and therefore degassed at a lower temperature than U, meaning it will become preferentially lost during overheating, leading to a lower than expected Th/U ratio. If some of the parents are lost during ^{4}He extraction then this will lead to an erroneously old age. There are a small number of grains listed in table **5.3** where this is a possibility (and this has been highlighted in the comments), which suggests that it is also a possibility that some of the unknowns analysed in the corresponding pan have been overheated and lost parent isotopes (this could provide an alternative explanation to implantation for some of the anomalous ages). Unusually high Th/U ratios may indicate a contamination problem with either the spike or the Teflon beakers used for sample dissolution, which could also lead to erroneous ages. There are no indications of this in any of the analyses for this project (see Appendix 3).

5.3 Results

All the data presented in table **5.2** has been plotted on the age vs. elevation (vertical profile) plots in figures **5.5** - **5.7**. This highlights the range of age dispersion seen in each sample, and how this varies across the vertical profile. It also highlights the potential anomalous results discussed in section 5.2.2. It can be seen that both profiles have a shared thermal history, so can be considered a single profile for modelling purposes. Qualitative predictions were made (in the Ph.D/grant proposal, see figure **5.6**) on the expected range of dispersion throughout the profile, based on the thermal history interpretations published by Persano *et al.*, (2007). Comparisons with this are made herein.

5.3.1 *Age vs. Elevation plots*

The anomalous ages/outliers discussed in section 5.2.2 have been highlighted (orange circles) on figure **5.5**. There are a number of other crystals which stand apart from the rest of the crystals in their sample, but are not considered outliers here because they still fall within the expected age range as defined (qualitatively) by the samples at neighbouring elevations. These crystals also do not stand out as anomalous on the (U-Th)/He isochron plots (figures **5.8** – **5.18**). They would likely no longer stand out if a greater number of crystals had been analysed for each sample. Even excluding the highlighted outliers (figure **5.6**), there is significant age dispersion throughout the profile (even greater than predicted, see discussion below), with dispersion in excess of 100% for some samples (see table **5.4**).

With the outliers included, the dispersion is in excess of 100% for most samples, and in excess of 200% for one sample (*SD13 – 02*).

Based on the thermal history reconstructions of Persano *et al.* (2007), the single grain age dispersion was predicted to be greatest between 600-800m in the vertical profile at c. 100%. The dispersion was expected to decrease towards the top of the profile, and decrease almost to zero at the base of the profile (figure **5.6** inset). This was due to the prediction that the upper middle portion of the profile had spent over 200Ma in the PRZ (Persano *et al.*, 2007), leading to maximum dispersion. The top of the profile in contrast had passed rapidly through the PRZ and remained at near surface temperatures until the present, leading to less dispersion despite the older age. The base of the profile was predicted to have spent most of its history below the base of the PRZ, only beginning to accumulate ^{4}He in the Tertiary. This would lead to very little dispersion.

The results shown in figures **5.5** and **5.6** are broadly in agreement with most of the predictions, particularly with the highest dispersion being present in samples around 800m in elevation. But as different numbers of crystals have been analysed for each sample, it is unreasonable to make like for like comparisons. It may be that the top two samples in the profile (*SD07 – 1* and *SD07 – 2*) would have just as high single grain age dispersion (if not more) as sample *SD13 – 02* if the same number of grains had been analysed. The main difference from the prediction is that much greater dispersion is present at the base of the profile, suggesting that the lowest samples cooled into the PRZ much earlier than Persano *et al.* (2007) predicted, and only cooled slowly to the surface. In fact the amount of dispersion exceeds expectations throughout the profile (with the exception of the very top), particularly when including the highlighted outliers (table **5.4**). Nearly every sample is dispersed well in excess of 100%, which goes to show that significant age dispersion should be considered the norm and not the exception when analysing multiple single grains from old samples.

On age-elevation plots, a break in slope (of the mean ages) has been taken to indicate a change in cooling rate at the corresponding time, as this can represent the fossil PRZ/PAZ (e.g. Gleadow and Fitzgerald, 1987; Fitzgerald and Gleadow, 1990; Fitzgerald *et al.*, 2006). Although the authors show that a linear regression line can be fitted through all their data points within the nominal 10% error used and therefore do not consider it a break of slope, a break of slope is apparent in the data of Persano *et al.* (2007) (figure **5.6**). This indicates a change to more rapid cooling at c. 50-60Ma (i.e. the onset of uplift/denudation), which perhaps coincidently agrees with their published thermal history.

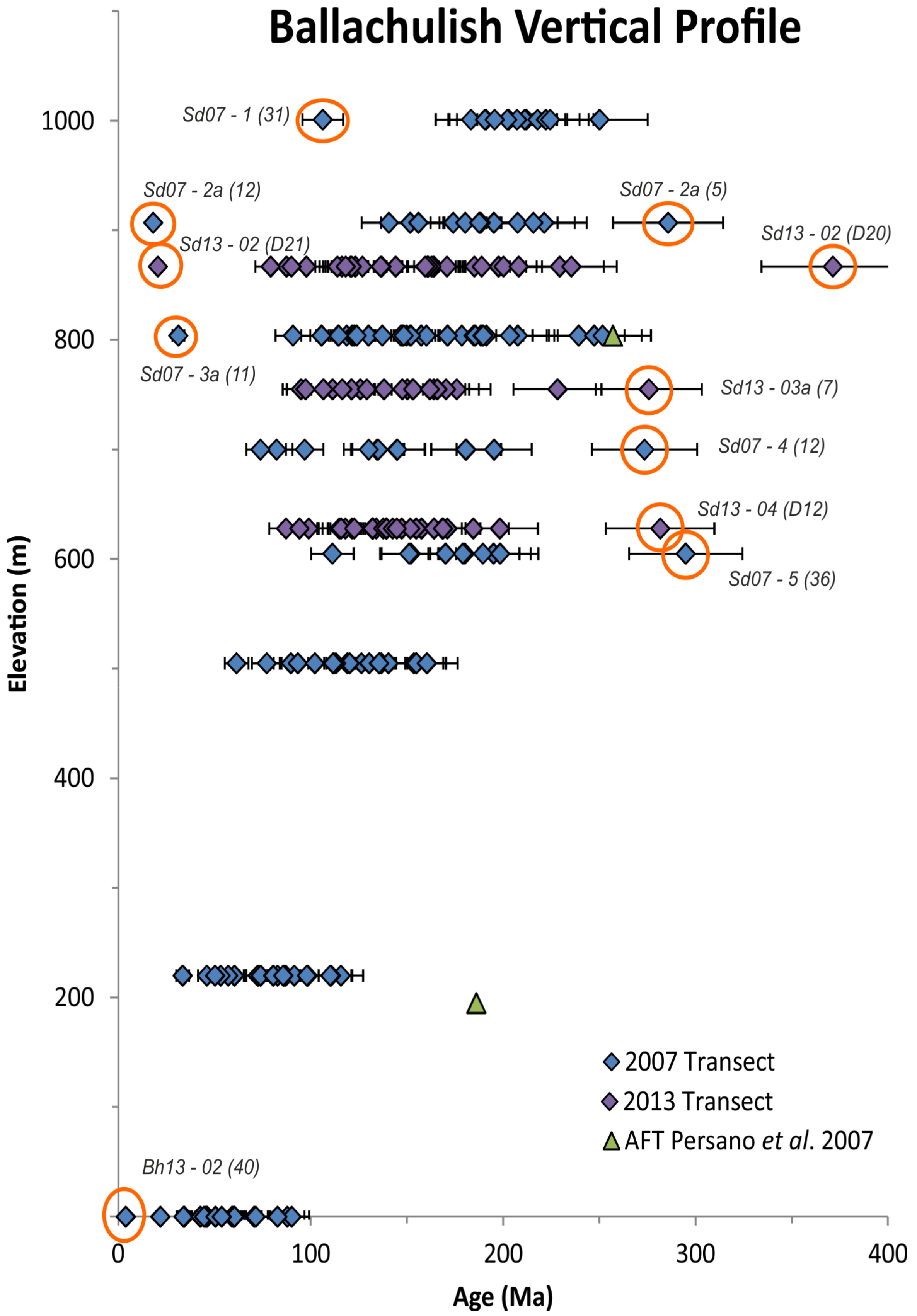

Figure 5.5: Age - Elevation plot 1.
Figure showing the age dispersion per sample as a function of elevation in the profile. The 2007 transect (north) is shown in blue diamonds and 2013 transect (south) in purple diamonds. It is evident that these transects share the same thermal history and so can be considered part of the same vertical profile. Error bars of a nominal 10% are given to the age to account for analytical error plus variation in age standards (Durango apatite). Anomalous ages discussed in section 5.2.2 of the text are circled orange. Also shown are the two published AFT ages of Persano *et al*. (2007) in green triangles.

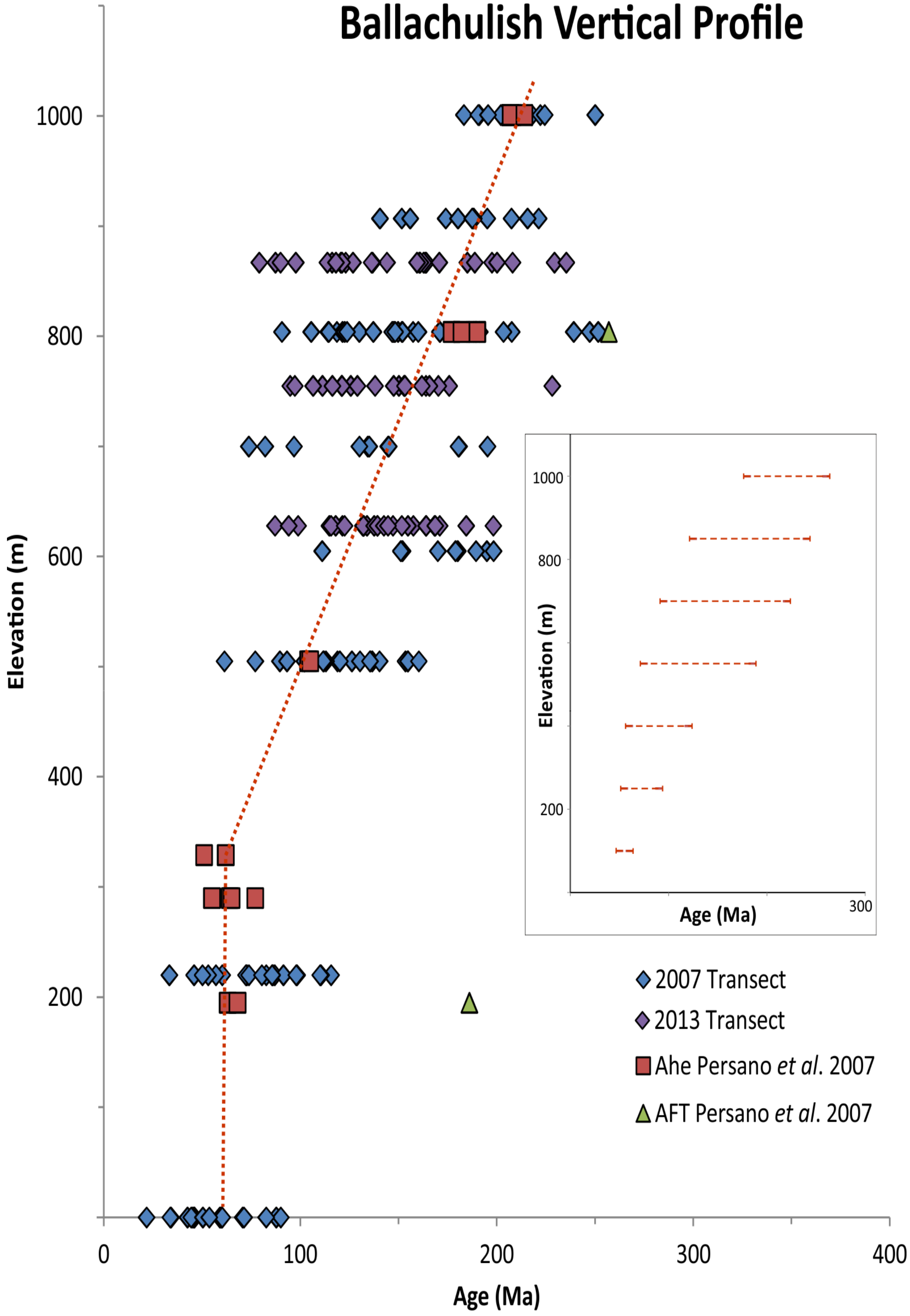

Figure 5.6: Age - Elevation plot 2.
Figure showing the age dispersion per sample as a function of elevation in the profile, as for plot 1, but with the highlighted anomalous ages omitted. Error bars are also omitted to reduce visual overcrowding. The 2007 transect (north) is shown in blue diamonds and 2013 transect (south) in purple diamonds. The published data of Persano *et al*. (2007) is shown in red squares (AHe multi-grain aliquots) and green triangles (AFT). Red dashed line shows the age-elevation trend for the AHe data of Persano *et al*. (2007). Inset – predicted age dispersion as a function of elevation based on the thermal history of Persano *et al*. (2007) (Ph.D. proposal).

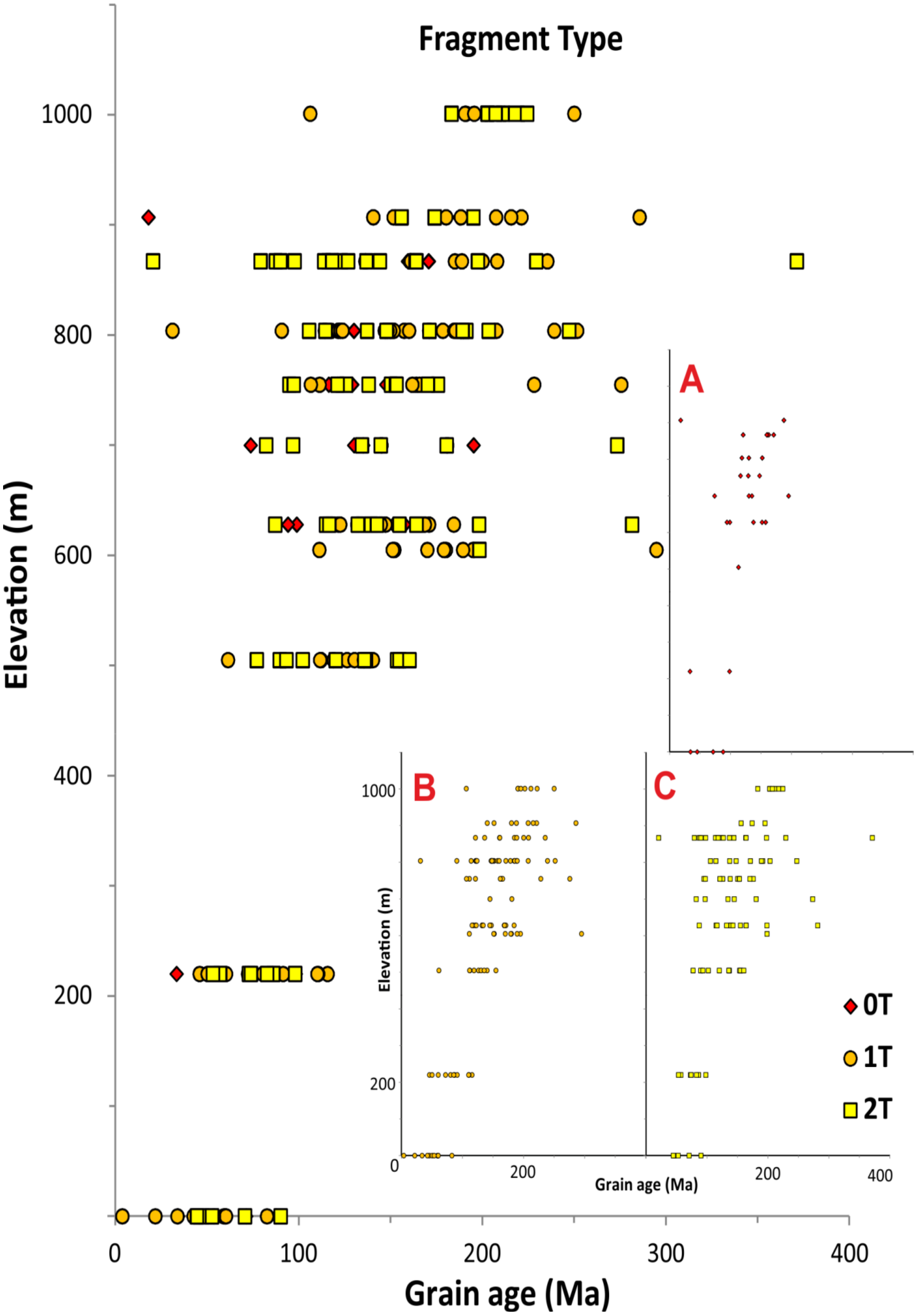

Figure 5.7: Age - Elevation plot 3.

Figure showing the age dispersion per sample as a function of elevation and fragment type. Red diamonds = 0T fragments, orange circles = 1T fragments and yellow squares = 2T whole crystals. Inset – **A**: only 0T fragments. **B**: only 1T fragments. **C**: only 2T whole crystals. In this instance, whole crystals (2T) show just as much age dispersion as 1T fragments. Fewer 0T crystals are routinely picked because the HelFRAG/QFrag programs currently only model 1T fragments, so 0T fragments can't be used for thermal history modelling. Therefore less dispersion is seen within the 0T fragments.

Table 5-4: Age Dispersion vs. Elevation.
Mean age = arithmetic mean. It is displayed here as it is used to calculate the age dispersion, but is not considered a meaningful value in terms of thermal history interpretation. Disp. = single grain age dispersion and is calculated as the range (max age – min age)/mean age (Brown *et al.*, 2013). * = values calculated with the highlighted anomalous ages from table **5.2** and figure **5.5** excluded.

Sample	Alt. (m)	Mean age (Ma)	Age Range (Ma)	Disp. %	Mean age*	Age Range*	Disp. %*
SD07 – 1	1001	201.2	143.9	**71.5**	208.0	66.8	**32.1**
SD07 – 2	907	178.5	267.6	**149.9**	183.4	69.7	**38.0**
SD13 – 02	867	153.2	350.8	**229.0**	150.2	156.3	**104.0**
SD07 – 3	804	157.9	220.5	**139.7**	161.7	161.0	**99.5**
SD13 – 03	755	147.9	180.8	**122.3**	141.5	131.0	**92.6**
SD07 – 4	700	147.6	199.7	**135.3**	136.2	113.1	**83.1**
SD13 – 04	628	144.4	194.5	**134.7**	139.7	111.1	**79.6**
SD07 – 5	605	182.1	183.7	**100.9**	169.5	87.2	**51.4**
SD07 – 6	505	121.3	98.9	**81.5**	N/A	N/A	**81.5**
BH15 – 05	220	78.2	82.3	**105.2**	N/A	N/A	**105.2**
BH13 – 02/ SD13 – 06	0	53.4	86.2	**161.5**	55.8	68.3	**122.4**

The new data does not show this break of slope, indicating that the observed break of slope in figure **5.6** is an artefact of only analysing a few grains per sample (in multi-grain aliquots). This suggests a different thermal history to the published history of Persano *et al.* (2007) for the BIC. Also multi grain aliquots effectively give a mean age for several crystals, whereas the new data is for single grain aliquots and these are not represented by a mean age. Trying to infer a break of slope for heavily dispersed single grain data is problematic, and there may not be any geological justification for doing so. Fitzgerald *et al.* (2006) discuss the issues with attempting to use heavily dispersed AHe data to interpret a fossil PRZ, with both the weighted mean and minimum AHe age used to try to represent the data (with their preferred solution lying somewhere between the two ages). The arithmetic mean was not considered useful.

5.3.1.1 Effect of broken grains: To highlight the effect of broken grains/fragments on the extent of dispersion, figure **5.7** shows the age-elevation plot with the data plotted as 0T, 1T and 2T crystals respectively. It can be seen that there is no significant difference in the amount of age dispersion between broken grains (0T and 1T) and whole grains (2T) despite the evidence from Brown *et al.* (2013) that fragmentation significantly increases age dispersion. This is because each fragment has originated from a different initial whole grain, and may have dispersed in either the older or younger direction depending on the type of fragment. Therefore the fragments are just as likely to have dispersed 'inwards' towards the median age of the sample as away from it. Figure **5.7** highlights that even if only whole grains are analysed (as is routine in some labs), the amount of natural age dispersion can still be significant, so it is still imperative to analyse a large number of grains per sample and model them as individual crystals. Picking only whole grains is not a solution for eliminating 'over dispersion'.

5.3.2 *Age vs. Grain size/eU plots*

Dispersion has been shown to sometimes correlate with either grain size (e.g. Farley, 2000; Reiners and Farley, 2001) or eU concentration (e.g. Flowers *et al.*, 2007; Flowers, 2009; Kohn *et al.*, 2009), but more often than not there is no strong correlation. This is because the three main causes of inherent natural dispersion (plus potential other factors such as composition) act simultaneously on the age, decoupling any apparent correlations between an individual factor and age (Brown *et al.*, 2013). However it is still worthwhile to generate such plots, as along with age histograms and (U-Th)/He isochron plots, they provide a detailed diagnostic of the causes of dispersion within each sample.

(U-Th)/He isochron plots have been used as a method of calculating the 'average' age of a sample as an alternative to the arithmetic mean (Vermeesch, 2008). This purpose is not explored here as for reasons already discussed in previous chapters, 'averaging' single grain ages is not considered helpful. An additional use of the plots is to highlight crystals which have inherited parentless ^{4}He. On a plot of ^{4}He concentration vs. ^{4}He production rate (P), all the data should plot on a simple linear regression that passes through the origin (P=^{4}He=0). If grains have inherited 'parentless' ^{4}He (through implantation or α-emitting inclusions) then they will plot above the 1:1 line (Vermeesch, 2008). Likewise if grains have apparently 'lost' ^{4}He then they will plot below the 1:1 line. Samples dominated by inclusions and/or implantation won't fit a single isochron; likewise samples with mixed provenance (e.g. sedimentary samples) may not fit a single isochron. For calculating the isochron age, the plots should ideally be made using elemental abundances (in moles) to remove some of the bias towards high eU grains (Vermeesch, 2008), however as this is not the purpose here, generating the plots in terms of number of atoms is sufficient for identifying samples which don't fit along the (U-Th)/He isochron.

Plotting the sample ages as a simple histogram can provide some indication of the thermal history in a way akin to fission track TLD plots. This is less reliable than for TLD, but can provide some insight, particularly if a sufficiently large sample size has been analysed. Rapidly cooled samples will have a narrower histogram (i.e. lower dispersion) than more slowly cooled samples. Bi-modal/multi-modal distributions can indicate different provenance for different grains if the source is a sedimentary rock, which in itself implies reburial. This is not applicable in this study as all samples are igneous in origin, although bi-modal distributions may still indicate shallow reburial. Broad and shallow histograms can indicate a more complex thermal history than a histogram with a well-defined central peak.

SD07 – 1: The top sample in the profile shows the least dispersion (71.5% [32.1%]) (table **5.4**). This may be partly an artefact of having fewer grains than some of the lower samples in the profile (15), or it may be as a result of its thermal history. With the exception of the already highlighted anomalous crystal, it shows a fairly strong positive correlation between grain size and age (figure **5.8 A**). Ages have experienced little deviation from the expected positive trend on account of the fragment effect, with the 1T fragments aligning just as well as the 2T whole grains. There is little or no correlation between eU and age (figure **5.8 B**). This is to be expected when there is already a correlation with grain size, which dominates the dispersion. Again the highlighted anomalous age clearly stands out on the age-eU plot.

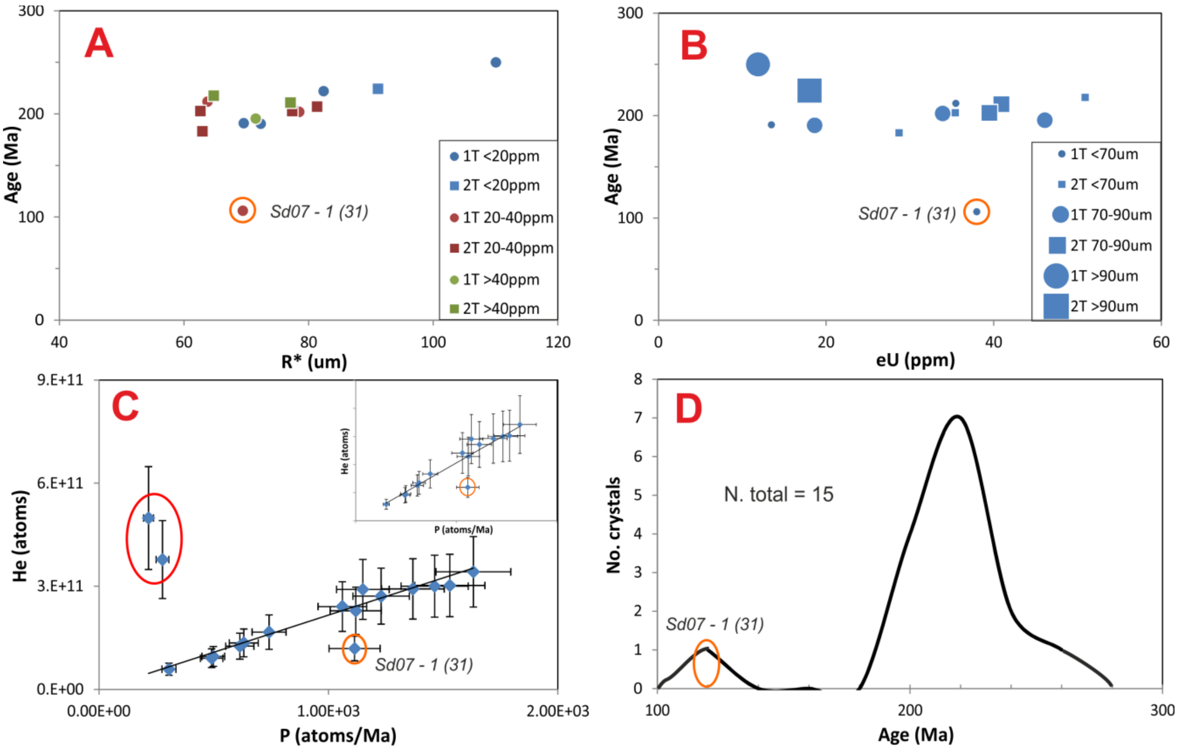

Figure 5.8: *SD07 – 1* age dispersion multi-variant plots.
A: grain age-R* (equivalent spherical radius) multi-variant plot. Circles = 1T fragments, squares = 2T whole crystals. Blue symbols = low (relative) eU, red symbols = medium eU and green symbols = high eU. **B**: grain age-eU multi-variant plot. Symbols as for **A**. Symbol size corresponds with (relative) grain size. **C**: (U-Th)/He isochron plot including the two likely zircons discussed in section 5.2.1 (highlighted red). Vertical error bars of 30% are shown to account for α-ejection related scatter (Vermeesch, 2008), horizontal error bars of a

nominal 10% are included to account for analytical uncertainty. $R^2 = -0.416$. Inset: (U-Th)/He isochron plot excluding the two zircons. $R^2 = 0.8667$. **D**: crystal age histogram with age bins of 20Myrs. Crystal *SD07 – 1 (31)* is highlighted on each plot.

The sample defines a strong (U-Th)/He isochron (figure **5.8 C**), with the two likely zircons discussed in section 5.2.1 clearly standing out as having 'parentless' ^{4}He (circled red). Including these two crystals gives a negative R^2 value for the linear regression, but when they are excluded the R^2 value is over 80%. Crystal *SD07 – 1 (31)* also stands out from the isochron as having less ^{4}He than expected, for reasons discussed in section 5.2.2. The R^2 value would be even higher if this crystal was also omitted. The age histogram (figure **5.8 D**) has a narrow peak and is slightly positively skewed, with the exception of Crystal *SD07 – 1 (31)*. This could indicate a rapidly cooled thermal history, though it may be down to the relatively small sample size.

SD07 – 2: The second highest sample in the profile has significant age dispersion (149.9%) but this is largely down to two major outliers at the extremes of the age range (figure **5.5**). With these excluded, the dispersion is similarly low to the top sample (38%) (table **5.4**). The two highlighted outliers clearly stand out on plots **A**, **B** and **C** in figure **5.9**. Excluding the outliers, there is a weak and shallow positive correlation between grain size and age, but this is almost flat so may not be a correlation at all, and rather just low dispersion. The largest grains in the sample have the lowest eU and vice versa, meaning each component largely cancels the other out.

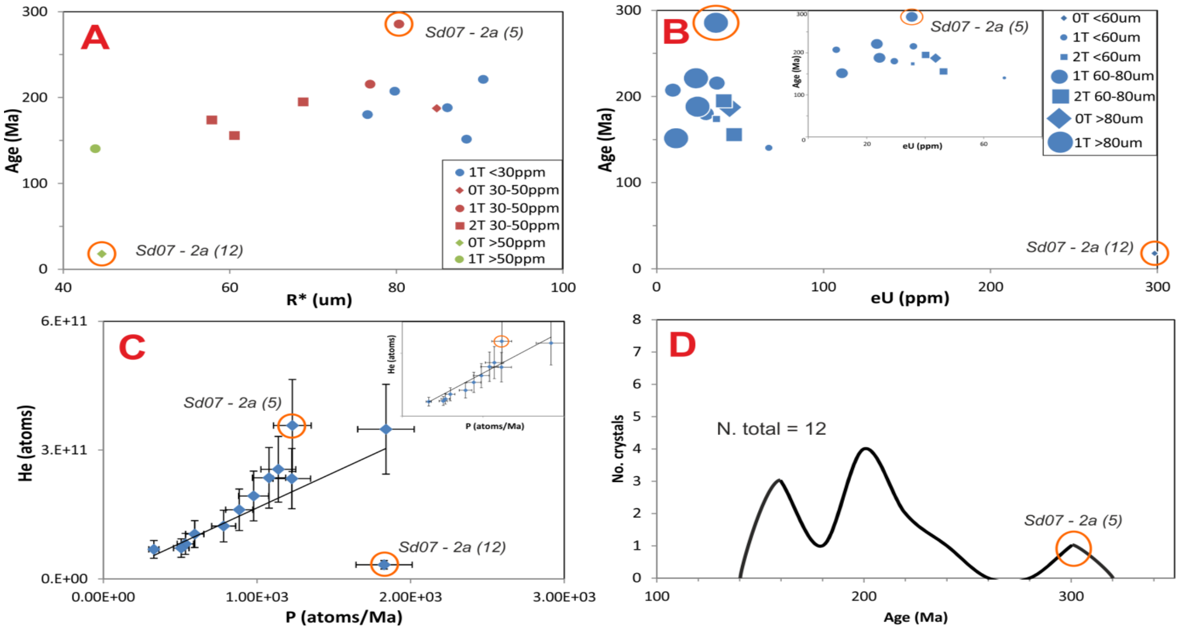

Figure 5.9: *SD07 – 2* age dispersion multi-variant plots.
A: grain age-R* (equivalent spherical radius) multi-variant plot. Symbols as for figure **5.8**. **B**: grain age-eU multi-variant plot. Symbols as for **A**. Symbol size corresponds with (relative) grain size. Inset: same plot with

crystal *SD07 – 2a (12)* excluded to provide a more useful horizontal scale. **C**: (U-Th)/He isochron plot. Vertical error bars of 30%, horizontal error bars of a nominal 10%. R^2 = 0.2017. Inset: (U-Th)/He isochron plot excluding crystal *SD07 – 2a (12)* which dominates the linear regression. R^2 = 0.8527. **D**: crystal age histogram with age bins of 20Myrs. Crystals *SD07 – 2a (5)* and crystal *SD07 – 2a (12)* are highlighted orange on each plot.

With the exception of the two highlighted crystals the sample defines a strong (U-Th)/He isochron (plot **C**), with an R^2 value of over 80% when crystal *SD07 – 2a (12)* is omitted. Crystal *(5)* has inherited some parentless ^{4}He, giving the old age, whereas crystal *(12)* has significantly less ^{4}He than it should, on account of the very high eU (c.300ppm) leading to interconnected radiation damage. The sample has a multi-modal age histogram (plot **D**), but this is largely down to the small sample size (12 crystals) leading to no discernible pattern.

SD13 – 02: This sample has the highest age dispersion in the profile when including two outlying ages (229%). Even when these are excluded the dispersion is one of the highest in the profile (104%) (table **5.4**). There is no apparent correlation with age and either grain size and/or eU (figure **5.10**), but there is a number of either very large and/or very high eU grains compared to other samples, and this contributes to the high dispersion. There is a slight inverse correlation between size and eU, with the largest grains (mostly) having low eU (and vice versa) and this leads to the two variables offsetting each other, masking any potential trend with age. Crystal *SD13 – 02 (D21)* clearly stands out as anomalous, as despite being the largest and highest eU grain, it is significantly younger. This is also seen on the inset isochron plot, where it can be seen to have significantly less ^{4}He than it should on account of interconnected radiation damage. Crystal *SD13 – 02 (D20)* is one of the largest in the sample but has relatively low eU.

The sample as a whole forms a less well defined (U-Th)/He isochron than other samples, even with Crystal *SD13 – 02 (D21)* excluded the R^2 value is only c. 50% (figure **5.10 C**). Crystal *SD13 – 02 (D20)* stands out above the isochron, and this has inherited noticeable amounts of parentless ^{4}He, but there are a number of other crystals which don't fit the isochron but still have acceptable ages. Two of these are circled green to demonstrate the fact that they have typical grain sizes and eU despite not fitting the isochron. This sample shows that even when grains are screened as meticulously as for this project, and every effort is made to minimise the effects of the imposed extraneous causes of dispersion, they can still contribute noticeable 'noise' to the dispersion signal.

The sample appears to have a bi-modal age distribution (figure **5.10 D**), but this is largely an artefact of the arbitrary age bins. There is only one age bin between the peaks, so if the bins had been ascribed different sizes or age intervals then the twin peaks may disappear. As the sample is igneous, the bi-modal distribution doesn't suggest crystals from two different sources. Aside from being bi-modal, the histogram is almost symmetrical, and is close to a normal distribution.

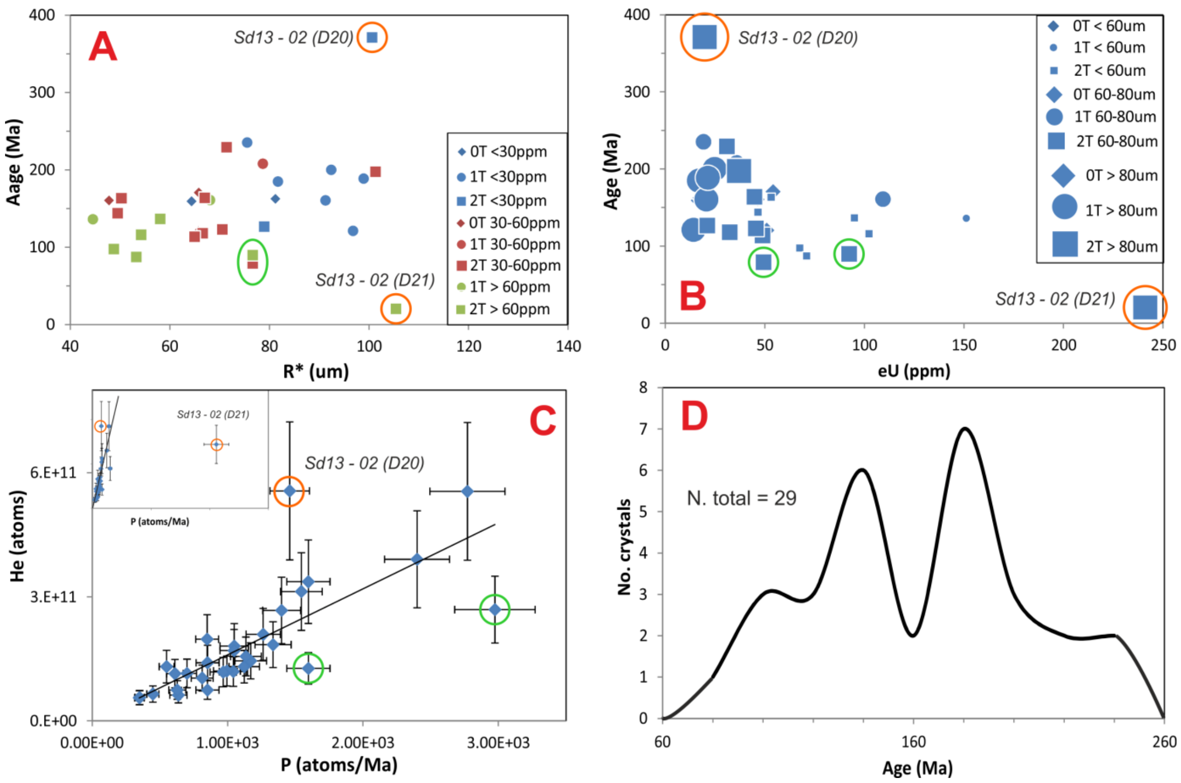

Figure 5.10: *SD13 – 02* age dispersion multi-variant plots.
A: grain age-R* (equivalent spherical radius) multi-variant plot. Symbols as for figure **5.8**. **B**: grain age-eU multi-variant plot. Symbols as for **A**. Symbol size corresponds with (relative) grain size. **C**: (U-Th)/He isochron plot excluding crystal *SD13 – 02 (D21)* which dominates the linear regression. Vertical error bars of 30%, horizontal error bars of a nominal 10%. R^2 = 0.5761. Inset: (U-Th)/He isochron plot including crystal *SD13 – 02 (D21)*. R^2 = -0.974 (not the trend line shown on plot which is manually drawn to match the larger plot). **D**: crystal age histogram with age bins of 20Myrs. Crystals *SD13 – 02 (D20)* and crystal *SD13 – 02 (D21)* are highlighted orange on each plot. Green circles: two additional outliers from the (U-Th)/He isochron which are not anomalous in terms of age or grainsize/eU.

SD07 – 3: This sample also has high dispersion (139.7% [99.5%]) (table **5.4**), as was predicted for samples of such elevation (c.800m). It has the most grains analysed of any sample in the profile (35) which may partially explain the high dispersion. As is common with such high dispersion, there is no correlation evident with age and either grain size and/or eU (figure **5.11**). Instead there is the common 'shot gun' scatter of ages as each component of dispersion works to decouple any correlation caused by another. The discussed outlier from this sample (crystal *SD07 – 3a (11)*) is highlighted in each plot, but it has a fairly typical size and eU concentration, and is only slightly more of an outlier on the isochron plot than a number of other crystals in the sample.

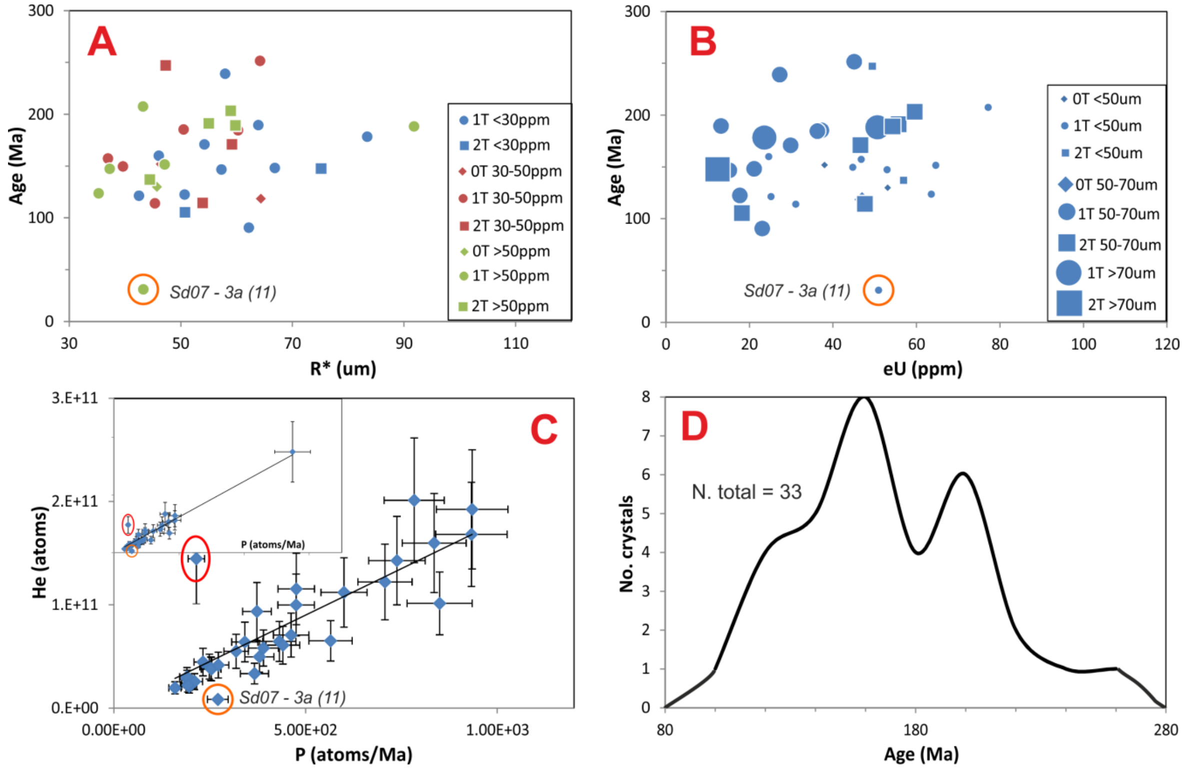

Figure 5.11: *SD07 – 3* age dispersion multi-variant plots.
A: grain age-R* (equivalent spherical radius) multi-variant plot. Symbols as for figure **5.8**. **B**: grain age-eU multi-variant plot. Symbols as for **A**. Symbol size corresponds with (relative) grain size. **C**: (U-Th)/He isochron plot with shortened scale (excluding the crystal on the extreme top right of the plot) to zoom in on the majority of the crystals. Vertical error bars of 30%, horizontal error bars of a nominal 10%. R^2 = 0.7203. Inset: (U-Th)/He isochron plot including the crystal in the extreme top right. R^2 = 0.9078. **D**: crystal age histogram with age bins of 20Myrs. Crystal *SD07 – 3a (11)* is highlighted orange on each plot. The omitted crystal with an age older than the age of intrusion is circled red on plot **C**.

The (U-Th)/He isochron is fairly noisy (R^2 value of c. 70%), implying that there is a noticeable contribution to dispersion from the imposed extraneous factors. The one omitted crystal which is older than the age of intrusion is circled red on the plot. This has clearly inherited 'parentless' ^{4}He which caused the very old age, and this is likely as a result of implantation. There are a number of other crystals which have potentially inherited some 'parentless' ^{4}He, but this is not enough to make them anomalous, and just contributes to the 'noise'. The highlighted outlying age (orange circle) has less ^{4}He than expected, but is not exceptionally high in eU concentration so this is not as a result of interconnected radiation damage. The most plausible explanation is an undetected pre-existing fracture in the crystal. The age histogram is positively skewed, and appears to be bi-modal, but as with sample *SD13 – 02* this is likely an artefact of the age bins and could be removed with a different selection of bin size/age.

SD13 – 03: This sample has similarly high dispersion to the above sample in the profile, as was predicted (122.3% [92.6%]). There is also no correlation with age and either grain size and/or eU, with plot **B** in particular showing a typical 'shot gun' scatter (figure **5.12**). The sample has quite a large range of grain sizes but (with the exception of 1 crystal) a relatively tight range in eU. It might therefore be expected that size would dominate the age dispersion, but this does not appear to be the case. The very high eU crystal doesn't appear to have reached the threshold value where radiation damage can become interconnected, causing an inverse relationship between eU and ^{4}He retentivity. This crystal is also the smallest crystal in the sample, so each component is offsetting the other in terms of dispersion, resulting in a 'normal' age for the crystal.

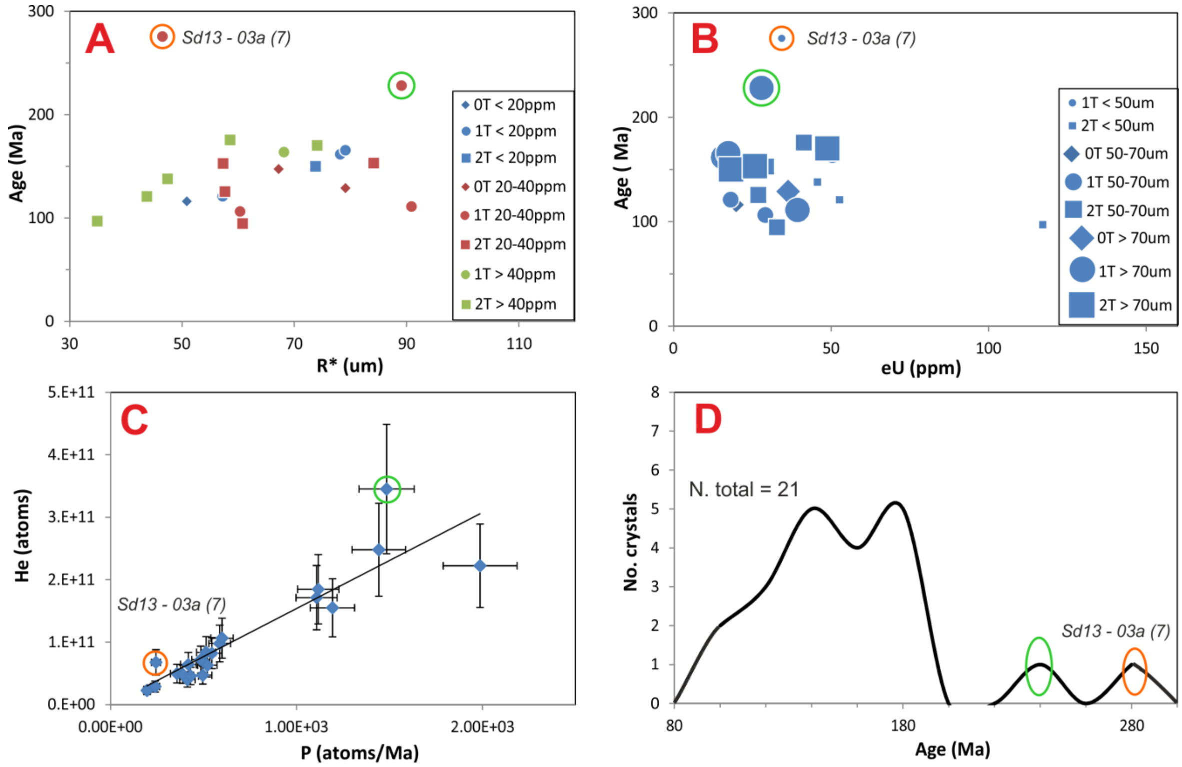

Figure 5.12: *SD13 – 03* age dispersion multi-variant plots.
A: grain age-R* (equivalent spherical radius) multi-variant plot. Symbols as for figure **5.8**. **B**: grain age-eU multi-variant plot. Symbols as for **A**. Symbol size corresponds with (relative) grain size. **C**: (U-Th)/He isochron plot. Vertical error bars of 30%, horizontal error bars of a nominal 10%. $R^2 = 0.818$. **D**: crystal age histogram with age bins of 20Myrs. Crystal *SD13 – 03 (7)* is highlighted orange on each plot. An additional crystal is circled green on each plot which wasn't considered an outlier but also appears to have inherited parentless ^{4}He.

The highlighted outlier (*SD13 – 03 (7)*) has gained some 'parentless' ^{4}He, giving the older age as can be seen in the isochron plot (**C**), but this is fairly marginal compared to some of the outliers from other samples. An additional crystal has been highlighted green which has also gained some 'parentless' ^{4}He, but wasn't considered a major outlier. This crystal does stand out from the rest of crystals in the sample, but it still falls within the expected age range as defined (qualitatively) by the neighbouring samples (see figure **5.5**). With these two crystals included the sample still has a fairly strong isochron ($R^2 > 80\%$). The age histogram (figure **5.12 D**) is negatively skewed (with the exception of the two highlighted older crystals) but has a broad, low peak.

SD07 – 4: This sample has dispersion of 135.3% (83.1% excluding the outlier) which is comparable to the surrounding samples. This is despite consisting of a much smaller number of grains (12). There is a reasonable positive correlation between age and grain size (figure **5.13 A**), and this is strong enough to account for the old age of crystal *SD07 – 4 (12)*, which is noticeably larger than the rest of the crystals in the sample. Size appears to dominate over eU meaning that there is little correlation between age and eU. There does appear to be a slight negative correlation (plot **B**), but the eU concentrations are too low to be causing connected radiation damage, so this is not a true correlation and rather down to the dominating effects of grain size on dispersion.

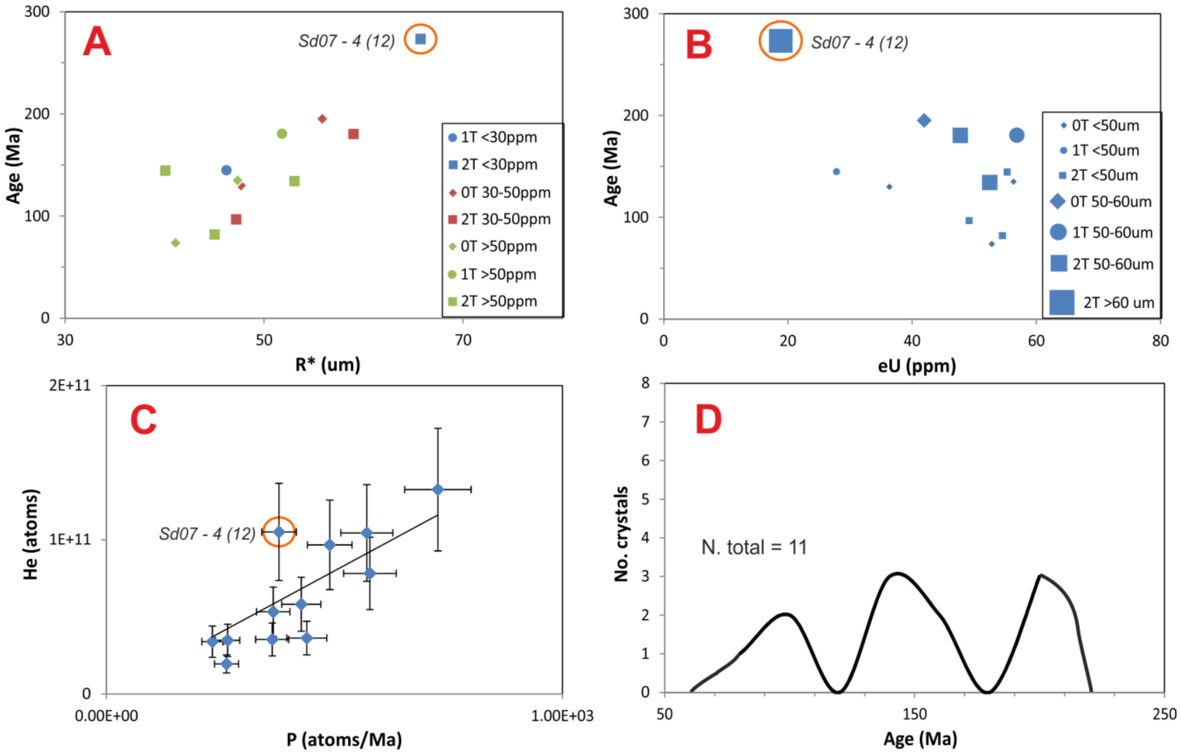

Figure 5.13: *SD07 – 4* age dispersion multi-variant plots.
A: grain age-R* (equivalent spherical radius) multi-variant plot. Symbols as for figure **5.8**. **B**: grain age-eU multi-variant plot. Symbols as for **A**. Symbol size corresponds with (relative) grain size. **C**: (U-Th)/He isochron plot. Vertical error bars of 30%, horizontal error bars of a nominal 10%. R^2 = 0.637. **D**: crystal age histogram with age bins of 20Myrs. Crystal *SD07 – 4 (12)* is highlighted orange on each plot.

The sample defines a reasonably strong (U-Th)/He isochron (plot **C**), but the small sample size leads to a lower R^2 value (c. 60%) than many of the other samples. The highlighted outlier (crystal *SD07 – 4 (12)*) stands out above the isochron, suggesting it has inherited some ^{4}He, but it is only a marginal outlier and its old age can be explained by the large grain size. The crystal might appear less of an outlier if more grains had been analysed in the sample. The sample has a multi-modal age histogram (plot **D**), but this is largely down to the small sample size so isn't indicative of any trends.

SD13 – 04: This sample has dispersion of 134.7% (79.6% excluding the outlier) and has the second highest number of grains analysed (30). There is little correlation with age and either grain size and/or eU, as is common of such large sample sizes. The largest grains tend to have low eU and vice versa so the two components largely offset each other (figure **5.14**). There is a hint of positive correlation with grain size, so of the two factors, size is slightly more dominant. The highlighted outlier (crystal *SD13 – 04 (D12)*) is one of the largest grains, which can partly explain the old age, but it also has one of the lowest eU concentrations in the sample, which should offset this. The sample shows a strong (U-Th)/He isochron ($R^2 >$ 80%) (plot **C**), with the exception of the highlighted outlier which has clearly inherited some 'parentless' ^{4}He, explaining the old age. The age histogram has a slight negative skew (plot **D**).

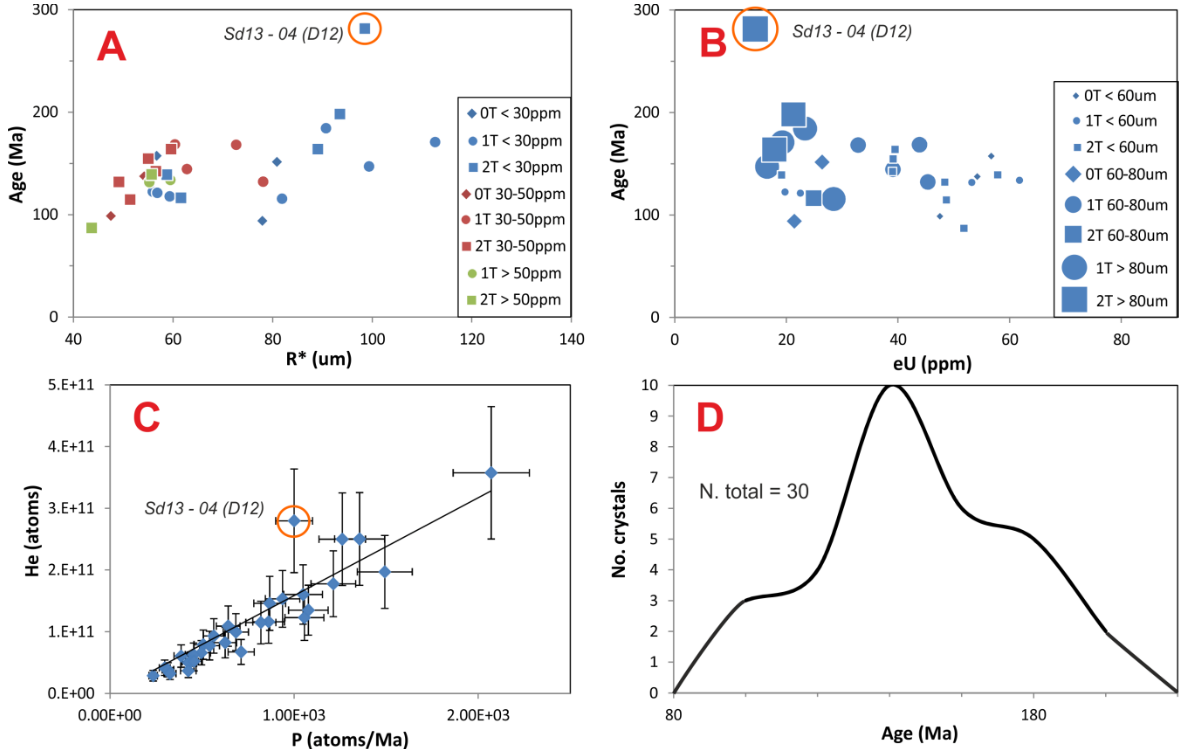

Figure 5.14: *SD13 – 04* age dispersion multi-variant plots.
A: grain age-R* (equivalent spherical radius) multi-variant plot. Symbols as for figure **5.8**. **B**: grain age-eU multi-variant plot. Symbols as for **A**. Symbol size corresponds with (relative) grain size. **C**: (U-Th)/He isochron plot. Vertical error bars of 30%, horizontal error bars of a nominal 10%. $R^2 = 0.8453$ **D**: crystal age histogram with age bins of 20Myrs. Crystal *SD13 – 04 (D12)* is highlighted orange on each plot.

SD07 – 5: This sample has slightly lower dispersion than the above samples in the profile (100.9%), particularly when the single outlier is excluded (51.4%). With the exclusion of the outlier it has the least dispersion in the profile, but this may be down to having the fewest grains analysed (10). There is no correlation with age and either grain size and/or eU (figure **5.15**), which is unusual for a sample with a small number of grains. Other samples of similarly small sizes in the profile (e.g. *SD07 – 1*) have shown a positive correlation between age and grain size. The anomalous grain (*SD07 – 5 (36)*) is neither exceptionally large or of high eU concentration, therefore parentless ^{4}He is the only explanation for the old age, and this is shown on the (U-Th)/He isochron (plot **C**). The plot has an R^2 value of c. 90% despite having very few grains. The age histogram is negatively skewed (plot **D**), but with so few grains analysed this does not give evidence for any particular pattern.

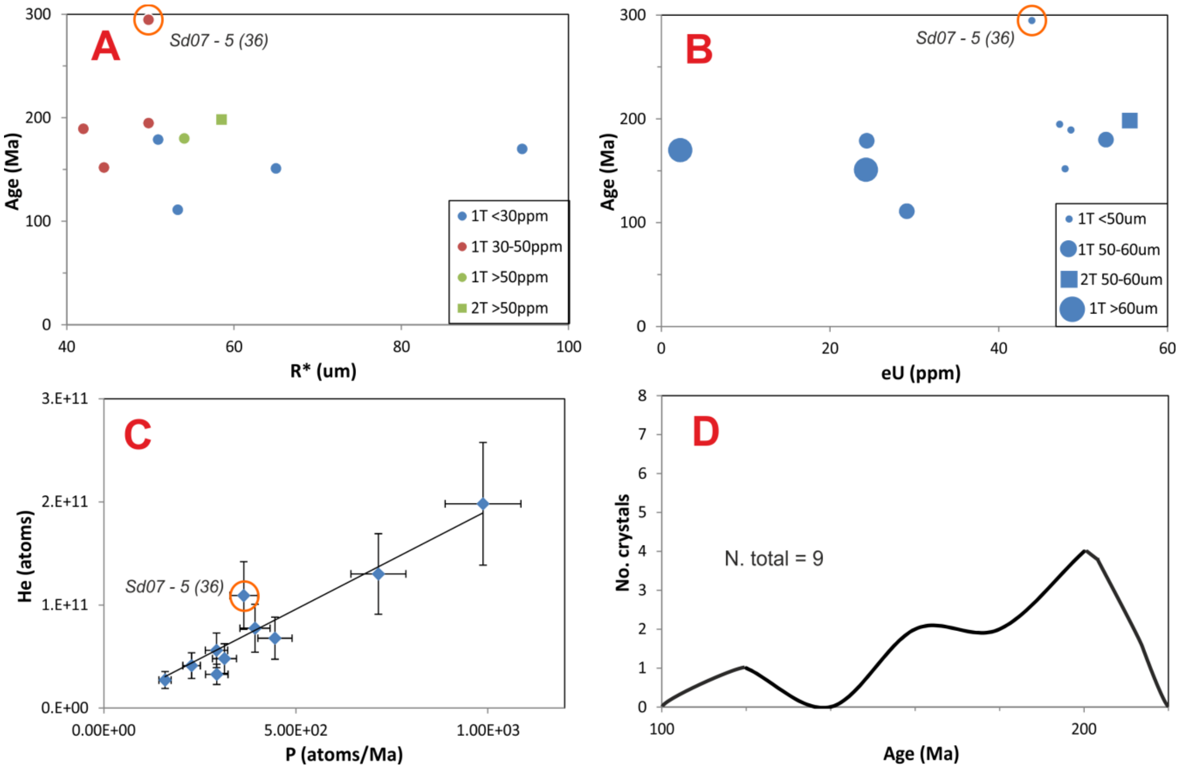

Figure 5.15: *SD07 – 5* age dispersion multi-variant plots.
A: grain age-R* (equivalent spherical radius) multi-variant plot. Symbols as for figure **5.8**. **B**: grain age-eU multi-variant plot. Symbols as for **A**. Symbol size corresponds with (relative) grain size. **C**: (U-Th)/He isochron plot. Vertical error bars of 30%, horizontal error bars of a nominal 10%. $R^2 = 0.8942$. **D**: crystal age histogram with age bins of 20Myrs. Crystal *SD07 – 5 (36)* is highlighted orange on each plot.

SD07 – 6: This sample has no outlying ages, and has dispersion of 81.5%. It has a moderate sample size of 20 grains, which likely explains the higher dispersion than the above sample in the profile. There is no apparent correlation between age and either grain size and/or eU concentration, with a 'shot gun' scatter present on both plots (figure **5.16 A** and **B**). The sample does have a very small range in eU concentration, with most crystals falling between 20-40ppm, whereas it has a much larger range in grain size, with a number of very large (R* > 100μm) crystals. Despite this, grain size does not appear to dominate the age dispersion trend, with the largest crystals being both young and old. The sample has a strong (U-Th)/He isochron ($R^2 > 90\%$) (plot **C**) and close to a normal age distribution (plot **D**).

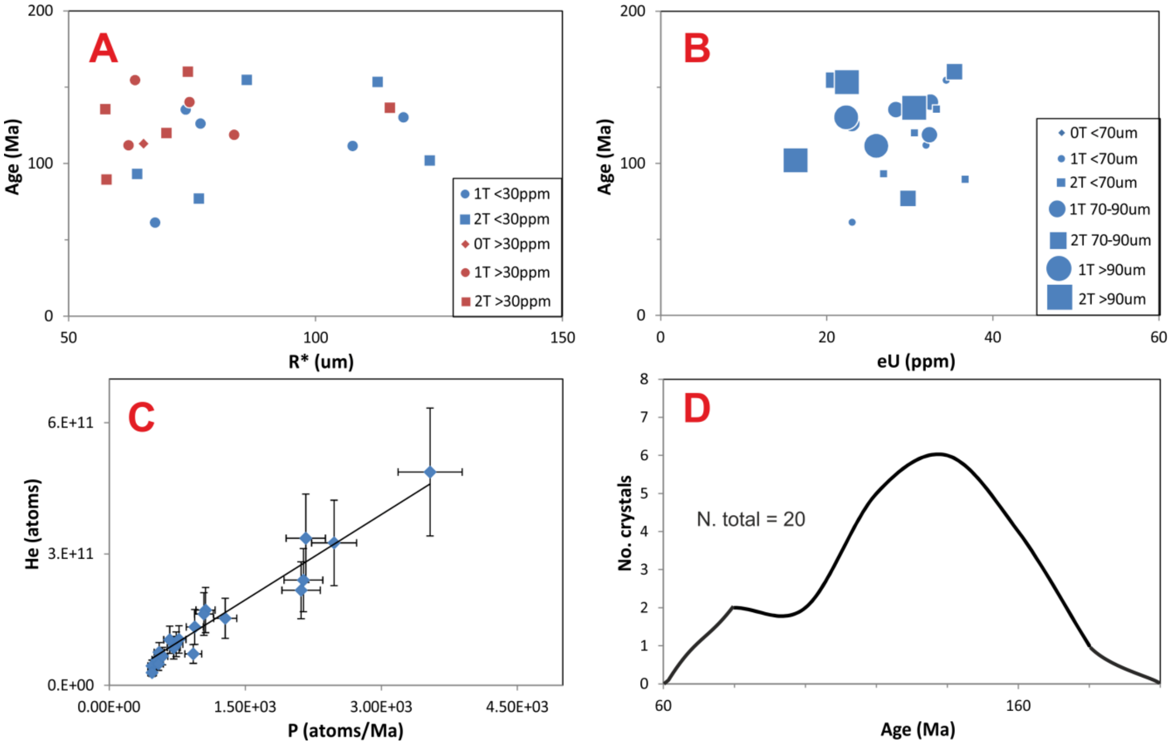

Figure 5.16: *SD07 – 6* age dispersion multi-variant plots.
A: grain age-R* (equivalent spherical radius) multi-variant plot. Symbols as for figure **5.8**. **B**: grain age-eU multi-variant plot. Symbols as for **A**. Symbol size corresponds with (relative) grain size. **C**: (U-Th)/He isochron plot. Vertical error bars of 30%, horizontal error bars of a nominal 10%. $R^2 = 0.9424$ **D**: crystal age histogram with age bins of 20Myrs.

BH15 – 05: This sample also has no outlying ages, and has dispersion of 105.2%. Despite this, it has two exceptionally high eU grains (figure **5.17 B**) which in contrast to the other very high eU grains found in other samples (e.g. *SD13 – 02 (D21)*), don't appear to have lost ^{4}He through interconnected radiation damage. One crystal in particular has an eU concentration of over 800ppm (circled green in figure **5.17**), which is by far the highest of any crystal in the profile. Based on the evidence from other high eU grains in the profile, it would be expected to have virtually no ^{4}He left, so in not having an anomalously young age, it is in itself an anomaly. The crystal is also very thin ($R < 30\mu m$) and would normally not be analysed by most labs due to the effects of α-ejection. It is therefore even more surprising that it doesn't have an erroneously young age.

The second very high eU crystal ($eU > 250ppm$) is also one of the smallest in the sample, but is not so thin that it wouldn't normally be analysed ($R > 30\mu m$) (circled blue). It has significantly lower eU than the crystal circled green, but is still above the rough threshold which would cause interconnected radiation damage (c. 150-200ppm based on the evidence from other samples in the profile). With or without these two crystals there is no apparent correlation between age and either grain size and/or eU concentration in this sample (plots

A and **B**). The sample has a strong (U-Th)/He isochron ($R^2 > 90\%$) (plot **C**) and the age histogram is negatively skewed (plot **D**).

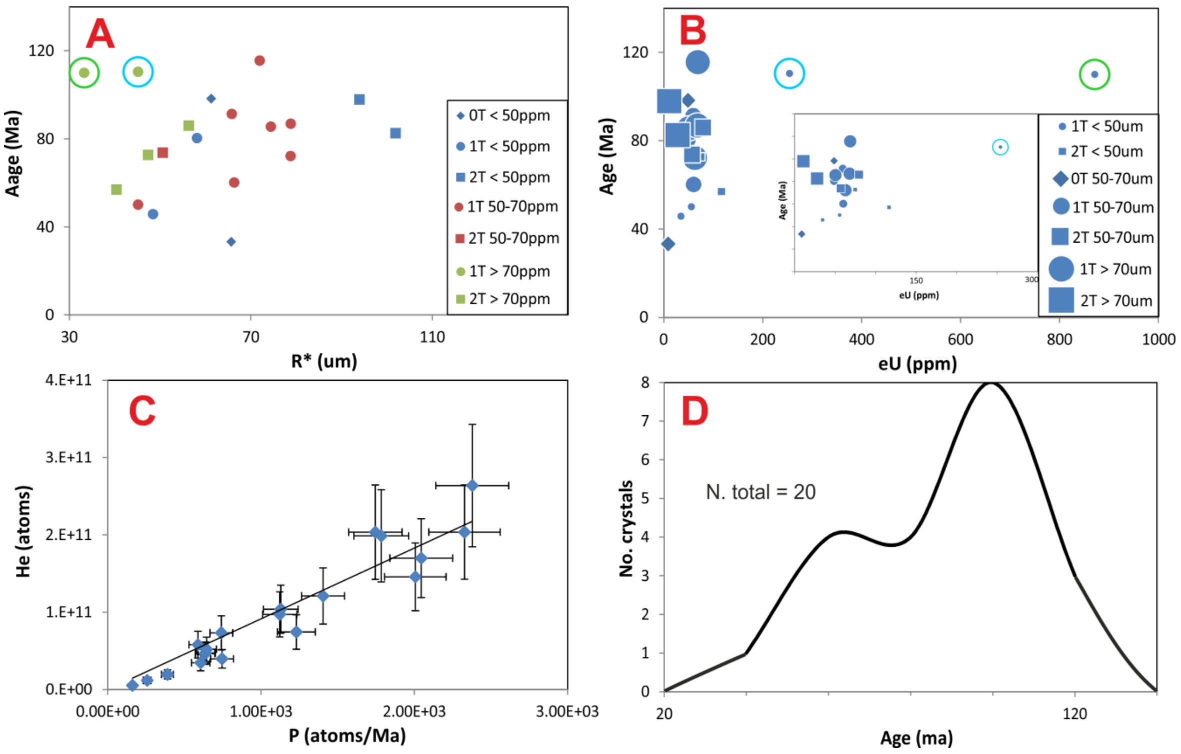

Figure 5.17: *BH15 - 05* age dispersion multi-variant plots.
A: grain age-R* (equivalent spherical radius) multi-variant plot. Symbols as for figure **5.8**. **B**: grain age-eU multi-variant plot. Symbols as for **A**. Symbol size corresponds with (relative) grain size. Inset: same plot with the very high eU grain omitted. **C**: (U-Th)/He isochron plot. Vertical error bars of 30%, horizontal error bars of a nominal 10%. $R^2 = 0.9002$ **D**: crystal age histogram with age bins of 20Myrs. Green circle > 800ppm grain. Blue circle > 300ppm grain.

BH13 – 02/SD13 – 06: These two samples are from sea level, giving the base of the vertical profile. They have been combined to increase the sample size to > 20 crystals as was the initial plan for every sample. It is expected that each sample has experienced the same thermal history, so baring minor compositional differences which may or may not play a part on dispersion; they should have a comparable range of ages. The combined samples have an age dispersion of 161.5%, and even when the highlighted outlier is excluded the dispersion is 122.4%. This is the highest in the profile (excluding outliers) which is contrary to the prediction that dispersion would decrease at the base of the profile. This may partially be down to compositional differences between the two samples affecting ^{4}He diffusivity, but there is no evidence of two distinct populations from the (U-Th)/He isochron plot (figure **5.18 C**).

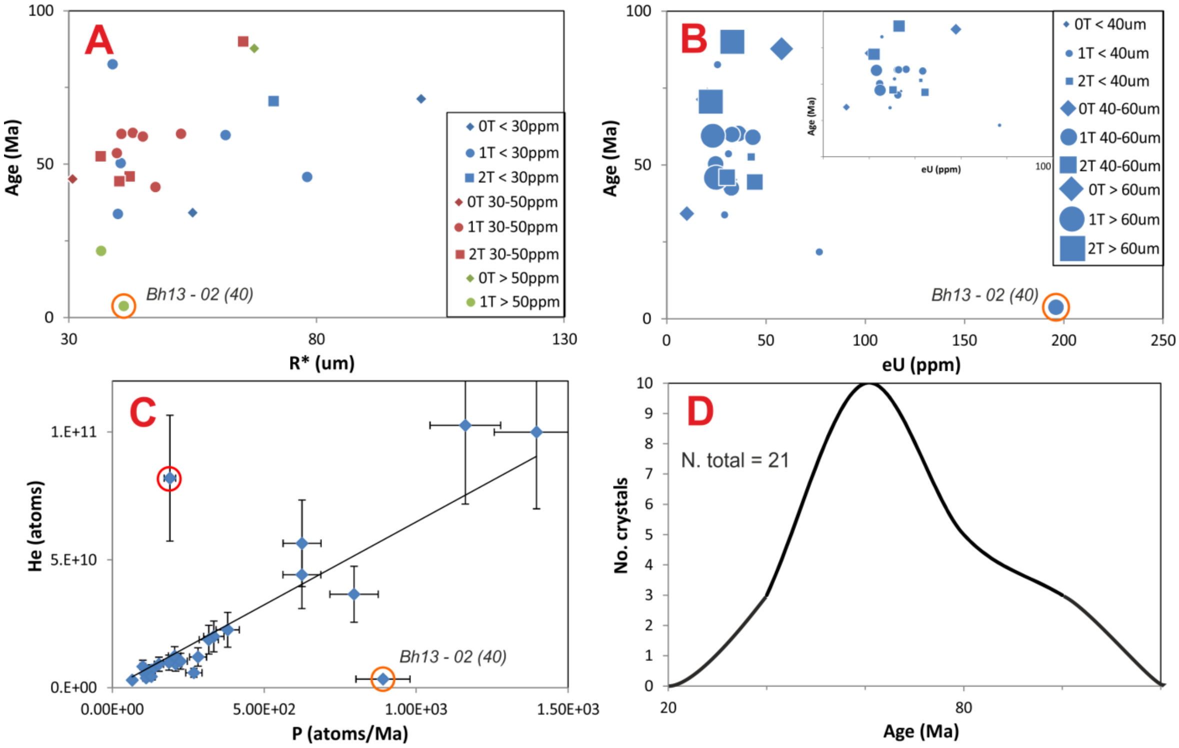

Figure 5.18: *BH13 – 02/SD13 - 06* age dispersion multi-variant plots.
A: grain age-R* (equivalent spherical radius) multi-variant plot. Symbols as for figure **5.8**. **B**: grain age-eU multi-variant plot. Symbols as for **A**. Symbol size corresponds with (relative) grain size. Inset: same plot with *BH13 – 02 (40)* omitted. **C**: (U-Th)/He isochron plot. Vertical error bars of 30%, horizontal error bars of a nominal 10%. R^2 = 0.55 **D**: crystal age histogram with age bins of 20Myrs. Crystal *BH13 – 02 (40)* is highlighted orange on each plot. The omitted crystal older (within error) than the intrusion age is circled red in plot **C**.

There is no correlation evident between age and either grain size and/or eU concentration (plots **A** and **B**). The highlighted outlier (crystal *BH13 – 02 (40)*) has the highest eU in the sample, and is small but comparable in size to a number of other crystals in the sample. The anomalously young age is clearly a consequence of the very high eU, leading to interconnected radiation damage, which reduces ^{4}He retentivity. This is in line with a number of the other anomalously young crystals from other samples in the profile and supports the recent findings of Gerin *et al.* (2017). The (U-Th)/He isochron plot also supports this as the crystal sits well below the isochron, meaning it has less ^{4}He than should be expected. The isochron plot also shows the crystal (circled red) which has been omitted from this sample (see section 5.2.1). This has inherited significant amounts of ‘parentless’ ^{4}He, leading to its erroneously old age (which is within error of the age of intrusion) (plot **C**). The isochron has a low R^2 value (c. 50%) when the two circled crystals are included, but without these the value is over 90% (0.9205). The sample has a positively skewed age histogram (plot **D**).

5.4 Discussion

Single grain age dispersion, from both inherent natural and imposed extraneous causes, is extensive in the BIC. Despite every effort being made to eliminate the imposed causes of dispersion, with a dataset of this size their impact is unavoidable. In some cases this has led to clear outliers which can be attributed to a specific factor with a degree of confidence (e.g. implantation leading to the old age of crystal *SD13 – 02 (D20)*). In many cases however, it just ads 'noise' to the more predictable inherent natural dispersion signal.

When a large number of grains are analysed per sample, it becomes increasingly unlikely that any strong correlation will be seen between age and either grain size and/or eU concentration. This is because all three factors of inherent natural dispersion (plus the unknown effects of compositional variation and the additional noise from the imposed extraneous factors) are acting simultaneously, and thus decouple any one correlation (Brown *et al.*, 2013). Where there is a hint of correlation in the BIC, it is grain size that dominates over eU concentration, and this is arguably only apparent for sample sizes smaller than c. 15 grains. More commonly the two factors offset each other, with large grains having low eU concentrations and vice versa (which is purely by chance and not causation). Total dispersion increases with increasing sample size, but it is not clear if the full range of possible dispersion has been reached, even by samples with more than 30 grains.

5.4.1 *Radiation damage effects*

One notable and perhaps unexpected trend in the data is that a number of grains with very high eU concentrations have very young ages (e.g. *BH13 – 02 (40)*). Accumulated radiation damage acts as traps for ^{4}He, inhibiting diffusion (see **Chapter 2**, section *2.2.1.2*). Grains with higher eU will accumulate more radiation damage for a given thermal history and would be expected to have older ages (e.g. Shuster *et al.*, 2006; Flowers *et al.*, 2009, Gautheron *et al.*, 2009), however this is not the case in some of these grains. Zircon typically has much higher eU concentrations than apatite (several hundred ppm) and therefore a much higher concentration of accumulated radiation damage. For eU concentrations of this magnitude, the radiation damage becomes interconnected; increasing ^{4}He diffusivity as eU concentration increases (Guenthner *et al.*, 2013). Gerin *et al.* (2017) provide the first diffusion model for apatite which takes account of this for very high eU grains, and Recanati *et al.* (2017) provide further empirical evidence for its validity.

The data presented here provides further evidence in support of the diffusion model of Gerin *et al.* (2017). The eU concentration threshold where ^{4}He diffusivity changes from decreasing as eU increases (negative relationship) to increasing as eU increases (positive relationship) appears to occur at c. 150-200ppm for the BIC. The exact value will vary with thermal history (as well as other factors such as composition and zonation) because the amount of accumulated radiation damage will increase over time, but this is offset by the rate of annealing which is temperature dependant. Consequently it is more helpful as a universal figure to consider the threshold in terms of 'damage density' (i.e. track density) as that figure will be reached at different eU concentrations for different thermal histories. However this parameter is difficult to establish on a grain which will undergo the routine AHe procedure, so it is problematic to empirically test for the true figure.

The evidence from the BIC isn't unequivocal. One sample significantly differs from the above observation – *BH15 – 05*. This sample has a crystal with by far the highest eU concentration of any in the profile (871ppm), and a second above the apparent threshold (254ppm). Despite this, each crystal has a 'normal' age and the ^{4}He diffusivity matches that of the rest of the sample, as shown by the (U-Th)/He isochron plot. This is difficult to explain, as if no switch from a negative to a positive relationship between radiation damage and ^{4}He diffusivity is assumed, then each crystal should be significantly older than the rest in the sample. As it stands the ages are in line with the rest of the sample. Another factor (such as composition) must also be contributing to these 'abnormally normal' ages. The diffusion kinetics in apatite is still an important area of research within the community, particularly for grains with very high eU abundances. Advancements in the radiation damage models used for thermal history modelling will greatly improve the robustness of thermal history reconstructions; however this is beyond the scope of this thesis.

5.4.2 *Parentless ^{4}He*

Despite every effort being made to eliminate the imposed extraneous causes of dispersion, a number of crystals have still clearly inherited 'parentless' ^{4}He. Due to the meticulous screening process (and the points highlighted by Vermeesch *et al.* (2007)), it is highly unlikely that the source of the parentless ^{4}He is mineral/fluid inclusions (with perhaps one exception already discussed). Implantation, either from 'bad neighbour/s' or grain boundary phases is the most likely cause.

There is no evidence of GBP's on any of the analysed crystals, as this is also avoided during screening. However Murray *et al.* (2014) show that GBP's may have disappeared by the time of analysis and still implanted significant parentless ^{4}He into a crystal. This can pose a significant problem as it is impossible to detect, but is most likely to affect sedimentary (and perhaps metamorphic) crystals which can experience physical changes during their history. All grains analysed here are igneous in origin, and although hydrothermal alteration is possible, this would most likely have occurred very early in the crystals history when the host rock is still hot, so any implanted ^{4}He won't have begun to accumulate.

'Bad neighbours' are far more plausible. Gautheron *et al.* (2012) argued that the chances of any given apatite crystal being surrounded by multiple 'bad neighbours', and then being selected for analysis is incredibly small. For a routine low temperature thermal history investigation where typically 3-6 grains are analysed from 5-10 samples, the chances of picking grains that have experienced significant implantation may be considered impossibly small (c.2-3% of 25 grains is less than 1 grain). Given that well over 200 individual crystals have been analysed during this project, and only 5-8 appear to have been implanted by significant amounts of ^{4}He, c. 2-3% of crystals is not an unexpected or problematic number.

5.4.3 *Additional 'noise'*

Aside from the highlighted outliers, there is additional 'noise' which adds to the age dispersion. This can be seen in a number of the (U-Th)/He isochron plots, which have crystals which lie off of the isochron beyond the accepted error, but don't stand out as significant outliers. There are a number of causes which can contribute to this noise, on top of the dispersion caused by the inherent components of the system.

5.4.3.1 Composition: The composition of apatite (variation between F^-, Cl^- and OH^- rich end members) is likely to have an effect on both the annealing rate of radiation damage (It is known to affect fission track annealing (e.g. Green *et al.*, 1986; Laslett *et al.*, 1987)) and the diffusive properties of undamaged crystals. This can therefore be expected to contribute to age dispersion. There has been some research towards quantifying this effect (e.g. Djimbi *et al.*, 2015) but as of yet it is not fully understood. It is also not routine (or practical) to measure the composition of apatite's which are to be analysed for AHe, meaning that a major change would likely be needed in the methodology to fully incorporate compositional variation into the diffusion models used for thermal history reconstructions. Unknown compositional variation could be the cause/a contributing factor to the outlying ages discussed in section 5.2.2 which have no other clear explanation.

5.4.3.2 Zonation: Another factor which is known to have an impact on AHe age dispersion is parent isotope zonation. This can cause ages to be either older or younger than expected depending on if zoned crystals are rim rich or core rich in parent isotopes. As both outcomes are possible within the same sample, this can 'average' out the effects, making it almost impossible to detect. It has been shown to cause dispersion greater than 15% on only the very extreme end member cases (Ault and Flowers, 2012; Gautheron *et al.*, 2012), and these extremes may not even be realistic in nature. In the majority of realistic zonation scenarios, the effect on dispersion is negligible. Majorly outlying ages are therefore highly unlikely to be as a consequence of zonation, but zonation can contribute noise to the dispersion signal, as seen on the (U-Th)/He isochron plots. The corresponding fission track mount for each sample has been examined for zonation, and no significant zonation was found. This does not exclude the possibility of small zonation factors contributing a few percent to the overall age dispersion.

5.4.3.3 Implantation: 'Parentless' ^{4}He has been shown to be the most likely contributor to a very small number of anomalously old ages. Far more likely is that a greater number of grains have inherited a much smaller amount of parentless ^{4}He, which is largely negligible, but ads noise to the (U-Th)/He isochron plots. Implantation may have occurred from a single 'bad neighbour', which isn't significant enough to cause a major outlier, but can add a few percent to the age dispersion. Equally, smaller amounts of ^{4}He may have been implanted from nearby apatite's (which are more likely to be found in close proximity to each other in a host rock) of slightly higher eU concentration. The effects of this would be negligible (i.e. less than the analytical uncertainty) but could still contribute a few percent to age dispersion. Ultimately many of the imposed extraneous factors on dispersion, which are considered negligible on their own, may combine to contribute a small but not insignificant percentage of noise to the overall dispersion signal.

5.4.4 *Fragment effect*

It is difficult to put a finger on the contribution of broken grains to age dispersion explicitly by looking at the raw data. It is easy to quantify when dealing with synthetic data, as the length of the original whole grain (and therefore the type of fragment, I or II) is known (Brown *et al.*, 2013). With real data this is an unknown. Figure **5.7** shows that there is no major difference in the percentage of dispersion when only fragments are considered compared to when only whole crystals are considered. Grain size and eU variation alone produce significant dispersion, and although fragmentation ads to this, as a grain can become both older and younger when it is broken (relative to the original whole grain) this may not increase the overall percentage of dispersion. Fragment ages can become dispersed 'inwards' towards the median as well as away from it.

This doesn't validate treating fragments as whole grains when it comes to thermal history reconstructions. The overall dispersion may not have increased, but an individual crystal fragment may have a drastically different age to its original whole crystal. As 2T dispersion alone can be well in excess of 100% (see table **5.4**), a single grain fragment may have an almost 100% error on its true whole grain age without appearing to increase the samples overall age dispersion. For example, a sample with a 'mean' age of 150Ma and dispersion of 100% will have ages ranging from c. 80Ma – 220Ma. An initial whole crystal with an age of 100Ma which becomes fragmented could produce a fragment with an age of 200Ma (100% error), which hasn't increased the samples overall age dispersion.

2T crystals are no more or less likely to show a correlation between age and either grain size and/or eU concentration than fragments. The scatter seen on the plots in figures **5.8** – **5.18** is similar for fragments and whole crystals. Again, it is possible to demonstrate the effect of fragmentation on these plots with synthetic data (Brown *et al.*, 2013) as the initial whole crystal is known (see figure **2.8**). With real data this is not the case, so it is impossible to show that fragmentation has pulled a particular crystal in *x* or *y* direction on the age vs. R* and age vs. eU plots. This does not mean that fragmentation hasn't contributed to the overall dispersion, nor does it mean that the effects of fragmentation on dispersion are unknown and unquantifiable (and therefore problematic). The effects of fragmentation on dispersion are quantifiable (Brown *et al.*, 2013; Beucher *et al.*, 2013) but are difficult to represent graphically with a real data set.

5.5 Conclusion

When multiple single grain aliquots per sample are analysed for (U-Th)/He, the age dispersion within each sample is significant. For sample sizes of c. 20 grains, total dispersion of well over 100% can be expected, and dispersion in excess of 200% is possible. This dispersion is the combination of both natural (i.e. 'good') and imposed (i.e. 'bad') factors. It is possible to pin point some of the 'bad' dispersion through the use of (U-Th)/He isochron plots and age vs. grain size/eU multi-variant plots, but the majority of the 'bad' dispersion just ads noise to the 'good' dispersion signal. The crystals which have clearly experienced 'bad' dispersion can be eliminated if desired, but the scientific justification for doing this is questionable, so they should arguably be retained in the dataset.

Even with clear outliers eliminated, dispersion can still be in excess of 100%. This should no longer be considered 'over dispersed' data (dispersion greater than that which can be accounted for through analytical uncertainty alone). The data is dispersed exactly as much as it should be, on account of the unique effective closure temperature of each and every grain, due to its specific geometry and composition. The fragment effect on this dispersion is not clear when purely considering the raw data, but this does not justify modelling fragments as if they are whole crystals. A fragment can have a drastically different age to its original whole crystal (easily representing 100% error with strongly dispersed data) within the bounds of the dispersion created by grain size and eU variation. Therefore to model fragments as whole crystals can be very misleading.

Calculating a mean age for a sample is unnecessary, except for providing qualitative comparisons between samples/within a profile. There is no singular representative AHe age for a given sample, and the desire to derive one has led to the misconception of 'over dispersed' data historically. Each crystal contains its own unique piece of thermal history information, and the more crystals which can be analysed per sample; the more robust the resultant thermal history reconstruction will be. Ultimately, the purpose of AHe dating is to reconstruct thermal histories, and not to 'date' a particular sample or suite of samples. The goal should be to analyse as many grains as possible, and to maximise the inherent natural dispersion by selecting a wide range of grain shapes and sizes.

CHAPTER 6

6. BALLACHULISH IGNEOUS COMPLEX: A NEW THERMAL HISTORY INTERPRETATION

(Aonach Eagach ridge, Glencoe. Ballachulish Igneous Complex (Sgorr Dhonuill) in the background)

6.1 Introduction

The overarching goal of this thesis has been to provide an empirical test of the new fragment model of Brown *et al.* (2013) and Beucher *et al.* (2013). Beucher *et al.,* (2013) demonstrated its effectiveness using a synthetic dataset (grains generated from the five WOLF thermal histories (Wolf *et al.*, 1998)); this chapter presents the first exploration of the technique using a real dataset, with all of its complexities and imperfections. The BIC has been chosen as the case study for reasons outlined in **Chapters 1** and **5.** The data has been modelled with both the HelFRAG and QFrag implementations of the fragment model, with an emphasis on the QTQt modelling technique.

6.1.1 *Previous works*

The BIC has been studied extensively over the years (e.g. Bailey and Maufe, 1916; Johnson and Frost, 1977; Pattison, 1985; Weiss and Troll, 1989; Harte and Voll, 1991; Pattison and Voll, 1991; Fraser *et al.*, 2000) and as such its geological history is well constrained (see **Chapter 5**). Important constraints for understanding its thermal history are that it was emplaced at 424 ± 4Ma, at a crustal depth of c. 10km (Fraser *et al.*, 2000) and at temperatures ranging from c. 850-1100°C (Weiss and Troll, 1989). Due to the preservation of volcanic sequences at the nearby igneous complexes of Glencoe and Ben Nevis, the complex must have been exhumed to near surface depths by the time of the Glencoe eruptions at c. 404Ma (Fraser *et al.*, 2000; 2004). There is no evidence of significant reburial in the geology of the area; therefore it must have remained close to surface depths for the remainder of its history.

The Glencoe Volcanic Complex (GVC) is the type example of a caldera/cauldron subsidence (Clough *et al.*, 1909). The ring fault surrounding the complex has experienced c. 1000m of downthrow during caldera formation, and the volcanic sequences have experienced an additional >700m of incremental subsidence within the caldera (Moore and Kokelaar, 1998), giving an estimate of c. 2km of total subsidence for the volcanic sequences. Accounting for this, the BIC must have uplifted c. 8km over the c. 20Myrs between its emplacement and the volcanic activity preserved at neighbouring Glencoe. This requires an average uplift/denudation rate of c. 0.4km Ma^{-1} between c. 424-404Ma (Fraser *et al.*, 2004).

Persano *et al.,* (2007) carried out the first detailed thermochronological study of the complex. They calculated that 1330 ± 230m of denudation has occurred in the area since a rapid cooling event (uplift) which took place between 61Ma and 47Ma. The cooling has been interpreted as under-plating driven uplift caused by the proto-Iceland plume, resulting in the isostatic readjustment of the land surface. Their published thermal history models are shown in figure **6.1** and AHe and AFT ages in table **6-1**. The thermal histories are predominantly generated using AFT data. The AHe data was used to examine monotonic cooling rates which can satisfy the data and fit within the AFT generated inverse models. This was done using the forward modelling software DECOMP (Bikker *et al.*, 2002) and provides the dashed lines seen on figure **6.1**.

Table 6-1: AHe (raw) and AFT ages of Persano *et al*. (2007). * _new QTQt synthetic AFT data_

Sample No.	Elevation (m)	AHe age (Ma) (no. grains)	AFT age (Ma) (no. grains)	MTL (μm) (no. tracks)	Dpar (μm)
_**SD1**_	1001	207 (1) 207 (5) 214 (5)			
_**SD3**_	804	177 (4) 190 (2) 182 (7)	257 ± 12 (20) _*215.6 (20)_	13.2 ± 1.9 (118) _*13.48 (78)_	2.1 ± 0.5
_**SD6**_	505	104 (4) 105 (6)			
_**SD13**_	329	62 (6) 51 (9)			
_**SD14**_	290	64 (16) 77 (13) 55 (3 65 (2)			
_**SD9**_	195	63 (3) 68 (11)	186 ± 6 (20) _*203.5 (20)_	11.2 ± 2.1 (107) _*13.0 (78)_	2.3 ± 0.5

The models generated by Persano *et al.* (2007) are not inconsistent with the assumption that the BIC must have been within the upper 2km of the crust by c. 400Ma. They use a palaeogeothermal gradient of 39 ± 9°C (determined through their inverse models) and the present day surface temperature of 5°C. Based on these values, the sample near the top of the profile (SD3) needs to be at c. 85°C by 400Ma, and this is possible within the good fit window of the models seen in figure **6.1 A**. The published thermal history of Persano *et al.* (2007) can be used as a benchmark with which to compare and contrast the new model inversions; however it is based on a much smaller AHe data set which used multi-grain aliquots, so should not unquestioningly be taken as the 'true' thermal history with which to try and replicate.

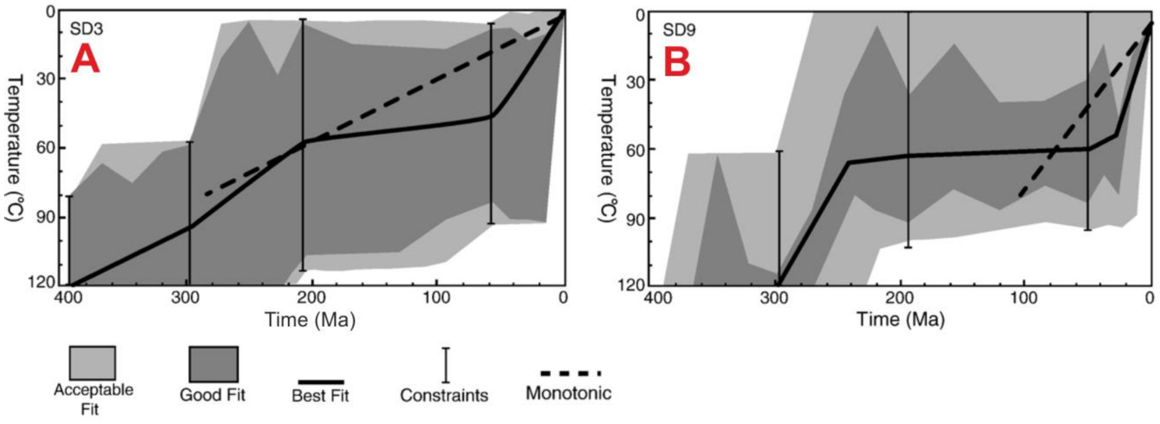

Figure 6.1: Thermal histories of Persano *et al*. (2007) for Sgorr Dhonuill.
Thermal history reconstructions generated using AFTSolve (Ketcham *et al*., 2000) to inverse model the AFT data, and DECOMP (Bikker *et al*., 2002) to forward model the AHe data. The solid line represents the best fit model for the AFT data, and the dashed line represents a monotonic cooling history which can account for all the AHe ages while being acceptable within the generated AFT model. Dark grey shaded region = good model fit, light grey shaded region = acceptable model fit. **A**: sample *SD3* (*SD07 – 3* in this thesis) from an altitude of 804m. **B**: sample *SD9* (not used in this thesis) from an altitude of 195m.

Using the best fit thermal history lines in figure **6.1** to generate synthetic AFT ages with QTQt gives an age of 215.6Ma (MTL – 13.48µm) for sample SD3, and 203.5Ma (MTL 13.0µm) for sample SD9. These ages differ from the published ages of Persano *et al.* (2007), suggesting that with the advancements in modelling techniques over the last decade or so, comparable thermal histories (and therefore geological interpretations) would not be made if the same data were to be re-modelled today.

6.1.1.1 Studies on surrounding complexes: Other thermochronological studies have been carried out on nearby igneous complexes (see figure **6.2**), and these should be expected to have experienced a broadly similar thermal history as the BIC and GVC. Hurford (1977) carried out an extensive fission track study on apatite, zircon and sphene (titanite) across 17 of the newer/late Caledonian igneous complexes in Scotland (including the BIC and GVC). The study predates the emergence of thermochronology as a discipline, and as such the interpretations of the meaning of the ages are primitive. Ages ranging from c. 230-280Ma across all the igneous bodies are quoted for AFT, and these are interpreted as either a very slow cooling rate of 0.8°C Myr^{-1} from the time of intrusion, or a partial or full resetting of the ages due to an undefined Permian heating event (leading to further magmatism and metasomatism).

Hurford (1977) dated two apatite's from Ballachulish; these gave ages of 169 ± 7Ma and 193 ± 11Ma. The altitude of the samples isn't given, but the supplied grid reference (NN 025,594) would place the samples close to sea level, so they would be expected to be younger than the samples of Persano *et al.* (2007) who report an AFT age of 186 ± 6Ma for a sample at 195m elevation (see table **6-1**). Other nearby ages are: Kentallen - 274 ± 13Ma, Rannoch Moor – 234 ± 7Ma, Ben Nevis – 237 ± 24Ma, Ben Cruachan – [298 ± 17Ma, 245 ± 23Ma], Ben Starav – 300 ± 1Ma and on the other side of the GGF, Strontian – [235 ± 15Ma, 241 ± 7Ma, 231 ± 24Ma, 231 ± 23Ma] (see figure **6.2**). It is difficult to make any retrospective thermal history interpretations based purely on the published ages, but the absence of any very young ages implies that the vast majority of uplift experienced by the igneous bodies occurred in the Palaeozoic, with less than c. 4km of uplift taking place since the Permian.

Thomson *et al.* (1999) also carried out AFT analyses on a number of samples from the Strontian pluton and surrounding area as part of a thermochronological study of the entire North West Highlands. They publish ages ranging from 202.5 ± 12.8Ma to 246.1 ± 12.8Ma (figure **6.2**). This matches the range of ages published by Hurford (1977) for the Strontian complex. The authors calculated that 1714 ± 143m of erosion/denudation had occurred in the Strontian region since 60Ma, which is slightly higher, but not inconsistent with the denudation calculated by Persano *et al.* (2007) for the BIC.

Holford *et al.* (2010) report slightly younger AFT ages for the Strontian granite than the previous authors, with ages ranging from 187.7 ± 9.2Ma to 213.7 ± 9.1Ma (figure **6.2**). This may be down to differences in sample elevation or chemistry, or may be down to improvements in the analytical procedure. Based on their new data, in conjunction with detrital samples from the offshore basins, they advocate multiple rapid phases of cooling and reheating (i.e. repeated uplift and burial) in the post Caledonian history of the west of Scotland. This involves at least 4-5 periods of moderate (>1-2km) reburial of the basement rocks, each followed by denudation to at or near surface depths. This interpretation differs strongly from the steady post Caledonian cooling reported by Persano *et al.* (2007) and is generally at odds with the broad consensus of the geological history of the west of Scotland.

New fission track data for the BIC is included in Appendix 6 (unpublished, data generated by A. Amin at the University of Glasgow). Ages range from 261 ± 26Ma at the summit (*SD07 – 1*) to 194 ± 21Ma at sea level (*BH13 – 02*). These ages are slightly older, but comparable to the sea level ages of Hurford (1977) and low elevation sample of Persano *et al.* (2007). A new AFT age for sample SD3 (*SD07 – 3*) is lacking, but the adjacent samples (above and below) have slightly younger ages (234 ± 23Ma and 238 ± 23Ma) compared to that of Persano *et al.* (2007) (257 ± 12Ma).

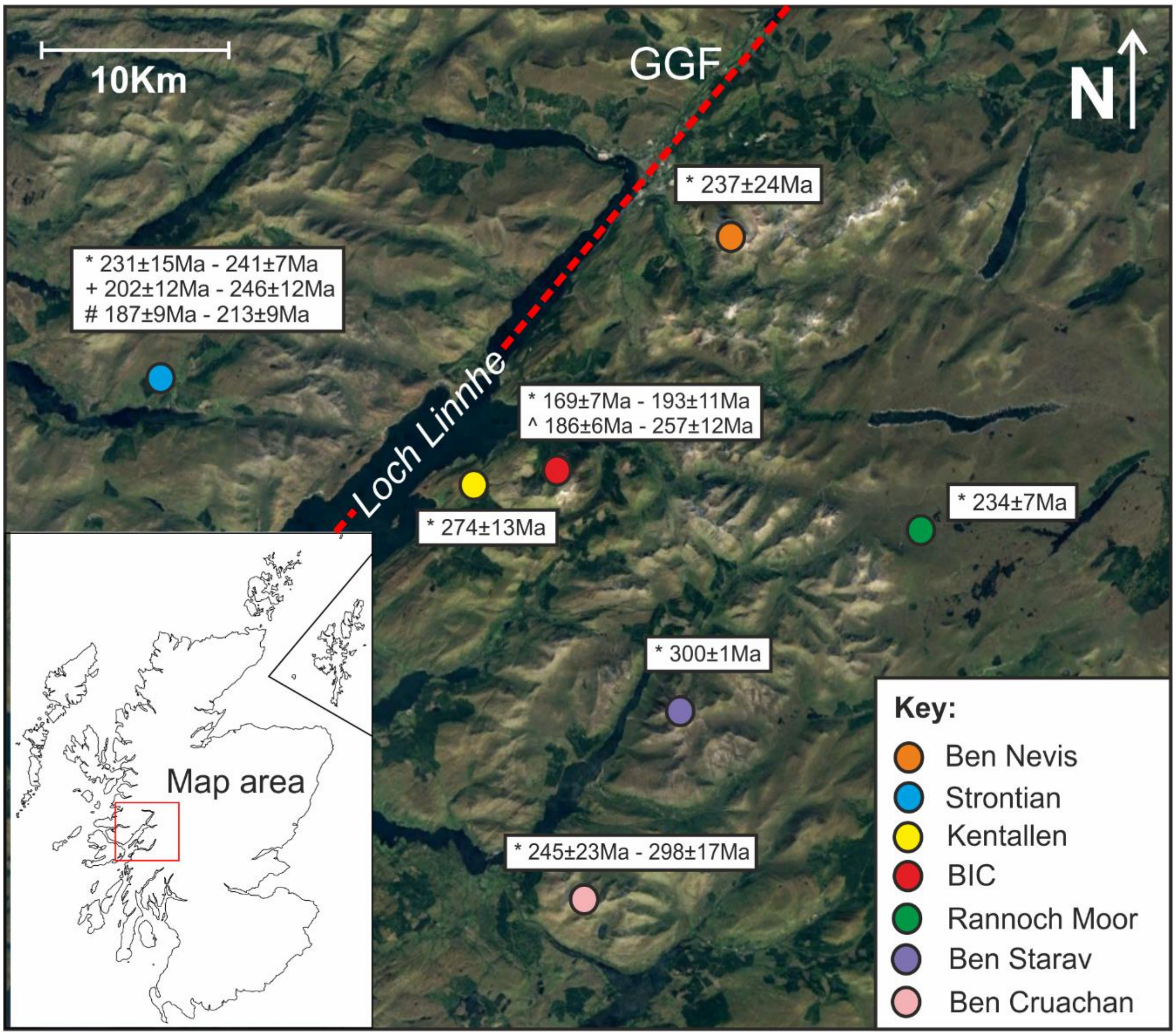

Figure 6.2: Published AFT data from surrounding igneous complexes.
The locations of the published AFT ages referred to in the text, showing the quoted ages. Where multiple ages are listed per publication at a given location, the age range is shown. Where multiple publications exist at the same location, the publications are delineated by the following symbols: * Hurford (1977), + Thomson *et al*. (1999), # Holford *et al*. (2010) and ^ Persano *et al*. (2007). Red dashed line indicates the Great Glen Fault (GGF).

6.2 HelFRAG Inversions

A selection of the new AHe data presented in this thesis (**Chapter 5**) has been modelled using the HelFRAG inversion technique (Brown *et al*., 2013; Beucher *et al*., 2013). Sample *SD07 – 5* has been used as a test case on account of only containing 10 grains, which makes the modelling process swifter (9 of which are fragments). Sample *SD07 – 3* (the focus of much of the subsequent QTQt modelling in this chapter) has then been modelled utilising a super computer cluster to speed up the process. The sample consists of 30 individual grains, which would have taken significantly longer than *SD07 – 5* to run using a single processor (see table **6-2**).

Table 6-2: HelFRAG experiment matrix.

Sample No.	No. of grains	No. of fragments	Model Iterations	Radiation damage model
SD07 - 5	10	9	10,000	No RD Gautheron 2009
SD07 - 3	30	21	10,000	No RD Gautheron 2009 RDAAM 2009

6.2.1 *Sample SD07 - 5*

This has been modelled both without a radiation damage model and using the radiation damage model of Gautheron *et al.* (2009) (figure **6.3**). Using a radiation damage model greatly increases the model run time (as is the case with QTQt) so the first test was carried out with 'no radiation damage' selected. The model has been run for 10,000 iterations, with a model space of 425 – 0Ma and 140 - 0°C. In HelFRAG the number of T-t points needs to be specified beforehand, and here the model uses 5 (possible range 2-6). The final T-t point is pinned at 5°C and 0Ma but other than that there are no T-t constraints within the model space.

The best fit model is shown in red, with all other accepted T-t paths shown in blue. The rejected T-t paths are shown in grey. The blues are colour contoured so that the darker the colour the more likely the T-t path (lower misfit). This is done on a purely arbitrary basis, with the threshold between grey and blue, and the contouring threshold for the blue being user defined. These are not representative of any statistical measure such as confidence/credibility intervals, and are purely chosen 'by eye'. The lower the misfit value, the more likely the thermal history, but exactly what constitutes low will differ from model to model.

6.2.1.1 No radiation damage model: Figure **6.3 A** shows the thermal history output when no radiation damage model is applied. The model is poorly constrained before about 230Ma, but the best fit model wants to be reheated from a fairly shallow depth to below the base of the PRZ before this time. In reality the model doesn't know anything about the history before this point, as there is no information retained within ^{4}He data. The best fit model (and many of the other accepted solutions) treats this as the ages being reset due to burial at about 230Ma, but the more logical interpretation given the known geology of the area is that the sample was too hot to start accumulating ^{4}He before this time. Defining a ‘hot’ start temperature for the model would likely provide clarity on this issue. HeIFRAG doesn’t have an option for using T-t constraints, but limiting the model space for the first T-t point can have a similar effect. After c. 230-200Ma the model wants to undergo simple monotonic cooling from below the depth of the PRZ to the surface. This portion of the thermal history is well constrained.

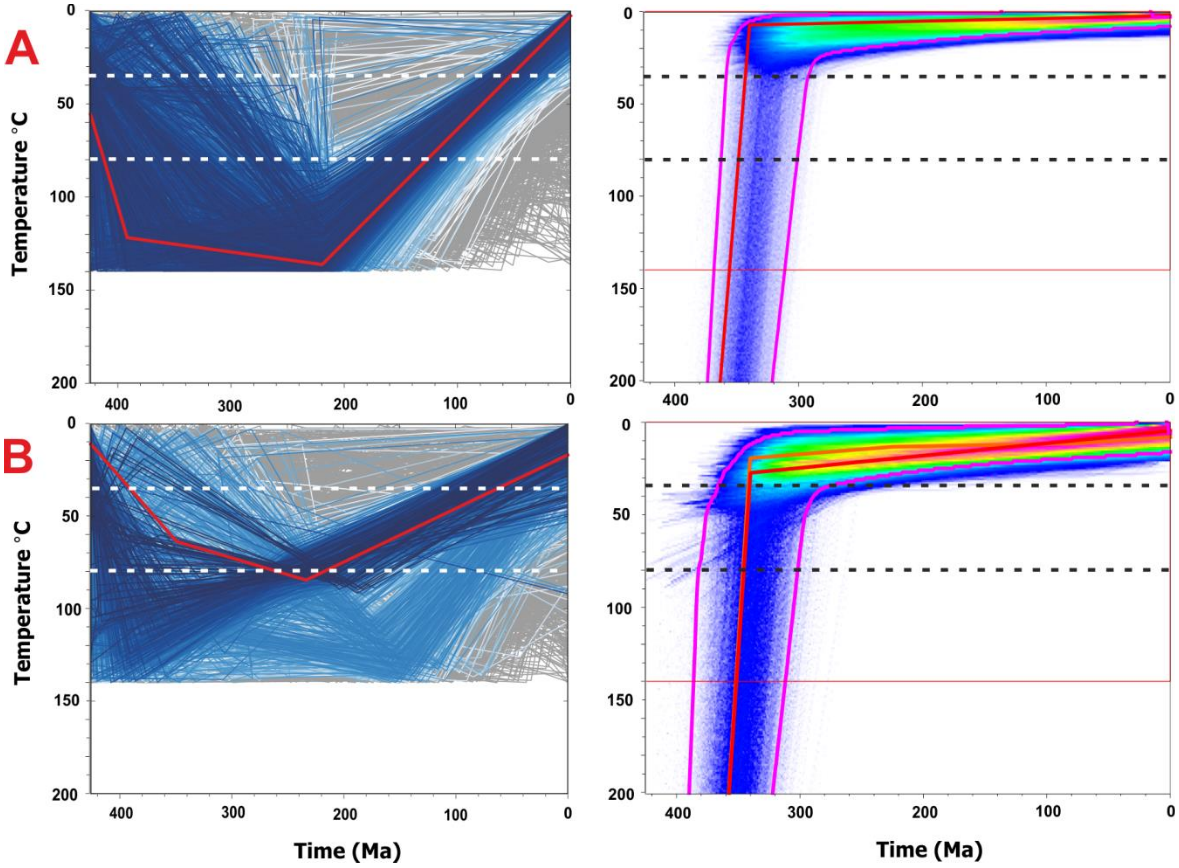

Figure 6.3: *SD07 – 5* Thermal history, HeIFRAG vs. QTQt.
Thermal history inversions for sample *SD07 – 5* modelled using HeIFRAG (left) and QTQt (right). HeIFRAG models run for 10,000 iterations with a model space of 0-425Ma and 0-140°C and a present day temperature of 5°C. No. of T-t points = 5. QTQt models run for 100,000 iterations after an initial burn in period of 10,000, with an initial T-t constraint of 800 ± 100°C at 424 ± 10Ma representing the age and depth of intrusion (Weiss and Troll, 1989; Fraser *et al*., 2000) and a surface temperature of 5°C. Solid red line = maximum likelihood thermal history, solid orange line = maximum posterior likelihood thermal history (QTQt models), solid pink lines = 95% credibility intervals (QTQt models). HeIFRAG: blue lines = accepted models, with the colour contoured to represent the model misfit. Darker = lower misfit (higher likelyhood). Grey lines = rejected models. QTQt: colour shading = probability density distribution. Brighter colours = higher probability (better fit), blues = low probability. **A**: modelled with no radiation damage model selected. **B**: modelled using the radiation damage model of Gautheron *et al*. (2009).

6.2.1.2 Radiation damage model of Gautheron et al. (2009): Figure **6.3 B** shows the model output when using the radiation damage model of Gautheron *et al.* (2009). This appears broadly similar to when modelled without a radiation damage model, but is even less well constrained. The best fit model again wants to reheat, but from an even shallower depth. It is then buried to a shallower depth than the thermal history with no radiation damage model, heating to a temperature of around 80°C instead of 140°C before cooling. Ultimately both of these temperatures are near or below the base of the PRZ, so the exact temperature is inconsequential, the important information is that the sample was at a depth below the PRZ before c. 230Ma. As with the previous model, providing a 'hot' start temperature would likely provide greater clarity on the initial portion of the thermal history. After c. 230-200Ma the model again wants to undergo simple monotonic cooling to the surface, but the initial temperature, and therefore the rate of cooling are poorly constrained. A not insignificant proportion of T-t pathways want to initiate cooling at around 150Ma instead of c. 230Ma, adding to this uncertainty.

6.2.2 *Sample SD07 – 3*

This has been modelled with no radiation damage model, and with both of the current radiation damage models (RDAAM – Flowers *et al.* (2009) and Gautheron *et al.* (2009)) (figure **6.4**). The model has again been run for 10,000 model iterations and with a comparable model space as for sample *SD07 - 5*, but this time the first T-t point has been restricted to temperatures between 120-150°C. This has the effect of placing a 'hot' initial T-t constraint indicating that the rock is an intrusion, forcing the models to start at a more realistic temperature than in figure **6.3**. Accepted models are shown in blue and rejected in grey, but in this instance the colour contouring of the blue lines is inverse to that of figure **6.3**, so that the light blue (almost white) lines have the best fit. Additionally the mean of all the accepted models is plotted in green.

6.2.2.1 No radiation damage model: Figure **6.4 A** shows the thermal history output when no radiation damage model is applied. Despite being forced to start hot, the majority of accepted models (as well as the best fit model) want to cool rapidly to the near surface, before experiencing reburial. The reality is that the model is very poorly constrained at this time, the data does not retain any thermal history information prior to the oldest ages of about 250Ma. As was the case for figure **6.3**, some geological knowledge needs to be applied to constrain the model. There is no evidence of significant reburial of the BIC in the geological record, so the logical interpretation of the models is that the sample was too hot to start accumulating ^{4}He prior to about 250Ma. After c. 250Ma there is a strong consensus within the models that the sample cooled very rapidly through the PRZ, and remained at the surface from c. 210Ma to present. The data fit (observed vs. predicted plots) is not perfect; the younger ages are over predicted by the generated model, whereas the older ages are under predicted, but for a real data set this shows a very good fit.

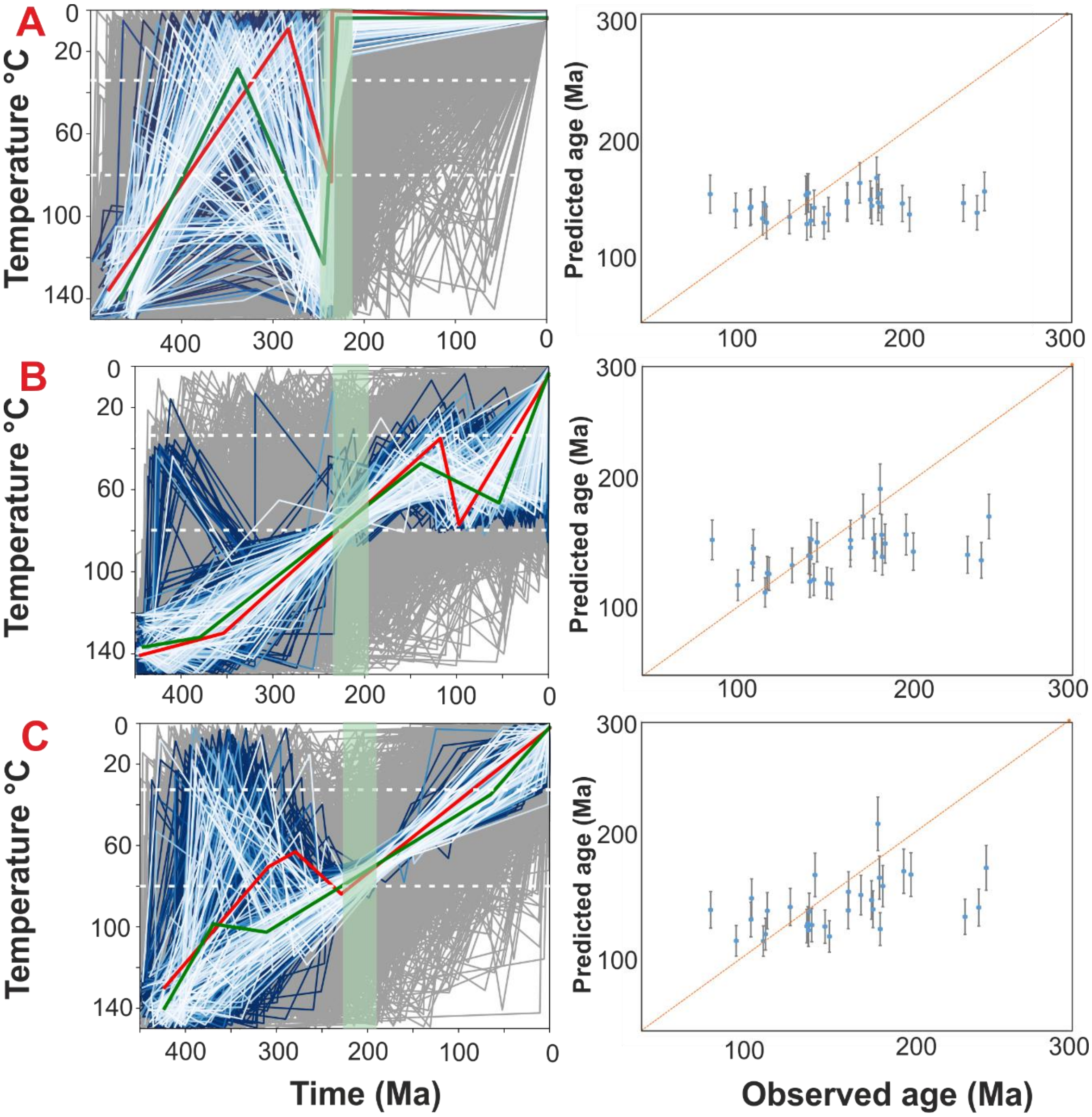

Figure 6.4: *SD07 - 3* HelFRAG thermal history.
Thermal history inversions for sample *SD07 – 3* modelled using HelFRAG. Models run for 10,000 iterations with a model space of 0-500Ma (**A**) or 0-450Ma (**B** and **C**) and 0-150°C. The present day temperature is set at 5°C. No. of T-t points = 5. 1st T-t point is limited to temperatures of 120-150°C. Solid red line = maximum likelihood thermal history, solid green line = average accepted thermal history. Blue lines = accepted models, with the colour contoured to represent the model misfit. Lighter = lower misfit (higher likelihood). Note, this is the opposite of the models in figure **6.2**. Grey lines = rejected models. Light green box indicates the time period where most accepted models pass into the PRZ. **A**: modelled with no radiation damage model selected. **B**: modelled with the radiation damage model of Gautheron *et al*. (2009). **C**: modelled using RDAAM (Flowers *et al*., 2009). Right hand panel shows the observed verse predicted plot for each model, with vertical error bars of 10% on the predicted ages.

6.2.2.2 Radiation damage model of Gautheron et al. (2009): Figure **6.4 B** shows the model output when using the radiation damage model of Gautheron *et al.* (2009). At first appearances this is drastically different to the models with no radiation damage model applied. The general trend is of a gradual monotonic cooling for much of the history, with a possible late reburial phase in the last 100Myrs. But there are some key similarities with the no radiation damage model version. Although better constrained, the initial part of the thermal history is still fairly poorly constrained, with a not insignificant number of potential thermal histories wanting to cool rapidly to the surface before reburial. The model then becomes much more constrained during its middle segment, which coincides with the sample passing into the base of the PRZ. This crucial event closely corresponds in timing with the same event in the no radiation damage model version, occurring at c. 230-200Ma (as highlighted by the green boxes in figure **6.4**). The difference being in the subsequent rate of ascent through the PRZ. After this point the model becomes less well constrained again, with the best fit thermal histories suggesting a period of reburial, however this segment of the thermal history can be satisfactorily explained by isothermal holding within the PRZ for much of the period followed by rapid cooling to the surface.

6.2.2.3 RDAAM (Flowers et al., 2009): Figure **6.4 C** shows the model output when using RDAAM. This is broadly similar to the thermal history when modelled using the radiation damage model of Gautheron *et al.* (2009). The thermal history can be explained by simple monotonic cooling throughout the history. The initial portion of the history is again poorly constrained, with many models wanting to cool rapidly before reburial. The history is then very well constrained in its mid-section, coinciding with entering the base of the PRZ at c. 230-200Ma, as was the case when using the Gautheron radiation damage model. Unlike when modelled using the Gautheron model, the history lacks the possible late stage reburial, preferring simple monotonic cooling out of the PRZ to the surface. This part of the thermal history is better constrained than the final 100Myrs of the Gautheron model history.

The observed verse predicted age plots when using either radiation damage model are broadly similar to the plot for no radiation damage model (figure **6.4** right panel). The same structure is apparent of younger ages being over predicted while older ages are under predicted, however the scatter is slightly more evenly and randomly distributed around the 1:1 line. This implies that the data fits the model slightly better when using a radiation damage model, which is as would be expected, but the differences are subtle.

6.2.3 *Comparison with QTQt*

Figure **6.3** also shows the equivalent QTQt outputs for sample *SD07 – 5*, the equivalent QTQt outputs for sample *SD07 – 3* can be found in figures **6.8** and **6.9**. Using QTQt the thermal history interpretation is drastically different. QTQt wants the samples to have been cold for most of their history, having passed through the PRZ before 300Ma, whereas the HelFRAG outputs do not cool through the PRZ until c. 230Ma at the earliest. The lack of an initial T-t constraint at the age of intrusion in figure **6.3** clearly hinders the HelFRAG inversions, but even taking that into account the model outcomes are drastically and incontrovertibly different.

The QTQt models have been prevented from reheating. This is not possible using HelFRAG, but if it were then the HelFRAG models would be significantly different. Currently the majority of T-t histories in the HelFRAG inversions favour histories which undergo reheating during their history, so the resultant thermal history would be very different if this were prevented. This is not to say that they would be a closer match to the QTQt thermal history however, as they would still need to be hot at c. 230Ma. Conversely allowing reheating in the QTQt models would not result in a thermal history similar to the HelFRAG version either. Preliminary test runs on the QTQt models (not presented here) showed very little difference in the resultant thermal history when reheating was allowed. Ultimately the two modelling techniques have converged on very different thermal history interpretations.

The evidence contained within this chapter is overwhelmingly in support of the thermal history presented by the QTQt model. This is also supported by the geological evidence which implies that the profile was cool from very early on in its history, and has experienced no significant reburial since. It seems likely that a combination of the small sample size (for *SD07 – 5*) and insufficient model iterations have led to an inaccurate thermal history reconstruction using HelFRAG in this instance. Beucher *et al.* (2013) ran their models for 20,000 iterations to achieve the desired misfit convergence; the 10,000 iterations used here may be insufficient. The authors also showed that a minimum of around 20 grains are required to achieve the optimum results, so again it is likely that the 10 grains of sample *SD07 – 5* is a too small sample size. However this explanation cannot be used for sample *SD07 – 3* which consists of 30 grains.

QTQt as an inversion tool is far more powerful and statistically robust than HelFRAG. HelFRAG was developed to demonstrate the fragment effect (Brown *et al.*, 2013; Beucher *et al.*, 2013), but is a more basic program than QTQt overall. The disparity between the model outputs from the two programs is most likely down to differences in the workings of QTQT verses HelFRAG, rather than differences in the treatment of broken grains by the QFrag approximation of the fragment model verses the HelFRAG version. This is because the data has been modelled in QTQt both with QFrag on and off (figures **6.6**, **6.8**-**6.12**). There are minor differences in both instances, but the overall thermal history interpretation is the same. Both cases are very different from the HelFRAG histories shown in figures **6.3** and **6.4**.

6.3 QTQt Inversions

As demonstrated in C**hapter 4**, the approximation of the fragment model of Brown *et al.* (2013) and Beucher *et al.* (2013) which has been incorporated into the QTQt software (Gallagher, 2012) can accurately return the correct thermal histories for a range of known theoretical T-t paths. QTQt has a user friendly interface, and where there is no access to computer clusters, provides a much more rapid alternative to HelFRAG, enabling the routine application of the fragment model. The new BIC data has been modelled here as individual samples and together in a profile to best constrain the most likely thermal history, as well as experimenting with the multitude of different options for modelling the data within the QTQt software (e.g. Flowers vs. Gautheron radiation damage models, fragment model on or off etc.).

6.3.1 *Modelling samples individually*

The entire profile covers over 1000m in elevation (see **Chapter 5**). Although the profile has experienced a single thermal history, different elevations will have passed through the PRZ at different times and as such, when modelled independently, should show a systematically changing thermal history. How this changes up the profile is in itself indicative of the nature of the entire thermal history, with very little change top to bottom demonstrating a very rapid cooling, whereas large differences in the timing of cooling events top to bottom indicating a very slow ascent through the PRZ.

Each sample has been modelled using the radiation damage model of Gautheron *et al.* (2009), resampling of the age (see section 6.3.3), fragment model on and the ‘no reheating’ model options. The initial T-t constraint at the age of intrusion has also been used (800 ± 100°C and 424 ± 10Ma) (see table **6-3**). The results are shown in figure **6.5**, which plots the model outputs in the order of their position on the vertical profile. The 2007 and 2013 transects have been plotted side by side for comparison.

Table 6-3: QTQt modelling parameters for samples modelled individually.

Model Iterations	Radiation damage model	Resampling option	T-t constraint	Fragment model	No reheat
100,000 (20,000 burn in)	Gautheron 2009	Resampled age	800 ± 100°C 424 ± 10Ma	On	On

6.3.1.1 2007 Transect: The upper half of the transect shows rapid monotonic cooling from intrusion to near surface depths, passing through the top of the PRZ by c. 250-300Ma. This is consistent in samples *SD07 – 1* down to *SD07 – 5* at an altitude of 605m. Between *SD07 – 5* and *SD07 – 6* (505m) there is a marked change, with the lower samples passing through the top of the PRZ between c. 100-150Ma (figure **6.5**). This means that the current exposure of the BIC straddled the 35°C isotherm for approximately 150Myrs between c. 300-150Ma, and that boundary occurs between 500-600m on the present day profile (as highlighted on figure **6.5**). Below 600m the samples all show the same thermal history as *SD07 – 6* (allowing for the elevation offsets).

This is useful thermal history information which isn't shown by modelling any singular sample, and only becomes apparent when comparing all the samples in the vertical profile, which demonstrates the value of sampling detailed vertical profiles for low temperature thermochronological studies as opposed to singular samples. The observation could also be explained by the presence of a fault cross cutting the profile at c. 550m and having significant vertical displacement (i.e. 1km or more), but no such fault exists at the BIC. Therefore this explanation can be discounted.

6.3.1.2 2013 Transect: The samples from the opposite side of the mountain should show the same thermal history as the 2007 transect. However this does not appear to be the case. Samples from the 2013 transect appear to have cooled through the PRZ 50-100myr later than the 2007 transect, crossing the 35°C isotherm at c. 200Ma instead of c. 300Ma. The Ballachulish fault cuts through the BIC, but this is not the cause of this disparity as sample *SD13 – 02* is on the same side of the fault as the 2007 transect (see **Chapter 5**, figures **5.2** and **5.3**). It should therefore show an almost identical thermal history to sample *SD07 – 2*.

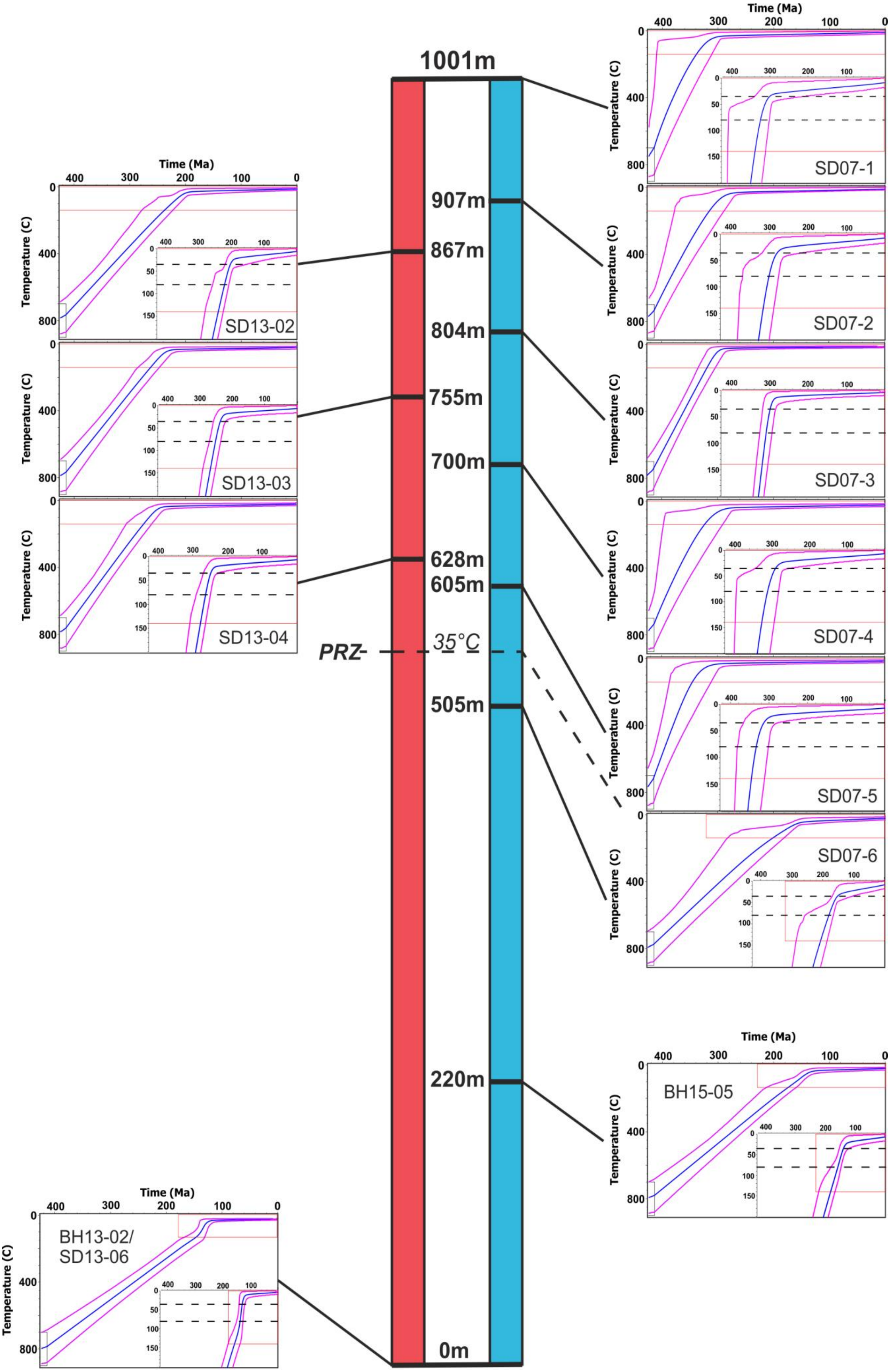

Figure 6.5: Sample by sample modelling using QTQt, plotted in elevation order.
Each sample plotted in its corresponding vertical position (to scale) in each profile - 2013 on the left and 2007 on the right. Samples modelled for 100,000 iterations after a burn in period of 20,000 iterations, using the

radiation damage model of Gautheron *et al*. (2009), resampling the age and preventing reheating. The fragment model is switched on. Individual plots showing the expected thermal history (solid blue line), 95% credibility intervals (solid pink lines) and model prior (red box). Inset: showing the same plot with expanded scale zoomed in on the upper 200°C to emphasise the PRZ. The PRZ is shown by horizontal dashed black lines at 80°C and 35°C. Fossil PRZ 35°C isotherm depicted on the vertical red and blue scale bars. See Appendix 4 for corresponding observed vs. predicted plots and probability density distributions.

The fault does appear to have undergone some noticeable vertical displacement (it is predominantly a sinstral strike-slip fault), as the lower elevation *SD13 – 03* and *04* samples crossed the 35°C isotherm c. 20myrs before *SD13 – 02*. Being of lower elevation they should have crossed the isotherm after *SD13 – 02*. This can't however explain the disparity between the two transects. Compositional differences cannot be used as an explanation for the disparity either, as all samples in the upper profile come from the central granitic core of the complex, so there is no systematic difference between the two sides. Any localised variation which might provide 'freak' results would not distinguish between the two profiles in such a way. This difference in the two profiles is therefore difficult to explain.

The combined sea level samples (*BH13 – 02* and *SD13 – 06*) have been plotted on the 2013 side of the plot (figure **6.5**), but this is purely for spatial reasons on the figure. Both samples are geographically separated from the main profiles owing to topography, so are not specifically related to one profile more than the other (although they are on the same side of the BF as samples *SD13 – 03* and *04,* as is *BH15 – 05*). The sea level samples show additional information not found higher up the profile. They show a pulse of rapid cooling between c. 150-120Ma, providing greater clarity on the final cooling/uplift phase of the BIC history.

6.3.2 *Modelling samples in a profile*

Modelling multiple samples together in a single vertical profile increases the robustness of the model inversions. All samples must have experienced the same thermal history (assuming there are no major fault displacements within the profile) and thus samples from different elevations contain thermal history information from different stages in the timeline. The top of a profile will pass through the PRZ first, and therefore will contain more thermal history information about the oldest portion of the timeline. The base passes through the PRZ last, and contains information about the younger portion of the timeline. Assuming there are differences between the top and bottom of the profile (which can be seen to be the case at the BIC purely from the distribution of ages alone, as well as the modelling in section 6.3.1) then a vertical profile can be considered to represent at least a portion of the fossil PRZ. This means that more thermal history information can be gathered from modelling the samples as a single vertical profile than individually.

All samples from the 2007 transect, plus the combined sea level 'sample' have been modelled together, giving a total of eight samples spanning an elevation range of 1001m. The three samples from the 2013 transect have been excluded from the profile because they appear to show a different thermal history to the rest of the profile (as seen in figure **6.5**) which is difficult to explain. However as these samples share similar elevations to samples in the 2007 transect, cutting them from the profile does not decrease its resolution.

The profile has been modelled using an initial temperature offset between the top and bottom samples of 26°C, but this has been allowed to vary through time (see Appendix 6 for temp-offset plots). As the profile spans effectively 1km in elevation, this can be thought of as the geothermal gradient. Given that the offset is allowed to vary, the exact number which is given as the initial offset is unimportant, as long as it is a sensible value. Here 26°C has been chosen as it is the present day average geothermal gradient under Scotland (website 2). It is sensible to expect this value to have varied through time; indeed Persano *et al.* (2007) calculated the geothermal gradient at Ballachulish to be 39 ± 9°C during the early Cenozoic based on their thermal history reconstructions.

A present day surface temperature of 5 ± 5°C has been used, which is applied to the top sample in the profile. This is considered a reasonable value for average surface temperatures on the summit of a mountain in the Scottish highlands. A present day offset temperature of 5 ± 5°C is also used, which is the difference between the top and bottom samples in the profile. This would give an average sea level surface temperature of around 10°C, which again is a realistic value for the Scottish highlands.

Two T-t constraints have been applied to the earliest portion of the thermal history which act upon the top sample in the profile (with the other samples at a corresponding temperature related to the calculated temperature offset (geothermal gradient) at the time). These are an initial T-t constraint for the age and depth of the intrusion at 800 ± 100°C and 424 ± 10Ma (Weiss and Troll, 1989; Fraser *et al.*, 2000) and a near surface constraint of 100 ± 50°C at 404 ± 10Ma as constrained by the presence of volcanic sequences at the nearby GVC (Fraser *et al.*, 2004). These T-t constraints are used because they broadly fall below the base of the PRZ so the data retains no information about this portion of the history, but the geological evidence for their inclusion is robust.

Initially the models have been prevented from accepting possible thermal history pathways which experience reheating (see table **6-4**). Again this is only applied to the top sample in the profile. This is because reheating requires burial, and there is no geological evidence of significant burial in the surrounding area. Burial would leave evidence in the sedimentary record, and although there are Mesozoic and younger sediments preserved in the Midland Valley Terrane and in the inner and outer Hebrides, none exist in the Ballachulish region. Equally, complete burial of the highlands in the past would require the erosion of an even larger and younger mountain chain in the vicinity, with which to provide the sediment. No such mountain chain is thought to have existed.

Table 6-4: QTQt modelling parameters for samples modelled in a profile.

	Fig. 6.6 panel A	**Fig. 6.6 panel B**	**Fig. 6.6 panel C**
Initial temp. offset	26°C	26°C	26°C
Present day surface temp.	5 ± 5°C	5 ± 5°C	5 ± 5°C
Present day offset temp.	5 ± 5°C	5 ± 5°C	5 ± 5°C
Model iterations	100,000 (100,000 burn in)	100,000 (100,000 burn in)	100,000 (100,000 burn in)
Radiation Damage Model	Gautheron 2009	Gautheron 2009	Gautheron 2009
Resampling option	Resample age	Resample age	Resample age
T-t constraints	800 ± 100°C at 424 ± 10Ma 100 ± 50°C at 404 ± 10Ma	800 ± 100°C at 424 ± 10Ma 100 ± 50°C at 404 ± 10Ma	800 ± 100°C at 424 ± 10Ma 100 ± 50°C at 404 ± 10Ma
Fragment model	On	Off	Off
No reheat	On	On	Off

6.3.2.1 Modelling fragments correctly as fragments: Firstly the profile has been modelled with the fragment model – QFrag switched on. This means that any whole crystals are modelled in the traditional way, but broken crystals are flagged as being fragments of initially larger unknown whole crystals, and modelled as per **Chapter 4**. The model output is shown in figure **6.6**, **A1** (top and bottom sample in the profile) and **A2** (every sample in the profile).

The initial part of the thermal history between the two T-t constraints shows very rapid monotonic cooling, which is controlled purely by the T-t constraints. The data retains very little information about this part of the history. The upper half of the profile (top 6 samples or 500m) cooled into the PRZ by the end of this time period, but the lower half (bottom 2 samples) were still below the PRZ after this rapid cooling. This is also seen in figure **6.5** where the samples are modelled individually.

There then followed a period of continued but less rapid cooling over the next c. 100Myrs, bringing the entire profile into the PRZ. This ended at c. 300Ma, with the top sample in the profile being close to having cooled out of the PRZ by this time. This is in agreement with the modelling in figure **6.5**, where without a T-t constraint at 404Ma, all the upper samples (above 600m) in the profile show rapid cooling from intrusion until c.300Ma, taking them through the PRZ before plateauing off thereafter. This portion of the thermal history is recorded in the data of the top five samples in the profile (*SD07 – 1* down to *SD07 – 5*).

Between c. 300Ma and c. 150Ma there was a hiatus in cooling, with minimal if any uplift experienced. Indeed the lowest samples in the profile appear to want to reheat, suggesting partial burial (the restriction on no reheating is only applied to the top sample in a profile, with the remaining samples acting according to the calculated temperature offset). It is highly implausible that the top of the profile can be undergoing slight uplift while the base experiences burial (but as the profile isn't truly vertical, it is possible that the lowest samples were buried by valley infill while the top continued to erode, however this is highly unlikely to have occurred by a significant enough amount as to be recorded by the data). It is far more likely that the data is indicating an increase in geothermal gradient at this time due to increased heat flux through the crust. This could indicate a possible thinning of the crust during this time period, or a pulse of igneous activity. This portion of the history isn't directly recorded by any of the samples modelled individually, but is implicit in the differences observed in the model outputs between *SD07 – 5* and *SD07 – 6*.

Following the c. 150Myr hiatus, the profile experienced very rapid uplift at around 140Ma, bringing the entire profile to the surface in less than 10Myrs. This portion of the thermal history is recorded by the samples in the lower 500m of the profile, but is most strongly observed in the samples from sea level which show a very rapid ascent through the PRZ at c. 140Ma (see figure **6.5**). Only negligible uplift/erosion has occurred since this time.

Using the expected model thermal history (as approximated for sample *SD07 – 3*) as a forward model template to generate synthetic AFT data gives an AFT age of 347.7Ma and MTL of 13.95µm. This is significantly older than the published age of Persano *et al.* (2007) for the same sample (257Ma), as well as being older than the new AFT data from similar elevations (see Appendix 6). This suggests that the proposed thermal history here is inconsistent with the available AFT data, however it is unrealistic to draw direct comparisons between a thermal history derived from multiple samples in a vertical profile and AFT data (synthetic or real) derived from a single sample.

6.3.2.2. Modelling fragments incorrectly as whole crystals: The profile has been modelled in exactly the same way, with the exception of the fragment model – QFrag being switched off (see table **6-4**). This means that all crystals are modelled in the traditional way regardless of if they are 1T (fragments) or 2T (whole crystals). The model outputs can be seen in figure **6.6** **B** and **C**.

As when modelled with QFrag, the profile follows rapid cooling between the two T-t constraints, but the entire profile cools to a shallower depth by the end of the second T-t constraint. As the top sample in the profile is restricted to the limits of the T-t constraint, the profile becomes bunched, resulting in an incredibly (and unrealistically) low temperature offset and geothermal gradient (see Appendix 4 for temp-offset plot). This suggests that in this instance the top of the profile wants to be much cooler than the T-t constraint allows it to be. This may be realistic, as the exact depth of the profile at this time is unknown. It needs to be within approx. 2km of the surface, but may well be shallower than expected.

The top of the profile could have experienced simple monotonic cooling between 404Ma and the present based on the model output. There is a small period of more rapid cooling possible at c. 100Ma but it is not certain. The rest of the profile however wants to undergo fairly rapid burial between about 160-140Ma. This is much more pronounced than when modelling the data using QFrag, suggesting that the model needs to be allowed to undergo reheating (table **6-4**). Model **C** in figure **6.6** shows this. When reheating is allowed, a much more sensible looking thermal history emerges with a sensible temperature offset in the early part of the history followed by a rapid and short lived period of burial and re-exhumation between about 160-100Ma.

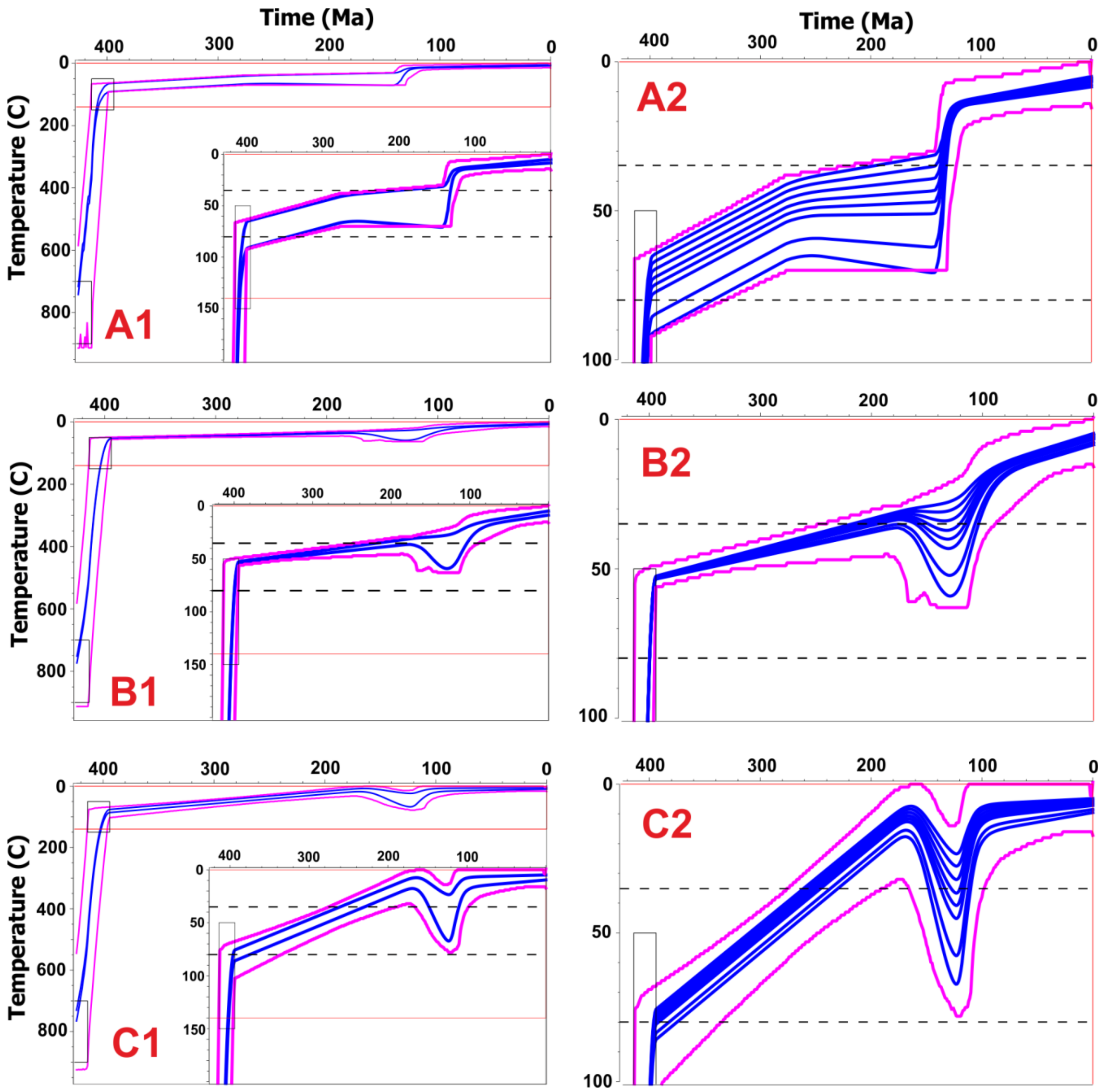

Figure 6.6: Modelling samples in profile.
Samples *SD07 – 1, SD07 – 2, SD07 – 3, SD07 – 4, SD07 – 5, SD07 – 6, BH15 – 05 and SD13 – 02/BH13 – 02* modelled in profile for 100,000 model iterations after a burn in period of 100,000 iterations. An initial T-t constraint of 800 ± 100°C at 424 ± 10Ma was used, along with a second T-t constraint at 100 ± 50°C at 404 ± 10Ma. The radiation damage model of Gautheron *et al*. (2009) was used and the age was resampled within the ascribed error of 10%. An initial temperature offset between the top and bottom samples of 26°C was used (the present day geothermal gradient under Scotland (website 2)) and this was allowed to vary over time. A present day surface temperature of 5 ± 5°C was used, with an offset between the top and bottom samples of 5 ± 5°C to account for the decrease in air temperature with altitude. Models **A** and **B** have reheating prevented, but model **C** has reheating enabled. Model **A** treats broken grains correctly as fragments, but models **B** and **C** treat broken grains incorrectly as whole grains. Panel **2** and inset on panel **1** are the same model outputs as in panel **1** but with expanded scales. Solid pink lines indicate the lower 95% credibility interval from the lowest sample in the profile (*SD13 – 02/BH13 – 02*) and the upper 95% credibility interval from the highest sample in the profile (*SD07 – 1*). Solid blue lines indicate the expected thermal history from the top and bottom samples in the profile (left panel) and each sample in the profile (right panel). See Appendix 4 for temp. offset plots (geothermal gradient).

Model output **C** may appear more sensible than **B**, giving support for the existence of a period of burial, but the reasons already outlined for preventing reheating are strong. It is far more likely that the apparent reheating of the base of the profile is as a result of increased crustal heat flow and a higher geothermal gradient at that time period as opposed to a period of burial. The irregularities observed in model output **B** actually provide evidence of the problems of modelling broken crystals incorrectly as whole crystals, rather than evidence for a period of burial for the BIC. In addition, the model output when treating fragments correctly as fragments (model **A**) is far more in keeping with the models produced when modelling samples individually (figure **6.5**), and is therefore considered a more robust thermal history reconstruction (granted the modelling in figure **6.5** uses the fragment model, the outcomes may well have supported figure **6.6** **B** and **C** had the modelling been carried out without using QFrag).

The expected thermal history T-t paths of model outputs **B** and **C** (again approximated for sample *SD07 – 3*) generate synthetic AFT ages of 370.0Ma (MTL 14.34µm) and 355.4Ma (MTL 14.15µm) (see table **6-5**). These are even older than the synthetic age for model output **A**, and therefore even further from the available AFT data. This may provide supporting evidence that model **A** (modelled with the fragment model on and no reheating) is the most consistent thermal history with the AFT data, but again it is unreasonable to draw direct comparisons between single sample AFT ages and thermal histories generated from a vertical profile.

Table 6-5: Synthetic AFT data forward modelled in QTQt using the T-t paths of figure **6.6**.

	Figure 6.6 model A	**Figure 6.6 model B**	**Figure 6.6 model C**
AFT age (Ma)	347.7	370.0	355.4
MTL (µm)	13.95	14.34	14.15

6.3.3 *Detailed analysis of a single sample*

The inbuilt options in QTQt allow for a multitude of different possible combinations of ways to model the same data. Sometimes all options may all reach the same conclusion, but in other instances changing the model parameters can result in important differences between model runs. It is impractical to model every sample using every possible combination of options, but here a logical sequence of possible combinations is provided for one selected sample (figures **6.7-6.12**). The sample chosen is *SD07 – 3* because it has a large number of grains (> 30), of which over half are fragments, allowing meaningful comparisons to be made between having the fragment model switched on or off. It is also one of the samples modelled by Persano *et al.* (2009) – SD3. This enables meaningful comparisons to be made between the published thermal history and the thermal history presented here.

Table 6-6: QTQt *SD07 - 3* experiment matrix.

No. Grains	Radiation damage model	Fragment model	Resampling option
All	RDAAM	On	No resampling
			Resampled age
			Resampled error
		Off	No resampling
			Resampled age
			Resampled error
	Gautheron	On	No resampling
			Resampled age
			Resampled error
		Off	No resampling
			Resampled age
			Resampled error
Fragments only	RDAAM	On	No resampling
			Resampled age
			Resampled error
		Off	No resampling
			Resampled age
			Resampled error
	Gautheron	On	No resampling
			Resampled age
			Resampled error
		Off	No resampling
			Resampled age
			Resampled error
20	Gautheron	On/Off	Resampled age
15	Gautheron	On/Off	Resampled age
10	Gautheron	On/Off	Resampled age
6	Gautheron	On/Off	Resampled age
3	Gautheron	On/Off	Resampled age

Firstly QTQt has the option for placing up to five T-t constraints that the thermal history must pass through. Placing T-t constraints is a necessity in some modelling software packages (e.g. HeFTy, (Ketcham, 2005)) but rather goes against the transdimensional MCMC modelling philosophy of QTQt (Gallagher, 2012). That being said, it can be considered logical to place a nailed on certainty T-t constraint such as the age of intrusion if modelling an igneous sample or the stratigraphic age if modelling a sedimentary sample. Doing so can help define the models start point.

There are currently three options for how to accommodate radiation damage in the programming. Firstly no radiation damage model can be applied, meaning that every crystal follows the same diffusion kinetics regardless of eU content. This may be a logical step to save computational run time if there is only a small range of eU concentrations within a sample, but otherwise it can be considered an over simplification as there is little doubt that radiation damage accumulation plays a significant role on diffusion kinetics (e.g. Shuster *et al.*, 2006). There is then a choice between two different radiation damage models, RDAAM (Flowers *et al.*, 2009) and the radiation damage model of Gautheron *et al.* (2009) (see **Chapter 2**, sections *2.2.1.2* and *2.2.2.6*). Each has its merits, and there is no clear answer as to which should be preferred. Indeed it is likely that both are currently oversimplifications of the full impacts of radiation damage (e.g. see the discussions of this topic in **Chapter 5** of this thesis).

AHe ages are inherently imprecise, far more than the true analytical uncertainty suggests. It is therefore possible to resample either the age or the input error of each crystal within the programming (but not both simultaneously), which tells the program that the age which it is given is not 100% certain. If the age is chosen to be resampled, then QTQt uses Monte Carlo sampling of the observed age, based on a normal distribution centred on the input age, with a standard deviation equal to the input error (see QTQt user guide). This means that the observed age which is modelled by the program can differ from the observed age which has been given as an input (within the bounds of the ascribed error margin) if doing so enables a better data fit than would otherwise be the case. In practice this not only accounts for uncertainties in the analytical process, but also the predictive model (i.e. diffusion kinetics), therefore resampling the age should arguably be considered best practice as a matter of routine.

Alternatively QTQt can resample the error, which samples a scaling factor between 0.1 and 10 which is used to determine the data fit (see QTQt user guide). This effectively means that the error is either increased (high scaling factor [>1]) making the data (observed ages) more precise, or decreased (low scaling factor [<1]) making the data less precise. This is to enable the error bars on the observed vs predicted plots to cross the 1:1 line. Resampling the error should be used when it is unclear how reliable the error estimates are.

The fragment model of Brown *et al.* (2013) and Beucher *et al.* (2013) can be switched on or off on a grain by grain basis. This enables you to simply model all grains as if they are whole; ignoring the fragment effect (this is standard practice for most researchers outside of the University of Glasgow research group), or to model fragments as fragments and whole crystals as whole crystals. It is even possible to model all crystals as fragments; there is little logic in doing this, but it shouldn't have a detrimental effect on the outcome providing our understanding of the fragment effect is accurate. It may therefore be beneficial in some instances to model all grains as fragments if observations haven't been made prior to analysis of the type of grain.

Finally, there is the option to prevent reheating (i.e. burial) within the model. This is a logical step in most situations as there should be evidence in the geological record of sedimentation if the sample has experienced reburial. This can be particularly useful when T-t constraints have been placed at near surface temperatures, but the model wants to still be warm/hot at those times. This can prevent unrealistic 'U' shaped depressions in the thermal history which have no geological justification. Unless where stated otherwise, reheating has been prevented in all thermal history models presented in this chapter, as there is no geological evidence of significant reburial around the BIC.

6.3.3.1 T-t constraints vs. no T-t constraints: To demonstrate the usefulness of providing as a minimum a T-t constraint for the age of intrusion, the sample has been modelled both with and without constraints (figure **6.7**). Both versions use the radiation damage model of Gautheron *et al.* (2009), have the fragment model on and no reheating. When given no constraints, it is common in some types of thermal history for the model output to start at the time corresponding to the top of the PRZ (c. 35°C), effectively giving a flat thermal history from that time to the present. This has been the case with many of the samples from the upper half of the BIC when modelled with no T-t constraints (modelling test runs with fewer iterations, not presented here). In the case of *SD07 – 3*, when run for 100,000 model iterations the model does go back further, starting at c. 350Ma (as shown in figure **6.7**) but it still doesn't know much about the oldest part of the thermal history.

Providing a T-t constraint at the age of intrusion forces the model to start at this point in time. In this instance a realistic intrusive temperature has also been chosen for the constraint window. A realistic temperature is not necessary if the aim is purely to force the model to start at a sufficiently old point in time, a temperature window hotter than c. 120°C will suffice. An accurate temperature is required however if the aim is to calculate the denudation rate for this portion of the thermal history. Here a T-t constraint has also been placed at 404Ma forcing the model to reach near surface temperatures at this point. This is because the BIC is thought to have reached near surface depths by this point in time (due to the nearby GVC). A very broad temperature window of 100 ± 100°C has been used here as the exact depth is unknown (though expected to be c. 2km (Fraser *et al.*, 2004)). This adds extra clarity to the portion of the thermal history which is unconstrained by the raw data alone.

Using the models as a template to generate synthetic AFT data in QTQt gives an age of 329.0Ma (MTL 14.7µm) for model **A** (no constraints) and 329.3Ma (MTL 14.65µm) for model **B** (T-t constraints). These ages are effectively the same, indicating that the portion of the thermal history which the AFT system is sensitive to (c. 70-130°C) is unaffected by the T-t constraints placed on model **B**. In this instance the AHe data adequately resolves this portion of the thermal history without the aid of T-t constraints.

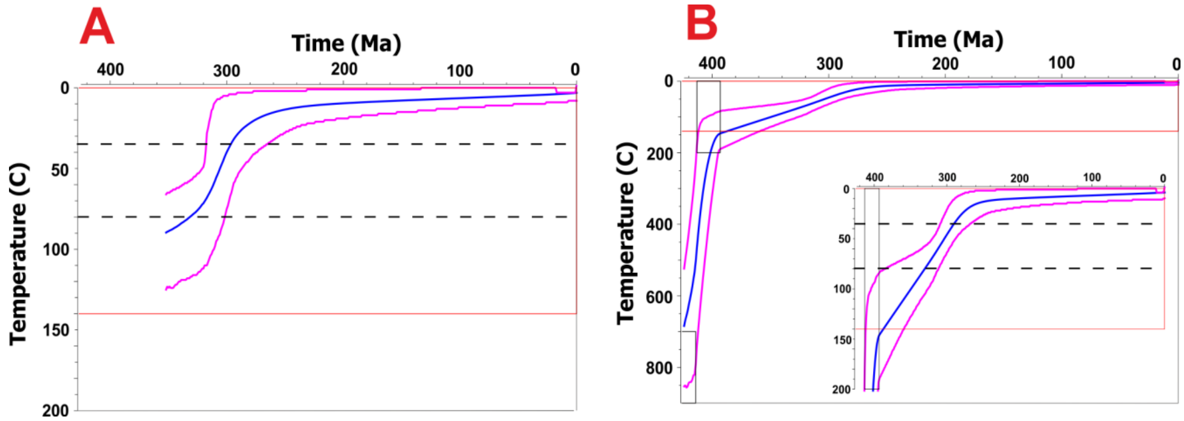

Figure 6.7: Thermal history inversion of *SD07 – 3* with and without T-t constraints.
Solid pink lines = 95% credibility intervals, solid blue line = expected thermal history. Models run with a burn-in period of 10,000 iterations and a post burn-in of 100,000 iterations. Each model uses the radiation damage model of Gautheron *et al.* (2009), has the fragment model switched on (for fragments) and no reheating selected. **A**: no T-t constraints were used. **B**: an initial T-t constraint of 800 ± 100°C at 424 ± 10Ma (intrusive age, (Weiss and Troll, 1989; Fraser *et al.*, 2000)) and a second 'near surface' constraint of 100 ± 100°C at 404 ± 10Ma (Fraser *et al.*, 2004) are used. Inset: expanded scale to emphasise the PRZ. See Appendix 4 for corresponding observed vs. predicted plots and probability density distributions.

It can be seen in figure **6.7** that there is a potential plateau in the temperature before the rapid cooling at c. 300Ma, but the raw data lacks the information to constrain the history before this point. Adding the two T-t constraints shows that the sample cooled extremely rapidly from intrusion to within a few km of the surface at c. 400Ma, and then continued to cool/uplift at a slower rate for another c. 100Ma before a possible final increase in uplift to the surface at c. 300Ma. In this instance the use of T-t constraints is beneficial, but similar conclusions can be drawn from the modelling without T-t constraints (as also demonstrated by the synthetic AFT data). This provides some validity to the chosen constraints, as the model is in lose agreement with them without being given that prior knowledge.

6.3.3.2 Modelling with RDAAM (Flowers et al., 2009): The models have been run for the remaining permutations with the use of the intrusive age constraint, but not the 'near surface' constraint. The intrusive age constraint defines the model start point, but the second constraint hasn't been used in these cases to allow maximum model freedom, and to explore which modelling options are able to find this part of the history based purely on the raw data.

Firstly the data has been modelled using the RDAAM of Flowers *et al.* (2009). The data has been modelled through three pairs of experiments: 1 – taking the observed age and input error as fact, 2 – resampling the observed age and 3 – resampling the input error (see table **6-6**). Each option has been run with the fragment model switched on (column **A** in figure **6.8**), and the fragment model switched off (column **B** in figure **6.8**).

In each modelling permutation the overall thermal history is broadly the same – rapid cooling/uplift from intrusion to the near surface at a given time, followed by very slow (if any) cooling/uplift for the remainder of the history. The differences come in the time that the sample reaches the PRZ, and therefore the rate of initial uplift. Every model can feasibly cool the sample into the PRZ by 404Ma, as shown by the upper pink line (95% credibility interval), but the plateauing off of the lower pink line and blue line (expected thermal history) occur at different points. The blue lines in QTQt outputs are an average of all the accepted models with weightings and a smoothing applied, they do not represent any single model run. The 'best fit' single thermal history model run (not shown here, see max. likelihood models on plots in Appendix 4) will often differ slightly from the blue line, but may be less realistic.

With the exception of the model for resampling the error and modelling fragments as whole grains (figure **6.8**, panel **B3**), the trend is of slower initial cooling but with a greater uncertainty as first the age is resampled, and then the error. This results in the plateauing of the blue line at younger ages, which should not strictly be interpreted as the model reaching the PRZ at a younger age (though this is one interpretation), as it can equally be interpreted as the model being less certain as to what time it needs to reach the PRZ by. This is not surprising, when resampling the age or the error you are telling the QTQt that you are less certain about the input you are giving it. It is therefore logical to expect the output to be less precise (broader 95% credibility intervals) as a result.

Synthetic AFT data for approximations of the thermal histories depicted in figure **6.8** **A** have been forward modelled in QTQt. Each forward model starts at c. 800°C and 420Ma and cools rapidly to the near surface by either c. 400Ma, c. 300Ma or c. 250Ma (see Appendix 6). The most rapid cooling (change in cooling rate at c. 400Ma) generates a synthetic AFT age of 355.4Ma (MTL 13.86), the middle option generates a synthetic age of 313.2Ma (MTL 14.99µm) and the slowest cooling rate (levelling off at c. 250Ma) generates an age of 266.1Ma (MTL 14.92µm). All these ages are older than the published age of Persano *et al.* (2007) for the same sample (257Ma), but as the new T-t paths shown in this chapter are very different to the published thermal history of Persano *et al.* (2007), the synthetic and published AFT ages should not be expected to be comparable.

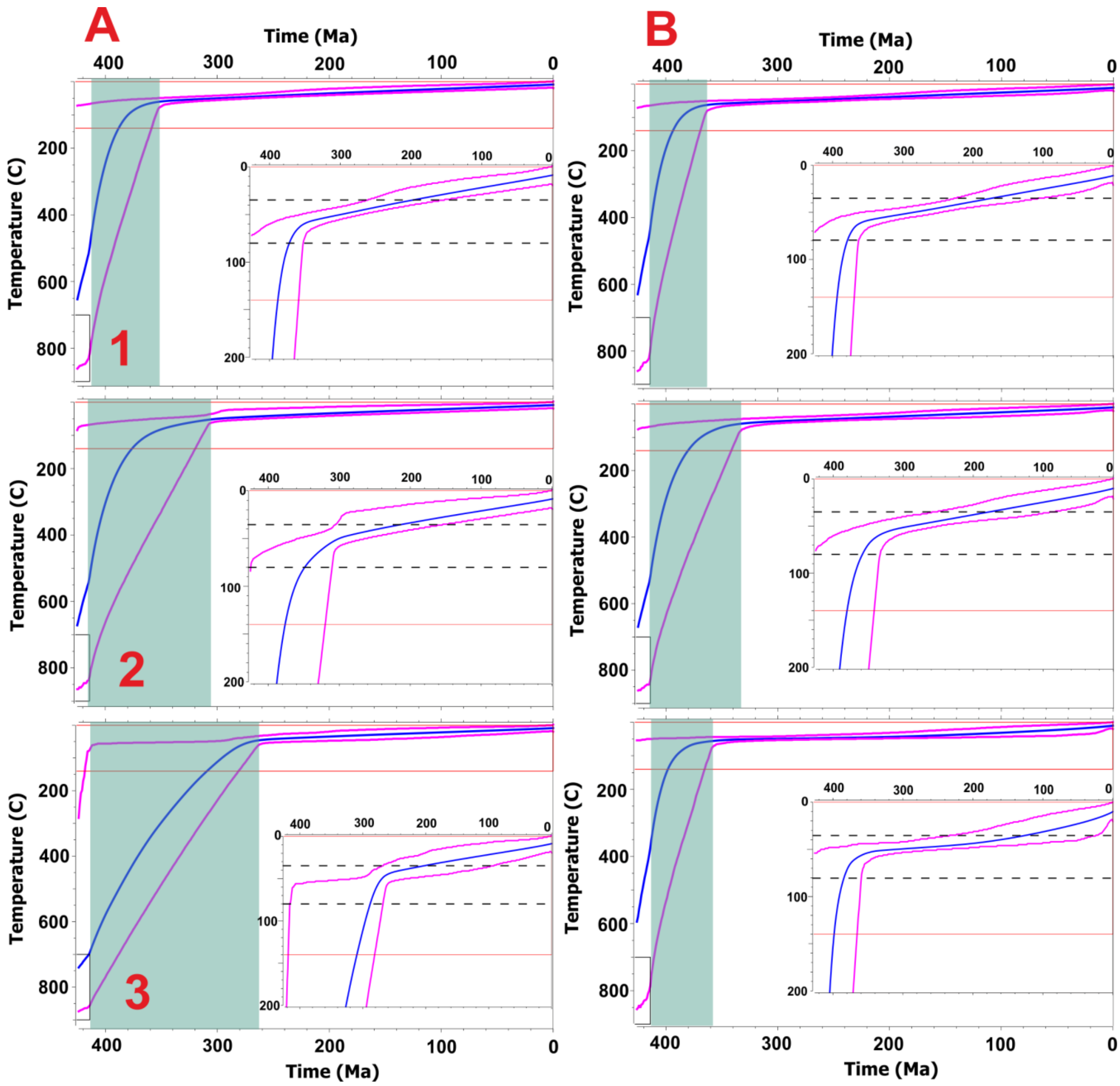

Figure 6.8: Thermal history inversion of *SD07 – 3* with RDAAM (Flowers *et al*., 2009).
Solid pink lines = 95% credibility intervals, solid blue line = expected thermal history. Models run with a burn-in period of 10,000-20,000 iterations and a post burn-in of 100,000 iterations, an initial T-t constraint of 800 ± 100°C and 424 ± 10Ma (intrusive age, (Weiss and Troll, 1989; Fraser *et al*., 2000)) and no reheating. Column **A**: fragment model turned on. Whole grains are treated as whole grains and 1T grains are treated explicitly as fragments of unknown initial length. Column **B**: fragment model turned off. All grains are treated as whole grains regardless of their true nature. Row **1**: no resampling of age or error. Row **2**: MCMC resampling of the age within a bell curve centred on the observed age and a standard deviation equal to the input error. Row **3**: resampling of the error with a scaling factor between 0.1 and 1. Green shading indicates period of rapid cooling for comparative purposes. Inset: same plot with an expanded vertical scale of 200°C to provide greater clarity of the PRZ (horizontal black dashed lines). See Appendix 4 for corresponding observed vs. predicted plots and probability density distributions.

There are subtle differences in the timing of the plateauing off of the thermal history between modelling fragments correctly as fragments and incorrectly as whole crystals (columns **A** and **B**). However the differences aren't systematic, and with the exception of resampling the error, they are incredibly small (and therefore not significant). It is unclear as to why resampling the error should lead to the biggest difference between having the fragment model on and off, but overall it is unsurprising that modelling the fragment data incorrectly as whole crystals can still return the same thermal history. This is because the thermal history appears to be very simple and involving very rapid initial cooling. As shown in **Chapter 4**, this type of thermal history is fairly easy to reconstruct. In addition there are a sufficient number of whole crystals in the sample to provide the program with enough accurate thermal history information to return the same thermal history.

6.3.3.3 Modelling with the radiation damage model of Gautheron et al. (2009): The same three pairs of experiments have been carried out using the radiation damage model of Gautheron *et al.* (2009) (see table **6-6**) as opposed to RDAAM (figure **6.9**). A major difference is apparent between these models and the models in figure **6.8**; the rate of initial cooling is much better constrained (narrower 95% credibility intervals) using the diffusion kinetics of Gautheron *et al.* (2009) than RDAAM. This does not mean that the thermal history inversion is better or more accurate however. It is actually less accurate, as we know the sample was within a few km of the surface at 404Ma (Fraser *et al.*, 2004) but this is not seen in most of the models in figure **6.9**. Another difference is the temperature (depth) that the sample reaches before halting its rapid cooling/uplift. When using RDAAM the thermal history plateaus off at a hotter temperature than when using the Gautheron model. This requires the sample to spend a greater period of time in the PRZ when using RDAAM.

There is very little difference between the models run without resampling and with resampling of the age in this case. There is a bigger difference when resampling the error. With the error resampled the initial cooling is less well constrained (broader credibility intervals) but this also means that the model is capable of reaching near surface depths closer to 404Ma. This means that despite being less well constrained, the model is actually more accurate to what we know to be the true thermal history (for the initial cooling). The fact that resampling the error gives the most accurate thermal history in this case may suggest that the error estimates (i.e. the input error) are unreliable. The uncertainty is not surprising as the error is set at a nominal 10%, but this is because the calculated analytical error highly underestimates the true error. The error may in reality be even greater than 10%.

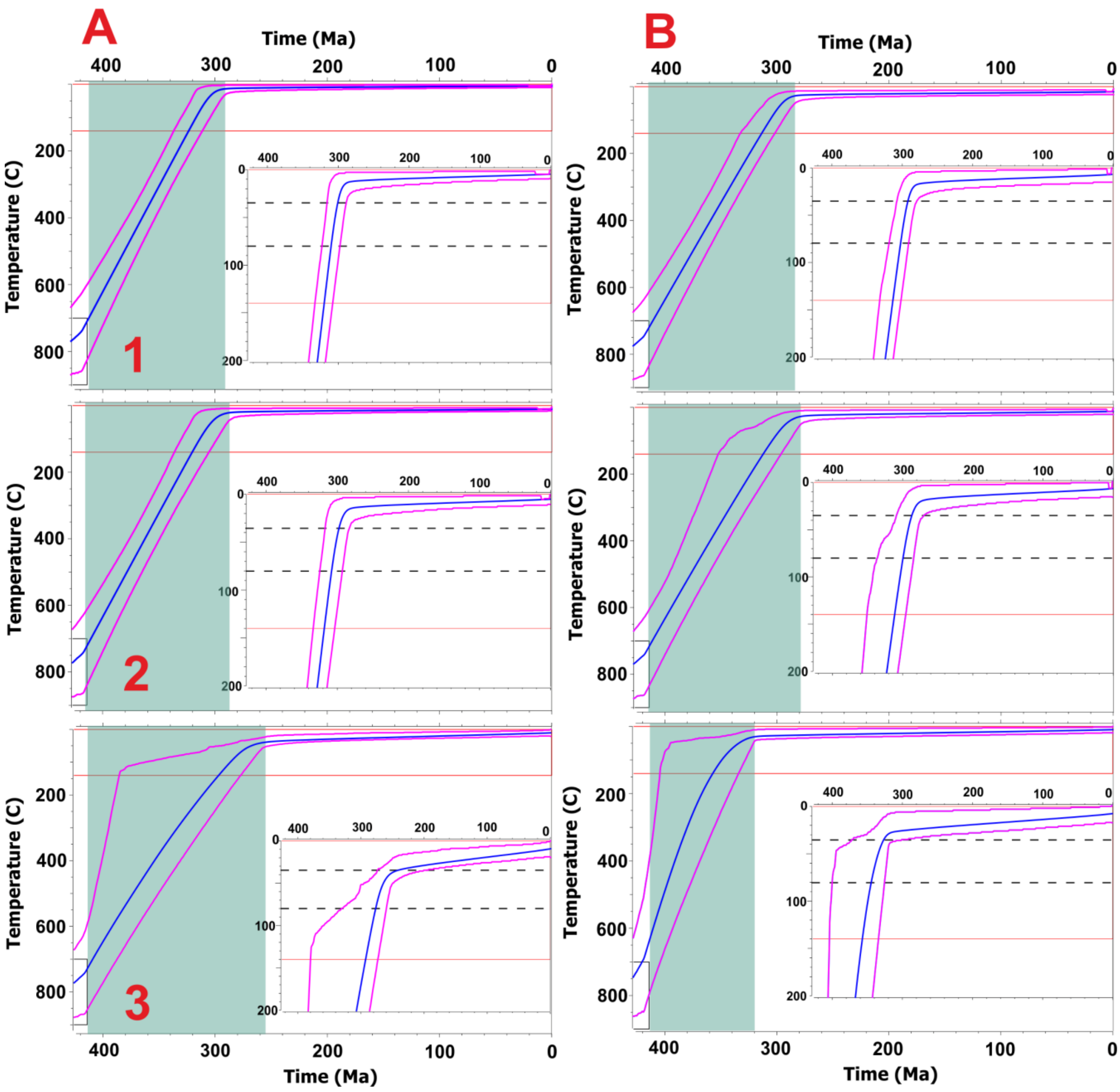

Figure 6.9: Thermal history inversion of *SD07 – 3* with Gautheron *et al*. (2009).
Solid pink lines = 95% credibility intervals, solid blue line = expected thermal history. Models run with a burn-in period of 10,000-20,000 iterations and a post burn-in of 100,000 iterations, an initial T-t constraint of 800 ± 100°C and 424 ± 10Ma (intrusive age, (Weiss and Troll, 1989; Fraser *et al*., 2000)) and no reheating. Column **A**: fragment model turned on. Whole grains are treated as whole grains and 1T grains are treated explicitly as fragments of unknown initial length. Column **B**: fragment model turned off. All grains are treated as whole grains regardless of their true nature. Row **1**: no resampling of age or error. Row **2**: MCMC resampling of the age within a bell curve centred on the observed age and a standard deviation equal to the input error. Row **3**: resampling of the error with a scaling factor between 0.1 and 1. Green shading indicates period of rapid cooling for comparative purposes. Inset: same plot with an expanded vertical scale of 200°C to provide greater clarity of the PRZ (horizontal black dashed lines). See Appendix 4 for corresponding observed vs. predicted plots and probability density distributions.

As with figure **6.8**, there is very little difference between the model outputs when modelling fragments as fragments (column **A**) verse modelling fragments as whole crystals (column **B**). The biggest difference is seen when resampling the error (figure **6.9 A3** and **B3**) where the plateauing off of the expected thermal history occurs at a younger age when the fragment model is turned on compared to when it is turned off. This is the same pattern as was observed using RDAAM.

6.3.3.4 Modelling fragments only with RDAAM (Flowers et al., 2009): To account for the fact that a significant amount of thermal history information is carried by the whole crystals in the sample, and this may be masking any evidence of the fragment effect; the same pairs of experiments have been carried out only using the broken crystals from *SD07 – 3* (see table **6-5**). This includes 21 crystals, so is still a suitably large sample size in its own right.

As with modelling the full complement of crystals, the RDAAM kinetics provide a less well constrained initial cooling. The same pattern is also observed of the history plateauing off at a younger age as first the age and then the error is resampled (figure **6.10**). Conversely the initial cooling becomes more constrained when the error is resampled, not less. It does increase when the age is resampled as per modelling the full sample.

Although the thermal history is still broadly the same, there is more of a difference between modelling the fragments as fragments (column **A**) or as whole crystals (column **B**). The expected thermal history (blue line) follows the same two stage cooling trend (although it plateaus above the PRZ when the fragment model is turned on, and within the PRZ when turned off) but the credibility interval (upper pink line) hints at a different thermal history. With the fragment model turned on there is the possibility within the credibility intervals for the sample to cool rapidly to near surface temperatures at 404Ma and then plateau for c. 100Ma. This can then be followed by a second brief rapid cooling at c. 300Ma before remaining near the surface until the present. This is what was seen in figure **6.7** when the use of T-t constraints was examined, and includes the initial part of the thermal history which we know to be accurate. With the fragment model turned off this intermediate plateau phase isn't seen in the model output. The maximum posterior likelihood model (see Appendix 4), also demonstrates the two stepped cooling when fragments are modelled as fragments, but not when modelled as whole grains.

When the age is resampled, the difference between using the fragment model or not is less apparent, although arguably still present. With the fragment model turned off the potential second rapid cooling phase at c. 300Ma is less pronounced, leading to the sample remaining at a higher temperature (and therefore in the PRZ) for longer. Unlike in previous figures, when the error is resampled there is effectively no difference in the model output between having the fragment model on or off.

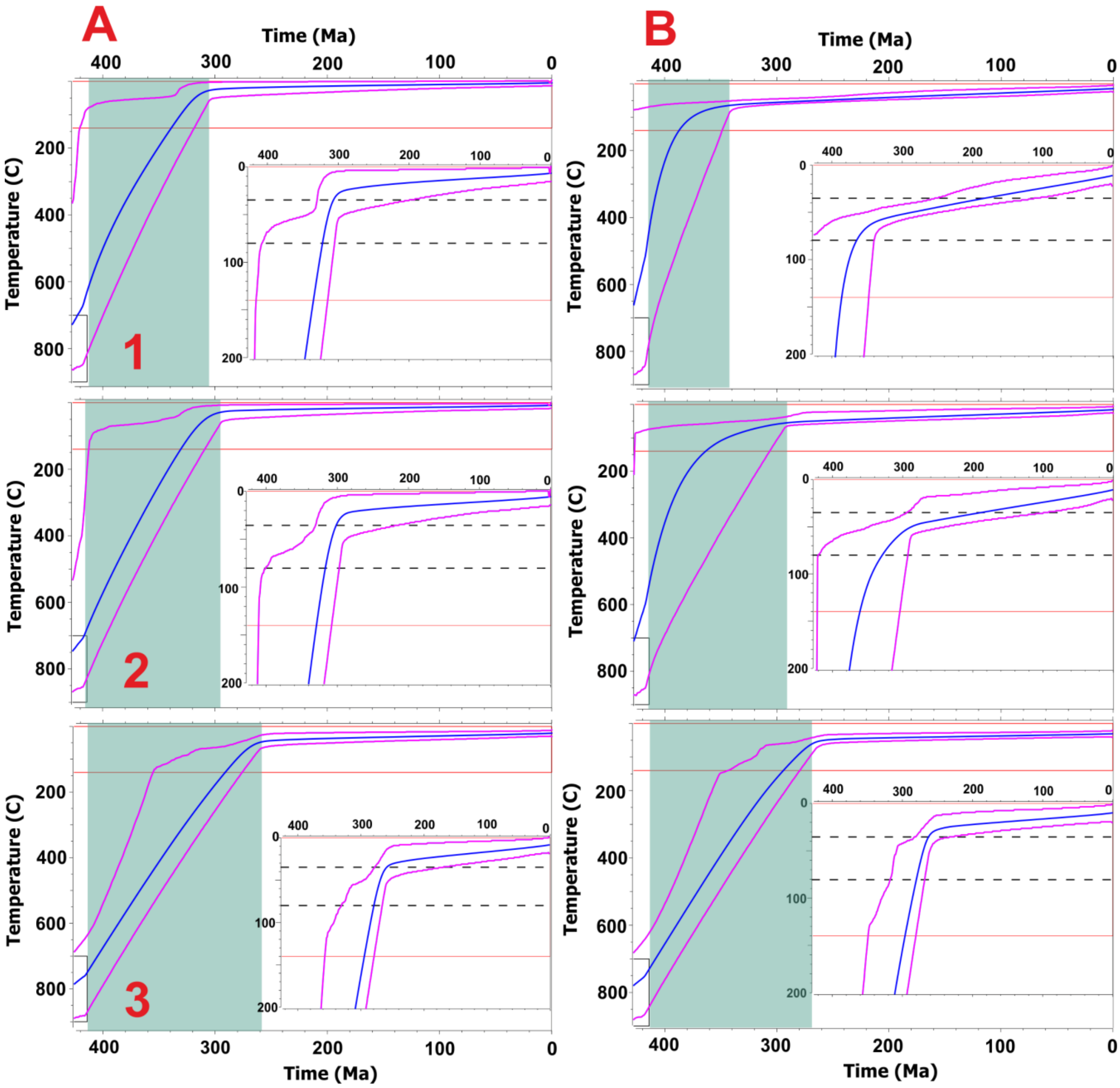

Figure 6.10: Thermal history inversion of *SD07 – 3* broken grains only with RDAAM (Flowers *et al*., 2009). Solid pink lines = 95% credibility intervals, solid blue line = expected thermal history. Models run with a burn-in period of 10,000-20,000 iterations and a post burn-in of 100,000 iterations, an initial T-t constraint of 800 ± 100°C and 424 ± 10Ma (intrusive age, (Weiss and Troll, 1989; Fraser *et al*., 2000)) and no reheating. Column **A**: fragment model turned on. Whole grains are treated as whole grains and 1T grains are treated explicitly as fragments of unknown initial length. Column **B**: fragment model turned off. All grains are treated as whole grains regardless of their true nature. Row **1**: no resampling of age or error. Row **2**: MCMC resampling of the age within a bell curve centred on the observed age and a standard deviation equal to the input error. Row **3**: resampling of the error with a scaling factor between 0.1 and 1. Green shading indicates period of rapid cooling for comparative purposes. Inset: same plot with an expanded vertical scale of 200°C to provide greater clarity of the PRZ (horizontal black dashed lines). See Appendix 4 for corresponding observed vs. predicted plots and probability density distributions.

6.3.3.5 Modelling fragments only with the radiation damage model of Gautheron et al. (2009): As before, the same set of experiments have been run for fragments only using the diffusion kinetics of Gautheron *et al.* (2009) (figure **6.11**). There is markedly less of a difference between modelling just fragments and modelling all the crystals in the sample when using the Gautheron kinetics as opposed to RDAAM. There is also very little difference in the output when using the fragment model or not (columns **A** and **B** in figure

6.11). Again the exception is when resampling the error, which shows a large difference in the rate and timing of the initial cooling, with over 100Ma differential between the respective times of plateauing. In this instance it is when the fragment model is switched on that the cooling is most rapid, plateauing c. 380Ma, whereas with the fragment model turned off the thermal history plateaus at c. 260Ma.

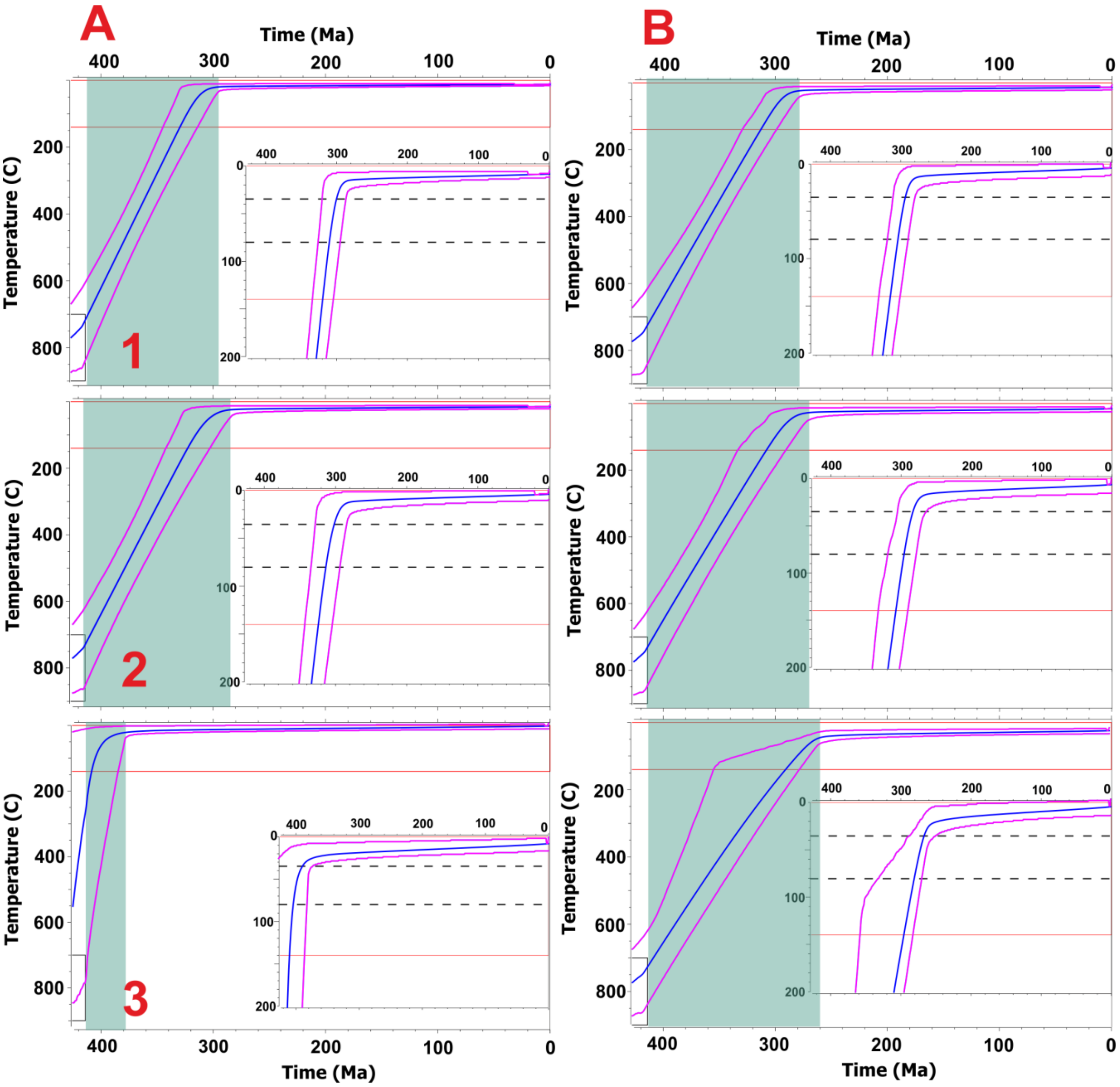

Figure 6.11: Thermal history inversion of *SD07 – 3* broken grains only with Gautheron *et al*. (2009). Solid pink lines = 95% credibility intervals, solid blue line = expected thermal history. Models run with a burn-in period of 10,000-20,000 iterations and a post burn-in of 100,000 iterations, an initial T-t constraint of 800 ± 100°C and 424 ± 10Ma (intrusive age, (Weiss and Troll, 1989; Fraser *et al*., 2000)) and no reheating. Column **A**: fragment model turned on. Whole grains are treated as whole grains and 1T grains are treated explicitly as fragments of unknown initial length. Column **B**: fragment model turned off. All grains are treated as whole grains regardless of their true nature. Row **1**: no resampling of age or error. Row **2**: MCMC resampling of the age within a bell curve centred on the observed age and a standard deviation equal to the input error. Row **3**: resampling of the error with a scaling factor between 0.1 and 1. Green shading indicates period of rapid cooling for comparative purposes. Inset: same plot with an expanded vertical scale of 200°C to provide greater clarity of the PRZ (horizontal black dashed lines). See Appendix 4 for corresponding observed vs. predicted plots and probability density distributions.

6.3.3.6 Modelling fewer grains using the radiation damage model of Gautheron et al. (2009): Traditionally AHe investigations involve only 3-5 grains per sample. Given the amount of natural dispersion possible (as shown in **Chapter 5**) this is highly inadequate to give a fair representation of the sample. Brown *et al*. (2013) stipulated that a minimum of c. 20 grains are required to make the most of the potential thermal history information contained within the natural dispersion.

To demonstrate the effect of modelling fewer grains, a number of grains have been systematically cut from the overall sample to give reduced sample sizes of 20, 15, 10, 6 and 3 grains respectively. Despite being systematic – the crystals were cut from the bottom of the list (as presented in **Chapter 5**) – this is also a random selection of grains. This is because the initial picking process gives a random selection of grains, and the order that these are analysed and therefore listed in the data table is also random. Therefore there is no de-selection bias by cutting from either the bottom or top of the list (or any point in the list for that matter). The selection is not random between each set however, as the same three grains are used in the set of six, and those six in the set of ten and so on. This means that any differences in the model output are due to having less grains overall and not different grains with different ages between each set.

All the models have been run with no reheating, using the radiation damage model of Gautheron *et al*. (2009) and with the initial T-t constraint of 800 ± 100°C and 424 ± 10Ma. The results are shown in figure **6.12**. Although all the models follow the same broad thermal history of rapid cooling to near surface depths followed by very little cooling until the present, there is a clear and systematic variation as the number of grains decreases. The timing of the plateauing becomes increasingly younger as the number of grains decreases, and the initial cooling becomes less well constrained. The change in the timing of the plateauing could partially be explained by the fact that the oldest grains in the sample are being cut, decreasing the age of the effective mean. But this is not strictly the case each time as the ages are distributed randomly; meaning that the effective mean age increases when cutting from ten to six and from six to three grains (c. 162 [10 grains], c. 163 [6 grains] and c. 171 [3 grains]).

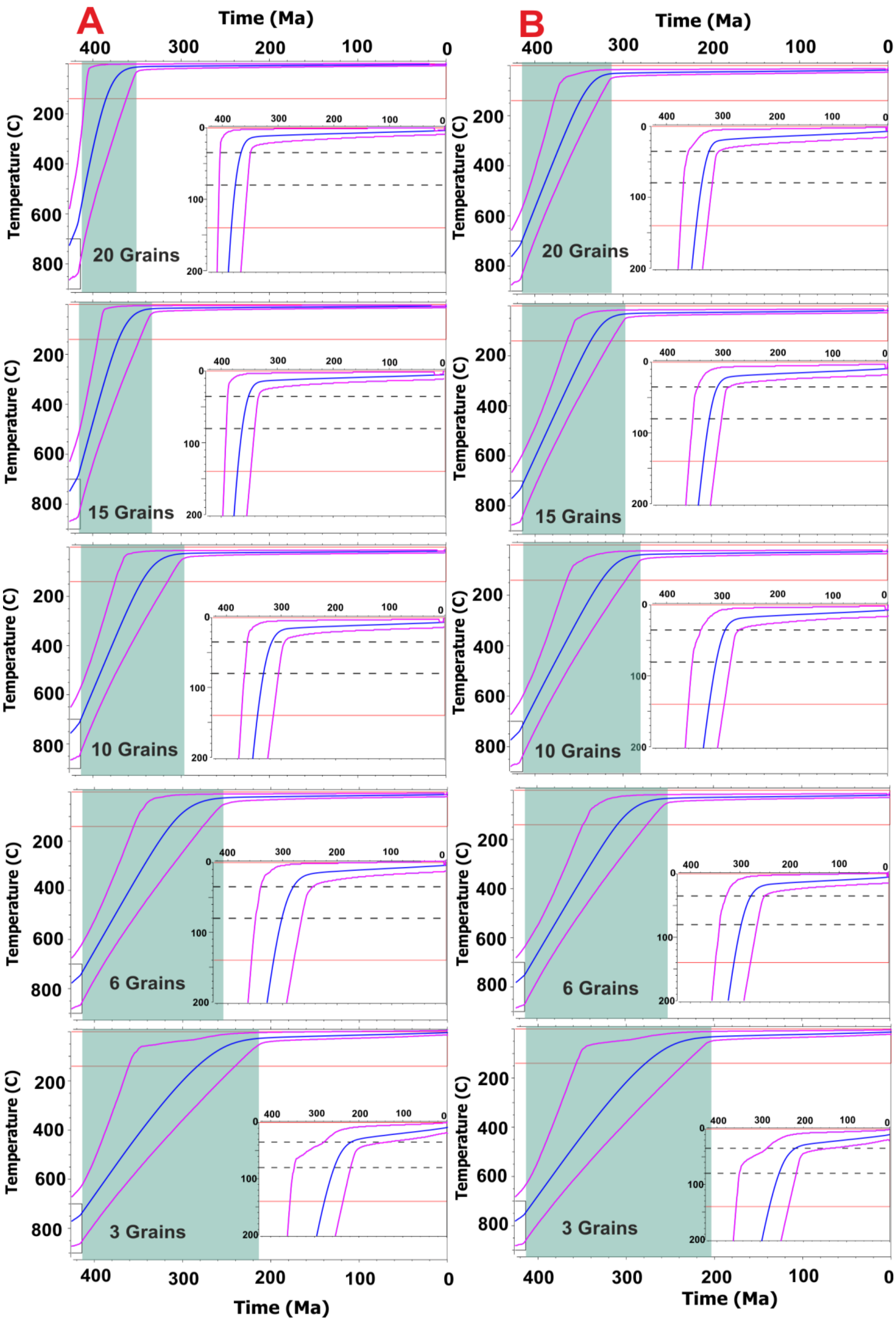

Figure 6.12: Thermal history inversion of *SD07 – 3* with Gautheron *et al*. (2009) using fewer grains. Solid pink lines = 95% credibility intervals, solid blue line = expected thermal history. Models run with a burn-in period of 10,000-20,000 iterations and a post burn-in of 100,000 iterations, an initial T-t constraint of 800 ± 100°C and 424 ± 10Ma (intrusive age, (Weiss and Troll, 1989; Fraser *et al*., 2000)) and no reheating. Column **A**: fragment model turned on. Whole grains are treated as whole grains and 1T grains are treated explicitly as

fragments of unknown initial length. Column **B**: fragment model turned off. All grains are treated as whole grains regardless of their true nature. Green shading indicates period of rapid cooling for comparative purposes. Inset: same plot with an expanded vertical scale of 200°C to provide greater clarity of the PRZ (horizontal black dashed lines). See Appendix 4 for corresponding observed vs. predicted plots and probability density distributions

An interesting observation is that when the full complement of grains in the sample are analysed (figure **6.9 A2** and **B2**), the plateau shifts the other way, i.e. it occurs at a younger age with 30 grains than it does with 20. This bucks the trend observed in figure **6.12**. The most logical explanation for this is that it is as a result of the age of the grains which have been cut, leading to an older effective mean (c. 164 for the whole sample vs. c.176 for 20 grains). It may also be down to the specific closure temperature of the grains which have been cut, related to their individual compositions and geometries.

The broadening of the credibility intervals as the number of grains decreases is not surprising. The model has much less information to work with so will inevitably become less well constrained as the number of grains decreases. This is one line of evidence as to the importance of analysing larger sample sizes. The fact that QTQt can still find a broadly accurate thermal history with only three grains is down to the simplicity of the thermal history. A more complicated thermal history such as one with reheating or multiple stages of cooling would likely return very different outcomes with three grains verses twenty.

The differences between modelling with the fragment model on or off are again very marginal or non-existent. The greatest difference is seen when modelling twenty grains, which shows some 20-30Myr difference in the age of plateauing of the thermal history, this occurring at an older age when using the fragment model. Modelling with fifteen grains shows a similar disparity, but this has all but gone by ten grains. Again this may partially be an artefact of the proportion of whole grains to fragments in each experiment, but is not solely the explanation because two of the three grains in the final experiment are fragments.

6.4 Thermal history interpretation

The thermal history of the BIC can be broadly divided into four distinctive phases of cooling/uplift starting from the time of intrusion. This interpretation is made based on the evaluation of all models presented here in conjunction; no one single model output depicts this full history. When modelled in profile a version of this history becomes clear, but it is the individual models which provide clarity and support for this thermal history interpretation. The earliest part of the history is constrained by prior geological knowledge, but the rest is derived from the data alone.

6.4.1 *Four phases of uplift*

Starting from the intrusion of the complex at c. 424Ma, the four phases of cooling/uplift are as follows:

1) Rapid uplift of c. 8km (from c. 10 - 2km depths) between c. 424 - 404Ma (Upper Silurian – Lower Devonian) at a rate of c. 0.4km Ma^{-1}.

2) Slower continued uplift/cooling between c. 404 and c. 300Ma (Lower Devonian – end Carboniferous). Likely up to c. 1km of denudation. Top of the profile uplifted above the PRZ by the end of the period.

3) Very slow/no uplift over 150Myrs from c. 300 - 150Ma (Permian – Upper Jurassic). Lower half of profile remaining in PRZ.

4) Rapid uplift at c. 140Ma (Lower Cretaceous) bringing the top of profile to within a few 10's to 100's of meters of the surface and the entire profile out of the PRZ. Only minor (<1km) erosion/denudation since c. 140Ma.

6.4.4.1 Phase 1: The initial very rapid cooling phase is based on the known geological constraints and is not recorded by any of the samples, which were all too hot to start accumulating significant ^{4}He at this point (some individual grains from the upper samples will have begun accumulating some ^{4}He by the end of this period). The age of intrusion is given as 424 ± 4Ma based on the U-Pb dating of zircons (Fraser *et al.*, 2000), the authors later giving an updated more precise age of 423 ± 0.3Ma (Fraser *et al.*, 2004). The age of the neighbouring GVC constrains the end of the rapid uplift at 404 ± 4Ma (Fraser *et al.*, 2000). For reasons discussed in section 6.1.1 this places the top of the BIC profile at a crustal depth of c. 2km at this time. This results in an average uplift/denudation rate of c. 0.4km Ma^{-1} for this period.

The very rapid uplift is a consequence of the ongoing Caledonian Orogeny, which assembled the major tectonic segments of the British Isles during this time. The uplift was caused by a combination of major thrusting and folding, as well as isostatic readjustment owing to the increased buoyancy of the heavily intruded crust. Numerous volcanic and igneous complexes were formed before and during this time period on what was then the continent of Laurentia.

The term ‘Caledonian Orogeny’ is a broad term which encompasses multiple phases of collisions and mountain building spanning some 200Myrs, and as such is more appropriately used as a geographic term as opposed to defining a specific time period (McKerrow *et al.*, 2000). The peak of regional metamorphism pre-dates the formation of the BIC, occurring at c. 470Ma (Dewey and Mange, 1999). The final closure of the Iapetus Ocean had occurred by c. 430Ma (Atherton and Ghani, 2002), with the rapid uplifting of the BIC during *Phase 1* therefore associated with the final continent-continent collisional stages of the Caledonian Orogeny. During this phase, rapid un-roofing of the ‘late’ Caledonian granites was seen across the Laurentian margin, with 10-20km of uplift and erosion reported throughout the Scottish and Irish Caledonides (Atherton and Ghani, 2002 and references therein). The end of *Phase 1* corresponds with the culmination of the Grampian phase of the wider orogeny, which ceased at c. 400Ma (Emsian stage, Lower Devonian) in the Scottish region of the Laurentian margin (McKerrow *et al.*, 2000).

The vast quantities of sediment eroded during this period of rapid un-roofing are hard to trace directly, having being dispersed far and wide and likely recycled. Late Silurian sediments are found in the Midland Valley (Cameron and Stephenson, 1985) and the Southern Uplands (Stone *et al.*, 2012), as well as in basins surrounding the Scottish mainland, but it is likely that a significant volume of sediment has been removed entirely from the Scottish region (Watson, 1983).

6.4.4.2 Phase 2: After c.400Ma the rate of uplift decreased rapidly, giving c. 100Myrs of steady uplift. This likely resulted in a further c. 1km of denudation. The thermal history inversions of samples in the upper 500m of the profile record this phase. It is unclear based on the models from individual samples whether this period saw steady uplift over the c. 100Myrs or minimal uplift for most of that time followed by a brief pulse of rapid uplift at the end of the period. Clarification on this is provided by modelling the samples in a vertical profile (figure **6.6**), which confirms the steady rate of cooling over the time period. The lower 500m of the profile remained below the PRZ prior to this uplift, only being brought into the PRZ at the culmination of the uplift. After the uplift, the 35°C isotherm cut across the present day profile at c. 500-600m elevation (see figure **6.5**).

The uplift during this phase corresponds with the ending of the Caledonian Orogeny. The latest tectonic movements directly associated with the Caledonian Orogeny ceased around c. 360Ma (McKerrow *et al.*, 2000), with the major collisions having ceased some 30Myrs earlier (c. 390Ma) at the end of the Acadian phase (Mendum, 2012). Post collision the uplift was as a result of the continued isostatic readjustment of the thickened crust.

Over recent decades the links between climate and erosion with uplift have become increasingly apparent (e.g. Molnar and England, 1990; Willett, 1999; Roe *et al.*, 2003; Clift *et al.*, 2008; West *et al.*, 2013). It is not just tectonics which drive uplift but also a positive feedback loop between relief, erosion and uplift with all three being influenced by the climate. Initial tectonically driven uplift creates enhanced relief, which encourages erosion of the uplifted material (influenced by climatic factors such as precipitation and glaciations). This removes sediment mass from the upland area, increasing its buoyancy and leading to isosatically driven uplift. This in turn leads to further erosion/denudation and continued uplift.

By the end of the Caledonian Orogeny a mountain chain of Alpine proportions existed in present day Scotland. Despite this, adjacent regions such as the Midland Valley and Moray Firth stood at or below sea level (e.g. Cameron and Stephenson, 1985). This large scale relief could have led to the continued passive, erosion driven uplift of the orogenic belt after collisional tectonics had ceased. Isostatic rebound as a result of both the high concentration of low density granitic plutons and the removal of erosional material from the mountains contributed to the gradual uplift during *Phase 2*.

Carboniferous sediments sourced from the eroding Scottish highlands are found within the Midland Valley (Cameron and Stephenson, 1985), as well as offshore (with isolated onshore outcrops) in basins of the Hebrides, Shetland basin, Moray firth and the North Sea. Many of the deposits of this time are shelf carbonates, but siliciclastic sediments directly derived from the orogenic belt occur within the successions.

6.4.4.3 Phase 3: Between c. 300-150Ma the area stabilised, with only very minor uplift, if any at all. For the duration of this time at least part of the lower half of the profile was within the PRZ, whereas the top of the profile was above the PRZ. Therefore only the lower half of the profile records information about this part of the thermal history. The top of the profile was likely within 1-1.5km of the surface by this time. Modelling the samples in profile provides evidence that towards the end of this period the geothermal gradient of the area increased (the lower samples appear to reheat), suggesting at an increased heat flow through the lower crust. This could potentially be associated with the early crustal thinning of the proto N. Atlantic region.

Sedimentation in the Midland Valley had all but ceased by the end of the Carboniferous (with minor exceptions). This was partially down to a shift in tectonic regime from extensional to compressional forces which related to tectonic events further south (Variscan Orogeny) (Cameron and Stephenson, 1985). This may also indicate a cessation of uplift in the Scottish highlands (as supported by the BIC thermal history), although sedimentation continued elsewhere.

At the end of the Variscan Orogeny and the formation of Pangea (Upper Carboniferous) a tensional stress regime developed in the region, forming numerous intra-continental basins. These include the Donegal, Minch and Sea of the Hebrides basins off of the north and west coasts of Scotland and Ireland (Hitchen *et al.*, 1995). Permo-Triassic sediments are found extensively in these basins indicating that erosion of the Scottish highlands continued through this time (despite the lack of uplift recorded in the BIC thermal history). This is predominantly in the form of red bed sandstones, shales and conglomerates. Deposition in the sedimentary basins encircling the Scottish mainland continued into the Jurassic, and this includes examples now exposed as terrestrial outcrops, e.g. on the Trotternish peninsula on Skye. The source of clastic sediments such as the Great Estuarine Series deposited during the Jurassic has been shown to be the Scottish highlands, as opposed to a postulated but largely unsupported northern landmass (Hudson, 1964), indicating that erosion of the highlands continued throughout this time period.

Despite the implied lack of uplift during *Phase 3* of the thermal history, the geological evidence supports continued erosion of the Scottish highlands. Denudation was ongoing during this phase, but at a lesser rate than seen in *Phase 2* (erosion may have been greater in other regions of the highlands at this time). The thermal history suggests at an increase in the geothermal gradient towards the end of the time period. This can mask some of the uplift which must have taken place to provide the sediment found in the depositional basins. The increased heat flow (raising the geothermal gradient) likely indicates the beginning of crustal thinning which led to continental rifting and ultimately the opening of the N. Atlantic.

6.4.4.4 Phase 4: The final phase involves rapid uplift at c. 140Ma, resulting in the final kilometre or so of denudation which brought the top of the profile to the surface. This is recorded by samples from the lower half of the profile, with each sample having passed through the top of the PRZ not long after 150Ma. Since this time only minor erosion and denudation have occurred, largely in the form of glaciations which have carved out the corries within the BIC and the sea lochs bounding its northern and western sides. The mountain summits likely remained above the top of the continental ice sheet at its maximum thickness and have thus seen very little erosion over the last 140Myrs.

Within the Hebridean basins there is a brief hiatus in sedimentation and an angular unconformity between rocks of upper Jurassic age and the limited lower Cretaceous deposits (Morton, 1992; Emeleous and Bell, 2005). This is thought to represent a short lived period of uplift and erosion of the Scottish margin, leading to basin inversion. The unconformity is also found in the basins of the northern North Sea (Kyrkjebo *et al.*, 2004). The causes of this period of uplift and basin inversion are unclear, but it does closely correspond with the timing of the rapid uplift seen in the thermal history of the BIC. A simple explanation for the rapid uplift at Ballachulish at this time is rift flank uplift following the completion of continental rifting and the beginnings of the N. Atlantic opening. This does not however provide an explanation for the basin inversion seen at this time, which requires a compressional tectonic event.

In the case of the North Sea the 'Late Cimmerian' or 'Base Cretaceous' unconformity has seen much debate, with little consensus on its causes. It has been attributed to a number of causes such as: far-field stresses from either the opening of the N. Atlantic or from the 'Cimmerian orogenic cycle' away to the south east (the timing of which in itself has been disputed), gravity driven crustal shortening, non-coaxial reactivation of extensional stresses, reactivation of basement structures and hanging wall rollover (see Kyrkjebo *et al.*, 2004 and Jackson and Larsen, 2008 and references therein). The unconformity in the west of Scotland is likely to be directly related to that of the North Sea.

Although it is not possible to provide a definitive answer as to the causes of the *Phase 4* uplift at the BIC based on the thermal history, the signal for a period of rapid uplift at this time is strong. The rapid cooling is recorded in the lowest samples of the profile individually (particularly the base sample) and is very distinctive when modelling the samples in a vertical profile. The timing of the cooling coincides well with a brief period of uplift and deformation recorded in the regional geology, and matches up with the timings of the beginnings of N. Atlantic opening (Hallam, 1971; Ziegler, 1988).

6.4.2 *Comparison with Persano et al. (2009)*

Sample *SD07 – 3* is the same sample as SD3 in Persano *et al.* (2009), re-analysed using different grains in single grain aliquots. It therefore provides a direct comparison between the methods and modelling techniques of the past and the new HelFRAG and QFrag techniques used in this study. The interpretations based on the full profile presented in Persano *et al.* (2007) can also be compared with the full profile of this study. Comparisons between the single grain ages of this study and the multi-grain aliquot ages of Persano *et al.* (2007) can be found in **Chapter 5**.

The inverse modelling presented in Persano *et al.* (2007) is based on their AFT dataset, so absolute comparisons can't be drawn here. However the two systems are linked so it should be possible to see similarities between the thermal history inversions of one thermochronometer and the other. The thermal history inversion seen in figure **6.1 A** bears no resemblance to any of the inversions presented in this chapter, meaning that a very different thermal history interpretation is required. This is supported by the much older synthetic AFT ages generated based on the new inversions compared to the published ages of Persano *et al.* (2007). The author's state that, based on their history, all of their samples must have cooled below 80°C no later than 100Ma (implying that they were likely hotter than 80°C prior to this point). This is technically in agreement with the inversions presented here, but the vast majority of models suggest that the profile was cooler than 80°C much earlier in the history, by at least 300Ma.

Based on their AHe age profile, the authors infer that the BIC either experienced slow monotonic cooling from the Mesozoic through to the present, or that the ages represent only a portion of a fossil PRZ, and that the profile experienced an acceleration in cooling rate sometime after the youngest recorded ages (i.e. after c. 80Ma). The monotonic cooling scenario was inconsistent with their AFT inversions, so they explored potential rapid cooling pathways post 80Ma which satisfied the AHe data (by using the forward modelling program DECOMP).

The modelling of SD3 (*SD07 – 3*) showed that the upper profile entered the PRZ at 295-252Ma, which is much more consistent with the inversions presented here. The modelling suggests that *SD07 – 3* entered the PRZ at around 300Ma, but although individual models are well constrained on this timing, there is a fair amount of uncertainty between models which use different modelling parameters. This gives a possible age range spanning c. 250-400Ma for *SD07 – 3* entering the PRZ. The differences lie in what happened after crossing the 80°C isotherm. All models presented here are in agreement that the upper profile continued ascending through the PRZ fairly rapidly, and had cooled below the base of the PRZ by c. 300Ma. In contrast the modelling in Persano *et al.* (2007) has sample SD3 undergoing steady cooling through the PRZ over c. 200Myrs before an accelerated cooling out of the PRZ at c. 50Ma. Sample SD9 (lower elevation) constrains the timing and rate of the accelerated cooling. The author's state that the cooling initiated between 61-47Ma and that 46°C of cooling occurred over a 1-10Myr time period.

The differences in thermal history reconstruction have major consequences for the tectonic/geodynamic interpretations. The major interpretation based on the modelling of Persano *et al.* (2007) is that of under-plating driven uplift associated with the proto-Iceland plume/hotspot and the subsequent British Tertiary Igneous Province (TIP). This is a perfectly sensible and valid interpretation based on their data, indeed it is rather striking that the new data here shows no evidence of the influence of the TIP and the rift to drift stage of the opening of the N. Atlantic. The implications for this being that any denudation during the Cenozoic has been insufficient to be recorded by the AHe thermochronometer, i.e. uplift has only been in the order of 10's to a few hundred metres at most in the region of the BIC.

Based on the geological constraint that the top of the BIC has been within c. 2km of the surface since c. 400Ma (Fraser *et al.*, 2004), and has experienced no significant burial since, volumetric constraints make it hard to support the significantly > 1km of denudation which is required to have occurred in the Cenozoic by the Persano *et al.* (2007) thermal history. The authors calculations require between c. 720-2880m of uplift and erosion during the Mesozoic (based on a geothermal gradient between 15-40°C km^{-1}) on top of the 1-2km of rapid erosion between 61-47Ma. Even excluding any late Palaeozoic uplift (which can be inferred to have been at least at the rate of their Mesozoic uplift), their calculated erosion rates likely exceed the total volume of overburden remaining at the BIC by 400Ma.

Using the same range of potential geothermal gradients (15-40°C km^{-1}) and based on the thermal history of the top sample in the profile (as seen in figure **6.6 A**), the thermal history inversion presented here gives an approximate volume of denudation since 400Ma of: *Phase 2 and 3* (c. 35°C cooling) = 875-2330m, *Phase 4* (c. 25°C cooling) = 625-1600m giving a total of 1400-3930m. This compares to an approximate total volume of denudation based on the Persano *et al.* (2007) thermal history of 1870-5940m assuming zero denudation before the Mesozoic (calculated by the Mesozoic denudation range of 720-2880m plus the Cenozoic 46°C cooling denudation range of 1150-3060m). Adding any Palaeozoic denudation onto the calculation (of which there is ample evidence of sedimentation in the Midland Valley and offshore basins) means that even the minimum estimate, which assumes a heightened geothermal gradient throughout, soon exceeds the c. 2km overburden limit. In contrast, given an 'average' geothermal gradient (i.e. 20-30°C km^{-1}), the calculations based on the thermal history presented here can be accommodated by the c. 2km denudation limit.

Both analytical and modelling low temperature thermochronological techniques have seen major advancements over the last decade (e.g. Flowers *et al.*, 2009; Gautheron *et al.*, 2009; Gallagher, 2012; Beucher *et al.*, 2013). Current methodology is far from the finished product (e.g. Djimbi *et al.*, 2015; Gerin et al., 2017) but the modelling presented here is likely to be a more robust representation of the true thermal history than that presented in Persano *et al.* (2007). However it is by no means perfect. It is important to note that the models presented here lack the additional constraints which would be provided by modelling in conjunction with AFT data.

6.5 Fragment model

Chapter 4 of this thesis demonstrated that modelling fragments incorrectly as whole grains can, under some circumstances, lead to perfectly sensible looking yet ultimately incorrect thermal history reconstructions, whereas modelling fragments correctly can lead to a more accurate reconstruction. This chapter has examined the fragment effect using a real dataset. Although the differences are generally subtle with this dataset, there are important differences in some instances.

6.5.1 *Modelling sample SD07 – 3*

Sample *SD07 – 3* has been the focus for testing the different ways of modelling data from a single sample using QTQt. One of these ways is the difference between having the fragment model – QFrag switched on or off. Section 6.3.3 demonstrates a logical progression of different modelling options, each making the comparison between having the fragment model on or off.

In general there is no significant difference in the model output when the fragment model is switched on compared to when it is switched off. This is largely down to the straight forward nature of the inferred thermal history, with a rapid ascent through the PRZ for this sample and no periods of reheating. As shown in **Chapter 4**, QTQt can generally resolve this type of thermal history without the need for the fragment model, even when other causes of natural dispersion are low. It can struggle to pin down the exact timing of the rapid cooling episode (and this is the case here), but the type of thermal history is easily resolved.

The greatest difference between the model outputs in regards to the timing of cooling is when the error is re-sampled. However this is not systematic. Re-sampling the error makes it easier to fit the data, but this can result in very large error bars to gain the fit. It is therefore not surprising that this can result in quite large variation between model outputs using the same data. It is perhaps also not surprising that the differences are un-systematic, as the error margin is increased in both directions. It is not so much that the fragment effect leads to the observed differences, rather a model parameter has been changed which has led to a different output. For example, there is just as much of a difference between the model outputs when comparing modelling with the radiation damage model of Flowers *et al.* (2009) verses Gautheron *et al.* (2009) with the fragment model on when re-sampling the error (when only modelling broken grains, see figures **6.10** and **6.11**).

The set of models with the greatest difference between having the fragment model on or off is when using the radiation damage model of Flowers *et al.* (2009) and only modelling broken grains (see figure **6.10**). Here, although the timing and rate of initial cooling appear similar, the temperature (depth) which the sample reaches before plateauing varies. This has consequences for the duration of time that the sample spent in the PRZ. When using the fragment model the history plateaus off at a shallower depth, meaning the sample spent less time in the PRZ than if the fragment model is switched off.

It should be expected that the differences between using the fragment model or not will be greatest when only using data from broken grains, as any whole grains in the dataset will mask the effects. In the case of sample *SD07 - 3* there is a reasonable number of whole grains within the dataset (10) to provide accurate thermal history information without the need for the fragment model. It is therefore surprising that the same differences aren't observed when using the radiation damage model of Gautheron *et al.* (2009), which sees very little difference (figure **6.11**). It is unclear whether this is a difference which will be systematic to any data set, i.e. RDAAM is more sensitive to the fragment effect, or if it is down to the specific set of circumstances surrounding this experiment.

RDAAM uses a cubed relationship between damage accumulation and ^{4}He retention whereas the model of Gautheron *et al.* (2009) uses a linear relationship. Therefore RDAAM can be considered more aggressive in its treatment of high eU grains. This does not necessarily mean that it is also more susceptible to the effects of the fragment model. The fragment model is unaffected by the eU of grains, purely concerned with the grain dimensions. The fact that the same disparity between the effects of RDAAM and the

Gautheron model aren't observed when the full set of grains are analysed suggests that there isn't a systematic 'RDAAM fragment effect'.

It was expected that the fragment effect would increase in importance as the sample size decreased. With large sample sizes (i.e. 20+) there can often be enough thermal history information within the natural variation in grain size and eU concentration alone without the need to treat fragments as fragments. With smaller sample sizes the fragment effect is expected to be more important. However this is not the case for this sample. What is more apparent is the importance of modelling large sample sizes irrespective of using the fragment model. There is a far greater difference in the output when comparing a model with twenty grains to three, verses comparing any number of grains with either the fragment model turned on or off.

6.5.2 *Modelling samples in profile*

When modelling the samples together in a vertical profile (figure **6.6**) there is a much greater difference between modelling with the fragment model on and off. This has significant implications for the resultant thermal history interpretations. When modelled without the fragment model, the thermal history output has a highly unrealistic geothermal gradient and an ultimately unlikely looking T-t path. This is in contrast to the sensible and realistic model output when modelled with the fragment model on. The fact that the model output when run without the fragment model is so unrealistic suggests that the program struggles to find a sensible solution which fits the data when fragments are incorrectly treated as whole crystals.

Modelling multiple samples in a vertical profile requires QTQt to find a solution which can satisfy all the samples, combining thermal history information from different segments of the profile. The program will always generate a thermal history, regardless of whether it is given sensible data (Vermeesch and Tian, 2014). Therefore the fact that the thermal history output is far more credible when using the fragment model suggests that the data when not treated correctly as fragments is of a lower quality (i.e. 'rubbish in = rubbish out'). This demonstrates the importance of modelling large datasets with the fragment model on.

Not only is the thermal history output more sensible and realistic when run with the fragment model on, it also contains the constituent parts of the history which were resolved by the individual samples. The deceleration in cooling rate at c. 300Ma (end of *Phase 2*) is seen throughout the samples of the upper half of the profile, including *SD07 - 3* which has been modelled extensively with the fragment model both on and off. This is evident in the thermal history from the vertical profile when modelled using the fragment model, but is absent when modelled in profile without the fragment model. The rapid cooling at c. 140Ma (*Phase 4*) is also less pronounced/absent from the profile when modelled without the fragment model. This is seen in the models for individual samples from the lower half of the profile, so further supports the thermal history output when modelling fragments as fragments. This provides strong evidence that the thermal history when treating fragments as fragments is the more accurate thermal history.

In the case of this dataset, the importance of the fragment effect has become much more evident when modelling multiple samples in a vertical profile. This is because the resultant thermal history is inevitably more complex. This also means that a significant number of samples have spent more time in the PRZ than is suggested when modelled individually (which is in keeping with the percentage of single grain age dispersion observed throughout the profile, which suggests that many of the samples experienced a residence time in the PRZ). When modelled individually, the majority of samples show a simple two stage thermal history (figure **6.6**). This involves relatively rapid monotonic cooling from intrusion to near the surface (taking the sample rapidly through the PRZ) followed by a plateauing off. When modelled in a profile, a more complex four stage thermal history appears. This inevitably requires more samples to have spent longer in the PRZ than first appearances, in order to 'marry' the constituent parts of the thermal history which are resolved by different sections of the vertical profile.

Given sufficient vertical offset, modelling samples in a vertical profile will always generate a more complex (and more complete) thermal history than when modelled individually. This will likely mean that important differences will emerge between modelling with the fragment model on or off, which may otherwise have been missed when modelling samples individually. It is therefore important to model profiles with the fragment model on even if tests on individual samples have suggested that the fragment effect is not important on a given dataset.

6.6 Concluding remarks

The purpose of this chapter has been twofold – to extensively test the fragment model (both HelFRAG and QFrag) on a real dataset, and applying the methodology to investigate the thermal history of the BIC. The testing of HelFRAG has been limited, but it has been seen to work and produce a sensible thermal history. However that thermal history differs drastically from the thermal history reconstructed with QTQt. This is likely down to the small sample size (for sample *SD07 – 5*, but not *SD07 – 3*) and insufficient model iterations leading to an inaccurate thermal history. Additionally QTQt is a more powerful and statistically robust thermal history inversion program than HelFRAG, so is preferred when interpreting the thermal history.

The testing of the QFrag implementation of the fragment model has been extensive. This has demonstrated the importance of analysing a suitably large number of grains per sample, with approximately 20 being desirable. Modelling 30+ grains doesn't have a demonstrable difference on the thermal history outcome in this instance compared to modelling only 20 grains. When modelling samples individually, modelling the desired number of grains appears to be of greater importance than modelling fragments correctly as fragments. But this is only likely to be the case for relatively simple thermal history T-t paths. It should therefore still be considered best practice to model with the fragment model on when information on the number of crystal terminations is known.

In a profile such as this, no one single sample contains the required information to resolve the entire thermal history. It is therefore paramount to sample and model multiple samples in a vertical profile. This enables a more complete and robust thermal history to be reconstructed, enabling interpretations to be made which would easily be overlooked if only one or two samples had been analysed from a location. When modelled in a profile, the fragment effect becomes much more important, and modelling broken crystals incorrectly as whole crystals will likely result in a noticeably different thermal history being interpreted.

There are many combinations of ways to model the same data by altering the model parameters in QTQt. These include using the radiation damage model of Gautheron *et al.* (2009) or Flowers *et al.* (2009) (or no radiation damage model), resampling the age or resampling the error. There is no single 'best practice' combination of parameters to use, however it is advisable to always use a radiation damage model (unless the range of eU in the samples is very low) and to resample either the age or the error. When time allows, it is best to model any data set in a logical progression of ways, and treat the process as ensemble modelling, looking for common trends within all the models as opposed to looking for the single best model output.

Through the application of the fragment model on this dataset a new and contrasting thermal history for the BIC is presented. The previous work of Persano *et al.* (2007) proposed underplating driven uplift associated with the proto-Iceland plume. This resulted in a rapid and short lived period of cooling/uplift between 61-47Ma giving 1-2km of denudation. The new history presented here advocates a period of rapid uplift at c. 140Ma giving c. 1km of denudation, with only 10's to 100's of metres of denudation having occurred since. This followed crustal thinning and increased heat flow as a result of the initial phases of the opening of the N. Atlantic. This new thermal history interpretation is by no means perfect, indeed it lacks AFT data which could provide further constraints on portions of the history which are poorly constrained by AHe data. However the volume of data analysed and presented here, combined with the systematic and comprehensive nature of the thermal history modelling process supports this new thermal history interpretation over the one presented in Persano *et al.* (2007).

CHAPTER 7

7. SUMMARY AND CONCLUSIONS

(Looking west along Glencoe, out towards Loch Leven and the Great Glen)

7.1 Summary

This thesis provides an extensive examination of the perceived problem of AHe single grain age dispersion, dispelling the concept of 'over dispersion'. Never before has such an extensive dataset been compiled for a single locality, with 10+ grains analysed for over 10 samples. Many of the samples consist of over 20 grains, with the largest samples comprising over 30. The data has been modelled using new inversion techniques developed to take advantage of the thermal history information contained within the natural single grain age dispersion, particularly that provided by the inclusion of grains with only one intact crystal termination (1T).

A comprehensive discussion on the causes and consequences of age dispersion has been provided in **Chapter 2**, along with the past, present and future developments in the AHe analytical and modelling techniques. Particularly important is the distinction made between the 'good' inherent natural dispersion and the 'bad' imposed extraneous dispersion. Ways to mitigate and/or account for the causes of imposed extraneous dispersion are outlined, whilst ways to maximise the inherent natural dispersion are suggested. It is therefore demonstrated that 'bad' dispersion is rarely a problem, and is often possible to fingerprint on grains for which it has acted upon.

Although AFT data is not used directly in this thesis, the AFT and AHe systems are inherently linked, and are typically used in conjunction for low temperature thermochronological studies. An outline of the principles and major developments of the AFT chronometer is provided in **Chapter 3**, along with its influence on the crucial early developments in thermal history inverse modelling techniques. A discussion of published AFT data from the region of the BIC is given in **Chapter 6**, providing context to past interpretations of the geological history of the area. New AFT data from the BIC is included in Appendix 6.

An approximation of the finite cylinder diffusion model used in HelFRAG has been developed for the QTQt modelling software (Gallagher, 2012) - QFrag. This was used extensively for the thermal history modelling in this thesis, but before it could be used for a real dataset it needed to be shown to work in a comparable way to HelFRAG. This has been demonstrated in **Chapter 4**, where the same five theoretical WOLF histories (Wolf *et al.*, 1998) are remodelled using the same synthetic fragment lists generated for Beucher *et al.* (2013).

The afore mentioned extensive single locality dataset is presented in **Chapter 5**. This demonstrates the full extent of single grain age dispersion possible when large numbers of grains are analysed per sample. A detailed analysis of the causes of this dispersion is presented, along with a discussion of anomalous data points and their causes. The data is presented in a series of age verse *x* multi-variant plots to highlight the trends (or lack of) within the distribution of ages. Such plots are shown to be useful for explaining apparent anomalous ages within a dataset.

Finally, the dataset from **Chapter 5** has been modelled using new and existing inversion techniques in **Chapter 6**. This simultaneously provides a real world test of the fragment model (as applied to HelFRAG and QFrag techniques) and a new and updated thermal history interpretation for the BIC and the wider UK N. Atlantic margin. The data is predominantly modelled using the inversion program QTQt, both with and without the fragment model (QFrag). A smaller test of the data with the HelFRAG inversion technique is also provided.

7.2 Future work

7.2.1 *Fragment model*

The next step in developing the fragment model is to extend its application to 0T grains. These are inherently more difficult to deal with, as even less is known about the original whole grain from which they derive. Consequently the HelFRAG approximation can't accurately deal with 0T grains. Progress has been made on another QFrag approximation which can deal with 0T grains (Gallagher and Wildman, pers. comm.), but this has yet to be fully tested to the levels seen in this thesis for 1T grains.

Another area for future development is finding ways in which to make the inversion process swifter and less computationally demanding. Modelling data sets such as this using the fragment model can take several weeks (QFrag) to several months (HelFRAG) per model run. This is not particularly practical for the routine application of the fragment model. HelFRAG can be run on super computer clusters, greatly speeding up the process, with the only limitation being on the number of cores available. Currently QTQt cannot be run on computer clusters, so developing a version which can is one avenue for speeding up the process (but not reducing computational demands). Other avenues have been explored for reducing the model run time and decreasing the computational demands, and these may be ready to be rolled out in the near future (Gallagher, pers. comm.).

7.2.2 *Ballachulish thermal history*

The next step for the thermal history reconstruction of the BIC is to model the fission track data, both independently, and in conjunction with the AHe data. This may simply support the current model, or provide additional information which results in a slightly different thermal history interpretation.

Currently colleagues at the University of Glasgow are carrying out comparable studies on a number of other igneous complexes neighbouring the BIC, such as Ben Starav and Ben Nevis. Further down the line it will be possible to combine the histories to build up a bigger picture of the evolution of the Scottish N. Atlantic margin. These studies may support the interpretations made here, or provide a different insight. This will confirm whether the events seen at the BIC are localised, or associated with the tectonic regime of the whole margin.

7.3 Conclusions

Herin lie the major conclusions formulated from the work of this thesis:

7.3.1 *Dispersion*

The biggest take home message from this project is that there is no such thing as 'over dispersion' when it comes to AHe single grain age data. Dispersion is real and extensive but ages are not 'over dispersed', for the most part they are dispersed exactly as much as they should be. It is not uncommon to find dispersion in excess of 100%, and in some instances this can be well in excess of 100%, but this should not be considered problematic. There will always be outlying or apparently 'anomalous' ages in a dataset, but these can largely be explained through a detailed and systematic analysis of the raw data. Where sufficient evidence exists for the recalcitrance of such ages then they can be discarded, but individual ages should not be omitted from datasets purely based on a statistical measure of their lack of fit. Often apparent 'outlying' ages will become encompassed by the rest of the data if a higher total number of grains are analysed.

As shown by Brown *et al.* (2013) and Beucher *et al.* (2013), far from being problematic, large dispersion is actually beneficial when it comes to reconstructing robust thermal histories. The greater the range of ages as a result of the three main causes of natural dispersion: grain size and eU variation, and the fragment effect, the more thermal history information that is retained within the data. This can then be exploited to reconstruct the thermal history. It is therefore desirable when choosing grains for analysis to try to maximise the range of natural age dispersion by selecting as wide a range of grain sizes and shapes as possible, plus a mixture of 1T and 2T grains.

7.3.2 *Mean ages*

The reporting of mean AHe ages should be considered obsolete. A mean age does not represent any meaningful geological event, it is merely the average age for the average type of grain measured. To coin a phrase: “the mean is meaningless”. The range of 'true' ages can be so wide (and skewed) that it is not well represented by the mean. A mean age (or some other form of average representation) can be honed in on by those unfamiliar with the complexities of the AHe system, detracting from the overall message trying to be presented. The plotting of mean ages on a map (± colour contouring) does not provide any meaningful information to a reader. The practice of trying to find a reproducible mean has likely been the root cause of the 'over dispersion' misconception.

Finding an effective and aesthetic method of graphically presenting ages if not reporting the mean may provide an additional challenge, but this should not be used to justify plotting mean ages on a map. The method presented here of creating age vs. elevation plots is an effective way of presenting the full data set when working with vertical profiles. The same method can be adopted when dealing with regional transects which cover a range of elevations, but purely for data representation purposes as any intra-sample comparison on the plot may become meaningless when dealing with large spatial offsets. To the casual reader it is ultimately the thermal history reconstructions which carry the most meaning, to the expert, the raw data table should be considered the source of key information.

7.3.3 *F_T correction*

The reporting of α-ejection corrected ages should also be considered unnecessary. As a single grain age does not represent any particular geological event (such as the age of crystallisation in geochronology), an F_T corrected age is no more or less 'correct' than the raw age. Presenting raw ages and 'corrected' ages in the literature provides confusion for readers less familiar with the technique. This does not mean to say that α-ejection is not an important issue. α-ejection does occur, and this leads to the loss of ^{4}He. However this is taken account of in most inversion programs (e.g. HeFTy and QTQt) which require the raw age as the input. It is far more useful to report the age which is required as the input.

Reporting the correction factor only provides information on the grain dimensions, which are already reported in the data table as a matter of routine.

7.3.4 *Sample size*

The traditional practice of measuring five or six grains per sample, likely resulting in only three or four 'good' analyses after 'outliers' have been rejected, is inadequate to gain a full representation of the samples history. It is highly unlikely that it will be possible to reconstruct the 'true' thermal history from such a small snapshot of the overall picture. Insufficient thermal history information will be retained by the small number of grains to interpret anything beyond the simplest thermal history T-t paths with any degree of certainty.

Brown *et al.* (2013) and Beucher *et al.* (2013) demonstrated that a minimum of approximately 20 grains per sample is required to maximise the thermal history information inferable from the data. This is also supported by the work in this thesis (**Chapter 6**). Analysing significantly more than 20 grains will decrease the likelihood of having natural outliers, that is to say grains with ages significantly separate from the main cluster of ages, but with no apparent cause. However analysing a much larger sample size (i.e. 30+ grains) has no demonstrable benefit on reconstructing the thermal history in this instance.

If time and budgets are limited, resources should be concentrated on analysing a higher number of grains from fewer samples. Spreading the resources thinly will likely result in multiple poor thermal history reconstructions, whereas concentrating the resources on one or two good samples will be far more beneficial for developing a meaningful interpretation. An attitude shift is required around what constitutes a proper AHe investigation, with 20+ grains becoming the norm. Researchers can then plan and budget accordingly.

7.3.5 *Profile modelling*

The benefits of sampling vertical profiles in low temperature thermochronology investigations have long been recognised (e.g. Fitzgerald and Gleadow, 1990; Fitzgerald, 1992; Fitzgerald *et al.*, 2006). This is reaffirmed in this study (**Chapter 6**). Individual samples each only contain information on a part of the total thermal history, therefore a very different regional interpretation could be reached if basing a study on individual samples, purely depending on the elevation at which the sample is derived. For example, if the lone sample at Ballachulish had been collected from below 600m then the interpretation would be made that the region had only experienced a single tectonic event at c. 140Ma, whereas if that sample were collected from above 600m in elevation then the interpretation would be reached that the area had experienced no major tectonic events since the sample had cooled gradually from its initial intrusion over 400Myrs ago.

When carrying out regional investigations in mountainous terrain it is far more beneficial to sample at fewer locations, but to collect at least three or four samples at each location in a vertical profile, maximising the elevation offset available. This is as opposed to spreading the sampling more thinly over a wider area, with only one sample per location. Sampling every 100m over 1km vertical profiles may be impractical on a routine basis. In broad terms this level of resolution won't improve the thermal history interpretation for regional perspectives, but for specific studies it can help pin down the timings and magnitudes of specific events. A minimum of three or four well-spaced samples will provide the bulk of the thermal history information which can be gleaned from a location.

7.3.6 *Fragment model*

Treating broken grains incorrectly as whole grains can, under some circumstances, generate perfectly sensible looking yet ultimately incorrect thermal histories (**Chapter 4**). There is no way of being able to work out from the data fit or any other parameter whether this is the case or not. The only way to investigate this is to model the data both with the fragment model on and off. Bearing this in mind, there is no meaningful benefit to not using the fragment model as a matter of routine.

The approximation of the fragment model which is incorporated into the QTQt software – QFrag, provides a successful, user friendly alternative to the more computationally demanding HelFRAG model. It has been shown to accurately replicate the results of HelFRAG when given a synthetic dataset (**Chapter 4**). It has also been extensively used on the real data set from the BIC (**Chapter 6**). Here the differences between modelling with and without the fragment model are less clear cut (on individual samples), but it is no less accurate than modelling in the traditional way, so there is no detriment to using QFrag routinely (other than time). It will be impossible to know whether modelling using the fragment model will return different results to modelling without until both methods have been adopted. It is therefore sensible to model using the fragment model as a matter of routine.

Where natural dispersion is sufficient through grain size and eU variation alone, there may be no significant difference, and therefore benefit to modelling using the fragment model (**Chapter 4**). However there is no quantifiable way of determining what exactly 'sufficient' eU and grain size variation entails. The more complex the true thermal history, the greater the likelihood that radiation damage induced dispersion will dominate over the fragment effect, meaning that a smaller natural eU range will be sufficient to make the fragment model redundant. However as the true thermal history is an unknown from the outset, it is impossible to say what a sufficiently large range in eU within a sample will be. It should therefore be considered best practice to model fragments as fragments as a matter of routine.

When modelling multiple samples in a profile, there is likely to be a much greater difference between the model outputs when using the fragment model or not (**Chapter 6**). This is because the resultant thermal history will invariably be much more complex than when modelling a single sample, and will therefore likely require various samples to have spent more time in the PRZ than is apparent when modelling the samples individually. The thermal history when modelled using the QFrag model is demonstrably more credible than when modelled without a fragment model on the BIC data set. It therefore should be considered the norm to model profiles using a fragment model.

7.3.7 *Ballachulish thermal history*

A new thermal history interpretation for the BIC has been developed based on the modelling of the new dataset with the program QTQt. This differs from the published thermal history interpretation of Persano *et al.* (2007). The new thermal history model requires four phases of cooling/uplift and denudation: Very rapid uplift from a crustal depth of c. 10km to c. 2km between c. 424-404Ma. Slower continued uplift from c. 404Ma until c. 300Ma. Little or no uplift between c. 300Ma and c. 140Ma, coinciding with an increase in the geothermal gradient towards the end of the period. A final period of rapid uplift at c. 140Ma, bringing the entire profile very near to the surface.

The new interpretation has consequences for the wider tectonic context. The first two phases are directly or indirectly related with the Caledonian Orogeny, with passive uplift continuing due to the enhanced relief after collisional tectonics ceased. *Phase 4* coincides with the earliest rifting and extensional tectonics associated with the opening of the N. Atlantic. The increase in geothermal gradient immediately prior to this uplift supports the theory of crustal thinning and extension at the time. There is no evidence in the new dataset of the c. 1-2km of rapid uplift occurring in the Cenozoic as published by Persano *et al*. (2007). This suggests that any under plating driven uplift associated with the British TIP and the proto-Iceland plume was insufficient in the Ballachulish region to be recorded by the AHe thermochronometer. It was therefore in the region of 10's to 100's of meters at most.

APPENDICES:

APPENDIX 1

1. APATITE (U-Th)/He METHODOLOGY

1.1 Mineral separation process

Initially 2-6Kg of material was collected from the outcrop and broken into manageable chunks (< fist sized) using a sledge hammer. If further breaking was required to achieve manageable chunks then this was carried out in lab using a hydraulic crusher/pulveriser. One piece was kept as a hand specimen for each sample, and the rest underwent the below process.

1.1.1 *Crushing*

The < fist-sized rock fragments were passed through a Jaw Crusher several times at increasingly smaller size increments between the jaw crusher blades. After each round the material was sieved using a < 500µm and < 3000µm sieve stack. The material already < 500µm in diameter was bagged at this stage and the material > 500µm but < 3000µm was put to one side. The material > 3000µm was then passed through the jaw crusher again and the process was repeated until all material was < 3000µm in diameter, or a sufficient amount (at least 2kg) was crushed for very large samples where all the material may not be required.

The material < 3000µm but > 500µm was then passed through a disk mill several times at increasingly smaller increments between the rotating disks. After each time the material was again sieved to separate out the material already < 500µm in diameter, which was added to the already bagged material. This process was then repeated until all the material was of the desired size, or a sufficient amount was the desired size for very large samples. Any remaining material was also bagged and labelled as > 500µm in case further material was required later down the line.

1.1.2 *Washing*

To remove the finest sediment (dust) from the sample, as well as separating out clays and low density material (apatite and zircon are relatively dense), the sample was next washed using a Gemini shaking table. The material was slowly passed over the vibrating table with the assistance of flowing water, settling in a series of groves which lead to four different collector buckets. The destination of the material is determined by its density (and to a lesser extent its size). The angle of the table, the frequency of the vibrations and the water flow can all be fine-tuned to separate out different minerals, but in this case the vast majority of apatite (and zircon) will end up in the collector bucket for the highest density material. The material from each collector bucket was then left to dry overnight, before the highest density separate (and occasionally the second highest if more material was required) was carried forward to the next stage of the separation process.

1.1.3 *Magnetic separation stage 1*

Next the material was passed through a Vertical Frantz magnetic separator. This was repeated a number of times to separate out the most magnetic of the remaining minerals (i.e. magnetite and biotite). The process would typically take 2-3 repetitions at increasing currents (e.g. 0.4A, 0.8A and 1A). The material was dropped through the magnetic field of the twin magnets where the non-magnetic material falls straight down into one collector beaker while the magnetic material is diverted by the magnetic field into a second collector beaker. The most strongly magnetic material would stick to the magnets, and this was also collected into the second beaker each time. The process can be repeated as many times as necessary, typically until no more material sticks to the magnets.

1.1.4 *Heavy liquid separation stage 1*

The remaining non-magnetic material was passed through the non-toxic heavy liquid LST (Lithium Heteropolytungstate solution) in a glass vial with dispenser tap. LST has a density of about 2.80g ml^{-1} at room temperature meaning apatite (which has a density of about 3.2g cm^{-3}) and other dense minerals sink, while the remaining less dense minerals (such as quartz and feldspars) float on the surface. To encourage the separation the material was agitated into a vortex to prevent the dense material from becoming ‘rafted’ by the ‘float’. The ‘sink’ was then decanted from the glass vial and rinsed thoroughly with de-ionized water before being left overnight on a hot plate to dry.

1.1.5 *Magnetic separation stage 2*

Once dry, the sample was passed through a Horizontal Frantz magnetic separator. Here the slope of the magnet and the current can be fine-tuned to separate out the desired minerals which are weakly magnetic. The material passes along a vibrating angled shelf, where the more magnetic minerals are attracted to the magnet and are channelled into one collector beaker, while the less magnetic material is channelled into another. The process can be repeated several times at different currents and angle of slope depending on the accessory minerals present in the sample until predominantly only apatite and zircon remain. The typical routine here was to use a side slope of 20° and a current of 0.5A, then to repeat this for 0.9A and 1.5A.

Often this was sufficient to produce a good quality apatite separate (with some zircon) which could then be used for AHe picking. Occasionally one or more of the stages would need repeating or more material would be needed to produce sufficient apatite. Additionally the sample might need a further stage of cleaning, particularly for AFT analysis.

1.1.6 *Heavy liquid separation stage 2*

If the final separate had a high percentage of zircon then this was separated out from the apatite using the toxic heavy liquid DMI (Di Methyl Iodide). DMI has a density of about 3.3g ml^{-1}meaning the apatite will float (density of about 3.2g cm^{-3}) and the much denser zircon (density of about 4.6g cm^{-3}) will sink. The 'sink' and 'float were then rinsed thoroughly using acetone before being left to dry on a hot plate. This would leave a clean apatite and zircon separate ready for analysis.

1.2 Grain picking

The apatite separate was observed under a Zeiss Stemi 2000-c binocular microscope at magnifications of x20-100. Grains were picked based on their clarity (lack of inclusions and fractures) and good euhedral crystal shape (where possible). As wide a range of crystal shapes and sizes as possible was chosen, as well as a decent number of 0T, 1T and 2T grain types. The chosen grains were placed on a blank microscope slide and photographed under the same binocular microscope using image capturing software.

Each grain was then observed individually under a Leitz Wetzlar 780306 petrographic microscope with up to x500 magnification, in both plain polarised (PPL) and cross polarised (XPL) light. This was to check for microscopic mineral/fluid inclusions which were otherwise missed in the picking process. For the purpose of this thesis only grains with no evidence of mineral or fluid inclusions were passed as good for AHe analysis.

The good grains (no inclusions) were measured (length and width) using the slide photographs and ImageJ photo processing and analysing software. They were also recorded as being 0T, 1T or 2T crystals respectively.

At this stage the chosen grains were placed in individual platinum tubes which were then closed at each end. Each tube was then placed in its own individually labelled plastic vial which would be used further down the line during the ICPMS stage of analysis. Prior to use the Pt tubes were first etched using 50% HNO_3 and HCL to remove any contaminants.

1.3 Helium extraction

1.3.1 *Loading*

The individual platinum tubes were loaded into a copper pan containing 2mm deep drilled holes, one Pt tube per hole. The pan was then loaded onto the helium line, where it was sealed tightly into a stainless steel chamber with a transparent crystal viewing port. The chamber was then pumped down overnight to create an ultra-high vacuum with a pressure of $< 10^{-9}$ torr using a combination of turbo molecular and ion pumps. As the chamber had been exposed to the atmosphere during loading, it also required baking to remove CH_4, H_2O and other volatiles from the side walls of the chamber and metal tubing. This was done using heating tape and a heating lamp set over the crystal viewing port (*note: this lamp created potential issues with overheating the chamber and partially degassing some samples, so was omitted from the procedure during later line runs*). These were also left on overnight.

1.3.2 *Degassing*

After confirming that there was no leak in the line, a number of cold blank and calibration runs were carried out to ascertain the background level of ^4He in the line (cold blanks) and to enable the ^4He concentration to be calculated (calibrations). Finally hot blanks were carried out (heating empty Pt tubes) to check that the Pt tube capsules were not a significant source of ^4He.

The samples were heated individually using a diode laser ($\lambda = 808$nm) to a temperature of c. 800°C for 1min. The temperature was gauged qualitatively by the colour of the Pt tube as viewed via a PC monitor. The crystals themselves are heated indirectly through contact with the Pt tube to a temperature which enables total diffusive loss of ^4He, but not so hot as to volatise the U, Th and Sm. After heating, the gas was left to accumulate in the line for 5min before the extraction line was opened to the HidenHAL3F quadropole mass spectrometer. After 1min H, ^4He, and CH_4 were measured over four cycles by the mass spectrometer. The process was then repeated to ensure that all ^4He had been degassed from the sample, which would give blank levels of ^{4}He on the second run if this were the case. This process was repeated again if the second run wasn't close to blank level.

Throughout the day repeated calibrations were carried out to track the stability of the measurements, as well as additional blanks to monitor if contamination was accumulating in the line. Once all samples in the pan had been degassed, the pan was unloaded and the Pt capsules returned to their original plastic vials ready for U, Th and Sm analysis.

1.4 U, Th and Sm analysis

1.4.1 *Spiking*

Each sample was placed in a clean Teflon beaker, where a set amount of spike was added. The spike was made up of a calibrated solution of known concentrations of ^{235}U, ^{230}Th and ^{149}Sm, which enabled the relative abundances of ^{238}U, ^{232}Th and ^{147}Sm of each sample to be calculated. The mass of spike added was weighed accurately using a mass balance, before adding 2ml of HNO_3 to dissolve the apatite crystal. The Teflon beakers were left on a hot plate for c. 48 hours to fully dissolve the crystal.

After use the Teflon beakers were cycled through a series of cleaning steps to enable them to be used again. This involved four stages, each being left on a hot plate overnight: 1 - adding a few ml of cleaning solution (containing hydrofluoric (HF) acid) to the inside of the beaker. 2 – Submerging in 50% HNO_3. 3 – Submerging in HCL. 4 – Submerging again in fresh HNO_3. Further cleaning solution would then be added to each beaker for 2 hours on a hot plate imediately prior to use.

1.4.2 *ICPMS*

Once fully dissolved, 1ml of the spike and sample solution was added back into the original small plastic vials and these were loaded onto the ICPMS. A blank HNO_3 vial was added at the start of the run to calculate the background U and Th measurements. A vial of U500 solution (solution with a known concentration of ^{238}U) was added to the run every three samples (including at the start and end of the run) to track the sensitivity of the ICPMS detection, which typically decreases during a run. The process was then repeated (topping up the vials with HNO_3 if required) for Sm analysis, this time with the addition of a vial of Sm10 solution (solution with a known concentration of ^{149}Sm) every ten samples.

APPENDIX 2

2. AFT METHODOLOGY

The mineral separation process is carried out as per Appendix 1. The same separate can be used for both AHe and AFT analysis, although AFT typically requires more material. DMI is more likely to be needed to produce good quality FT mounts. The below outlined sample preparation procedure is in line with the external detector method (EDM) which was used in this study. Other methods exist which require different preparation procedures.

2.1 Sample preparation

2.1.1 *Slide mounting*

To produce fission track slides, a proportion of the mineral separate was sprinkled onto epoxy resin spread over a 16mm-16mm glass slide. A sufficient amount of material was used so as to cover the area of the slide, providing enough countable grains for a robust analysis while avoiding overcrowding of the slide. This is to make it possible to distinguish individual prints on the external detector sheets. A needle was used to break the surface tension of the resin and encourage the grains to settle onto the glass surface, while evenly distributing the grains. The resin was left for at least 24 hours until it had set hard. Sample numbers were scratched onto the reverse of each slide using a diamond-tip pen to aid identification.

2.1.2 *Slide polishing*

Once set, the slides were polished down to leave a thin layer of resin of single grain thickness. This involved a multi-stage process of polishing and grinding down on a Buehler Beta grinder-polisher machine. First a coarse p800 grinding paper was attached to the rotating drum of the machine to remove the convex top surface of the resin, exposing the grains which had settled on the glass slide. This resulted in severe scratching of the grain surfaces, which would be enhanced further when etched. To remove the scratches further grinding with first p1200 and then p4000 fine grinding paper was carried out.

Next a soft felt surface was used on the rotating drum of the machine with the addition of 1µm aluminium oxide micro-polish solution. This is to remove any remaining micro-chips/pits and scratches on the grain surface resulting in smooth, clear grains. If required an even finer polish (0.3µm) can be used at this stage.

2.1.3 *Etching*

To reveal the spontaneous fission tracks in the apatite grains so that they can be observed under an optical microscope, the mounts first require chemical etching. This involves submerging the slide in chemical etchant for a set time at a specific temperature. The procedure needs to be adhered to precisely, as each variable affects the annealing calibrations which are ultimately used during thermal history modelling. In the Glasgow lab 5.5 molar HNO_3 etchant is used, this is maintained in a water bath at 20 ± 1°C. Each slide was fully submerged in the etchant for 20 seconds before being quenched in a beaker of cold de-ionized water to prevent over-etching.

2.1.4 *Irradiating*

Once etched, a mica external detector sheet was placed flat against the polished slide surface. This and the slide were then wrapped tightly in plastic film to hold the detector in place. The sample slides were then loaded into an irradiation tube with standards placed at the top, middle and bottom of the tube. The tubes were sent for irradiation at the Oregon State University Radiation Centre, U.S.A where they were exposed to a neutron flux which induced the fission of ^{235}U within the sample grains.

The induced fission tracks were picked up on the mica detector sheets, which were then etched following the same procedure as per the grain mount (only the detector sheets were etched this time around). The grain mount and detector sheet were then mounted onto a single standard sized microscope slide so that the induced prints represent a mirror image of the grain mount. The correct orientation was achieved by punching pin holes on three of the four corners prior to removing the external detector from the grain mount. A central reference point (cross hatch) was also added to each slide between the mount and detector.

2.2 Sample analysis

The samples were analysed on an Axioplan 2 *imaging* microscope with a GTCO CalComp Drawing Board VI FT Stage Systems following the EDM. Where possible 20+ grains per sample were analysed, counting the number of spontaneous tracks within a pre defined grid area on each crystal, and the induced tracks over the same area on the corresponding external detector print. Only grains which were aligned with their polished surface parallel to the crystallographic C-axis were chosen. This was done by observing the uniform alignment of etch pits if the euhedral crystal shape was not preserved. 3-5 D_{par} measurements (etch pit lengths and widths) were also made on each grain to determine the compositional characteristics of the grains which are important for understanding annealing rates.

Ideally 100 confined horizontal track lengths per sample were also measured (or as many as possible if < 100). This was also done on c-axis aligned grains but could be measured on any number of grains within the sample to achieve the desired total number. The angle of the track to the C-axis was also measured if not parallel, to account for annealing anisotropy. Track lengths were measured using a digitising tablet, which was calibrated against a stage graticule. Track lengths were measured to ascertain the track length distribution (TLD) of the sample.

With each irradiation tube analysed, the three standards (top middle and bottom) are also counted, these standards are either Durango apatite, Mount Dromedary or Fish Canyon tuffs. A dosimeter from each end of the tube is also counted to measure the neutron flux down the tube, which is a vital parameter for determining the concentration of parent nuclei from the induced track counts.

APPENDIX 3

3. DURANGO AGE VS. Th/U RATIO

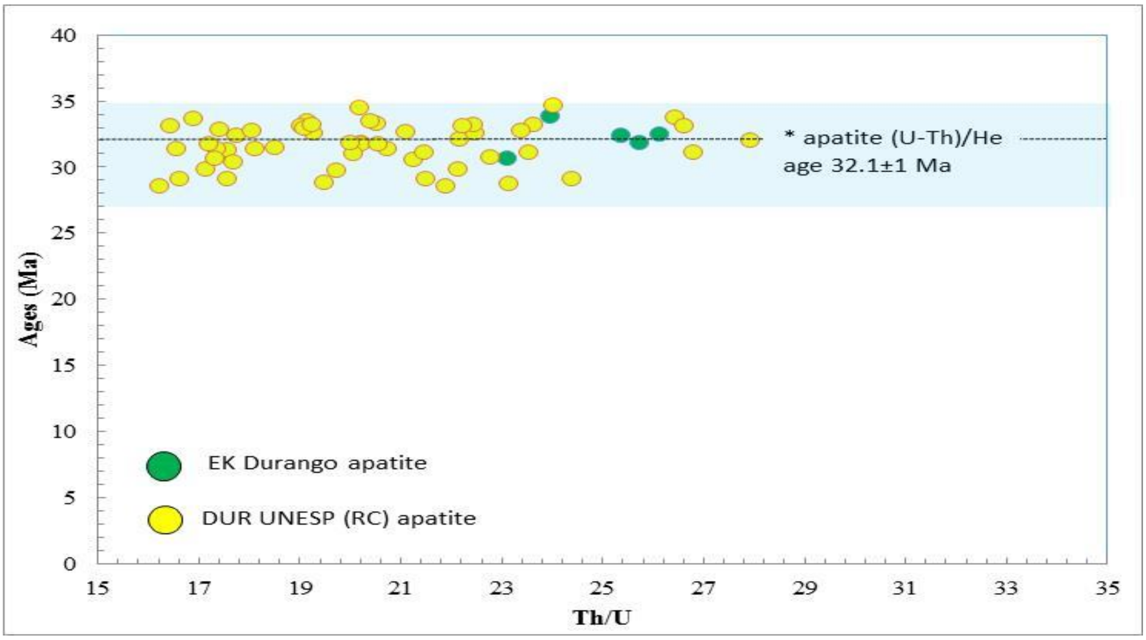

Figure A3.1: Durango age verse Th/U ratio.
Durango age verse Th/U ratio as measured at UNESP (Sao Paulo State University) showing the broad range of possible Th/U ratios. Green circles indicate the results from the Durango crystal currently used in SUERC laboratories which has a much narrower spread of 25±2 for the ratio (Stuart, pers. com.).

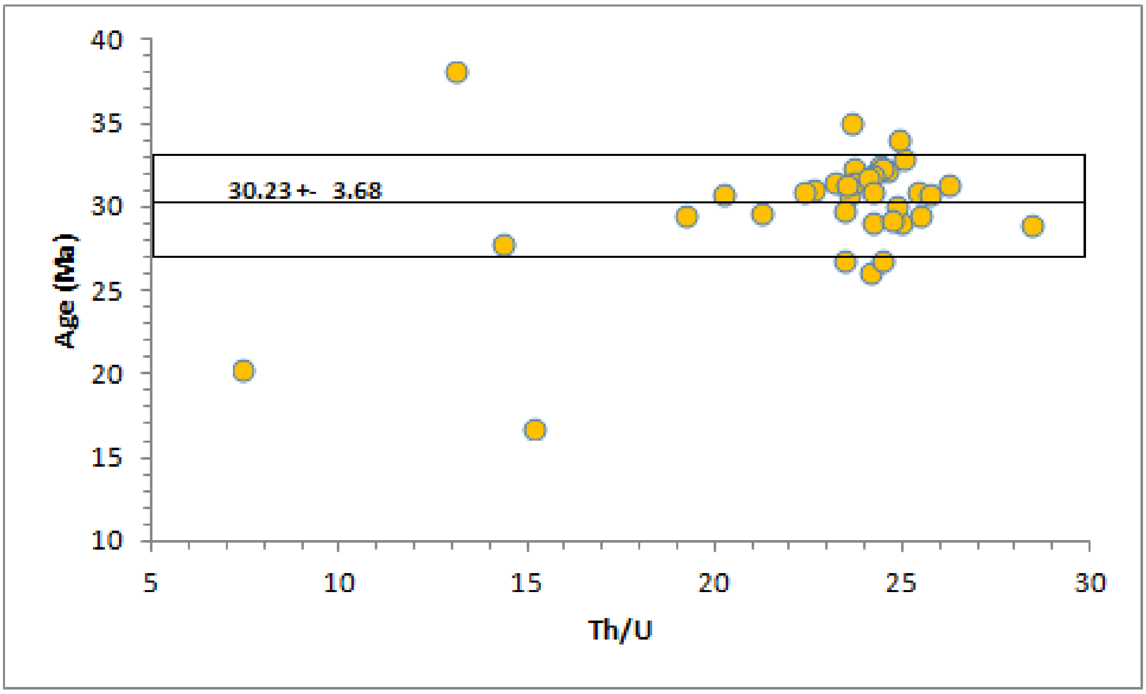

Figure A3.2: Durango age verse Th/U ratio (this study).
Durango age verse Th/U ratio as measured at SUERC during the duration of this study showing the strong clustering of ratios around c. 25. A number of strong outliers are also present and these may have underlying analytical causes.

APPENDIX 4

4. CHAPTER 6 SUPLEMENTARY PLOTS

4.1 Figure 6.5 colour and Observed vs. Predicted plots

Sd07 - 1

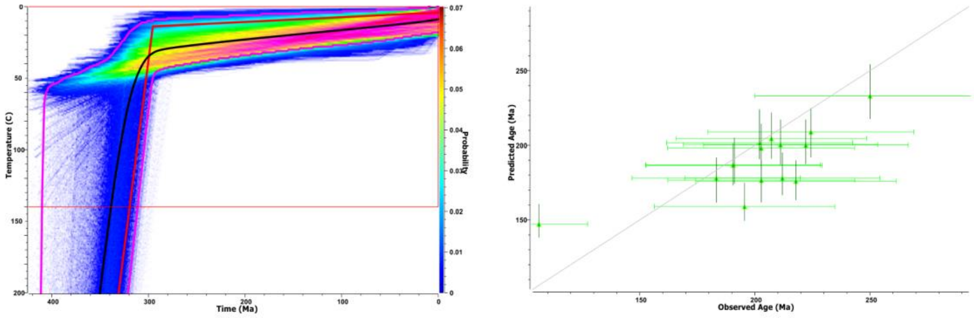

Sd07 - 2

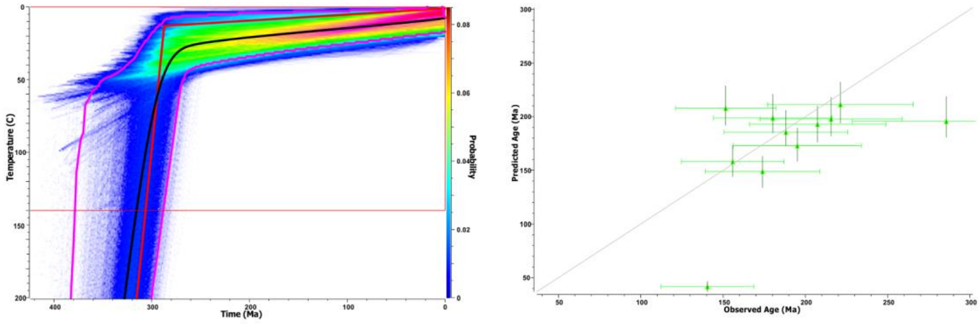

Sd07 - 4

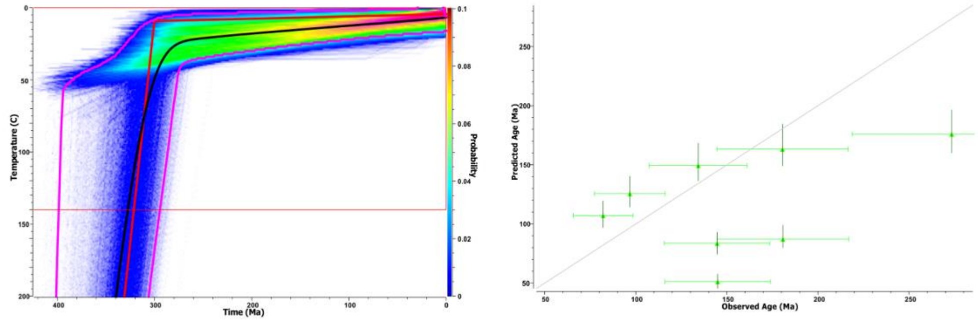

Sd07 - 5

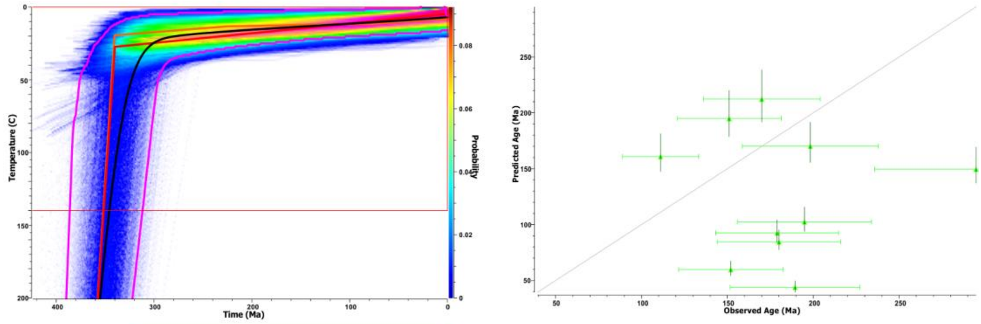

Sd07 - 6

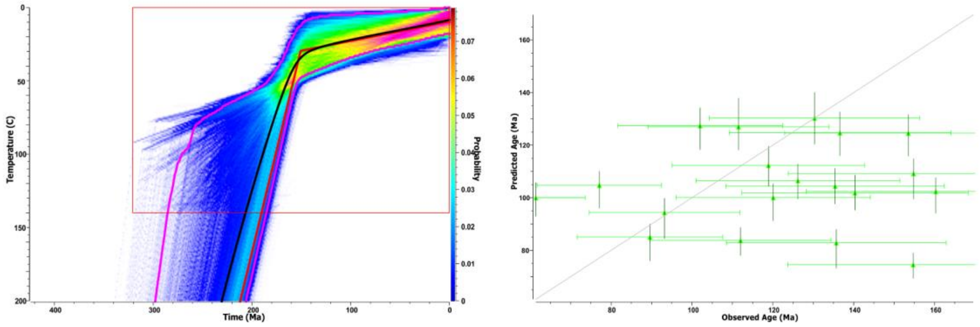

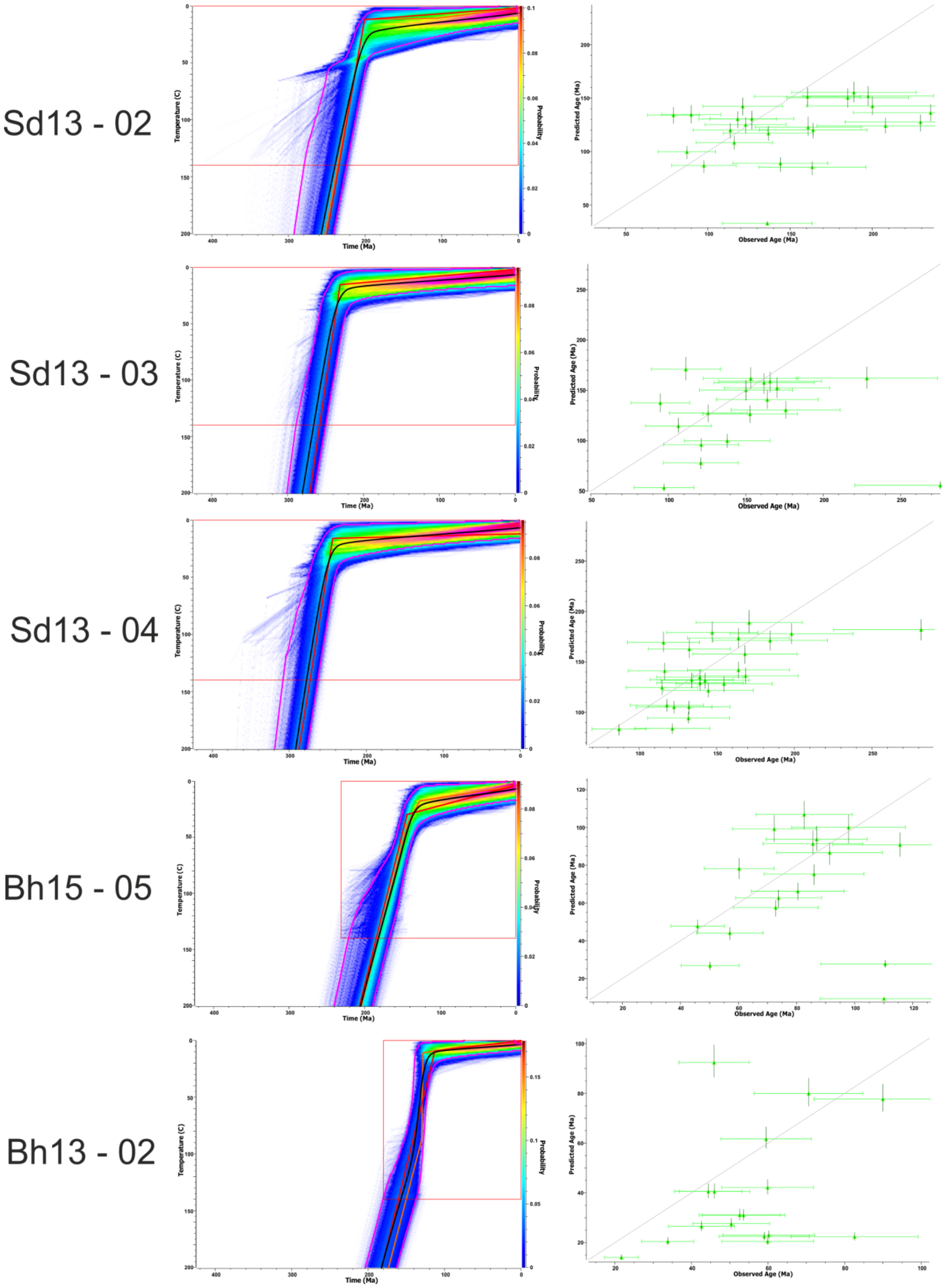

Figure A4.1: Corresponding marginal probability distribution and Observed vs. Predicted age plots for figure **6.5**.

Shown on the left are the thermal history outputs as per figure **6.5** with additional colour shading indicating the marginal probability distribution. Brighter colours (pinks and reds) indicate higher probability and darker colours (blues indicate lower probability. Also included are the maximum likelihood thermal history (solid red line) and maximum posterior likelihood (solid orange line where different to the max likelihood model). Solid pink lines indicate the 95% credibility intervals and solid black line the expected thermal history as per figure **6.4**. Shown on the right are the observed age verses the predicted age plots for each model output.

4.2 Figure 6.6 temperature offset plots

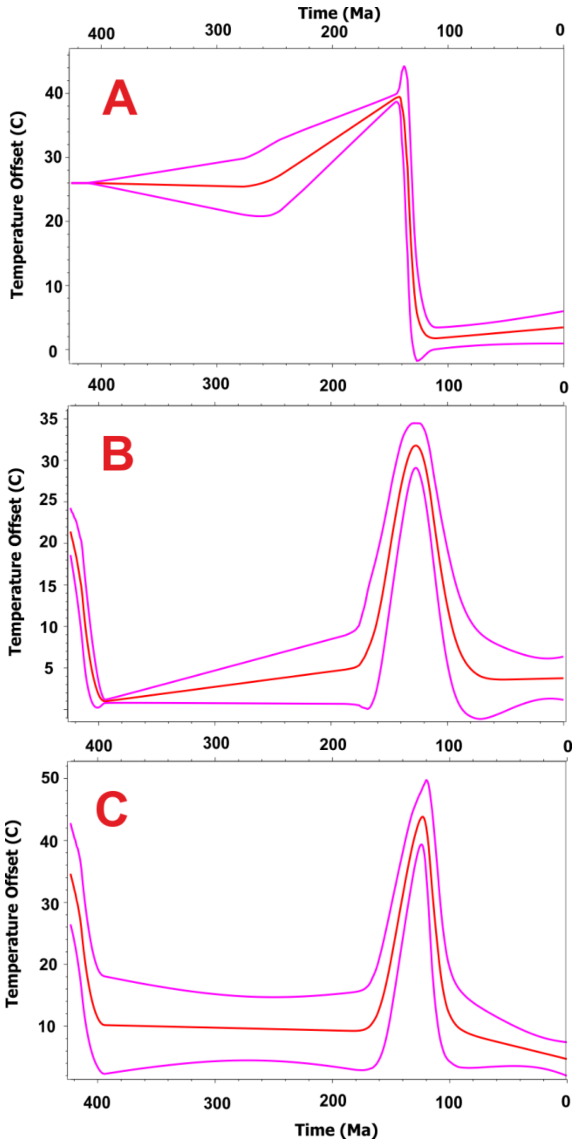

Figure A4.2: Corresponding temperature offset plots for figure **6.6**.
Temperature offset between the top and bottom samples in the profile, which in this instance can be considered the palaeogeothermal gradient in °C Km^{-1} as the vertical profile spans 1001m. Solid red line is the offset between the expected thermal histories and solid pink lines the offset between the upper 95% credibility interval of the top sample and the lower 95% credibility interval of the bottom sample.

4.3 Figure 6.7 colour and Observed vs. Predicted plots

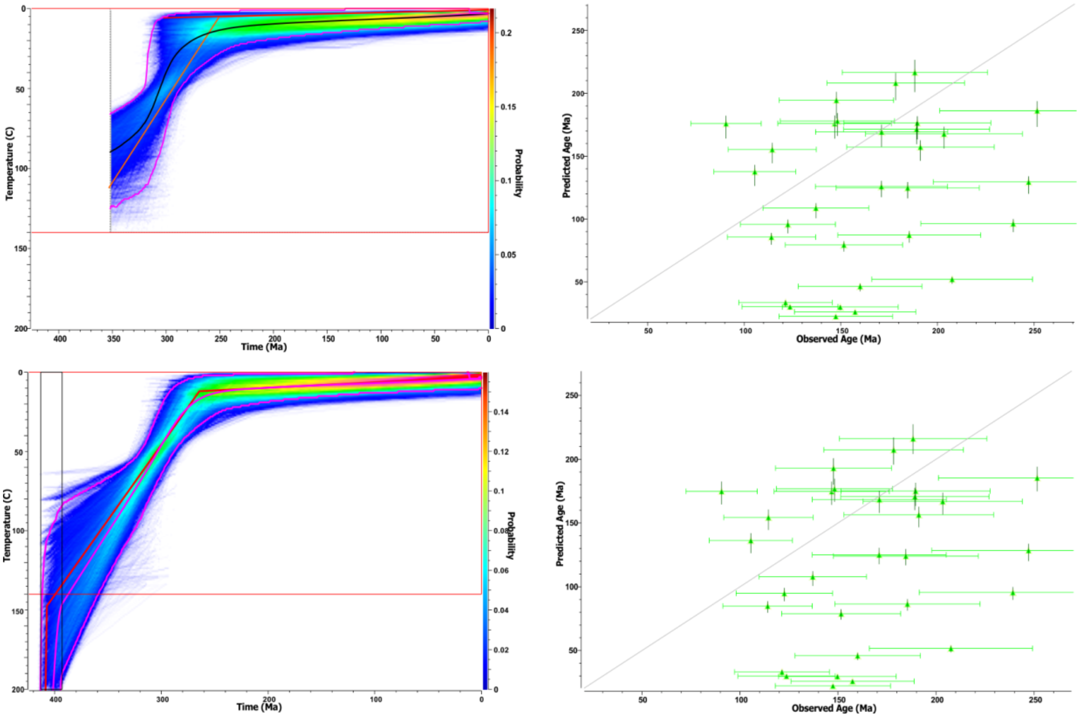

Figure A4.3: Corresponding marginal probability distribution and Observed vs. Predicted age plots for figure **6.7**.

The thermal history outputs as per figure **6.7** with additional colour shading indicating the marginal probability distribution. Brighter colours (pinks and reds) indicate higher probability and darker colours (blues indicate lower probability. Also included are the maximum likelihood thermal history (solid red line) and maximum posterior likelihood (solid orange line where different to the max likelihood model). Solid pink lines indicate the 95% credibility intervals and solid black line the expected thermal history as per figure **6.6.** Inset: the observed age verses the predicted age plots for each model output.

4.4 Figure 6.8 colour and Observed vs. Predicted plots

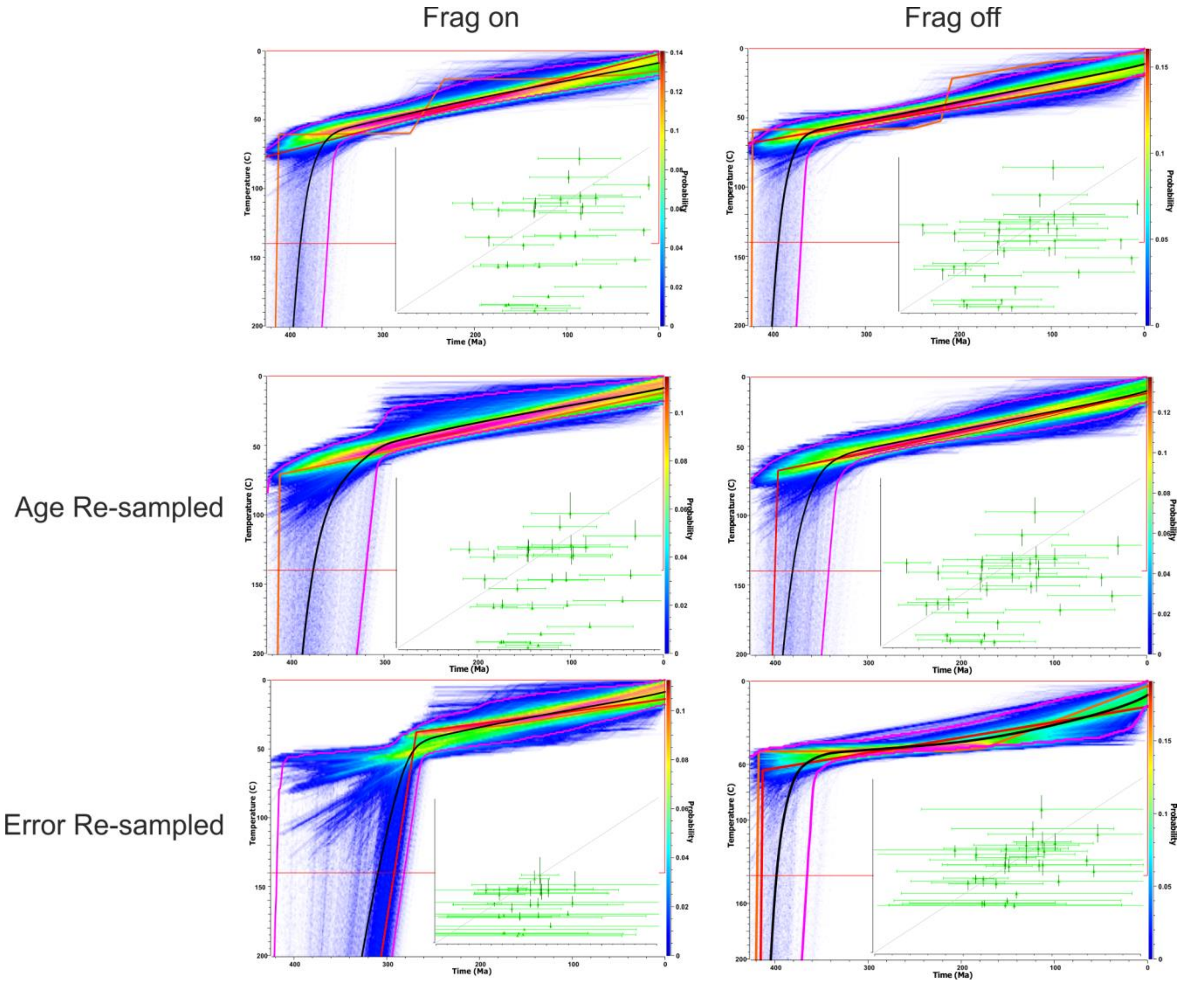

Figure A4.4: Corresponding marginal probability distribution and Observed vs. Predicted age plots for figure **6.8**.
The thermal history outputs as per figure **6.8** with additional colour shading indicating the marginal probability distribution. Brighter colours (pinks and reds) indicate higher probability and darker colours (blues indicate lower probability. Also included are the maximum likelihood thermal history (solid red line) and maximum posterior likelihood (solid orange line where different to the max likelihood model). Solid pink lines indicate the 95% credibility intervals and solid black line the expected thermal history as per figure **6.7.** Inset: the observed age verses the predicted age plots for each model output.

4.5 Figure 6.9 colour and Observed vs. Predicted plots

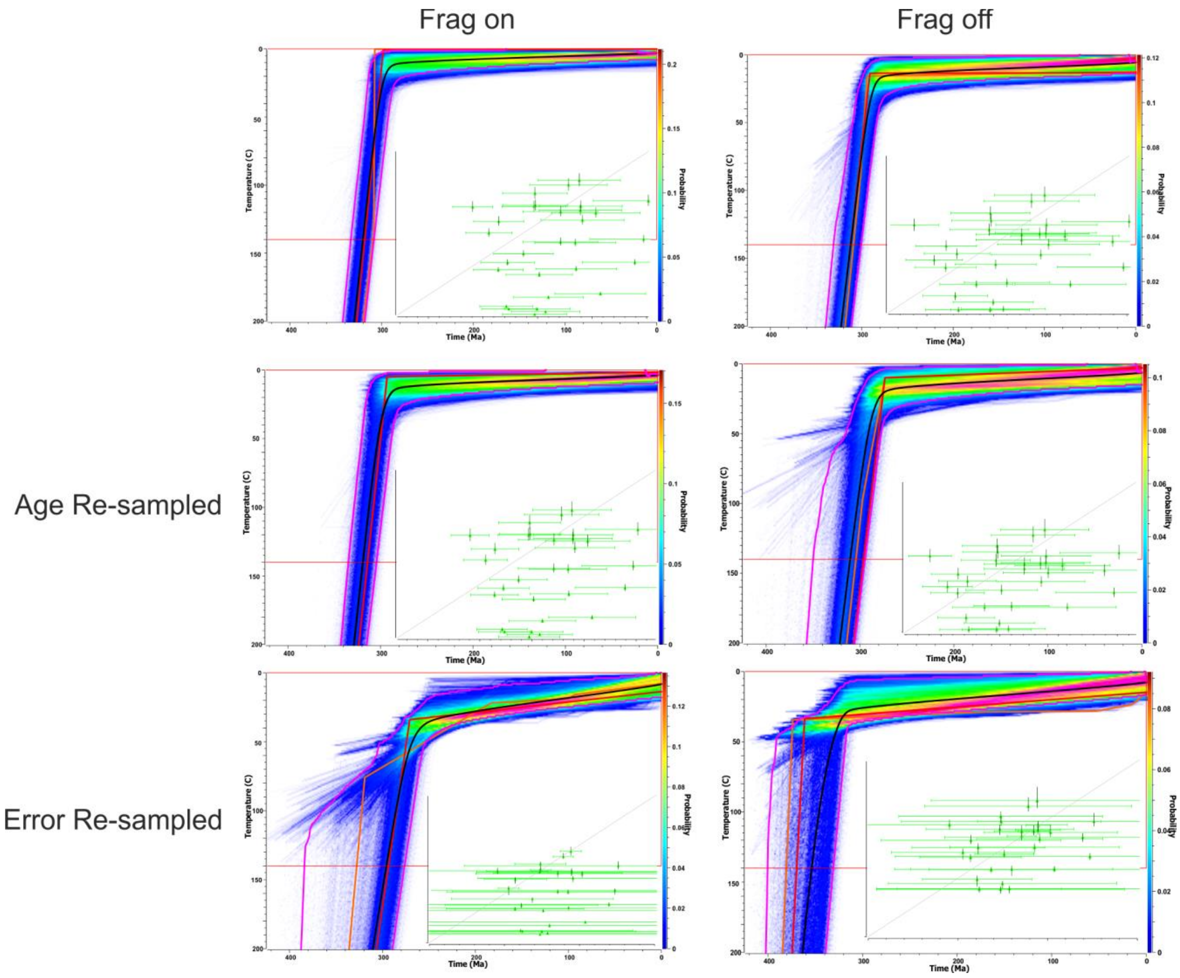

Figure A4.5: Corresponding marginal probability distribution and Observed vs. Predicted age plots for figure **6.9**.

The thermal history outputs as per figure **6.9** with additional colour shading indicating the marginal probability distribution. Brighter colours (pinks and reds) indicate higher probability and darker colours (blues indicate lower probability. Also included are the maximum likelihood thermal history (solid red line) and maximum posterior likelihood (solid orange line where different to the max likelihood model). Solid pink lines indicate the 95% credibility intervals and solid black line the expected thermal history as per figure **6.8.** Inset: the observed age verses the predicted age plots for each model output.

4.6 Figure 6.10 colour and Observed vs. Predicted plots

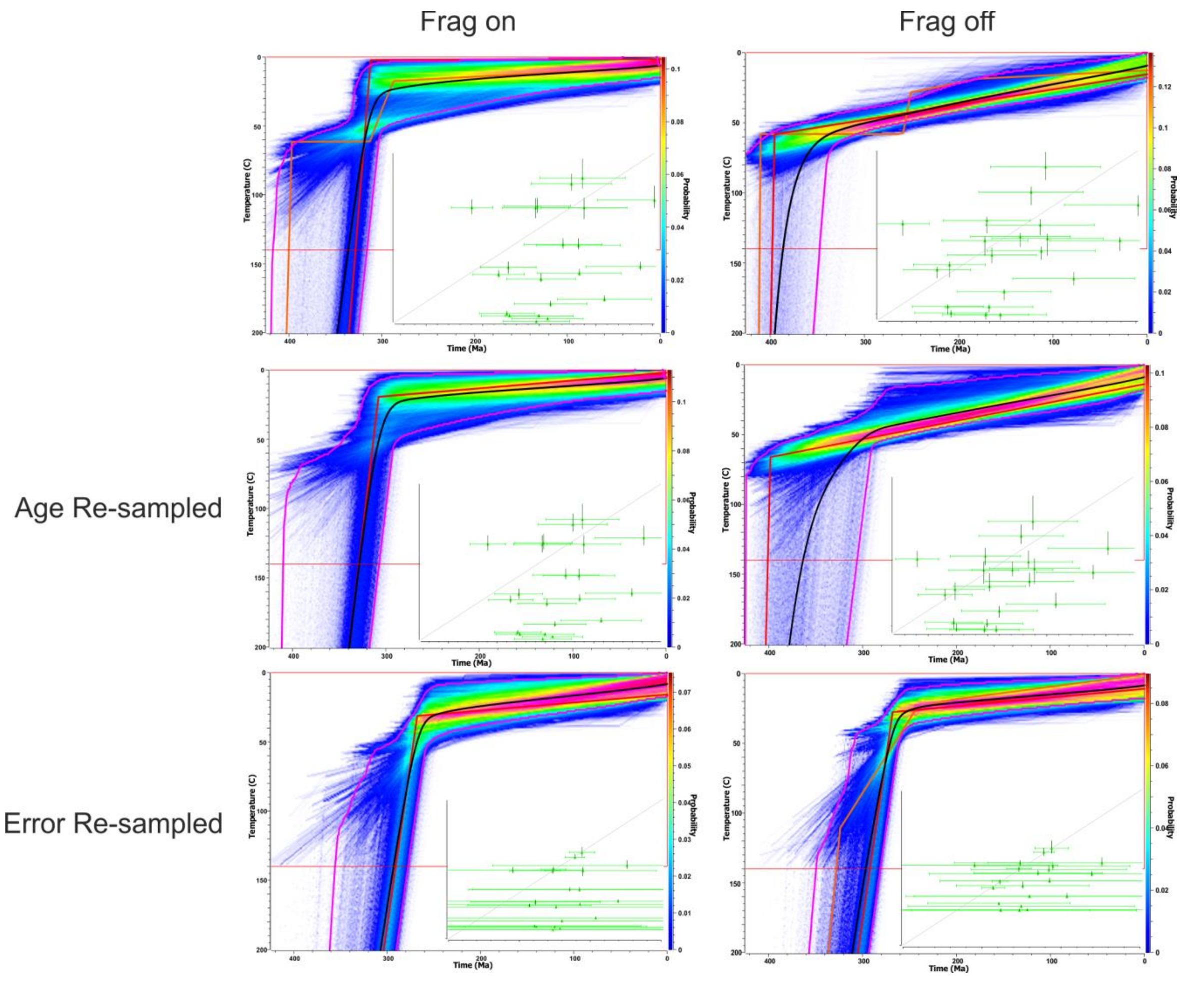

Figure A4.6: Corresponding marginal probability distribution and Observed vs. Predicted age plots for figure **6.10**.

The thermal history outputs as per figure **6.10** with additional colour shading indicating the marginal probability distribution. Brighter colours (pinks and reds) indicate higher probability and darker colours (blues indicate lower probability. Also included are the maximum likelihood thermal history (solid red line) and maximum posterior likelihood (solid orange line where different to the max likelihood model). Solid pink lines indicate the 95% credibility intervals and solid black line the expected thermal history as per figure **6.9.** Inset: the observed age verses the predicted age plots for each model output.

4.7 Figure 6.11 colour and Observed vs. Predicted plots

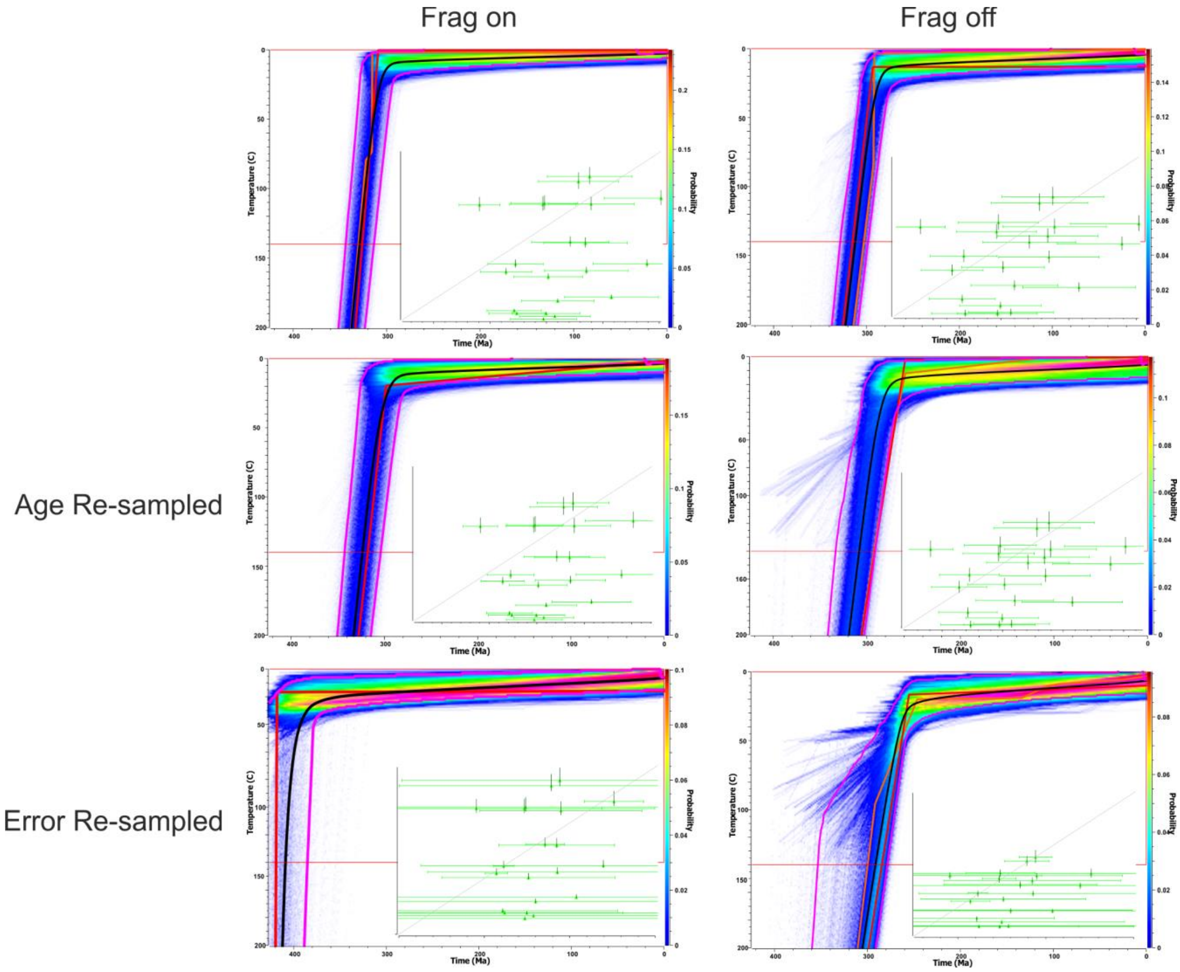

Figure A4.7: Corresponding marginal probability distribution and Observed vs. Predicted age plots for figure **6.11**.
The thermal history outputs as per figure **6.11** with additional colour shading indicating the marginal probability distribution. Brighter colours (pinks and reds) indicate higher probability and darker colours (blues indicate lower probability. Also included are the maximum likelihood thermal history (solid red line) and maximum posterior likelihood (solid orange line where different to the max likelihood model). Solid pink lines indicate the 95% credibility intervals and solid black line the expected thermal history as per figure **6.10.** Inset: the observed age verses the predicted age plots for each model output.

4.8 Figure 6.12 colour and Observed vs. Predicted plots

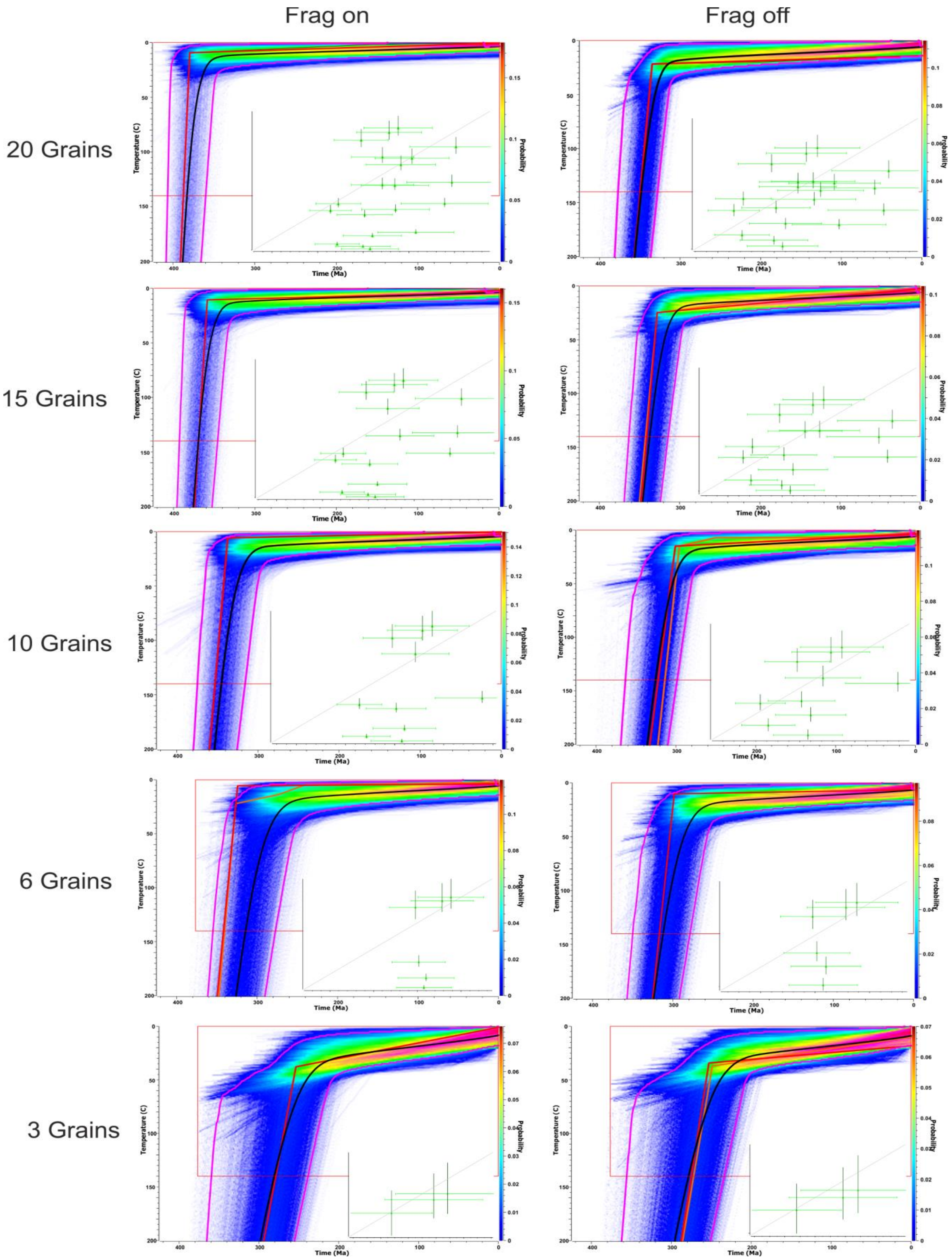

Figure A4.8: Corresponding marginal probability distribution and Observed vs. Predicted age plots for figure **6.12**.

The thermal history outputs as per figure **6.12** with additional colour shading indicating the marginal probability distribution. Brighter colours (pinks and reds) indicate higher probability and darker colours (blues indicate lower probability. Also included are the maximum likelihood thermal history (solid red line) and maximum posterior likelihood (solid orange line where different to the max likelihood model). Solid pink lines indicate the 95% credibility intervals and solid black line the expected thermal history as per figure **6.11.** Inset: the observed age verses the predicted age plots for each model output.

APPENDIX 5

5. CHAPTER 4 FRAGMENT LISTS

5.1 Experiment 1

Table A5-1: Experiment 1, WOLF-1.
L_f = Fragment length, L_0 = Initial grain length, R = cylindrical radius (half width), eRF = Equivalent spherical radius of the fragment, eRG = Equivalent sphereical radius of the initial whole grain.

Grain no.	L_f µm	L_0 µm	R µm	eRF µm	eRG µm	Frag. age	Grain age	^{4}He nmol	U ppm	Th ppm
1	40	400	75	39	95	35.5	37.6	4.7	19.7	19.9
2	55	400	75	48	95	36.2	37.6	4.8	19.7	19.9
3	70	400	75	54	95	36.6	37.6	4.8	19.7	19.9
4	85	400	75	60	95	36.9	37.6	4.9	19.7	19.9
5	100	400	75	64	95	37.1	37.6	4.9	19.7	19.9
6	115	400	75	68	95	37.2	37.6	4.9	19.7	19.9
7	130	400	75	71	95	37.3	37.6	4.9	19.7	19.9
8	145	400	75	74	95	37.4	37.6	4.9	19.7	19.9
9	160	400	75	77	95	37.5	37.6	4.9	19.7	19.9
10	175	400	75	79	95	37.5	37.6	4.9	19.7	19.9
11	190	400	75	81	95	37.6	37.6	4.9	19.7	19.9
12	205	400	75	82	95	37.6	37.6	4.9	19.7	19.9
13	220	400	75	84	95	37.6	37.6	5.0	19.7	19.9
14	235	400	75	85	95	37.7	37.6	5.0	19.7	19.9
15	250	400	75	87	95	37.7	37.6	5.0	19.7	19.9
16	265	400	75	88	95	37.7	37.6	5.0	19.7	19.9
17	280	400	75	89	95	37.7	37.6	5.0	19.7	19.9
18	295	400	75	90	95	37.8	37.6	5.0	19.7	19.9
19	310	400	75	91	95	37.8	37.6	5.0	19.7	19.9
20	325	400	75	91	95	37.8	37.6	5.0	19.7	19.9
21	340	400	75	92	95	37.8	37.6	5.0	19.7	19.9
22	355	400	75	93	95	37.8	37.6	5.0	19.7	19.9
23	370	400	75	94	95	37.8	37.6	5.0	19.7	19.9
24	385	400	75	94	95	37.8	37.6	5.0	19.7	19.9

Table A5-2: Experiment 1, WOLF-2.

Grain no.	L_f µm	L_0 µm	R µm	eRF µm	eRG µm	Frag. age	Grain age	^{4}He nmol	U ppm	Th ppm
1	40	400	75	39	95	33.8	39.3	4.4	19.7	19.9
2	55	400	75	48	95	35.5	39.3	4.7	19.7	19.9
3	70	400	75	54	95	36.5	39.3	4.8	19.7	19.9
4	85	400	75	60	95	37.3	39.3	4.9	19.7	19.9
5	100	400	75	64	95	37.8	39.3	5.0	19.7	19.9
6	115	400	75	68	95	38.2	39.3	5.0	19.7	19.9
7	130	400	75	71	95	38.5	39.3	5.1	19.7	19.9
8	145	400	75	74	95	38.7	39.3	5.1	19.7	19.9
9	160	400	75	77	95	38.9	39.3	5.1	19.7	19.9
10	175	400	75	79	95	39.1	39.3	5.1	19.7	19.9

11	190	400	75	81	95	39.2	39.3	5.2	19.7	19.9
12	205	400	75	82	95	39.3	39.3	5.2	19.7	19.9
13	220	400	75	84	95	39.4	39.3	5.2	19.7	19.9
14	235	400	75	85	95	39.5	39.3	5.2	19.7	19.9
15	250	400	75	87	95	39.6	39.3	5.2	19.7	19.9
16	265	400	75	88	95	39.7	39.3	5.2	19.7	19.9
17	280	400	75	89	95	39.7	39.3	5.2	19.7	19.9
18	295	400	75	90	95	39.8	39.3	5.2	19.7	19.9
19	310	400	75	91	95	39.8	39.3	5.2	19.7	19.9
20	325	400	75	91	95	39.9	39.3	5.2	19.7	19.9
21	340	400	75	92	95	39.9	39.3	5.2	19.7	19.9
22	355	400	75	93	95	39.9	39.3	5.3	19.7	19.9
23	370	400	75	94	95	39.9	39.3	5.2	19.7	19.9
24	385	400	75	94	95	39.8	39.3	5.2	19.7	19.9

Table A5-3: Experiment 1, WOLF-3.

Grain no.	L_f µm	L_0 µm	R µm	eRF µm	eRG µm	Frag. age	Grain age	^{4}He nmol	U ppm	Th ppm
1	40	400	75	39	95	27.6	38.4	3.6	19.7	19.9
2	55	400	75	48	95	30.3	38.4	4.0	19.7	19.9
3	70	400	75	54	95	32.3	38.4	4.3	19.7	19.9
4	85	400	75	60	95	33.8	38.4	4.4	19.7	19.9
5	100	400	75	64	95	34.9	38.4	4.6	19.7	19.9
6	115	400	75	68	95	35.8	38.4	4.7	19.7	19.9
7	130	400	75	71	95	36.5	38.4	4.8	19.7	19.9
8	145	400	75	74	95	37.0	38.4	4.9	19.7	19.9
9	160	400	75	77	95	37.5	38.4	4.9	19.7	19.9
10	175	400	75	79	95	37.9	38.4	5.0	19.7	19.9
11	190	400	75	81	95	38.2	38.4	5.0	19.7	19.9
12	205	400	75	82	95	38.4	38.4	5.1	19.7	19.9
13	220	400	75	84	95	38.7	38.4	5.1	19.7	19.9
14	235	400	75	85	95	38.9	38.4	5.1	19.7	19.9
15	250	400	75	87	95	39.1	38.4	5.1	19.7	19.9
16	265	400	75	88	95	39.2	38.4	5.2	19.7	19.9
17	280	400	75	89	95	39.3	38.4	5.2	19.7	19.9
18	295	400	75	90	95	39.5	38.4	5.2	19.7	19.9
19	310	400	75	91	95	39.6	38.4	5.2	19.7	19.9
20	325	400	75	91	95	39.6	38.4	5.2	19.7	19.9
21	340	400	75	92	95	39.6	38.4	5.2	19.7	19.9
22	355	400	75	93	95	39.6	38.4	5.2	19.7	19.9
23	370	400	75	94	95	39.4	38.4	5.2	19.7	19.9
24	385	400	75	94	95	39.1	38.4	5.1	19.7	19.9

Table A5-4: Experiment 1, WOLF-4.

Grain no.	L_f µm	L_0 µm	R µm	eRF µm	eRG µm	Frag. age	Grain age	^{4}He nmol	U ppm	Th ppm
1	40	400	75	39	95	27.8	37.9	3.7	19.7	19.9
2	55	400	75	48	95	30.5	37.9	4.0	19.7	19.9
3	70	400	75	54	95	32.4	37.9	4.3	19.7	19.9
4	85	400	75	60	95	33.8	37.9	4.4	19.7	19.9

5	100	400	75	64	95	34.8	37.9	4.6	19.7	19.9
6	115	400	75	68	95	35.6	37.9	4.7	19.7	19.9
7	130	400	75	71	95	36.2	37.9	4.8	19.7	19.9
8	145	400	75	74	95	36.7	37.9	4.8	19.7	19.9
9	160	400	75	77	95	37.1	37.9	4.9	19.7	19.9
10	175	400	75	79	95	37.5	37.9	4.9	19.7	19.9
11	190	400	75	81	95	37.7	37.9	5.0	19.7	19.9
12	205	400	75	82	95	38.0	37.9	5.0	19.7	19.9
13	220	400	75	84	95	38.2	37.9	5.0	19.7	19.9
14	235	400	75	85	95	38.4	37.9	5.1	19.7	19.9
15	250	400	75	87	95	38.5	37.9	5.1	19.7	19.9
16	265	400	75	88	95	38.7	37.9	5.1	19.7	19.9
17	280	400	75	89	95	38.8	37.9	5.1	19.7	19.9
18	295	400	75	90	95	38.9	37.9	5.1	19.7	19.9
19	310	400	75	91	95	39.0	37.9	5.1	19.7	19.9
20	325	400	75	91	95	39.1	37.9	5.1	19.7	19.9
21	340	400	75	92	95	39.1	37.9	5.1	19.7	19.9
22	355	400	75	93	95	39.1	37.9	5.1	19.7	19.9
23	370	400	75	94	95	38.9	37.9	5.1	19.7	19.9
24	385	400	75	94	95	38.6	37.9	5.1	19.7	19.9

Table A5-5: Experiment 1, WOLF-5.

Grain no.	L_f µm	L_0 µm	R µm	eRF µm	eRG µm	Frag. age	Grain age	^{4}He nmol	U ppm	Th ppm
1	40	400	75	39	95	22.1	38.5	2.9	19.7	19.9
2	55	400	75	48	95	26.5	38.5	3.5	19.7	19.9
3	70	400	75	54	95	29.6	38.5	3.9	19.7	19.9
4	85	400	75	60	95	31.9	38.5	4.2	19.7	19.9
5	100	400	75	64	95	33.6	38.5	4.4	19.7	19.9
6	115	400	75	68	95	34.9	38.5	4.6	19.7	19.9
7	130	400	75	71	95	35.8	38.5	4.7	19.7	19.9
8	145	400	75	74	95	36.6	38.5	4.8	19.7	19.9
9	160	400	75	77	95	37.2	38.5	4.9	19.7	19.9
10	175	400	75	79	95	37.8	38.5	5.0	19.7	19.9
11	190	400	75	81	95	38.2	38.5	5.0	19.7	19.9
12	205	400	75	82	95	38.6	38.5	5.1	19.7	19.9
13	220	400	75	84	95	38.9	38.5	5.1	19.7	19.9
14	235	400	75	85	95	39.2	38.5	5.2	19.7	19.9
15	250	400	75	87	95	39.4	38.5	5.2	19.7	19.9
16	265	400	75	88	95	39.6	38.5	5.2	19.7	19.9
17	280	400	75	89	95	39.8	38.5	5.2	19.7	19.9
18	295	400	75	90	95	40.0	38.5	5.3	19.7	19.9
19	310	400	75	91	95	40.2	38.5	5.3	19.7	19.9
20	325	400	75	91	95	40.3	38.5	5.3	19.7	19.9
21	340	400	75	92	95	40.4	38.5	5.3	19.7	19.9
22	355	400	75	93	95	40.3	38.5	5.3	19.7	19.9
23	370	400	75	94	95	40.1	38.5	5.3	19.7	19.9
24	385	400	75	94	95	39.5	38.5	5.2	19.7	19.9

5.2 Experiment 2

Table A5-6: Experiment 2, WOLF-1
L_f = Fragment length, L_0 = Initial grain length, R = cylindrical radius (half width), eRF = Equivalent spherical radius of the fragment, eRG = Equivalent sphereical radius of the initial whole grain.

Grain no.	L_f µm	L_0 µm	R µm	eRF µm	eRG µm	Frag. age	Grain age	^{4}He nmol	U ppm	Th ppm
1	108	220	100	78	103	38.4	38.4	5.0	19.7	19.9
2	61	260	61	46	74	35.3	36.2	4.6	19.7	19.9
3	97	384	92	71	111	37.9	38.5	5.0	19.7	19.9
4	92	437	92	69	114	37.9	38.6	5.0	19.7	19.9
5	105	448	99	76	122	38.3	38.9	5.0	19.7	19.9
6	114	273	98	79	108	38.3	38.5	5.0	19.7	19.9
7	71	360	57	47	74	35.2	36.0	4.6	19.7	19.9
8	154	426	95	88	117	38.5	38.7	5.1	19.7	19.9
9	202	489	71	79	93	37.3	37.4	4.9	19.7	19.9
10	107	524	64	60	86	36.3	36.9	4.8	19.7	19.9
11	221	593	77	86	102	37.8	37.9	5.0	19.7	19.9
12	126	219	81	74	89	37.6	37.5	5.0	19.7	19.9
13	194	342	99	98	115	38.8	38.7	5.1	19.7	19.9
14	225	378	64	75	82	36.8	36.7	4.8	19.7	19.9
15	289	418	76	90	96	37.8	37.7	5.0	19.7	19.9
16	306	457	66	81	87	37.1	37.0	4.9	19.7	19.9
17	356	525	86	104	111	38.5	38.4	5.1	19.7	19.9
18	349	556	90	107	116	38.7	38.6	5.1	19.7	19.9
19	148	219	78	77	86	37.6	37.3	4.9	19.7	19.9
20	211	252	91	95	100	38.5	38.1	5.1	19.7	19.9
21	226	306	81	89	96	38.0	37.8	5.0	19.7	19.9
22	367	369	75	93	93	37.7	37.5	5.0	19.7	19.9
23	444	467	83	105	106	38.4	38.1	5.0	19.7	19.9
24	215	351	73	82	91	37.5	37.4	4.9	19.7	19.9
25	214	442	70	79	91	37.3	37.3	4.9	19.7	19.9

Table A5-7: Experiment 2, WOLF-2.

Grain no.	L_f µm	L_0 µm	R µm	eRF µm	eRG µm	Frag. age	Grain age	^{4}He nmol	U ppm	Th ppm
1	108	220	100	78	103	41.2	41.3	5.4	19.7	19.9
2	61	260	61	46	74	33.7	35.8	4.4	19.7	19.9
3	97	384	92	71	111	40.0	41.8	5.3	19.7	19.9
4	92	437	92	69	114	39.8	42.0	5.2	19.7	19.9
5	105	448	99	76	122	41.0	43.0	5.4	19.7	19.9
6	114	273	98	79	108	41.2	41.7	5.4	19.7	19.9
7	71	360	57	47	74	33.5	35.4	4.4	19.7	19.9
8	154	426	95	88	117	41.7	42.4	5.5	19.7	19.9
9	202	489	71	79	93	38.6	38.8	5.1	19.7	19.9
10	107	524	64	60	86	36.0	37.5	4.7	19.7	19.9
11	221	593	77	86	102	39.8	40.1	5.2	19.7	19.9
12	126	219	81	74	89	39.3	38.9	5.2	19.7	19.9
13	194	342	99	98	115	42.7	42.4	5.6	19.7	19.9
14	225	378	64	75	82	37.3	37.1	4.9	19.7	19.9
15	289	418	76	90	96	39.9	39.5	5.3	19.7	19.9

16	306	457	66	81	87	38.1	37.8	5.0	19.7	19.9
17	356	525	86	104	111	41.8	41.5	5.5	19.7	19.9
18	349	556	90	107	116	42.4	42.1	5.6	19.7	19.9
19	148	219	78	77	86	39.2	38.5	5.2	19.7	19.9
20	211	252	91	95	100	41.7	40.7	5.5	19.7	19.9
21	226	306	81	89	96	40.4	39.8	5.3	19.7	19.9
22	367	369	75	93	93	39.3	39.2	5.2	19.7	19.9
23	444	467	83	105	106	41.4	40.8	5.4	19.7	19.9
24	215	351	73	82	91	39.0	38.7	5.1	19.7	19.9
25	214	442	70	79	91	38.5	38.5	5.1	19.7	19.9

Table A5-8: Experiment 2, WOLF-3.

Grain no.	L_f μm	L_0 μm	R μm	eRF μm	eRG μm	Frag. age	Grain age	^{4}He nmol	U ppm	Th ppm
1	108	220	100	78	103	43.1	43.3	5.7	19.7	19.9
2	61	260	61	46	74	27.0	30.6	3.5	19.7	19.9
3	97	384	92	71	111	40.1	44.8	5.3	19.7	19.9
4	92	437	92	69	114	39.6	45.4	5.2	19.7	19.9
5	105	448	99	76	122	42.7	47.9	5.6	19.7	19.9
6	114	273	98	79	108	43.1	44.6	5.7	19.7	19.9
7	71	360	57	47	74	26.4	29.7	3.5	19.7	19.9
8	154	426	95	88	117	44.5	46.3	5.9	19.7	19.9
9	202	489	71	79	93	36.6	37.2	4.8	19.7	19.9
10	107	524	64	60	86	31.1	33.9	4.1	19.7	19.9
11	221	593	77	86	102	39.6	40.4	5.2	19.7	19.9
12	126	219	81	74	89	38.4	37.6	5.1	19.7	19.9
13	194	342	99	98	115	47.2	46.4	6.2	19.7	19.9
14	225	378	64	75	82	33.6	33.2	4.4	19.7	19.9
15	289	418	76	90	96	39.9	38.9	5.3	19.7	19.9
16	306	457	66	81	87	35.2	34.6	4.6	19.7	19.9
17	356	525	86	104	111	44.7	43.9	5.9	19.7	19.9
18	349	556	90	107	116	46.3	45.6	6.1	19.7	19.9
19	148	219	78	77	86	38.1	36.5	5.0	19.7	19.9
20	211	252	91	95	100	44.0	41.9	5.8	19.7	19.9
21	226	306	81	89	96	41.2	39.6	5.4	19.7	19.9
22	367	369	75	93	93	38.2	38.1	5.0	19.7	19.9
23	444	467	83	105	106	43.2	42.3	5.7	19.7	19.9
24	215	351	73	82	91	37.7	37.0	5.0	19.7	19.9
25	214	442	70	79	91	36.3	36.4	4.8	19.7	19.9

Table A5-9: Experiment 2, WOLF-4.

Grain no.	L_f μm	L_0 μm	R μm	eRF μm	eRG μm	Frag. age	Grain age	^{4}He nmol	U ppm	Th ppm
1	108	220	100	78	103	42.0	42.1	5.5	19.7	19.9
2	61	260	61	46	74	27.4	30.9	3.6	19.7	19.9
3	97	384	92	71	111	39.3	43.5	5.2	19.7	19.9
4	92	437	92	69	114	38.9	44.0	5.1	19.7	19.9
5	105	448	99	76	122	41.6	46.2	5.5	19.7	19.9
6	114	273	98	79	108	42.0	43.3	5.5	19.7	19.9
7	71	360	57	47	74	26.9	30.1	3.5	19.7	19.9

8	154	426	95	88	117	43.3	44.8	5.7	19.7	19.9
9	202	489	71	79	93	36.4	36.9	4.8	19.7	19.9
10	107	524	64	60	86	31.4	34.0	4.1	19.7	19.9
11	221	593	77	86	102	39.0	39.7	5.1	19.7	19.9
12	126	219	81	74	89	37.9	37.2	5.0	19.7	19.9
13	194	342	99	98	115	45.5	44.9	6.0	19.7	19.9
14	225	378	64	75	82	33.7	33.3	4.4	19.7	19.9
15	289	418	76	90	96	39.3	38.4	5.2	19.7	19.9
16	306	457	66	81	87	35.2	34.6	4.6	19.7	19.9
17	356	525	86	104	111	43.5	42.7	5.7	19.7	19.9
18	349	556	90	107	116	44.8	44.2	5.9	19.7	19.9
19	148	219	78	77	86	37.7	36.3	5.0	19.7	19.9
20	211	252	91	95	100	42.9	40.9	5.6	19.7	19.9
21	226	306	81	89	96	40.4	39.0	5.3	19.7	19.9
22	367	369	75	93	93	37.8	37.6	5.0	19.7	19.9
23	444	467	83	105	106	42.2	41.3	5.6	19.7	19.9
24	215	351	73	82	91	37.4	36.7	4.9	19.7	19.9
25	214	442	70	79	91	36.1	36.2	4.8	19.7	19.9

Table A5-10: Experiment 2, WOLF-5.

Grain no.	L_f µm	L_0 µm	R µm	eRF µm	eRG µm	Frag. age	Grain age	^{4}He nmol	U ppm	Th ppm
1	108	220	100	78	103	43.7	43.9	5.7	19.7	19.9
2	61	260	61	46	74	22.0	27.9	2.9	19.7	19.9
3	97	384	92	71	111	39.9	46.0	5.2	19.7	19.9
4	92	437	92	69	114	39.2	46.7	5.2	19.7	19.9
5	105	448	99	76	122	43.0	49.4	5.7	19.7	19.9
6	114	273	98	79	108	43.7	45.5	5.8	19.7	19.9
7	71	360	57	47	74	21.3	26.7	2.8	19.7	19.9
8	154	426	95	88	117	45.5	47.7	6.0	19.7	19.9
9	202	489	71	79	93	36.3	37.1	4.8	19.7	19.9
10	107	524	64	60	86	28.5	32.8	3.8	19.7	19.9
11	221	593	77	86	102	40.0	41.1	5.3	19.7	19.9
12	126	219	81	74	89	38.4	37.1	5.0	19.7	19.9
13	194	342	99	98	115	48.6	47.7	6.4	19.7	19.9
14	225	378	64	75	82	32.4	31.7	4.3	19.7	19.9
15	289	418	76	90	96	40.5	39.2	5.3	19.7	19.9
16	306	457	66	81	87	34.6	33.7	4.6	19.7	19.9
17	356	525	86	104	111	46.2	45.1	6.1	19.7	19.9
18	349	556	90	107	116	47.9	47.1	6.3	19.7	19.9
19	148	219	78	77	86	38.1	35.8	5.0	19.7	19.9
20	211	252	91	95	100	45.4	42.3	6.0	19.7	19.9
21	226	306	81	89	96	42.1	39.9	5.5	19.7	19.9
22	367	369	75	93	93	38.2	38.0	5.0	19.7	19.9
23	444	467	83	105	106	44.6	43.2	5.9	19.7	19.9
24	215	351	73	82	91	37.7	36.7	5.0	19.7	19.9
25	214	442	70	79	91	35.9	36.1	4.7	19.7	19.9

5.3 Experiment 3

Table A5-11: Experiment 3, WOLF-1.
L_f = Fragment length, L_0 = Initial grain length, R = cylindrical radius (half width), eRF = Equivalent spherical radius of the fragment, eRG = Equivalent sphereical radius of the initial whole grain.

Grain no.	L_f µm	L_0 µm	R µm	eRF µm	eRG µm	Frag. age	Grain age	^{4}He nmol	U ppm	Th ppm
1	108	220	100	78	103	38.36	38.38	12.5	48.41	49.50
2	61	260	61	46	74	35.40	36.27	18.6	78.08	79.85
3	97	384	92	71	111	38.02	38.59	28.9	113.22	115.79
4	92	437	92	69	114	37.92	38.61	21.3	83.55	85.44
5	105	448	99	76	122	38.38	38.95	27.2	105.42	107.80
6	114	273	98	79	108	38.43	38.59	28.0	108.53	110.99
7	71	360	57	47	74	35.24	36.08	17.6	74.18	75.85
8	154	426	95	88	117	38.41	38.61	3.8	14.84	15.17
9	202	489	71	79	93	37.34	37.42	13.7	54.66	55.89
10	107	524	64	60	86	36.41	36.97	25.6	104.63	107.00
11	221	593	77	86	102	37.79	37.91	15.7	61.69	63.09
12	126	219	81	74	89	37.58	37.45	4.3	17.18	17.56
13	194	342	99	98	115	38.86	38.78	25.3	96.83	99.02
14	225	378	64	75	82	36.86	36.78	18.0	72.62	74.26
15	289	418	76	90	96	37.65	37.51	1.6	6.25	6.39
16	306	457	66	81	87	37.12	37.01	13.0	52.32	53.50
17	356	525	86	104	111	38.45	38.34	9.7	37.48	38.33
18	349	556	90	107	116	38.55	38.47	2.2	8.59	8.79
19	148	219	78	77	86	37.70	37.44	29.5	116.35	118.98
20	211	252	91	95	100	38.58	38.23	27.9	107.76	110.19
21	226	306	81	89	96	38.01	37.78	10.4	40.60	41.52
22	367	369	75	93	93	37.62	37.51	6.3	24.98	25.55
23	444	467	83	105	106	38.25	38.03	2.2	8.59	8.79
24	215	351	73	82	91	37.50	37.39	12.0	47.64	48.71
25	214	442	70	79	91	37.35	37.37	23.7	94.48	96.62

Table A5-12: Experiment 3, WOLF-2.

Grain no.	L_f µm	L_0 µm	R µm	eRF µm	eRG µm	Frag. age	Grain age	^{4}He nmol	U ppm	Th ppm
1	108	220	100	78	103	45.29	45.47	14.8	48.41	49.50
2	61	260	61	46	74	42.53	44.51	22.3	78.08	79.85
3	97	384	92	71	111	51.40	53.25	39.3	113.22	115.79
4	92	437	92	69	114	48.65	50.81	27.4	83.55	85.44
5	105	448	99	76	122	51.74	53.69	36.8	105.42	107.80
6	114	273	98	79	108	52.12	52.84	38.2	108.53	110.99
7	71	360	57	47	74	41.85	43.70	20.8	74.18	75.85
8	154	426	95	88	117	37.27	38.04	3.7	14.84	15.17
9	202	489	71	79	93	43.98	44.28	16.2	54.66	55.89
10	107	524	64	60	86	47.10	48.55	33.2	104.63	107.00
11	221	593	77	86	102	46.05	46.48	19.1	61.69	63.09
12	126	219	81	74	89	36.00	35.80	4.2	17.18	17.56
13	194	342	99	98	115	52.44	52.46	34.3	96.83	99.02
14	225	378	64	75	82	45.22	45.08	22.1	72.62	74.26
15	289	418	76	90	96	32.44	32.23	1.4	6.25	6.39

16	306	457	66	81	87	43.15	42.94	15.2	52.32	53.50
17	356	525	86	104	111	43.70	43.54	11.0	37.48	38.33
18	349	556	90	107	116	35.51	35.45	2.1	8.59	8.79
19	148	219	78	77	86	50.92	50.45	40.0	116.35	118.98
20	211	252	91	95	100	52.48	51.81	38.2	107.76	110.19
21	226	306	81	89	96	43.17	42.69	11.8	40.60	41.52
22	367	369	75	93	93	38.53	38.45	6.5	24.98	25.55
23	444	467	83	105	106	34.57	34.28	2.0	8.59	8.79
24	215	351	73	82	91	43.25	43.04	13.9	47.64	48.71
25	214	442	70	79	91	48.48	48.65	30.9	94.48	96.62

Table A5-13: Experiment 3, WOLF-3.

Grain no.	L_f µm	L_0 µm	R µm	eRF µm	eRG µm	Frag. age	Grain age	^{4}He nmol	U ppm	Th ppm
1	108	220	100	78	103	67.33	68.51	22.3	48.41	49.50
2	61	260	61	46	74	64.54	69.67	34.5	78.08	79.85
3	97	384	92	71	111	80.17	83.01	61.7	113.22	115.79
4	92	437	92	69	114	75.93	80.07	43.2	83.55	85.44
5	105	448	99	76	122	80.71	83.67	57.8	105.42	107.80
6	114	273	98	79	108	81.24	82.55	59.9	108.53	110.99
7	71	360	57	47	74	63.00	68.05	32.0	74.18	75.85
8	154	426	95	88	117	34.83	36.57	3.5	14.84	15.17
9	202	489	71	79	93	65.72	67.37	24.6	54.66	55.89
10	107	524	64	60	86	73.82	76.91	52.6	104.63	107.00
11	221	593	77	86	102	70.69	72.43	29.8	61.69	63.09
12	126	219	81	74	89	33.38	33.05	3.9	17.18	17.56
13	194	342	99	98	115	81.86	82.22	53.9	96.83	99.02
14	225	378	64	75	82	69.85	70.49	34.7	72.62	74.26
15	289	418	76	90	96	22.63	22.33	0.9	6.25	6.39
16	306	457	66	81	87	63.68	64.17	22.8	52.32	53.50
17	356	525	86	104	111	62.08	62.38	15.9	37.48	38.33
18	349	556	90	107	116	27.45	27.27	1.6	8.59	8.79
19	148	219	78	77	86	79.58	79.33	62.9	116.35	118.98
20	211	252	91	95	100	81.95	81.24	60.0	107.76	110.19
21	226	306	81	89	96	61.48	61.01	17.1	40.60	41.52
22	367	369	75	93	93	43.57	44.05	7.4	24.98	25.55
23	444	467	83	105	106	25.78	25.50	1.5	8.59	8.79
24	215	351	73	82	91	63.05	63.48	20.6	47.64	48.71
25	214	442	70	79	91	76.08	77.01	49.0	94.48	96.62

Table A5-14: Experiment 3, WOLF-4.

Grain no.	L_f µm	L_0 µm	R µm	eRF µm	eRG µm	Frag. age	Grain age	^{4}He nmol	U ppm	Th ppm
1	108	220	100	78	103	59.34	59.73	19.4	48.41	49.50
2	61	260	61	46	74	56.73	60.46	29.9	78.08	79.85
3	97	384	92	71	111	70.66	73.72	54.5	113.22	115.79
4	92	437	92	69	114	66.64	70.40	37.8	83.55	85.44
5	105	448	99	76	122	71.16	74.38	51.1	105.42	107.80
6	114	273	98	79	108	71.67	73.19	53.0	108.53	110.99
7	71	360	57	47	74	55.43	58.99	27.7	74.18	75.85
8	154	426	95	88	117	32.98	34.12	3.3	14.84	15.17
9	202	489	71	79	93	57.83	58.52	21.4	54.66	55.89

10	107	524	64	60	86	64.67	67.31	45.9	104.63	107.00
11	221	593	77	86	102	62.01	63.00	25.9	61.69	63.09
12	126	219	81	74	89	31.52	30.82	3.6	17.18	17.56
13	194	342	99	98	115	72.21	72.74	47.7	96.83	99.02
14	225	378	64	75	82	61.19	61.19	30.1	72.62	74.26
15	289	418	76	90	96	22.41	22.08	0.9	6.25	6.39
16	306	457	66	81	87	56.14	55.75	19.8	52.32	53.50
17	356	525	86	104	111	55.01	54.50	13.9	37.48	38.33
18	349	556	90	107	116	27.08	26.80	1.6	8.59	8.79
19	148	219	78	77	86	70.03	69.89	55.5	116.35	118.98
20	211	252	91	95	100	72.25	71.78	53.1	107.76	110.19
21	226	306	81	89	96	54.45	53.27	14.9	40.60	41.52
22	367	369	75	93	93	39.86	39.54	6.7	24.98	25.55
23	444	467	83	105	106	25.48	25.07	1.5	8.59	8.79
24	215	351	73	82	91	55.67	55.24	17.9	47.64	48.71
25	214	442	70	79	91	66.67	67.35	42.8	94.48	96.62

Table A5-15: Experiment 3, WOLF-5.

Grain no.	L_f µm	L_0 µm	R µm	eRF µm	eRG µm	Frag. age	Grain age	^{4}He nmol	U ppm	Th ppm
1	108	220	100	78	103	80.38	79.99	26.4	49.20	49.75
2	61	260	61	46	74	75.87	78.31	40.3	79.35	80.25
3	97	384	92	71	111	85.41	86.75	66.0	115.06	116.36
4	92	437	92	69	114	83.82	85.70	47.7	84.91	85.86
5	105	448	99	76	122	86.13	87.52	62.0	107.13	108.33
6	114	273	98	79	108	86.36	86.65	64.0	110.30	111.54
7	71	360	57	47	74	74.94	77.33	37.8	75.39	76.23
8	154	426	95	88	117	46.18	47.52	4.6	15.08	15.25
9	202	489	71	79	93	78.60	78.52	29.2	55.55	56.17
10	107	524	64	60	86	80.82	82.17	57.6	106.33	107.53
11	221	593	77	86	102	81.42	81.51	34.2	62.69	63.40
12	126	219	81	74	89	46.03	43.81	5.3	17.46	17.65
13	194	342	99	98	115	87.15	86.78	57.6	98.40	99.51
14	225	378	64	75	82	79.91	79.29	39.5	73.80	74.63
15	289	418	76	90	96	12.07	11.30	0.5	6.35	6.42
16	306	457	66	81	87	77.40	76.43	27.5	53.17	53.77
17	356	525	86	104	111	77.47	76.26	19.7	38.09	38.52
18	349	556	90	107	116	25.55	24.38	1.5	8.73	8.83
19	148	219	78	77	86	84.64	83.83	67.2	118.24	119.57
20	211	252	91	95	100	86.74	85.66	63.8	109.51	110.74
21	226	306	81	89	96	76.83	75.04	21.1	41.26	41.73
22	367	369	75	93	93	61.98	60.71	10.4	25.39	25.68
23	444	467	83	105	106	21.76	20.63	1.2	8.73	8.83
24	215	351	73	82	91	77.36	76.32	25.0	48.41	48.95
25	214	442	70	79	91	82.94	82.78	53.4	96.02	97.10

Table A5-16: Experiment 3a, WOLF-2

Grain no.	L_f µm	L_0 µm	R µm	eRF µm	eRG µm	Frag. age	Grain age	^{4}He nmol	U ppm	Th ppm
1	108	220	100	78	103	46.32	46.38	1.8	5.90	5.97
2	61	260	61	46	74	36.98	39.10	0.9	2.95	5.97
3	97	384	92	71	111	43.64	45.48	1.1	3.94	2.99
4	92	437	92	69	114	45.42	47.69	2.1	6.89	6.97

5	105	448	99	76	122	45.99	47.94	1.7	5.90	3.98
6	114	273	98	79	108	45.51	46.05	1.4	4.92	2.99
7	71	360	57	47	74	36.95	38.94	1.0	2.95	7.96
8	154	426	95	88	117	46.75	47.43	1.8	5.90	4.98
9	202	489	71	79	93	44.33	44.58	2.1	7.87	2.99
10	107	524	64	60	86	40.95	42.40	1.5	5.90	3.98
11	221	593	77	86	102	44.18	44.54	1.4	7.87	3.98
12	126	219	81	74	89	44.24	43.86	1.6	5.90	3.98
13	194	342	99	98	115	47.92	47.65	2.0	4.92	6.97
14	225	378	64	75	82	41.61	41.39	1.3	5.90	2.99
15	289	418	76	90	96	44.95	44.54	1.7	5.90	4.98
16	306	457	66	81	87	43.30	42.99	1.8	5.90	7.96
17	356	525	86	104	111	47.09	46.74	2.0	4.92	7.96
18	349	556	90	107	116	46.70	46.43	1.4	4.92	2.99
19	148	219	78	77	86	42.22	41.52	0.9	2.95	3.98
20	211	252	91	95	100	46.87	45.87	1.9	5.90	6.97
21	226	306	81	89	96	46.08	45.41	2.1	6.89	6.97
22	367	369	75	93	93	43.44	43.27	1.3	3.94	6.97
23	444	467	83	105	106	45.38	44.85	1.3	3.94	5.97
24	215	351	73	82	91	43.53	43.22	1.4	4.92	4.98
25	214	442	70	79	91	42.96	43.00	1.4	4.92	4.98

Table A5-17: Experiment 3a, WOLF-4

Grain no.	L_f µm	L_0 µm	R µm	eRF µm	eRG µm	Frag. age	Grain age	^{4}He nmol	U ppm	Th ppm
1	108	220	100	78	103	56.72	56.85	2.2	5.90	5.97
2	61	260	61	46	74	36.88	41.26	0.9	2.95	5.97
3	97	384	92	71	111	50.24	54.24	1.3	3.94	2.99
4	92	437	92	69	114	55.26	59.88	2.6	6.89	6.97
5	105	448	99	76	122	55.83	59.87	2.1	5.90	3.98
6	114	273	98	79	108	54.50	55.67	1.7	4.92	2.99
7	71	360	57	47	74	37.29	41.36	1.0	2.95	7.96
8	154	426	95	88	117	57.60	59.00	2.2	5.90	4.98
9	202	489	71	79	93	53.54	54.06	2.5	7.87	2.99
10	107	524	64	60	86	46.16	49.23	1.7	5.90	3.98
11	221	593	77	86	102	52.33	53.10	1.7	4.92	3.98
12	126	219	81	74	89	52.67	51.86	2.0	5.90	3.98
13	194	342	99	98	115	60.04	59.49	2.5	5.90	6.97
14	225	378	64	75	82	47.01	46.53	1.4	4.92	2.99
15	289	418	76	90	96	54.40	53.54	2.1	5.90	4.98
16	306	457	66	81	87	51.49	50.86	2.2	5.90	7.96
17	356	525	86	104	111	58.75	58.04	2.5	5.90	7.96
18	349	556	90	107	116	57.21	56.65	1.7	4.92	2.99
19	148	219	78	77	86	47.22	45.67	1.0	2.95	3.98
20	211	252	91	95	100	58.20	56.06	2.4	5.90	6.97
21	226	306	81	89	96	56.96	55.56	2.6	6.89	6.97
22	367	369	75	93	93	50.69	50.46	1.5	3.94	6.97
23	444	467	83	105	106	54.59	53.51	1.6	3.94	5.97
24	215	351	73	82	91	51.17	50.50	1.7	4.92	4.98
25	214	442	70	79	91	50.03	50.12	1.7	4.92	4.98

Table A5-18: Experiment 3a, WOLF-5

Grain no.	L_f µm	L_0 µm	R µm	eRF µm	eRG µm	Frag. age	Grain age	^{4}He nmol	U ppm	Th ppm
1	108	220	100	78	103	69.30	69.44	2.7	5.90	5.97
2	61	260	61	46	74	45.14	51.51	1.1	2.95	5.97
3	97	384	92	71	111	61.86	66.46	1.6	3.94	2.99
4	92	437	92	69	114	67.88	72.65	3.1	6.89	6.97
5	105	448	99	76	122	68.31	72.50	2.5	5.90	3.98
6	114	273	98	79	108	66.77	68.04	2.0	4.92	2.99
7	71	360	57	47	74	46.14	52.00	1.2	2.95	7.96
8	154	426	95	88	117	70.23	71.68	2.7	5.90	4.98
9	202	489	71	79	93	66.43	67.03	3.1	7.87	2.99
10	107	524	64	60	86	57.94	61.77	2.1	5.90	3.98
11	221	593	77	86	102	64.85	65.76	2.1	4.92	3.98
12	126	219	81	74	89	65.18	64.25	2.4	5.90	3.98
13	194	342	99	98	115	72.68	72.12	3.0	5.90	6.97
14	225	378	64	75	82	59.03	58.42	1.8	4.92	2.99
15	289	418	76	90	96	67.26	66.27	2.6	5.90	4.98
16	306	457	66	81	87	64.32	63.57	2.7	5.90	7.96
17	356	525	86	104	111	71.64	70.87	3.0	5.90	7.96
18	349	556	90	107	116	69.90	69.28	2.1	4.92	2.99
19	148	219	78	77	86	58.54	56.48	1.2	2.95	3.98
20	211	252	91	95	100	71.20	68.70	2.9	5.90	6.97
21	226	306	81	89	96	69.89	68.36	3.2	6.89	6.97
22	367	369	75	93	93	63.02	62.71	1.9	3.94	6.97
23	444	467	83	105	106	67.48	65.96	2.0	3.94	5.97
24	215	351	73	82	91	63.66	62.86	2.1	4.92	4.98
25	214	442	70	79	91	62.44	62.55	2.1	4.92	4.98

Table A5-19: Experiment 3b, WOLF-2

Grain no.	L_f µm	L_0 µm	R µm	eRF µm	eRG µm	Frag. age	Grain age	^{4}He nmol	U ppm	Th ppm
1	108	220	100	78	103	48.04	48.11	3.1	9.84	8.96
2	61	260	61	46	74	42.62	44.81	5.0	19.68	8.96
3	97	384	92	71	111	49.74	51.59	7.0	23.62	9.95
4	92	437	92	69	114	44.65	46.95	1.9	2.95	19.90
5	105	448	99	76	122	51.25	53.21	8.0	27.55	4.98
6	114	273	98	79	108	49.38	49.92	4.6	14.76	9.95
7	71	360	57	47	74	42.27	44.34	5.2	16.73	25.87
8	154	426	95	88	117	51.06	51.75	6.6	18.70	21.89
9	202	489	71	79	93	45.30	45.55	3.1	6.89	24.88
10	107	524	64	60	86	43.27	44.73	3.1	11.81	6.97
11	221	593	77	86	102	49.17	49.53	6.3	21.65	7.96
12	126	219	81	74	89	45.18	44.80	2.5	4.92	21.89
13	194	342	99	98	115	49.74	49.46	3.6	7.87	22.89
14	225	378	64	75	82	44.61	44.38	3.6	8.86	25.87
15	289	418	76	90	96	49.60	49.18	7.1	20.66	23.88
16	306	457	66	81	87	46.06	45.75	4.1	14.76	6.97
17	356	525	86	104	111	50.32	49.97	5.1	16.73	7.96
18	349	556	90	107	116	49.80	49.53	3.9	9.84	19.90
19	148	219	78	77	86	46.40	45.68	3.4	10.82	10.95
20	211	252	91	95	100	52.02	51.00	8.5	26.57	15.92
21	226	306	81	89	96	50.47	49.79	7.6	25.58	8.96

22	367	369	75	93	93	46.96	46.78	4.1	9.84	25.87
23	444	467	83	105	106	51.66	51.11	8.2	27.55	7.96
24	215	351	73	82	91	49.09	48.77	7.4	26.57	5.97
25	214	442	70	79	91	48.83	48.87	8.3	26.57	20.9

Table A5-20: Experiment 3b, WOLF-4

Grain no.	L_f µm	L_0 µm	R µm	eRF µm	eRG µm	Frag. age	Grain age	^{4}He nmol	U ppm	Th ppm
1	108	220	100	78	103	60.85	60.97	3.9	9.84	8.96
2	61	260	61	46	74	52.31	56.51	6.2	19.68	8.96
3	97	384	92	71	111	64.73	67.84	9.1	23.62	9.95
4	92	437	92	69	114	53.86	58.56	2.2	2.95	19.90
5	105	448	99	76	122	67.19	70.35	10.5	27.55	4.98
6	114	273	98	79	108	63.69	64.67	5.9	14.76	9.95
7	71	360	57	47	74	52.07	55.99	6.4	16.73	25.87
8	154	426	95	88	117	66.92	68.07	8.7	18.70	21.89
9	202	489	71	79	93	56.58	57.08	3.9	6.89	24.88
10	107	524	64	60	86	52.55	55.50	3.8	11.81	6.97
11	221	593	77	86	102	64.01	64.66	8.2	21.65	7.96
12	126	219	81	74	89	55.71	54.93	3.0	4.92	21.89
13	194	342	99	98	115	64.25	63.74	4.6	7.87	22.89
14	225	378	64	75	82	55.70	55.25	4.5	8.86	25.87
15	289	418	76	90	96	64.93	64.20	9.3	20.66	23.88
16	306	457	66	81	87	58.31	57.71	5.2	14.76	6.97
17	356	525	86	104	111	65.69	65.06	6.6	16.73	7.96
18	349	556	90	107	116	64.61	64.12	5.1	9.84	19.90
19	148	219	78	77	86	58.41	56.97	4.2	10.82	10.95
20	211	252	91	95	100	68.75	66.97	11.3	26.57	15.92
21	226	306	81	89	96	66.25	65.08	9.9	25.58	8.96
22	367	369	75	93	93	59.81	59.55	5.2	9.84	25.87
23	444	467	83	105	106	68.27	67.27	10.9	27.55	7.96
24	215	351	73	82	91	64.09	63.53	9.7	26.57	5.97
25	214	442	70	79	91	63.85	63.93	10.9	26.57	20.9

Table A5-21: Experiment 3b, WOLF-5

Grain no.	L_f µm	L_0 µm	R µm	eRF µm	eRG µm	Frag. age	Grain age	^{4}He nmol	U ppm	Th ppm
1	108	220	100	78	103	73.59	73.71	4.8	9.84	8.96
2	61	260	61	46	74	64.98	69.37	7.7	19.68	8.96
3	97	384	92	71	111	77.04	79.78	10.9	23.62	9.95
4	92	437	92	69	114	66.26	71.20	2.7	2.95	19.90
5	105	448	99	76	122	79.19	81.85	12.3	27.55	4.98
6	114	273	98	79	108	76.23	77.12	7.1	14.76	9.95
7	71	360	57	47	74	64.65	68.81	8.0	16.73	25.87
8	154	426	95	88	117	78.95	79.95	10.2	18.70	21.89
9	202	489	71	79	93	69.49	70.03	4.8	6.89	24.88
10	107	524	64	60	86	65.37	68.61	4.8	11.81	6.97
11	221	593	77	86	102	76.49	77.10	9.8	21.65	7.96
12	126	219	81	74	89	68.46	67.63	3.7	4.92	21.89
13	194	342	99	98	115	76.69	76.22	5.5	7.87	22.89
14	225	378	64	75	82	68.65	68.17	5.6	8.86	25.87

15	289	418	76	90	96	77.20	76.53	11.0	20.66	23.88
16	306	457	66	81	87	71.37	70.75	6.4	14.76	6.97
17	356	525	86	104	111	78.11	77.53	7.9	16.73	7.96
18	349	556	90	107	116	77.12	76.65	6.1	9.84	19.90
19	148	219	78	77	86	71.34	69.85	5.2	10.82	10.95
20	211	252	91	95	100	80.55	78.92	13.3	26.57	15.92
21	226	306	81	89	96	78.40	77.32	11.8	25.58	8.96
22	367	369	75	93	93	72.70	72.35	6.3	9.84	25.87
23	444	467	83	105	106	80.24	79.23	12.8	27.55	7.96
24	215	351	73	82	91	76.47	75.95	11.6	26.57	5.97
25	214	442	70	79	91	76.11	76.18	13.0	26.57	20.90

Table A5-22: Experiment 3c, WOLF-2

Grain no.	L_f µm	L_0 µm	R µm	eRF µm	eRG µm	Frag. age	Grain age	^{4}He nmol	U ppm	Th ppm
1	108	220	100	78	103	54.20	54.26	17.9	52.15	37.81
2	61	260	61	46	74	45.54	47.78	12.0	44.28	17.91
3	97	384	92	71	111	51.19	53.06	10.9	31.49	32.84
4	92	437	92	69	114	48.85	51.16	6.3	13.78	41.79
5	105	448	99	76	122	50.90	52.88	7.6	20.66	29.85
6	114	273	98	79	108	53.56	54.11	14.6	48.22	8.96
7	71	360	57	47	74	45.80	47.92	14.0	51.17	22.89
8	154	426	95	88	117	48.15	48.84	3.0	5.90	23.88
9	202	489	71	79	93	46.28	46.54	3.9	12.79	10.95
10	107	524	64	60	86	42.88	44.36	2.9	9.84	10.95
11	221	593	77	86	102	50.47	50.84	9.0	31.49	5.97
12	126	219	81	74	89	51.66	51.28	14.2	49.20	5.97
13	194	342	99	98	115	54.42	54.15	12.7	38.38	19.90
14	225	378	64	75	82	40.96	40.74	1.1	2.95	8.96
15	289	418	76	90	96	52.61	52.19	15.8	51.17	18.91
16	306	457	66	81	87	46.74	46.43	5.4	13.78	32.84
17	356	525	86	104	111	50.19	49.84	5.1	13.78	20.90
18	349	556	90	107	116	54.99	54.72	16.4	47.23	32.84
19	148	219	78	77	86	50.65	49.92	11.0	38.38	7.96
20	211	252	91	95	100	50.44	49.43	5.5	16.73	14.93
21	226	306	81	89	96	51.85	51.16	11.6	32.47	37.81
22	367	369	75	93	93	50.01	49.82	9.1	29.52	16.92
23	444	467	83	105	106	53.97	53.41	16.0	47.23	31.84
24	215	351	73	82	91	50.74	50.42	12.4	36.41	36.82
25	214	442	70	79	91	50.61	50.65	13.5	44.28	21.89

Table A5-23: Experiment 3c, WOLF-4

Grain no.	L_f µm	L_0 µm	R µm	eRF µm	eRG µm	Frag. age	Grain age	^{4}He nmol	U ppm	Th ppm
1	108	220	100	78	103	71.92	72.01	23.8	52.15	37.81
2	61	260	61	46	74	58.81	62.57	15.5	44.28	17.91
3	97	384	92	71	111	67.39	70.29	14.3	31.49	32.84
4	92	437	92	69	114	63.29	67.22	8.1	13.78	41.79
5	105	448	99	76	122	66.68	69.88	10.0	20.66	29.85
6	114	273	98	79	108	70.96	71.76	19.4	48.22	8.96
7	71	360	57	47	74	59.52	63.01	18.2	51.17	22.89

8	154	426	95	88	117	61.29	62.59	3.8	5.90	23.88
9	202	489	71	79	93	58.53	59.02	4.9	12.79	10.95
10	107	524	64	60	86	51.71	54.68	3.5	9.84	10.95
11	221	593	77	86	102	66.39	67.01	11.8	31.49	5.97
12	126	219	81	74	89	68.31	67.71	18.7	49.20	5.97
13	194	342	99	98	115	72.22	71.82	16.9	38.38	19.90
14	225	378	64	75	82	45.67	45.20	1.3	2.95	8.96
15	289	418	76	90	96	69.85	69.21	21.1	51.17	18.91
16	306	457	66	81	87	60.12	59.54	7.0	13.78	32.84
17	356	525	86	104	111	65.54	64.91	6.6	13.78	20.90
18	349	556	90	107	116	73.15	72.76	21.8	47.23	32.84
19	148	219	78	77	86	66.75	65.55	14.6	38.38	7.96
20	211	252	91	95	100	65.99	64.09	7.2	16.73	14.93
21	226	306	81	89	96	68.64	67.54	15.4	32.47	37.81
22	367	369	75	93	93	65.69	65.40	11.9	29.52	16.92
23	444	467	83	105	106	71.85	70.93	21.3	47.23	31.84
24	215	351	73	82	91	67.05	66.54	16.4	36.41	36.82
25	214	442	70	79	91	66.90	66.97	17.9	44.28	21.89

Table A5-24: Experiment 3c, WOLF-5

Grain no.	L_f μm	L_0 μm	R μm	eRF μm	eRG μm	Frag. age	Grain age	^{4}He nmol	U ppm	Th ppm
1	108	220	100	78	103	82.54	82.61	27.4	52.15	37.81
2	61	260	61	46	74	70.99	74.54	18.7	44.28	17.91
3	97	384	92	71	111	79.07	81.49	16.8	31.49	32.84
4	92	437	92	69	114	75.64	79.14	9.7	13.78	41.79
5	105	448	99	76	122	78.67	81.38	11.8	20.66	29.85
6	114	273	98	79	108	81.96	82.61	22.4	48.22	8.96
7	71	360	57	47	74	71.49	74.77	21.9	51.17	22.89
8	154	426	95	88	117	73.90	75.16	4.6	5.90	23.88
9	202	489	71	79	93	71.49	71.99	6.0	12.79	10.95
10	107	524	64	60	86	64.44	67.76	4.3	9.84	10.95
11	221	593	77	86	102	78.39	78.95	14.0	31.49	5.97
12	126	219	81	74	89	79.70	79.18	21.9	49.20	5.97
13	194	342	99	98	115	83.05	82.73	19.4	38.38	19.90
14	225	378	64	75	82	57.32	56.70	1.6	2.95	8.96
15	289	418	76	90	96	80.86	80.31	24.4	51.17	18.91
16	306	457	66	81	87	72.86	72.28	8.5	13.78	32.84
17	356	525	86	104	111	77.90	77.32	7.9	13.78	20.90
18	349	556	90	107	116	83.54	83.23	24.9	47.23	32.84
19	148	219	78	77	86	78.56	77.48	17.2	38.38	7.96
20	211	252	91	95	100	78.39	76.54	8.6	16.73	14.93
21	226	306	81	89	96	80.06	79.10	18.0	32.47	37.81
22	367	369	75	93	93	77.82	77.45	14.2	29.52	16.92
23	444	467	83	105	106	82.59	81.74	24.6	47.23	31.84
24	215	351	73	82	91	78.61	78.15	19.2	36.41	36.82
25	214	442	70	79	91	78.43	78.49	21.0	44.28	21.89

APPENDIX 6

6. BALLACHULISH AFT DATA

Table A6-1: Table of new BIC AFT Data.
*MTL not corrected for angle from C-axis. _*SDx_: _AFT data of Persano et al. (2007)._

Sample no.	Elevation (m)	N_s	N_i	N_s/N_i (no. crystals)	AFT Age (Ma) ± 1σ	MTL* (µm) ± 1σ (no. tracks)
SD07 – 1	1001	727	417	1.74 (20)	261 ± 26	11.42 ± 2.26 (91)
SD07 – 2	907	817	518	1.58 (20)	234 ± 23	11.92 ± 1.76 (100)
SD13 – 02	867	980	618	1.59 (18)	224 ± 21	11.06 ± 1.89 (85)
_*SD3_	_804_	_2923_	_2771_	_1.05 (20)_	_257 ± 12_	_13.2 ± 1.90 (118)_
SD13 – 03	755	843	510	1.65 (16)	231 ± 22	11.68 ± 2.29 (82)
SD07 – 4	700	853	520	1.64 (17)	238 ± 23	11.13 ± 1.88 (52)
SD13 – 04	628	595	379	1.57 (16)	216 ± 22	11.99 ± 1.59 (63)
SD07 – 5	605	758	507	1.50 (18)	217 ± 21	11.66 ± 1.61 (100)
SD07 – 6	512	848	561	1.51 (18)	216 ± 21	11.69 ± 1.90 (61)
BH15 – 05	220	1346	839	1.60 (17)	219 ± 20	12.18 ± 1.54 (100)
_*SD9_	_195_	_1769_	_3470_	_0.5 (20)_	_186 ± 6_	_11.2 ± 2.1 (107)_
SD13 – 06 / BH13 – 02	0	383	272	1.40 (10)	194 ± 22	12.14 ± 1.35 (86)

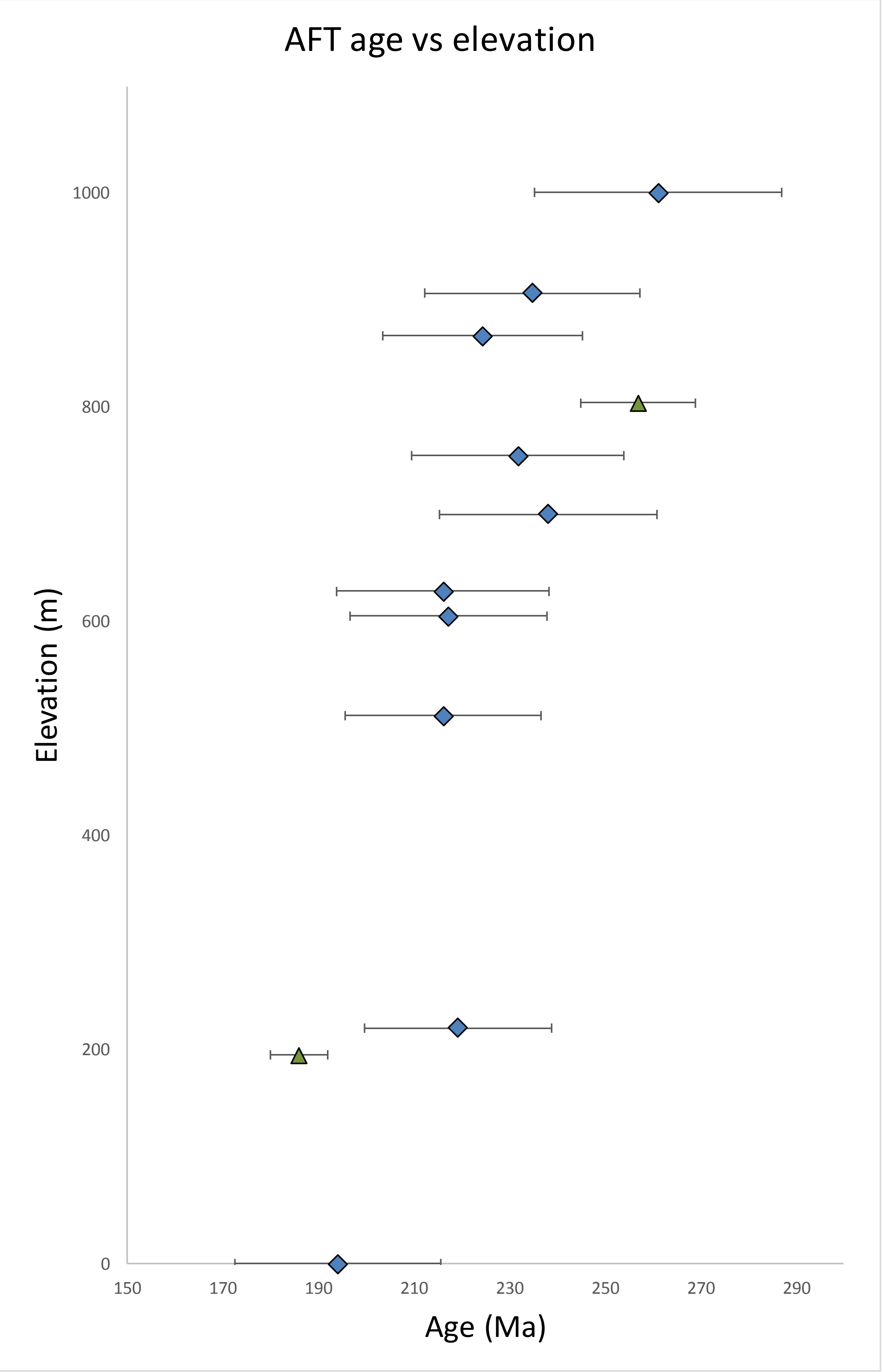

Figure A6.1: New BIC AFT data age vs. elevation plot.
Figure showing the AFT age as a function of elevation for each sample. Horizontal error bars indicate the 1σ analytical error. AFT data of Persano *et al*. (2007) shown in green triangles.

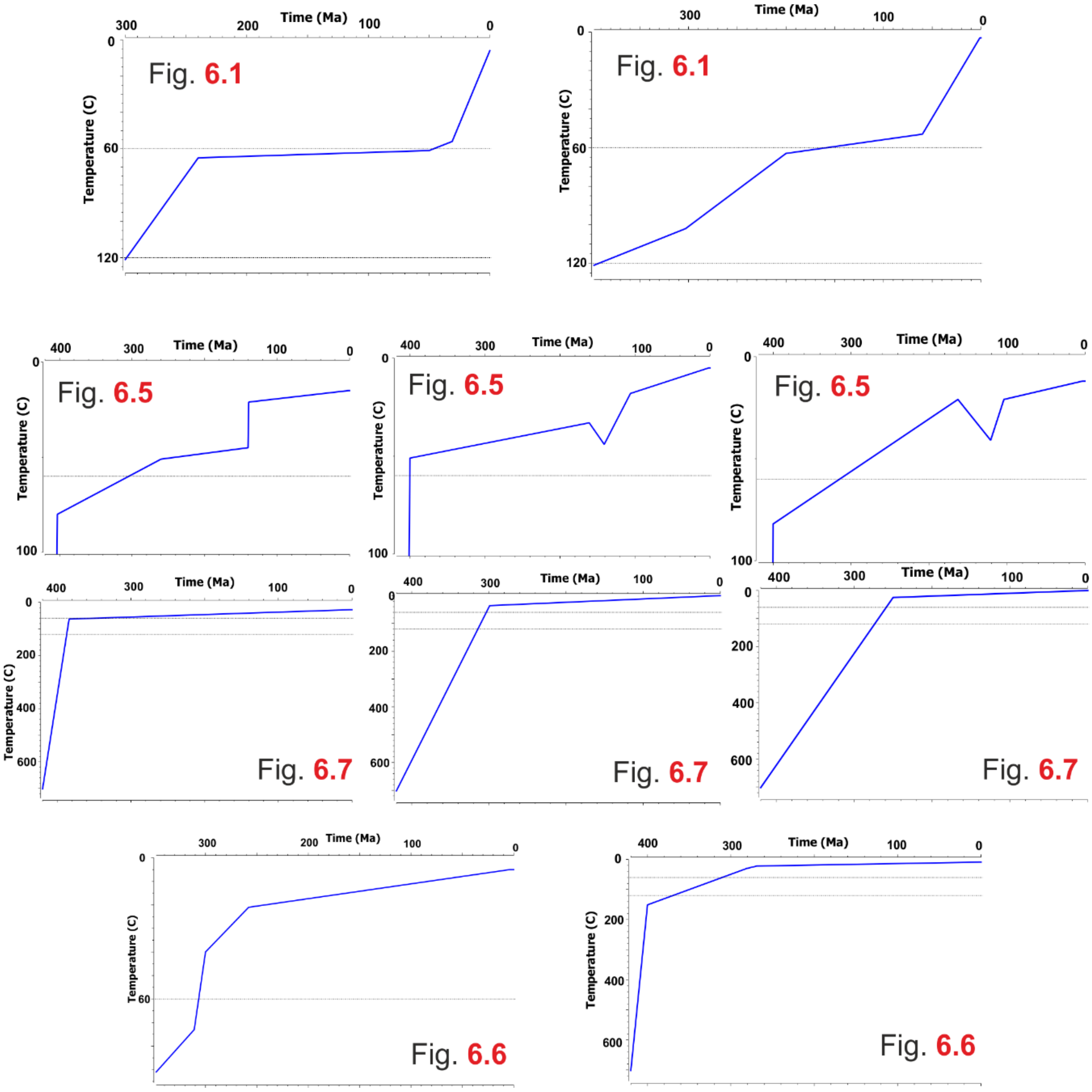

Figure A6.2: T-t paths used to generate synthetic AFT ages discussed in chapter 6.

APPENDIX 7

7. ELECTRONIC ANNEX DIRECTORY

Contained within are all the raw data spread sheets used to record data and calculate AHe and AFT ages.

1. AFT Folder
    1.1. AFT ages (excel file): summary of counts, length measurement and ages
    1.2. AFT Length Folder
        1.2.1. SD07 – [*x*] length (text file): raw track length measurement data
2. AHe Folder
    2.1. Grainsize (excel file): all grain dimensions data
    2.2. R* error (excel file): R* conversion error calculation spreadsheet
    2.3. Helium Folder
        2.3.1. Year [*date*] Folder
            2.3.1.1. Pan [*date*] (excel file): raw helium extraction data and calibrations
    2.4. ICPMS Folder
        2.4.1. U/Th Folder
            2.4.1.1. Raw Folder
                2.4.1.1.1. U/Th [*date*] (excel file): raw ICPMS data
            2.4.1.2. Blank corr Folder
                2.4.1.2.1. U/Th [date] (excel file): blank corrected ICPMS data

- 2.4.2. Sm Folder
  - 2.4.2.1. Raw Folder
    - 2.4.2.1.1. Sm [*date*] (excel file): raw ICPMS data
  - 2.4.2.2. Blank corr Folder
    - 2.4.2.2.1. Sm [date] (excel file): blank corrected ICPMS data

2.5. Ages Folder

- 2.5.1. Year [*date*] Folder
  - 2.5.1.1. Pan [*date*] (excel file): age calculation spreadsheet
- 2.5.2. Summary Folder
  - 2.5.2.1. Ballachulish AHe age summary plots (excel file)

LIST OF REFERENCES:

Abdulin, F., Sole, J., Meneses-Rocha, J. J., Solari, L., Shchepetilnikova, V. and Ortega-Obregon. 2015. LA-ICP-MS-based apatite fission track dating of the Todos Santos Formation sandstones from the Sierra de Chiapas (SE Mexico) and its tectonic significance. *Int. Geol. Rev*. **58:1**, 32-48

Anderson, J. G. C. 1937. Etive Granite Complex. *Quart. Journ. Geol. Soc.* **93,** 487-533

Atherton, M. P. and Ghani, A. A. 2002. Slab breakoff: a model for Caledonian, Late Granite syn-collisional magmatism in the orthotectonic (metamorphic) zone of Scotland and Donegal, Ireland. *Lithos*. **62**, 65-85

Ault, A. K. and Flowers, R. M. 2012. Is apatite U–Th zonation information necessary for accurate interpretation of apatite (U–Th)/He thermochronometry data? *Geochem. Cosmo. Acta*. **79**, 60–78

Bailey, E. B. and Maufe, H. B. 1916. *The geology of Ben Nevis and Glen Coe and the surrounding country: explanation of sheet 53. Memoirs of the Geological Survey of Scotland.* Published by the British Geological Survey (Edinburgh)

Bauldwin, S. L. and Lister, G. S. 1998. Thermochronology of the South Cyclades Shear Zone, Ios, Greece: effects of ductile shear in the argon partial retention zone. *Jour. Geophys. Res*. **103:73**, 15-36

Belloni, F. F., Keskes, N. and Hurford, A. J. 2000. Strategy for fission-track recognition via digital image processing, and computer-assisted track measurement. (Abstract.). In: *9th International Conference on Fission-track Dating and Thermochronology*. Geological Society of Australia Abstracts. **58**, 15–17

Beucher, R., Brown, R. W., Roper, S., Stuart, F. and Persano, C. 2013. Natural age dispersion arising from the analysis of broken crystals. Part II: Practical application to apatite (U-Th)/He thermochronometry. *Geochem. Cosmo. Acta*. **102**, 395-416

Bigazzi, G., 1981. The problem of the decay constant λf of ^{238}U. *Nucl. Tracks*. **5**, 35-44

Blackburn, T. J., Stockli, D. F., Walker, J. D., 2007. Magnetite (U–Th)/He dating and its application to the geochronology of intermediate to mafic volcanic rocks. *Earth Planet. Sci. Lett*. **259**, 360–371

Blythe, A. E., Burbank, D. W., Carter, A., Schmidt, K. and Putkonen, J. 2007. Plio-Quaternary exhumation history of the central Nepalese Himalaya: 1. Apatite and zircon fission track and apatite [U-Th]/He analyses. *Tectonics*. **26:3**, 1-16

Boyce, J. W. and Hodges, K. V. 2005. U and Th zoning in Cerro de Mercado (Durango, Mexico) fluorapatite: Insights regarding the impact of recoil redistribution of radiogenic ^{4}He on (U–Th)/He thermochronology. *Chem. Geol*. **219:1-4**, 261-274

Brown, W. R., Beucher, R., Roper, S., Persano, C., Stuart, F. and Fitzgerald, P. 2013. Natural age dispersion arising from the analysis of broken crystals. Part I: Theoretical basis and implications for the apatite (U-Th)/He thermochronometer. *Geochem. Cosmo. Acta*. **122**, 478-497

Cameron, I. B. and Stephenson, D. 1985. *British regional geology: The Midland Valley of Scotland*. Third edition. Reprint 2014. Keyworth, Nottingham: British Geological Survey

Carrapa, B., DeCelles, P. G., Reiners, P. W., Gehrels, G. E. and Sudo, M. 2009. Apatite triple dating and white mica 40Ar/39Ar thermochronology of syntectonic detritus in the Central Andes: A multiphase tectonothermal history. *Geology*. **37:5**, 407-410

Carter, T. J., Kohn, B. P., Foster, D. A. and Gleadow, A. J. W. 2004. How the Harcuvar Mountains metamorphic core complex became cool: Evidence from apatite (U-Th)/He thermochronometry. *Geology*. **32:11**, 985-988

Chew, D. M. and Donelick, R. A. 2012. Combined apatite fission track and U-Pb dating by LA-ICPMS and its application in apatite provenance analysis. Mineralogical Association of Canada Short Course 42, St. John's NL, May 2012, 219-247

Clark, M. K., Farley, K. A., Zheng, D. Wang, Z and Duvall, A. R. 2010. Early Cenozoic faulting of the northern Tibetan Plateau margin from apatite (U–Th)/He ages. *Earth Planet. Sci. Lett*. **296:1-2**, 78-88

Clift, P. D., Hodges, K. V., Heslop, *D.*, Hannigan, *R.*, Van Long, *H. and* Calves, G. 2008. Correlation of Himalayan exhumation rates and Asian monsoon intensity, *Nat. Geosci*, **1:12**, 875–880

Clough, C. T. H., Maufe, H. B., and Bailey, E. B., 1909. The cauldron subsidence of Glencoe and the associated igneous phenomena. *Geol. Soc. Lon. Quart. Journ.* **65**, 611–678

Cocks, L. R. M. and Fortey, R. A. 1982. Faunal evidence for oceanic separations in the Palaeozoic of Britain. *Jour. Geol. Soc.* **139,** 465-478

Cocks, L. R. M., McKerrow, W. S. and van Staal, C. R. 1997. The margins of Avalonia. *Geol. Mag.* **134:5,** 627-636

Cogné, N., Doepke, D., Chew, D., Stuart, F. M. and Mark, C. 2016. Measuring plume-related exhumation of the British Isles in Early Cenozoic times. *Earth Plan. Sci. Lett.* **456**, 1-15

Condon, D. J., McLean, N., Noble, S. R., and Bowring, S. A., 2010. Isotopic composition (238 U/235 U) of some commonly used uranium reference materials. *Geochem. Cosmo. Acta,* **74:24**, 7127-7143

Corrigan, J. D. 1991. Inversion of apatite fission track data for thermal history information. *Jour. Geophys. res.* **96**, 10347-10360

Crowhurst, P. V., Green, P. F. and Kamp, P. J. J. 2002. Appraisal of (U-Th)/He apatite thermochronology as a thermal history tool for hydrocarbon exploration: An example from the Taranaki Basin, New Zealand. *AAPG Bulletin.* **86:10**, 1801-1819

Danisik, M., Panek, T., Dalibor, M., Istvan, D. and Wolfgang, F. 2008. Apatite fission track and (U-Th)/He dating of teschenite intrusions gives time constraints on accretionary processes and development of planation surfaces in the Outer Western Carpathians. *Zeitschrift für Geomorphologie.* **52:3**, 273-289

Danisik, M., Sachsenhofer, R. F., Privalov, P. A., Panova, E. A., Frisch, W. and Spiegal, C. 2008. Low temperature thermal evolution of the Azov Massif (Ukrainian Shield — Ukraine) — implications for interpreting (U–Th)/He and fission track ages from cratons. *Tectonophysics.* **456**, 171–179

Davies, J. H., and von Blanckenburg, F., 1995. Slab breakoff, a model of lithosphere detachment and its test in the magmatism and deformation of collisional orogens. *Earth Planet. Sci. Lett*. **129**, 85– 102

Dewey, J. F., and Mange, M. 1999. Petrography of Ordovician and Silurian sediments in the western Irish Caledonides: traces of a short-lived Ordovician continent-arc collision orogeny and the evolution of the Laurentian Appalachian – Caledonian margin. In: MacNiocaill, C., Ryan, P.D. (Eds.), Continental Tectonics. *Jour. Geol. Soc. Lond. Spec. Pub*., **164**, 55–107

Dodson, M., 1973. Closure temperature in cooling geochronological and petrological systems. *Contrib. Mineral. Petrol*. **40**, 259-274

Donelick, R. A. 1993. A method of fission track analysis utilizing bulk chemical etching of apatite. Patent 5267274, U.S.A.

Donelick, R. A. 1995. A method of fission track analysis utilizing bulk chemical etching of apatite. Patent 658800, Australia

Donelick, R. A., Roden, M. K., Mooers, J. D., Carpenter, B. S. and Miller, D. S. 1990. Etchable length reduction of induced fission tracks in apatite at room temperature (23°): Crystallographic orientation effects and "initial" mean lengths. *Int. Journ. of Radiation Applications and Instruments. Part D. Nuclear Tracks and Radiation Measurements*. **17:3**, 261-265

Donelick, R. A., Ketcham, R. A. and Carlson, W. D. 1999. Variability of apatite fission-track annealing kinetics: II. Crystallographic orientation effects. *American Mineralogist*. **84**, 1224–1234

Donelick, R. A., O'sullivan, P. B. and Ketcham, R. A., 2005. Apatite fission track analysis. *Rev. Min. Geochem*. **58**, 49-94

Ehlers, T. A. and Farley, K. A. 2003. Apatite (U^Th)/He thermochronometry: methods and applications to problems in tectonic and surface processes. *Earth Planet. Sci. Lett*. **206**, 1-14

Emeleus, C. H. and Bell, B. R. 2005. *British regional geology: The Palaeogene volcanic districts of Scotland*. Fourth edition. Keyworth, Nottingham: British Geological Survey

Farley, K. A. 2000. Helium diffusion from apatite: General behaviour as illustrated by Durango fluorapatite. *Jour. Geophys. Res.* **105**, 2903-2914

Farley, K. A. 2002. (U-Th)/He dating: techniques, calibrations and applications. *Rev. Min. Geochem.* **47**, 819-844

Farley, K. A., Wolf, R. A. and Silver, L. T. 1996. The effects of long alpha-stopping distances on (U-Th)/He ages. *Geochem. Cosmo. Acta.* **60:21**, 4223-4229

Farley, K. A., Kohn, B. P. and Pillans, B. 2002. The effects of secular disequilibrium on (U–Th)/He systematics and dating of Quaternary volcanic zircon and apatite. *Earth Planet. Sci. Lett.* **201:1**, 117-125

Farley, K. A., Shuster, D. L., Watson, E. B., Wanser, K. H. and Balco, G. 2010. Numerical investigations of apatite 4He/3He thermochronometry, *Geochem. Geophys. Geosys.* **11:10**, 1-18

Fernandes, P., Cogné, N., Chew, D. M., Rodrigues, B., Jorge, R. C. G. S., Marques, J., Jamal, D., Vasconcelos, L. 2015. The thermal history of the Karoo Moatize-Minjova Basin, Tete Province, Mozambique: an integrated vitrinite reflectance and apatite fission track thermochronology study. *Jour. of African Earth Sciences.* **112**, 55-72

Fillon, C. Gautheron, C. and van der Beek, P. 2013. Oligocene-Miocene burial and exhumation of the Southern Pyrenean foreland quantified by low-temperature thermochronology. *Jour. Geol. Soc.* **170**, 67–77

Fitzgerald, P. G. 1992. The Transantarctic Mountains of southern Victoria Land: the application of apatite fission track analysis to a rift shoulder uplift. *Tectonics.* **11**, 634– 662

Fitzgerald, P. G., Gleadow, A. J. W. 1990. New approaches in fission track geochronology as a tectonic tool: examples from the Transantarctic Mountains. *Nuclear Tracks.* **17**, 351–357

Fitzgerald P. G., Baldwin, S. L., Webb, L. E. and O'Sullivan, P. B. 2006. Interpretation of (U–Th)/He single grain ages from slowly cooled crustal terranes: A case study from the Transantarctic Mountains of southern Victoria Land. *Chem. Geol.* **225**, 91-120

Fleischer, R. L., Price, P. B., Symes, E. M. and Miller, D. S. 1964. Fission track ages and track-annealing behavior of some micas. *Science*. **143**, 349-351

Flerov, G. N. and Petrzhak, H. A. 1940. Spontaneous fission of uranium. *Jour. Phys. USSR*. **3,** 275-280

Flerov, G. N. and Petrzhak, H. A. 1940. Spontaneous fission of uranium. *Physical Review*. **58:1**, 89

Flowers, R., Shuster, D., Wernicke, B. and Farley, K. 2007. Radiation damage control on apatite (U–Th)/He dates from the Grand Canyon region, Colorado Plateau. *Geology* **35:5**, 447–450

Flowers, R. M. Wernicke, B. P. and Farley, K. A. 2008. Unroofing, incision, and uplift history of the southwestern Colorado Plateau from apatite (U-Th)/He thermochronometry. *GSA Bulletin*. **120:5-6**, 571-587

Flowers, R. M. 2009. Exploiting radiation damage control on apatite (U–Th)/He dates in cratonic regions. *Earth Planet. Sci. Lett*. **277:1**, 148–155

Flowers, R. M., Ketcham, R. A., Shuster, D. L. and Farley, K. A. 2009. Apatite (U–Th)/He thermochronometry using a radiation damage accumulation and annealing model. *Geochem. Cosmo. Acta*. **73**, 2347–2365

Flowers R. M. and Kelley S. A. 2011 Interpreting data dispersion and inverted dates in apatite (U–Th)/He and fission-track datasets: an example from the US midcontinent. *Geochem. Cosmo. Acta*. **75:18**, 5169–5186.

Flowers R. M and Farley, K. A. 2012. Apatite ^{4}He/^{3}He and (U-Th)/He Evidence for an Ancient Grand Canyon. *Science*. **338:6114**, 1616-1619

Fox, M., Tripathy-Lang, A., Shuster, D. L., Winn, C., Karlstrom, K. and Kelley, S. 2017. Westernmost Grand Canyon incision: Testing thermochronometric resolution. *Earth Planet. Sci. Lett*. **474**, 248-256

Fraser, G. L., Pattison, D. R. M. and Heaman, L. M. 2000. Geochronological and petrological investigations in the Ballachulish area, Scotland: local exhumation rates and implications for U-Pb geochronology of metamorphic processes. *GeoCanada 2000* Abstract

Fraser, G. L., Pattison, D. R. M. and Heaman, L. M. 2004. Age of the Ballachulish and Glencoe Igneous Complexes (Scottish Highlands), and paragenesis of zircon, monazite and baddeleyite in the Ballachulish Aureole. *Jour. Geol. Soc., Lon.* **161**, 447–462

Galbraith, R. F. and Laslett, G. M. 1993. Statistical models for mixed fission track ages. *Nucl. Tracks Radiat. Meas.,* **21:4**, 459-470

Gallagher, K. 1995. Evolving temperature histories from apatite fission-track data. *Earth Planet. Sci. Let.* **136**, 421-435

Gallagher, K. 2012. Transdimensional inverse thermal history modelling for quantitative thermochronology. *Jour. Geophys. Res.* **117,** 1-16

Gallagher, K., Brown, R. and Johnson, C. 1998. Fission track analysis and its applications to geological problems. *Annu. Rev. Earth Planet. Sci.* **26,** 519–572

Gautheron, C., Tassan-Got, L., Barbarand, J. and Pagel, M. 2009. Effect of alpha-damage annealing on apatite (U–Th)/He thermochronology. *Chem. Geol.* **266**, 157–170

Gautheron, C. and Tassan-Got, L. 2010. A Monte Carlo approach to diffusion applied to noble gas/helium thermochronology. *Chem. Geol.* **273**, 212-224

Gautheron, C., Tassan-Got, L., Ketcham, R. A. and Dobson, K. J. 2012. Accounting for long alpha-particle stopping distances in (U–Th–Sm)/He geochronology: 3D modeling of diffusion, zoning, implantation, and abrasion. *Geochem. Cosmo. Acta.* **96**, 44–56

Gautheron, C., Espurt, N., Barbarand, J., Roddaz, M., Baby, P., Brusset, S., Tassan-got, L. and Douville, E. 2013a. Direct dating of thick- and thin-skin thrusts in the Peruvian Subandean zone through apatite (U-Th)/He and fission track thermochronometry. *Basin Res.* **25,** 419–435

Gautheron, C., Barbarand, J, Ketcham, R. A., Tassan-Got, L., van der Beek, P., Pagel, M., Pinna-Jamme, R., Couffignal, F. and Fialin, M. 2013b. Chemical influence on α-recoil damage annealing in apatite: Implications for (U–Th)/He dating. *Chem. Geol.* **351**, 257-267

Gerin, C., Gautheron, C., Oliviero, E., Bachelet, C., Djimbi, D. M., Seydoux-Guillaume, A-M., Tassan-Got, L., Sarda, P., Roques, J. and Garrido, F. 2017. Influence of vacancy damage on He diffusion in apatite, investigated at atomic to mineralogical scales. *Geochem. Cosmo. Acta.* **197**, 87-103

Gleadow, A. J. W. and Duddy, I. R., 1981. A natural long term annealing experiment for apatite. *Nucl. Tracks.* **5**, 169-174

Gleadow, A. J. W., Duddy, I. R. and Lovering, J. F., 1983. Fission track analysis: a new tool for the evaluation of thermal histories and hydrocarbon potential. *APEA (Aust. Pet. Eng. Assoc.)* **23**, 93-102

Gleadow, A. J. W., Duddy, I. R., Green, P. F., and Lovering, J. F. 1986a. Confined fission track lengths in apatite: a diagnostic tool for thermal history analysis. *Cont. Min. Petro.* **94:4**, 405-415

Gleadow, A. J., Duddy, I. R., Green, P. F., and Hegarty, K. A. 1986b. Fission track lengths in the apatite annealing zone and the interpretation of mixed ages. *Earth Planet. Sci. Lett.* **78:2**, 245-254

Gleadow, A. J. and Fitzgerald P. G. 1987. Uplift history and structure of the Transantarctic Mountains: new evidence from fission track dating of basement apatites in the Dry Valleys area, southern Victoria Land. *Earth Planet. Sci. Lett.* **82:1-2**, 1-14

Gleadow, A. J., Gleadow, S. J., Belton, D. X., Kohn, B. P., Krochmal, M. S. and Brown, R. W. 2009. Coincidence mapping – a key strategy for the automatic counting of fission tracks in natural minerals. *Geol. Soc. Lon. Spec. Pub.* **324,** 25-36

Gold, R. Roberts, H. J., Preston, C. C., McNeece, J. P. and Ruddy, F. H. 1984. The status of automated nuclear scanning systems. *Nucl. Track.* **8:1-4**, 187-197

Green, P. F. 1981. "Track-in-track" length measurements in annealed apatites. *Nucl. Tracks.* **5**, 121 – 128

Green, P. F., 1985. Comparison of zeta calibration baselines for fission-track dating of apatite, zircon and sphene. *Chem. Geol.* **58**, 1-22

Green, P. F., Duddy, I. R., Gleadow, A. J. W., Tingate, P. R. and Laslett, G. M., 1986. Thermal annealing of fission tracks in apatite, 1. A qualitative description. *Chem. Geol. (Isot. Geosci. Sect.)*. **59**, 237-253

Green, P. F., Crowhurst, P. V. and Duddy, I. R. 2004. Integration of AFTA and (U-Th)/He thermochronology to enhance the resolution and precision of thermal history reconstruction in the Anglesea-1 well, Otway Basin, SE Australia. PESA Eastern Australasian Basins Symposium II. Adelaide, 19–22 September, 2004

Green, P. F. and Duddy, I. R. 2006. Interpretation of apatite (U– Th)/He ages and fission track ages from cratons. *Earth Planet. Sci. Lett*. **244**, 541–547

Green, P. F., Crowhurst, P. V., Duddy, I. R., Japsen, P. and Holford, S. P. 2006. Conflicting (U–Th)/He and fission track ages in apatite: Enhanced He retention, not anomalous annealing behaviour. *Earth Planet. Sci. Lett*. **250**, 407-427

Guenthner, W. R., Reiners, P. W., Ketcham, R. A., Nasdala, L and Giester, G. 2013. Helium diffusion in natural zircon: Radiation damage, anisotropy, and the interpretation of zircon (U-Th)/He thermochronology. *American Jour. Sci.* **313,** 145-198

Hallam, A. 1971. Mesozoic Geology and the Opening of the North Atlantic. *The Journal of Geology*. **79:2**, 129-157

Harte, B and Voll, G. 1991. The setting of the Ballachulish intrusive igneous complex in the Scottish Highlands. **In**: *Equilibrium and Kinetics in contact metamorphism: The Ballachulish Igneous complex and its Aureole*. Edited by Voll, G., Topel, J., Pattison, D. R. M. and Seifert, F. published by Springer Verlag (Heidelberg). 3-17

Hasebe, N., Barbarand, J., Jarvis, K., Carter, A. and Hurford, A., 2004. Apatite fission-track chronometry using laser ablation ICP-MS. *Chem. Geol.* **207**, 135-145

Hiess, J., Condon, D. J., McLean, N., and Noble, S. R., 2012. 238U/235U systematics in terrestrial uranium-bearing minerals. *Science*, **335:6076,** 1610-1614

Hitchen, K., Stoker, M. S., Evans, D. and Beddoe-Stephens, B. 1995. Permo-Triassic sedimentary and volcanic rocks in basins to the north and west of Scotland. *Geol. Soc. Lon. Spec. Pub.* **91**, 87-102

Holford, S. P., Green, P. F., Hillis, R. R., Underhill, J. R., Stoker, M. S. and Duddy, I. R. 2010. Multiple post-Caledonian exhumation episodes across NW Scotland revealed by apatite fission-track analysis. *Jour. Geol. Soc. Lon.* **167**, 675–694

House, M. A., Wernicke, B. P. and Farley, K. A. 1998. Dating topography of the Sierra Nevada, California, using apatite (U–Th)/He ages. *Nature*. **396**, 66-69

House, M. A., Farley, K. A. and Kohn, B. P. 1999. An empirical test of helium diffusion in apatite: borehole data from the Otway basin, Australia. *Earth Planet. Sci. Lett*. **170:4**, 463-474

House, M. A., Farley, K. A. and Stockli, D. 2000. Helium chronometry of apatite and titanite using Nd-YAG laser heating. *Earth Planet. Sci. Lett*. **183:3-4**, 365-368

Hudson, J. D. 1964. The Petrology of the Sandstones of the Great Estuarine Series, and the Jurassic Palaeogeography of Scotland. *Proceedings of the Geologists' Association*. **75:4**, 499-527

Hurford, A. J., 1977. A preliminary fission track dating survey of Caledonian "newer and last granites" from the Highlands of Scotland. *Scot. Jour. Geol.* **13:4**, 271-284

Hurford, A. J., 1990. Standardization of fission track dating calibration: Recommendation by the Fission Track Working Group of the I.U.G.S. Subcommission on Geochronology. *Chem. Geol. (Isot. Geosci. Sect.).* **80,** 171-178

Hurford, A. J. and Green, P. F. 1982. A user's guide to fission track dating calibration. *Earth Planet. Sci. Lett*. **59**, 343-354

Hurford, A. J. and Green, P. F. 1983. The zeta age calibration of fission track dating. *Isotope Geosci.* **1**, 285-317

Hurley, P. M. 1954. The helium age method and distribution and migration of helium in rocks. **In** *Nuclear Geology* (Ed. Faul, H.). 301-329. John Wiley

Jackson, C. A. L. and Larsen, E. 2008. Temporal constraints on basin inversion provided by 3Dseismic andwell data: a case study fromthe South Viking Graben, offshore Norway. *Basin Research*. **20**, 397–417

Johnson, M. R. W. and Frost, R. T. C. 1977. Fault and lineament patterns in the southern highlands of Scotland. *Geologie en Mijnbouw*. **56**, 287-294

Ketcham, R. A. 2005. Forward and reverse modelling of low-temperature thermochronometry data. *Rev. Min. Geochem*. **58**, 275-314

Ketcham, R. A., Donelick, R. A. and Donelick, M. B. 2000. AFTSolve: A program for multi-kinetic modeling of apatite fission-track data. *Geol. Materials Res*. **2:1**, 1-32

Ketcham, R. A., Carter, A. Donelick, R. A., Barbarand, J. and Hurford, A. J. 2007. Improved measurement of fission-track annealing in apatite using C-axis projection. *American Mineralogist*. **92:5-6**, 799-810

Kohn, B. P., Lorencak, M., Gleadow, A. J. W., Kohlmann, F., Raza, A., Osadetz, K. G. and Sorjonen-ward, P. 2009. A reappraisal of low-temperature thermochronology of the eastern Fennoscandia Shield and radiation-enhanced apatite fission-track annealing. *Geol. Soc. Lond. Spec. Publ.* **324:1**, 193–216

Kyrkjebo, R., Gabrielsen, R. H and Faliede, J. I. 2004. Unconformities related to the Jurassic–Cretaceous synrift–post-rift transition of the northern North Sea. *Jour. Geol. Soc.* **161**, 1-17

Laslett, G. M. 1984. The relationship between fission track length and track density in apatite. *Nucl. Tracks*. **9:1**, 29-38

Laslett, G. M., Kendall, W. S., Gleadow, A. J. W. and Duddy, I. R. 1982. Bias in measurements in fission track length distributions. *Nucl. Tracks*. **6:2-3**, 79-85

Laslett, G. M., Green, P. F., Duddy, I. R., and Gleadow, A. J. W. 1987. Thermal annealing of fission tracks in apatite 2. A quantitative analysis. *Chem. Geol. (Isot. Geosci. Sect.).* **65,** 1-13

Leventhal, J. S. 1975. An evaluation of the uranium-thorium-helium method for dating young basalts. *Jour. Geophys. Res.* **80**, 1911-1914

Lippolt, H.J., Leitz, M., Wernicke, R.S. and Hagedorn, B., 1994. (Uranium+thorium)/helium dating of apatite: experience with samples from different geochemical environments. *Chem. Geol; Isotope Geoscience* **112**, 179–191

Lui, W., Zhang, J., Sun, T. and Wang, J. 2014. Application of apatite U–Pb and fission-track double dating to determine the preservation potential of magnetite–apatite deposits in the Luzong and Ningwu volcanic basins, eastern China. *Jour. Geochem. Explor.* **138,** 22–32

Liu, D., Li, H., Sun, Z., Pan, J., Wang, M., Wang, H. and LuceChevalier, M. 2017. AFT dating constrains the Cenozoic uplift of the Qimen Tagh Mountains, Northeast Tibetan Plateau, comparison with LA-ICPMS Zircon U–Pb ages. *Gondwana Research.* **41**, 438-450

Maurette, M., Pellas, P. and Walker, R. M. 1964. Etude des traces de fission fossils dans le mica. *Bull. Soc. Franc. Mineral. Crist.* **87**, 6-17

McDowell, F. W., McIntosh, W. C. and Farley K. A. 2005. A precise 40Ar–39Ar reference age for the Durango apatite (U–Th)/He and fission-track dating standard. *Chem. Geol.* **214,** 249– 263

McInnes, B. I. A., Farley, K. A., Sillitoe, R. H. and Kohn, B. P. 1999. Application of apatite (U-Th)/He thermochronometry to the determination of the sense and amount of vertical fault displacement at the Chuquicamata porphyry copper deposit, Chile. *Economic Geology*. **94:6**, 937-947

McKerrow, W. S., Macniocaill, C. and Dewey, J. F. 2000. The Cakedonian Orogeny redefined. *Jour. Geol. Soc. Lond.* **157**, 1149-1154

Meesters, A. G. C. A. and Dunai, T. J. 2002a. Solving the production–diffusion equation for finite diffusion domains of various shapes Part I: Implications for low-temperature (U–Th)/He thermochronology. *Chem. Geol.* **186,** 333– 344

Meesters, A. G. C. A. and Dunai, T. J. 2002b. Solving the production–diffusion equation for finite diffusion domains of various shapes Part II: Application to cases with a-ejection and nonhomogeneous distribution of the source. *Chem. Geol.* **186,** 347– 363

Mehta, P. P. and Rama. 1969. Annealing effects in muscovite and their influence on dating by fission track method. *Earth Planet. Sci. Lett.* **7**, 82-86

Mendum, J. R. 2012. Late Caledonian (Scandian) and Proto-Variscan (Acadian) orogenic events in Scotland. *Open University Geological Society Journal.* **33:1**, 37-52

Min, K., Reiners, P. W., Wolff, J. A., Mundil, R. and Winters, R. L. 2006. (U–Th)/He dating of volcanic phenocrysts with high-U–Th inclusions, Jemez Volcanic Field, New Mexico. *Chem. Geol.* **227**, 223–235

Molnar, P. *and* England, P. 1990. Late Cenozoic uplift of mountain ranges and global climate change: Chicken or egg? *Nature.* **346**, 29–34

Moore, I. and Kokelaar, P. 1998. Tectonically controlled piecemeal caldera collapse: a case study of Glencoe volcano, Scotland. *Bull. Geol. Soc. Am,* **110:11**, 1448–1466

Morton, N. 1992. Dynamic stratigraphy of the Triassic and Jurassic of the Hebrides Basin, NW Scotland. *Geo. Soc. Lon. Spec. Pub.* **62**, 97-110

Murray, K. E., Orme, D. A. and Reiners, P. W. 2014. Effects of U–Th-rich grain boundary phases on apatite helium ages. *Chem. Geol.* **390**, 135-151

Naeser, C. W., 1967. The use of apatite and sphene for fission track age determinations. *Bull. Geol. Soc. Am.* **78**, 1523-1526

Naeser, C. W. and Faul, H. 1969. Fission track annealing in apatite and sphene. *Jour. Geophys. Res.* **74,** 705-710

Pattison, D. R. M. 1985. Petrogenesis of politic rocks in the Ballachulish thermal aureole. *University of Edinburgh Ph.D thesis (unpublished)*

Pattison, D. R. M and Harte, B. 2001. *The Ballachulish Igneous Complex and Aureole: A Field Guide*. Published by Edinburgh Geological Society. Printed in Great Britain by Bell and Bain Ltd., Glasgow.

Pattison, D. R. M. and Voll, G. 1991. Regional geology of the Ballachulish area. **In**: *Equilibrium and Kinetics in contact metamorphism: The Ballachulish Igneous complex and* *its Aureole*. Edited by Voll, G., Topel, J., Pattison, D. R. M. and Seifert, F. Published by Springer Verlag (Heidelberg). 19-38

Persano, C., Stuart, F. M., Bishop, P and Barford, D. N. 2002. Apatite (U–Th)/He age constraints on the development of the Great Escarpment on the southeastern Australian passive margin. *Earth Planet. Sci. Lett.* **200:1-2**, 79-90

Persano, C., Barford, D. N., Stuart, F. M. and Bishop, P. 2007. Constraints on early Cenozoic underplating-driven uplift and denudation of western Scotland from low temperature thermochronometry. *Earth Planet. Sci. Lett.* **263**, 404-419

Petford, N., Miller, J. A. and Briggs, J. 2003. The automated counting of fission-tracks in an external detector by image analysis. *Computers and Geosciences*. **19**, 585–591

Piazolo, S., Prior, D. and Holness, M. D. 2005. The use of combined cathodoluminescence and EBSD analysis: A case study investigating grain boundary migration mechanisms in quartz. *Journal of Microscopy*. **217:2**, 152–161

Price, P. B., and Walker, R. M. 1962a. Observation of fossil particle tracks in natural micas. *Nature*. **196**, 732

Price, P. B., and Walker, R. M. 1962b. Observations of charged particle tracks in solids, *Jour. Appl. Phys.* **33**, 3400

Price, P. B. and Walker, R. M. 1963. Fossil Tracks of Charged Particles in Mica and the Age of Minerals. *Jour. Geophys. Res.* **68**, 4847-486

Rabbel, W. and Meissner, R. 1991. The shape of the intrusion based on geophysical data. **In**: *Equilibrium and Kinetics in Contact Metamorphism: The Ballachulish Igneous Complex and its Aureole*. Edited by Voll, G., Topel, J., Pattison, D. R. M. and Seifert, F. published by: Springer Verlag (Heidelberg). 121-134

Read, H. H. 1961. Aspects of Caledonian magmatism in Britain. *Liv. Man. Geol. Jour.* **2**, 653– 683

Recanati, A., Gautheron, C., Barbarand, J., Missenard, Y., Gallagher, K. and Pinna, R. 2017. Helium trapping in apatite damage: insights from overly dispersed (U-Th-Sm)/He dates. Goldschmidt 2017 Abstract

Reiners, P. W. and Farley, K. A. 2001. Influence of crystal size on apatite (U–Th)/He thermochronology: an example from the Bighorn Mountains, Wyoming. *Earth Planet. Sci. Lett*. **188:3–4**, 413–420

Roe, G. H., Montgomery, *D. R. and* Hallet, B. 2003. Orographic precipitation and the relief of mountain ranges, *Jour. Geophys. Res*. **108**, 2315

Ross, R. J., Naeser, C. W., Izett, G. A., Bassett, M. G. and Hughes, C. P. 1978. Fission track dating of Lower Palaeozoic bentonites in British stratotypes, 3rd. Int. Symp. on the Ordovician System, *Progr. Abstr*., Ohio State Univ., Colombus, Ohio

Ross, R. J., Naeser, C. W. and Izett, G. A. 1979. Fission track dating of Lower Palaeozoic volcanic ashes in British Stratotypes, **in**: *Short papers of the 4th Int. Conf. Geochronology, Cosmochronology and Isotope Geology*. Zartman, R. E. ed., *U.S. Geol. Surv*. Open File Rep. 78-701. 363-365.

Rutherford, E. 1905. Present problems in radioactivity. *Pop. Sci. Month*. **May**, 1-34

Schildgen, T. F. Hodges, K. V. Whipple, K. X. Reiners, P. W. and Pringle, M. S. 2007. Uplift of the western margin of the Andean plateau revealed from canyon incision history, southern Peru. *Geology*. **35:6**, 523-526

Seiler, C., Gleadow, A. J. and Kohn, B. P. 2013. Apatite fission track dating by LA-ICP-MS and External Detector Method: How do they stack up? American Geophysical Union, Fall Meeting 2013, abstract #T42C-07

Shuster, D. L. and Farley, K. A., 2005. 4He/3He thermochronometry: theory, practice and potential applications. *Rev. Min. Geochem*. **58**, 181-203

Shuster, D. L., Flowers, R. M. and Farley, K. A. 2006. The influence of natural radiation damage on helium diffusion kinetics in apatite. *Earth Planet. Sci. Lett*. **249**, 148–161

Silk, E. C. H. and Barnes, R. S. 1959. Examination of Fission Fragment Tracks with an Electron Microscope. *Phil. Mag.* **4**, 970

Smith, M. J. and Leigh-Jones, P. 1985. An automated microscope scanning stage for fission-track dating. *Nucl. Tracks.* **10:3**, 395-400

Soderlund, P., Juez-Larre, J., Page, L. M. and Dunai, T. J. 2005. Extending the time range of (U–Th)/He thermochronometry in slowly cooled terranes: paleozoic to cenozoic exhumation history of southeast Sweden. *Earth Planet. Sci. Lett.* **239**, 266–275

Spiegel, C., Kohn, B., Belton, D., Berner, Z. and Gleadow, A. 2009. Apatite (U–Th–Sm)/He thermochronology of rapidly cooled samples: The effect of He implantation. *Earth Planet. Sci. Lett.* **285**, 105–114

Spotila, J. A., Farley, K. A. and Sieh, K. 1998. Uplift and erosion of the San Bernardino Mountains associated with transpression along the San Andreas Fault, California, as constrained by radiogenic helium thermochronometry. *Tectonics.* **17:3**, 360-378

Stephens, W. E. 1988. Granitoid plutonism in the Caledonian orogen of Europe. **In:** *The Caledonian-Appalachian Orogen*. Edited by Harris, A. L. and Fettes, D. J.; published by Geol. Soc. Lon. Special Publications. **38,** 389-403

Stephens, W. E. and Halliday, A. N. 1984. Geochemical contrasts between late Caledonian granitoid plutons of northern, central and southern Scotland. *Transac. Royal Soc. Edin., Earth Sc.* **75**, 259-73

Stock, G. M., Ehlers, T. A. and Farley, K. A. 2006. Where does sediment come from? Quantifying catchment erosion with detrital apatite (U-Th)/He thermochronometry. *Geology.* **34:9**, 725-728

Stockli, D. F., Farley, K. A. and Dumitru, T. A. 2000. Calibration of the apatite (U-Th)/He thermochronometer on an exhumed fault block, White Mountains, California. *Geology.* **28:11**, 983-986

Stone, P., McMillan, A. A., Floyd, J. D., Barnes, R. P. and Phillips, E. R. 2012. *British regional geology: South of Scotland*. Fourth edition. Keyworth, Nottingham: British Geological Survey

Storzer D. 1970. Fission track dating of volcanic glasses and the thermal history of rocks. *Earth Planet. Sci. Lett.* **8**, 55-60

Storzer, D. and Wagner, G. A. 1969. Correction of thermally lowered fission track ages of tektites. *Earth Planet. Sci. Lett.* **5**, 463-468

Strutt, R. J. 1905. On the radioactive minerals. *Proc. Roy. Soc.* **A76**, 88-101

Thiel, K. and Herr, W. 1976. The ^{238}U spontaneous fission decay constant redetermined by fission tracks. *Earth Planet. Sci. Lett.* **30**, 50-56

Thomson, K., Underhill, J. R., Green, P. E, Bray, R. J. and Gibson, H. J. 1999. Evidence from apatite fission track analysis for the post-Devonian burial and exhumation history of the northern Highlands, Scotland. *Marine and Petroleum Geology,* **16**, 27-39

Tranel, L. M., Spotila, J. A., Kowelewski, M. J. and Waller, C. M. 2011. Spatial variation of erosion in a small, glaciated basin in the Teton Range, Wyoming, based on detrital apatite (U-Th)/He thermochronology. *Basin Research.* **23:5**, 571-590

Vermeesch, P., Seward, D., Latkoczy, C., Wipf, M., Gunther, D. and Baur, H. 2007. α-Emitting mineral inclusions in apatite, their effect on (U–Th)/He ages, and how to reduce it. *Geochem. Cosmo. Acta.* **71**, 1737–1746

Vermeesch, P. 2008. Three new ways to calculate average (U–Th)/He ages. *Chem. Geol.* **249**, 339-347

Vermeesch, P. 2010. HelioPlot, and the treatment of overdispersed (U–Th–Sm)/He data. *Chem. Geol.* **271:3-4**, 108-111

Vermeesch, P. and Tian, Y. 2014. Thermal history modelling: HeFTy vs. QTQt. *Earth Sci. Rev.* **139**, 279–290

Wadatsumi, K. and Masumoto, S. 1990. Threedimensional measurement of fission-tracks: Principles and an example in zircon from the Fish Canyon Tuff. *Nuclear Tracks and Radiation Measurements.* **17**, 399–406.

Wagner, G. A., 1968. Fission track dating of apatites. *Earth Planet. Sci. Lett.* **4**, 411-415

Wagner, G. A. and Reimer, G. M. 1972. Fission track tectonics: the tectonic interpretation of fission track apatite ages. *Earth Planet. Sci. Lett.* **14,** 263-268

Wagner, G. A. and Storzer, D. 1972. Fission track length reductions in minerals and the thermal history of rocks. *Trans. Am. Nucl. Soc.* **15**, 127

Watson, J. 1983. The ending of the Caledonian Orogeny in Scotland. *Jour. Geol. Soc. Lon.* **141**, 193-214

Weiss, S. and Troll, G. 1989. The Ballachulish Igneous Complex, Scotland: Petrography, Mineral Chemistry, and Order of Crystallization in the Monzodiorite-Quartz Diorite Suite and in the Granite. *Jour. Pet.* **30:5**, 1069-1115

West A. J., Fox, *M.,* Walker, *T. T.,* Carter, *A.,* Harris, *T.,* Watts, *A. B. and* Gantulga, B. 2013. Links between climate, erosion, uplift, and topography during intracontinental mountain building of the Hangay Dome, Mongolia, *Geochem. Geophys. Geosyst.*, **14**, 5171–5193

Wildman, M., Brown, R., Beucher, R., Persano, C., Stuart, F., Gallagher, K., Schwanethal, J. and Carter, A. 2016. The chronology and tectonic style of landscape evolution along the elevated Atlantic continental margin of South Africa resolved by joint apatite fission track and (U-Th-Sm)/He thermochronology. *Tectonics*, **35:3**, 511-545

Willett, C. D., Fox, M and Shuster, D. L. 2017. A helium-based model for the effects of radiation damage annealing on helium diffusion kinetics in apatite. *Earth Planet. Sci. Lett.* **477**, 195-204

Willett, S. D. 1999. Orogeny and orography: The effects of erosion on the structure of mountain belts. *Jour. Geophys. Res.*, **104**, 28,957–28,981

Wolf, R. A., Farley, K. A. and Silver, L. T. 1996. Helium diffusion and low-temperature thermochronometry of apatite. *Geochem. Cosmo. Acta.* **60:21**, 4231-4240

Wolf, R., Farley, K. and Kass, D. 1998. Modeling of the temperature sensitivity of the apatite (U–Th)/He thermochronometer. *Chem. Geol.* **148:1–2**, 105–114

Zeitler, P. K., Herczeg, A. L., Mcdougall, I. and Honda, M., 1987. U-Th-He dating of apatite: A potential thermochronometer. *Geochem. Cosmo. Acta*. **51**, 2865-2868

Zeitler, P. K., Enkelmann, E., Thomas, J. B., Watson, E. B., Ancuta, L. D. and Idleman, B. D. 2017. Solubility and trapping of helium in apatite. *Geochem. Cosmo. Acta.* **209**, 1-8

Ziegler, P. A. 1988. Evolution of the Arctic-North Atlantic and the Western Tethys. AAPG Memoir 43

Website sources:

Website 1: http://www.autoscan.com/ Last updated (18/04/2017). Accessed (05/05/2017)

Website 2: http://www.bgs.ac.uk/research/energy/geothermal/ Accessed (07/09/2017)